Research & Technology Centre

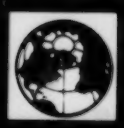

TITLE: FABRICATION AND EVALUATION OF WELDED JOINT STRUCTURES IN MARINE ENVIRONMENTS - PHASE I

Final Report: M.J. Pates, D.J. Burns
U.H. Mohaupt, J.G. Kalbfleisch,
R.S. Lambert, R. Yee

Work on the project was conducted under the auspices of the Canada Centre for Mineral and Energy Technology, Energy, Mines and Resources Canada.

DSS File No. 15SQ.23440-3-9104

DSS Contract Serial No. 0SQ83-00282

CANMET Project No.

CANMET Scientific Authority: Dr. O. Vosikovsky

Date: March 1988

225 pp

MICROMEDIA

FABRICATION AND EVALUATION OF WELDED JOINT STRUCTURES IN MARINE ENVIRONMENTS - PHASE I

"FATIGUE CRACK DEVELOPMENT, THICKNESS AND CORROSION EFFECTS IN WELDED PLATE-TO-PLATE AND PIPE-PLATE JOINTS"

by

D.J. BURNS[1] Professor

U.H. MOHAUPT[1] Adjunct Professor

J.G. KALBFLEISCH[2] Professor

S. LAMBERT[1] Research Assistant

R. YEE[1] Research Assistant

M.J. PATES[3] Project Manager

[1]Mechanical Engineering
[2]Statistics
University of Waterloo
Waterloo, Ontario, Canada N2L 3G1

[3]Program Manager
Materials Technology Centre
Fleet Technology Limited

TABLE OF CONTENTS

	Page
ABSTRACT	i
RÉSUMÉ	ii
1 INTRODUCTION	3
2 FATIGUE TESTS ON T-PLATE JOINTS	4
2.1 Test Joints and Material	4
2.2 Fatigue Test Procedure	5
2.3 Fatigue Crack Detection and Sizing	6
2.3.1 ACPD Measurements at CANMET	6
2.3.2 DCPD Measurements at Waterloo	6
2.4 Test Results	7
2.4.1 Crack Development and Life Definitions	7
2.4.2 Fatigue Tests in Air	8
2.4.3 Fatigue Test in Seawater	9
2.4.4 Statistical Analysis of S-N Data	9
2.4.4.1 Tests at Waterloo - Initiation Life (N_i)	9
2.4.4.2 Tests at Waterloo - Propagation Life (N_p)	10
2.4.4.3 Tests at Waterloo - Total Life (N_T)	10
2.4.4.4 Comparison of CANMET and Waterloo Data	11
3 FATIGUE TESTS ON PIPE-PLATE JOINTS	12
3.1 Specimens, Test Rig and Equipment	13
3.1.1 Specimen Design	13
3.1.2 Test Rig and Equipment	14
3.2 Pipe-Plate Test Results	15
3.2.1 Results for PP0	15
3.2.1.1 Static testing	16
3.2.1.2 Fatigue testing	16
3.2.2 Results for PP1 - Tested In Air	19
3.2.3 Results for PP2 - Tested In Air	23
3.2.4 Results for PP3 - Free Corrosion	25
3.2.5 Results for PP4 - Free Corrosion	26

Page

3.2.6 Results for PP5 - Optimum Cathodic Protection 28
3.2.7 Results for PP6 - Optimum Cathodic Protection 29
3.2.8 Results for PP7 - Cathodic Over-Protection 30
3.2.9 Results for PP8 - Cathodic Over-Protection 31

4 DISCUSSIONS AND CONCLUSIONS 33

4.1 Thickness Effect 33
4.1.1 Effect of Specimen Width On Fatigue Life 34
4.1.2 Fracture Mechanics Models For Predicting Propagation Life 35
4.2 Pipe-Plate Discussion 37
4.2.1 Results in Air 38
4.2.1.1 Initial stress distribution 38
4.2.1.2 Crack shape development 39
4.2.1.3 Crack growth behaviour 40
4.2.1.4 Stress intensity factors 40
4.2.2 Influence of Seawater 42
4.2.2.1 Crack growth rates 44
4.3 Conclusions 45

5 ACKNOWLEDGEMENTS 47

REFERENCES 48

TABLES and FIGURES 50

APPENDIX 1 - Fabrication Details

ABSTRACT

Potential drop techniques have been used to detect the early stages of crack development and to size fatigue cracks in plate-to-plate welded T-joints. This data has been used to assess the influence that stress amplitude, plate thickness and environment have on fatigue crack initiation and propagation. Statistical techniques have been used to interpret the data. Fatigue tests in air indicate that increasing plate thickness decreases initiation and propagation life. Tests in artificial seawater, with or without cathodic protection, indicate that fatigue life is reduced by a factor of 2.5 to 3 with free corrosion and that the beneficial effects, if any, of cathodic protection are too small and variable to account for in life assessments.

A pipe-to-plate specimen has been developed to model the fatigue behavior of welded T-tubular joints. Potential drop techniques have been used to monitor crack development in pipe-plate specimens. This data is compared with similar data for a T-tubular and T-plate joints. Crack growth rates have been used to derive empirical stress intensity factors for comparison with like data published for various tubular configurations. These comparisons indicate that the pipe-plate specimen is a reasonable model of a tubular joint.

Tests on pipe-plate specimens in artificial seawater with free corrosion, optimum cathodic protection or cathodic over-protection confirm the trends observed in the T-plate tests and highlight the influence that these environments have on crack shape development and crack growth rates.

RÉSUMÉ

Les techniques de pertes de potentiel ont été utilisées pour observer les étapes initiales de propagation des fissures et pour évaluer les dimensions des fissures dans les joints plaque à plaque en T. Cette base de données a été employée pour évaluer l'influence de l'amplitude des contraintes, de l'épaisseur de la plaque et de l'environnement sur l'initiation et la propagation des fissures de fatigue. Des techniques statistiques ont été utilisées pour interpréter les résultats. Les tests de fatigue à l'air libre indiquent que le temps d'initiation et de propagation de la fissure diminuent avec une augmentation de l'épaisseur de la plaque. Les tests effectués dans l'eau de mer artificielle, avec ou sans protection cathodique, indiquent que la durée en fatigue est réduite par un facteur de 2.5 à 3 dans le cas de corrosion libre, et que les effets bénéfiques de la protection cathodique, s'ils existent, sont trop petits et variables pour être pris en considération lors de l'évaluation de la durée de vie.

Un spécimen tube sur plaque a été développé pour modéliser le comportement en fatigue d'un joint tubulaire soudé en T. Les techniques de pertes de potentiel ont été employées pour observer le développement de la fissure dans les specimens tube sur plaque. Ces données sont comparées avec des données similaires pour un joint tubulaire soudé en T et pour des joints plaque à plaque en T. Les taux de croissance des fissures ont été utilisés pour obtenir des facteurs empiriques d'intensification des contraintes pour comparer avec des résultats semblables publiés pour plusieurs configurations tubulaires. Ces comparaisons indiquent que le spécimen tube sur plaque est un modéle approprié pour décrire le comportement d'un joint tubulaire.

Les tests sur les spécimens tube sur plaque dans l'eau de mer artificielle avec corrosion libre, protection cathodique optimale ou surprotection cathodique confirment les tendances observées dans les tests sur les joints plaque à plaque en T. De plus, l'influence que ces environnements ont sur le profil de la fissure et sur son taux de croissance a été mise en lumiére.

1 INTRODUCTION

Fatigue tests on welded tubular joints for offshore structures have shown that multiple cracks initiate at the weld toe early in the fatigue life. These grow and coalesce until eventually a large single crack, that tends to be semi-elliptical, forms and propagates through the tube wall. Failure of the tubular joint is usually defined as crack breakthrough the tube wall. In most cases the cracks propagate through the wall of the main tubular member (chord) rather than through the so-called brace tube, see Figure 1(a) which shows a simple T-tubular joint.

The deleterious effects of increasing plate thickness, and of seawater on the fatigue life of tubular joints has received more attention in recent years. Some data has been obtained by testing tubular joints but most of the published data is for so-called plate-to-plate joints, with controlling cyclic stress in the brace (chord) plate. Figure 1(b) shows the T-plate specimen which has been used extensively in the Canadian offshore fatigue program.

The aims of the fatigue test program funded by this contract and of a complementary program at CANMET/PMRL were:

a) to assess the deleterious effect that increasing plate thickness has on the fatigue life of welded joints

b) to assess the deleterious effect that the seawater environment is likely to have on the fatigue life of welded joints on offshore structures. Since cathodic protection systems are used on such structures, this required tests in artificial seawater under three conditions: free corrosion, optimum cathodic protection and cathodic overprotection.

The T-plate specimen shown in Figure 1(b) has been used for tasks (a) and (b). In addition a pipe-to-plate specimen, Figure 1(c), has been developed and used for part of task (b). This specimen offers advantages of cost and ease of analysis compared to tubular joints, Figure 1(a). At the same time it more accurately models tubular crack shape development and large crack growth behaviour than do plate to plate joints.

In section 2 of this report, the test program on T-plate joints, funded by this contract, is presented and correlated with the results of the complementary program at CANMET.

In section 3 of this report, the test program on pipe-plate joints is presented and the results compared with T-plate data and some of the data obtained in another CANMET program on stiffened tubular joints[1].

A feature of the Canadian offshore steel research program on T-plate, pipe-to-plate and tubular (pipe-to-pipe) welded joints has been to use potential drop techniques, with periodic beachmarking on some tests, to detect fatigue crack initiation sites along the weld toe and to monitor crack shape development. In many previous studies of thickness and seawater effects, little or no attempt was made to detect crack initiation and to monitor

crack shape development. Without this physical information, it is difficult to assess the value of some of the linear elastic fracture mechanics (LEFM) assessments that have been made of geometric parameters influencing the thickness effect, and of the influence of cathodic protection on the fatigue life of tubular joints.

The DC potential drop system used in the fatigue programs at Waterloo is described briefly in sections 2 and 3; a detailed discussion of the procedures used to calibrate this DCPD system is given in reference[2]. The AC potential drop system used in the T-plate fatigue program at CANMET is also briefly described in section 2 since the two data sets are compared and combined when assessing the significance of thickness and environment.

The general discussion in section 4 includes some LEFM interpretations of the data. Professor R. Bell of Carleton University has worked closely with the authors on this aspect of the work, see [3,4] and his reports to CANMET/PMRL [5,6].

2 FATIGUE TESTS ON T-PLATE JOINTS

2.1 Test Joints and Material

The T-plate joints had attachment and base plates of equal thickness, see Figure 1(b) and Table 1. The minimum specified yield was 350 MPa; the average of two tests was 421, 405, 390, 370, and 350 MPa for thicknesses of 16, 26, 52, 78 and 103 mm respectively. Chemical compositions and details of the full penetration welds are given in Appendix 1.

The 26 to 78 mm thick plates, manufactured to Lloyd's LT60 specification, were made from the same heat and were normalized. The 16 and 103 mm plates were manufactured to CSA G40.21 Grade 350 WT specification. The 16 mm plate was control rolled. The 103 mm plate, cast as an ingot, was supposed to be normalized. However, after fatigue tests of the first specimens which experienced brittle pop-ins, it was discovered that this heat treatment had not been performed. This means that the 103 mm plate was tested in the as-rolled condition with a fairly coarse ferritic grain structure (40 μm diameter close to the surface, 63 μm close to the centre thickness)[7].

The width (W) of the T-plates, see Figure 1(b), was always 203 mm. The loading spans (L) used in the CANMET tests are listed in Table 1; these were determined by the frame dimensions and actuator capacities of the machines. The loading span (L) used in the Waterloo tests was always nine times the thickness of the plate. This ratio of L/T was chosen because it ensured that the nominal tensile stress in the attachment plate of the specimens was similar to that in the brace of T-tubular joints subjected to axial brace loading. At the time it was argued that the magnitude of the nominal brace (attachment) stress might influence the initiation or direction or rate of growth of fatigue cracks.

The ratio L/T = 9 was obtained as follows. The nominal stress range (σ) in an attachment plate of thickness t, is given by $\sigma = F/Wt$ where W is plate width and F is actuator force. If the reaction supports on the base plate of thickness T, and width W are set at a span L, see Figure 1(b), the nominal bending stress range (S) at the weld toe, ignoring

weld thickness, is given by

$$S = \frac{(F/2)(L-t)T/2}{1/12WT^3} \quad (1)$$

Therefore the ratio of this stress range (S) to the nominal stress range (σ) in the attachment plate is

$$S/\sigma = 1.5\frac{(L-t)t}{T^2} \quad (2)$$

If the stress ratio in the T-plate is to be similar to that in a T-tubular joint subjected to axial loading then published stress concentration factors (SCF) for tubular joints must be substituted for S/σ in equation (2) remembering that in the present tests t=T.

2.2 Fatigue Test Procedure

All joints were tested in the as-welded condition with a load ratio (R) of 0.05 and constant amplitude cycling. As mentioned earlier the loads were applied through the attachment plate. The weld toe (hot spot) stress ranges and the alignment of the specimens were checked by strain gauges, near the weld toes on each side of the attachment. The weld toe on one side of the attachment was ground to ensure that cracking initiated on the other side, thereby reducing by half the number of potential drop probes required to monitor crack development. In only one case did cracks also initiate at the ground toe.

The constant amplitude loads were servo-controlled to produce hot spot stress ranges (S) of up to 300 MPa. For the in-air tests, the loading frequency was in the range 2.5 to 8.0 Hz. For the tests in ASTM standard D1141 synthetic seawater, the frequency was 0.2 Hz and the temperature was 5 $\pm$ 2°C.

Seawater was stored in and recirculated through a 400 litre capacity plastic insulated storage tank. Two hundred litre batches of artificial seawater were prepared at the beginning of each test. The heavier trace elements, stock solution number 3 in the standard, were not used. The seawater was filtered with polyethylene wool to remove rust particles as it was returned to the reservoir. In all tests, air was bubbled through the seawater.

The seawater was cooled using a purpose-built refrigeration unit designed in-house by M. Kaptein. This used freon to cool a glycol workinig fluid, which was circulated through 12.7 mm O.D. stainless steel coils in the reservoir to cool the seawater. The desired temperature was maintained by adjusting the load on the refrigeration system through the use of a parallel heat exchanger in the glycol circuit.

Some specimens were tested in seawater with cathodic protection. Cathodic protection was achieved with an impressed current potentiostat, designed in-house by M. Van Reenen. This system maintains the desired potential between the specimen and a reference electrode immersed in the seawater. The current was impressed through a platinum foil counter electrode, and this current was adjusted via a feedback circuit to obtain the desired level of protection. For these tests, protection levels of -0.850 and -1.050 volts, with respect to a AG/AgCl reference electrode, were used. These correspond to -0.870 and -1.070 volts

with respect to the Calomel electrode actually used to monitor the tests. These constitute optimum and excessive (over-) protection levels, respectively.

2.3 Fatigue Crack Detection and Sizing

2.3.1 ACPD Measurements at CANMET

A combination of beachmarking and AC potential drop measurements was used to determine the shape and the maximum depth of growing fatigue cracks. Four to six beachmarks were produced on each specimen. The first beachmark was made by ink staining to indicate the number and shape of initiated cracks. The first beachmark was applied when the deepest crack reached 2-4 mm depth. The remaining beachmarks were made by a 50% reduction of the load range and doubling the frequency for an appropriate number of cycles to produce a small crack extension. These beachmarks were produced after 3-8 mm crack depth increments. After completion of each test the specimens were broken, and the lengths and maximum depths of each crack indicated by beachmarks were measured to determine their shape, defined by aspect ratio a/2c = max depth/surface length. The maximum depths were also used for calibration of ACPD measurements.

A Unit Inspection Crack Micro-Gauge was used for ACPD measurements. Eighteen probe pairs were spot welded at 10 mm spacing along one weld toe and monitored throughout the test. The depth of the crack when it was first detected depended on its relative location to the ACPD probes. It is estimated that a 0.2 mm deep crack might be detected if a probe pair happened to be located at the middle of the surface length (2c) of the first crack. If the nearest probe pair happened to be not over the crack or not over the crack centre, the sensitivity was lower. An examination of ink stains and PD data indicates that this probe layout and equipment was likely to detect surface cracks with a depth (a) of about 0.5 mm. By chance this also happens to be the detection level estimated for the probe layout and DCPD equipment used in the tests at Waterloo.

2.3.2 DCPD Measurements at Waterloo

A schematic of the pulsed DCPD system designed by M. Van Reenen for this and other crack measurement studies is shown in Figure 2. Two copper bars, screwed to the ends of the base plate, were connected to a 50 Amp power supply. The current was pulsed approximately twice a second. Each active probe pair consisted of two 0.9 mm wires spot welded to the surface, equidistant from the weld toe. The span (s) of the probe pair was 6.35 mm and the pitch (b) of the probe pairs was 12.7 mm. A total of thirteen active pairs plus one reference probe was used. The span for the reference pair was 6.35 mm.

After extensive studies it has been shown that calibrations based on aluminum foil replicas of cracked T-plates can be used to size cracks once coalescence has occurred. When coalescence occurs the crack tends to be a semi-ellipse of low aspect ratio. Prior

to coalescence, the DCPD system will detect but not size the small cracks that form at points along the weld toe.

To illustrate this detection capability, Figure 3 shows the cracks detected by ink staining in two of the T-plate joints tested at Waterloo. This ink staining was done sometime after the PD probes had first detected cracking. It will be noticed that the cracks tend to be semi-elliptic with aspect ratios (a/2c) of 0.25 to 0.33. The data on crack depth (a) and potential drop measurements obtained from probes located somewhere along the crack surface lengths (2c) have been used to prepare Figure 4. This plot of normalized voltage against crack depth differentiates between voltage measurements obtained from probe pairs at or near the centre of a surface crack and measurements from probe pairs well to one side of the crack centre. Figure 4 also shows theoretical estimates, prepared by R. Yee, of the relationship between normalized voltage and crack depth. These estimates were obtained using a These estimates were obtained using a solution for semi-elliptic cracks in a semi-infinite space[8]. Estimates are shown for two aspect ratios, and for two probe positions, see inset diagrams on Figure 4.

The agreement between experimental data and the theoretical solutions is reasonable considering the difference between real and theoretical geometry. Also, the theoretical solutions indicate that crack depths of 0.5 mm should be detectable if electrical noise does not mask the crack signals.

2.4 TEST RESULTS

2.4.1 Crack Development and Life Definitions

Figure 5 and 6 are schematics of crack size and shape development in these T-plate joints. Two crack growth curves, G and H, are shown on Figure 5. In both cases micro-cracks exist or form along the weld toe. Some then coalesce to form small semi-elliptic cracks of low aspect ratio. As these micro-cracks grow, their aspect ratios tend to increase. During the next phase of growth, there is a transition into the macro-crack region. Adjacent cracks interact and coalesce to produce another semi-elliptic crack of lower aspect ratio.

This interaction and coalescence eventually leads to the formation of a dominant irregular crack, Figure 6(b), which then tends to develop into a dominant semi-elliptic crack, usually of low aspect ratio, Figure 6(c).

The difference between cases G and H on Figure 5 is that the next transition is from a semi-elliptic to an edge crack, Figure 6(d), and this occurs at a much smaller crack depth, (a_E compared to $a_{E'}$) in case G. As a result of this earlier transition, the test life of specimen G is shorter than that of specimen H. This occurs because of the significant differences between crack tip stress intensity factors for semi-elliptic and edge cracks.

In this report, the endurance or total life of a specimen (N_T) is that when the maximum crack depth (a) is half of the plate thickness. In some cases, e.g. case G, this crack depth (a_T) is reached after an edge crack has formed and in other cases, e.g. H, before edge cracking.

The detection band for the ACPD and DCPD systems, 0.2 to 0.5 mm, depending on probe position, lies in the micro/macro crack transition region. Detection of a crack of about 0.5 mm depth is used herein to define the end of crack initiation i.e. a crack initiation life (N_i).

2.4.2 Fatigue Tests in Air

Table 2 summarizes the life data obtained in these tests. This data has been used to prepare Figures 7, 8 and 9, which are S-N curves for total life (N_T), initiation life (N_i) and propagation life (N_p) respectively. Visual examination of these three figures clearly indicates that fatigue life (N_i, N_p or N_T) reduces with increase in section thickness and that a statistical analysis is desirable if the thickness effect is to be quantified.

Figures 10 and 11 are plots of N_i/N_T and N_p/N_T against hot spot stress range (S). Figure 10 shows that usually between 20 and 40% of the life had gone before the PD systems detected small cracks about 0.5 mm deep. Visual examination of these curves indicates that there may be a tendency for the initiation ratio (N_i/N_T) to reduce with increase in stress range. However it must be remembered that the total life (N_T) will be reduced if an edge crack forms before the crack depth has reached the defined limit of 50% of plate thickness. This free edge effect will be discussed further in section 4.

Potential drop measurements indicate that for most of the propagation life, the maximum crack depth (a) is less than 20% of the plate thickness (T). Figures 12, 13 and 14 are plots of a/T against percentage of propagation life for all of the plate thicknesses. These figures also indicate that stress range has little or no influence on the relationship between a/T and $\%N_P$. Superimposing the data from Figure 8 and 10 for 26, 52 and 78 mm specimens shows that the relationship between a/T and $\%N_p$ is also independent of plate thickness. The 16 mm data, Figure 12, and the 103 mm data, Figure 14, tend to lie above the data for the other thicknesses. However, as mentioned earlier, brittle pop-ins occurred in the tests on 103 mm joints while the free edge effect (illustrated on Figure 5 by curves G and H) was not an issue in the 16 mm joints (see discussion in Section 4). These factors may well explain any differences between the sets of data on Figure 12-14.

As shown schematically in Figure 6, crack initiation and coalescence leads to the development of a so-called dominant irregular crack with a maximum depth (a_B) and then a dominant semi-elliptic crack with a maximum depth (a_D). Figures 15 and 16 show estimates of a_B and a_D based on beachmark and potential drop measurements. Although there is considerable scatter, these figures suggest that the development of a dominant crack is independent of plate thickness. In other words, coalescence is effectively finished at smaller values of a/T in thicker plates. This observation together with data in Figures 12-14 show that the coalescence phase forms a smaller percentage of the propagation life as the plate thickness is increased. This may be one of the factors contributing to the thickness effect observed in these and other studies. An attempt will be made to illustrate the significance of this difference when crack growth is modelled with LEFM techniques in

Section 4.

Figures 12-16 are based on estimates of maximum crack depth (a). By examining beachmarks and ink stains on the fracture surfaces, it was also possible to estimate the aspect ratios of the various cracks developing along the weld length. For example, five individual cracks in Figure 6(a) eventually coalesce to form one dominant crack, Figure 6(c). Observations of this type have been used to prepare Figure 17. The trend is very clear; as the crack depth increases, its aspect ratio approaches a value of 0.1. The aspect ratio remains at this value if the crack does not reach the free edge. This is shown by path 1,2 on Figure 17. If the crack does reach a free edge, the aspect ratio tends to zero as shown by Figure 6(d) and paths 1 and 2 in Figure 17.

2.4.3 Fatigue Test in Seawater

Table 3 summarizes the test conditions and lives, N_i and N_T, obtained in corrosion fatigue tests on 26 and 78 mm thick T-plate joints. The tests were in synthetic seawater with free corrosion, optimum cathodic protection (-0.85v vs Ag/AgCl) or cathodic over-protection (-1.05v). An examination of the PD data obtained during tests with free corrosion indicated that there were far more initiation sites than in the in-air tests and that an almost straight fronted crack formed when the maximum crack depth was $\leq$ 5 mm. The effect of cathodic protection was to reduce the number of initiation sites to a value comparable to that observed in the in-air tests. This data will now be used for statistical comparisons with the S-N data obtained in air.

2.4.4 Statistical Analysis of S-N Data

Since there were differences in loading spans, test machines and crack monitoring techniques used at CANMET and Waterloo, it was decided to first analyse the two sets of data separately. For convenience the following symbols are used: Y is log life, x is log stress range, ϕ is the reciprocal of thickness T, Δ^2 is the variance and df are the degrees of freedom. Natural logarithms are used throughout.

2.4.4.1 Tests at Waterloo-Initiation Life (N_i)

A series of five parallel lines in x, with a different intercept for each specimen size, was found to give a good fit to the in-air data (Δ^2 = 0.2249, 16 df). A simplification of this model, is that the intercepts are approximately linear in ϕ, the reciprocal of specimen size. The fitted model is then

$$E(Y) = 31.819 + 36.250\phi - 4.150x \qquad (3)$$

with Δ^2 = 0.2042, 19 df. Residual plots are acceptable except for one very large residual corresponding to specimen # 2 of size 16 mm. Investigation revealed that due to human error there were far fewer than usual PD measurements available for estimating the initiation time for this specimen.

The data were reanalysed with the out-lying point (16 mm # 2) removed. The fitted model was then

$$E(Y) = 32.240 + 30.807\phi - 4.214x \tag{4}$$

with $\Delta^2 = 0.1446$, 18 df.

Using this model, equation (4), one can predict "in-air" initiation times for those data points excluded from the analysis i.e # 2,16 mm and the corrosion fatigue tests, see Table 4.

As expected specimen # 2, 16 mm, had a much larger initiation life than predicted; another in air 16 mm specimen, #4, shows a similar trend but there is no obvious explanation for this except scatter. Table 4 shows that initiation occured much earlier in specimens tested with free corrosion, optimum cathodic protection or cathodic over protection. The actual initiation lives being less than half the predicted in-air lives.

2.4.4.2 Tests at Waterloo-Propagation Life (N_p)

Again, a series of five parallel lines in x gives a reasonable fit to the in-air data, ($\Delta^2 = 0.0969$, 16 df), and the intercepts are approximately linear in ϕ. The fitted model is

$$E(Y) = 30.295 + 32.846\phi - 3.601x \tag{5}$$

with $\Delta^2 = 0.1116$, 19 df. In this case specimen 78 mm #3 has a large positive residual and specimen 16 mm # 4 has a large negative residual. However, no explanation has been found which would justify removing them from the analysis.

Table 5 shows predicted propagation times, based on model equation (5), for data points excluded from the analysis. For 16 mm specimen # 2, the propagation time is much smaller than model (5) would predict, which is consistent with the earlier conclusion that its initiation time was overestimated. For specimens tested under free corrosion, optimum cathodic protection or cathodic over protection, propagation times are all about 28% of the values predicted by model (5) for in-air tests.

2.4.4.3 Tests at Waterloo - Total Life (N_T)

The initiation and propagation models, equations (4) and (5), together can be used to predict total lifetime. Very similar results are obtained by analysing the total lifetime data directly. A series of five parallel lines in x gives a reasonable fit to the data ($\Delta^2 = 0.0942$, 17 df), and the intercepts are approximately linear in ϕ. The fitted model is

$$E(Y) = 31.132 + 333.360\phi - 3.7106x \tag{6}$$

with $\Delta^2 = 0.0956$, 20 d.f. Two points, 16 mm # 4 and 78 mm # 3, give large positive residuals.

Table 6 compares "in-air" predictions from model, equation (6), with observed total lifetimes for specimens tested in seawater, with or without cathodic protection. For comparison, the predicted in-air lifetimes from models equation (4) and (5) are 3,087,743 cycles for the 26 mm specimens, and 1,349,044 cycles for the 78 mm specimens.

2.4.4.4 Comparison of CANMET and Waterloo Data

An analysis similar to that used for the Waterloo data was attempted for the CANMET data. A series of five parallel lines in x appeared to give a reasonable fit to the CANMET, in-air data for initiation life, for propagation life, and for total life. However, because there was less data, it was not possible to check the parallel line models as thoroughly as with the Waterloo data. The following are the variance estimates for parallel line models for the in-air, CANMET data.

Initiation	$\Delta^2 = 0.0297$, 8 df
Propagation	$\Delta^2 = 0.0139$, 8 df
Total	$\Delta^2 = 0.0089$, 8 df

Note that the variance estimates are smaller by an order of magnitude than those for the Waterloo data. The CANMET data show an almost perfect linear relationship between log life and log stress; there is much more scatter in the Waterloo data.

As mentioned earlier, the Waterloo results show a linear dependence of log life on ϕ, the reciprocal of specimen thickness, as assumed in the models, equations (4), (5) and (6). Models assuming this linear dependence do not adequately fit the CANMET data, because of the small differences in lifetimes observed in tests on 16 mm and 26 mm specimens. Recognizing this difference, it was decided to re-analyse the two sets of data, separately and together, using a parallel straight line model

$$E(Y) = \alpha + \beta x + e \tag{7}$$

where e is an error term and the slope, β, is assumed to be the same for all specimen sizes. Therefore the intercept, α, reflects the thickness effect plus any effect of the environment. This means that the effect of a particular environment, e.g. free corrosion, is assumed to be the same for all specimen thicknesses. This model, equation (7), was fitted to each data set by least squares. Various statistical tests and graphs were used to check the assumptions of linearity, equality of slopes and additivity on the log scale.

Table 7 summarizes the predictions of this model for specimens tested in air at a stress range (S) of 150 MPa. The analyses for initiation (N_i) and propagation life (N_p) did not include specimen # 2, 16 mm because of the known error in defining the initiation/propagation boundary for this specimen. As well as showing the effect of thickness on life, this table brings out another difference between the Waterloo and CANMET data sets; N_i, N_p and N_T for Waterloo tests were generally larger than for the CANMET tests. This difference may be caused by batch differences or differences in restraint in the loading fixtures used at Waterloo and CANMET; the latter having less degrees of freedom. This difference and the much smaller variance of the CANMET data set indicates that it is not strictly correct from a statistical viewpoint to combine these in-air data sets. Nevertheless, both data sets give a clear indication of trends. In particular both data sets indicate that increasing plate thickness decreases propagation life (N_p); the propagation life for a 103

mm specimen being about one seventh that for a 16 mm specimen. Except for a difference for 103 mm specimens, both data sets indicate that increasing plate thickness also decreases initiation life (N_i).

This model, equation 7, was also fitted to each of the data sets obtained in seawater. To illustrate the effects of free corrosion, optimum cathodic protection and cathodic over-protection, Table 8 lists correction factors, ψ_1, ψ_2 and ψ_3 respectively, that must be applied to air lives predicted by equation (7) for each thickness, see Table 7. In addition, Table 8 lists the slopes (β) and the error variances for the parallel straight line model. Note that in these environments, the variances for the Waterloo and CANMET sets are of the same order.

As mentioned earlier, N_i, N_p and N_T for air tests were generally larger for the Waterloo data. This may partly explain why the correction factors, ψ_1, ψ_2 and ψ_3 are smaller for the Waterloo data. The correction factors for the Waterloo data show that cathodic protection, optimum or over-protection, had very little if any beneficial effect from a fatigue viewpoint. The correction factors for the CANMET data show that cathodic protection, particularly optimum protection, had a small beneficial effect.

Ignoring the statistical differences between the in-air data obtained at Waterloo and CANMET, an overall analysis of the T-plate data shows that the seawater environment reduces the fatigue life by a factor of about 2.5 to 3.0 and that the beneficial effects, if any, of cathodic protection are too small to be recognized in fatigue design guidelines or codes.

3 FATIGUE TESTS ON PIPE-PLATE JOINTS

The pipe-plate specimen has been developed as an alternative specimen to study the fatigue behaviour of tubular welded joints. This specimen is illustrated schematically in Figure 1c. The pipe-plate specimen consists of a pipe welded at right angles to the centre of a flat plate. Under test, the plate is constrained along the edges and a horizontal load is applied to the top of the pipe (brace). This produces a cantilevered bending action in the brace and results in local through-thickness bending stresses in the plate along the weld toe. The constraint on the plate edges is adjusted such that these stresses are maximum at the zero degree or hot-spot location shown in Figure 1(c). Under cyclic loading, fatigue cracks initiate along the weld toe in the plate near the hot-spot. These cracks then grow and coalesce to form a single semi-elliptic crack which eventually penetrates the plate thickness. The fact that the material to be tested must only be supplied in plate form, coupled with the very simple specimen geometry, means that the material and fabrication costs for this specimen are much lower than for a full tubular joint. At the same time, the pipe-plate has no free edges as do plate-plate joints. Thus the pipe-plate is a better model of tubular joint fatigue behaviour, and more appropriate for the study of the influence of seawater on the fatigue behaviour of tubular welded joints. The simple geometry also leads to a simpler analysis which makes the pipe-plate specimen a very powerful tool in

the assessment of LEFM analyses of fatigue crack behaviour in tubular welded joints.

In this section, the test results for the pipe-plate specimens will be presented and discussed. Eight specimens were provided and tested as part of the contract. In addition, a preliminary specimen was fabricated at the University of Waterloo under the supervision of M.J. Pates of AMCA International. All subsequent specimens were fabricated by AMCA in Ottawa. The test matrix for the pipe-plate specimens is shown in Table 9. All tests were performed with constant amplitude loading. The first three specimens were tested in air.

The preliminary specimen, designated PP0, was used to assess the overall feasibility of this model; in particular, to determine how to constrain the base plate, and to determine whether fatigue cracks grew in a manner similar to that in tubular joints. The testing of this specimen led to a revised specimen design which was used in all subsequent tests. The next two specimens, designated PP1 and PP2, were tested in air at hot-spot stress levels of 240 and 160 MPa, respectively. These tests in air were also compared with those from tubular joints to establish the suitability of this specimen to model tubular joint fatigue behaviour. In addition, these three tests in air were used to verify and calibrate the DCPD crack monitoring technique, and to assess Stress Intensity Factor (SIF) calculation procedures. Subsequently, tests were conducted in a seawater environment. Two specimens were tested under freely corroding conditions, two with cathodic protection, and two with cathodic over-protection.

3.1 Specimens, Test Rig and Equipment

3.1.1 Specimen Design

The first pipe-plate specimen, PP0, is shown in Figure 18. It was fabricated at the University of Waterloo from a 457 mm OD pipe with a 12.7 mm wall thickness, welded to the centre of a 26 mm thick plate. The welding procedure was developed by AMCA International based on tubular joint details in the UKOSRP I program, which in turn were based on AWS D1.1 (1976).

The plate material was the same as that used for the T-plate specimens. The pipe material was a structural steel with a minimum 350 MPa yield.

The weld specification is included in Appendix 1. The weld toe length along the base plate was kept to a maximum of 12 mm and the pipe (brace) weld toe length to less than 18 mm. A dime test was used to control the weld toe profile. For specimen PP0, the diameter of the dime was 12 mm and the wire was 1 mm.

The plate for PP0 was approximately 1830 mm long by 1220 mm wide. An extensive array of holes were provided along the edges of the plate to allow for a range of different configurations when bolting the specimen to the load fixture. This allowed a study of varying plate constraint on the stress distribution along the weld.

As a result of the stress analysis and subsequent fatigue testing of PP0, the specimen design was altered, Figure 19. In this design, used for all subsequent tests, the pipe wall

thickness was increased from 12.7 to 30 mm, and the plate size was reduced, with fewer holes specified along its edges. The increased pipe thickness necessitated a change in the welding specification. The revised welding specification is included in Appendix 1. The weld reinforcement was increased to 25 mm along the plate and 41 mm along the pipe. In addition, the weld toe at the pipe was ground. A dime test, with a 25 mm diameter dime and a 1 mm diameter wire, was used to control the weld toe geometry at the plate.

3.1.2 Test Rig and Equipment

In Figure 20, the pipe-plate specimen is shown clamped to the base of the loading fixture. Loading was applied using an MTS servo-hydraulic system. The load is applied horizontally through the pipe, via a pin and yoke arrangement, approximately 1220 mm above the plate surface. This produces a general cantilevered bending in the pipe, and a local bending through the thickness of the plate at the weld toe. With the smaller plate, Figure 19, it was necessary to apply further constraint at the tension end of the plate to obtain a suitable stress distribution. This was achieved by mounting a girder transversely over the tension side of the plate, Figure 20, and by using bolts to bear on the plate surface through a 12.7 mm thick steel pad.

To expose the weld area, on the tension side, to seawater for specimens PP3-PP8, a plexiglas tank was constructed. It consists of a 1.5 mm thick by 150 mm high wall glued to the specimen plate, concentric with, and 100 mm from, the brace, Figure 21. Dividers at the brace neutral axis ensured that seawater flowed only in the 180° test section. The remaining 180° section was left empty to act as an emergency reservoir in the event of an overflow of the test section. Seawater was pumped in at one divider and pumped out at the other to ensure uniform exposure to fresh seawater with no stagnation. A single pump was used to pump seawater in and two, in parallel, were used to pump seawater out. Insulated, 12.7 mm I.D. flexible hoses were used throughout. The flow rate was controlled by adjusting a valve on the input side. Float switches were used to shut off the input and/or output pumps to control the seawater level in the test section. A third float switch acted to shut off all pumps in the event of a very low water level, resulting from a major leak in the system. For the first specimen in seawater, PP3, the seawater in the reservoir was stirred and aerated using a propeller mixer. In all subsequent tests, air was bubbled through the seawater under pressure.

Four specimens, PP5 through PP8, were tested in seawater with cathodic protection. The reference electrode had a plastic tube attached to the end which extended to the weld toe near the hot-spot to measure the potential near the steel surface. The current was impressed through a platinum foil counter electrode, and this current was adjusted via a feedback circuit to obtain the desired level of protection.

For the tests in air, data was collected from strain gauges and potential drop probes throughout the test. For the tests in seawater the strain gauges were removed after the desired load level for testing had been established, and only potential drop readings were

taken during the test. To facilitate this data acquisition, software was written by S. Lambert for a PRO 380 micro-computer, made available through a WATDEC grant. These programs allowed the PRO 380 to control FLUKE and OPTILOG data acquisition subsystems. In addition, potential drop readings were taken with an Analog Data Module (ADM), also supplied through WATDEC. Post-processing routines were written to create most of the plots shown later in this section.

3.2 Pipe-Plate Test Results

As mentioned, the preliminary specimen (PP0) was used to assess how to constrain the specimen and the accuracy of the DCPD crack monitoring system. These results highlighted some problems which resulted in a new specimen design and a more thorough examination of DCPD. All subsequent specimens conformed to the revised design. Two specimens were tested in air (PP1 and PP2), two in seawater with free corrosion (PP3 and PP4), two in seawater with cathodic protection (PP5 and PP6), and two in seawater with cathodic over-protection (PP7 and PP8). For each environment, tests were conducted at hot-spot stress levels of 240 or 160 MPa, under constant amplitude loading at an R-ratio (minimum stress/maximum stress) of 0.05.

3.2.1 Results for PP0

Static tests were performed to determine the influence of plate constraint on the stress distribution. An artificial defect was then introduced at the weld toe at the hot-spot location with a slitting saw. The specimen was cycled through a hot-spot stress range of 175 MPa at an R-ratio of 0.05. This stress range was increased to 225 MPa after 417890 cycles to accelerate the test. During testing, an ink stain and beachmarks were used to mark the fracture surface for comparison with DCPD predictions.

Specimen PP0 was bolted directly to the flat base of the test rig. Although the plate was distorted in the welding process, no attempt was made to accommodate this distortion. This introduced residual reaction strains in the plate which could be typically of the order of 300 μstrain in the vicinity of the weld toe. A wide variety of constraint conditions were examined to study the effect of plate edge constraint on the stress distribution. A typical constraint condition is shown in Figure 22.

Strain gauges were mounted on the plate surface. In general, gauges were mounted both on the top and bottom of the plate to distinguish membrane and bending components of stress. Strain gauges were also mounted on the outside surface of the pipe.

Potential drop probes were spot-welded along the weld toe on the plate and the weld reinforcement as shown in Figure 23. These active probes were concentrated in a region within 165 mm from the hot-spot ($\pm$ 37°). In addition, far-field reference probes were mounted about 100 mm radially outward from the weld toe at 15° increments from the hot-spot. The potential drop probe locations are given in Table 10. The current was input

to the top of the plate at five discrete locations, distributed at equal distances from the weld toe and covering a region within 45° of the hot-spot. The current was removed from the centre of the plate at the bottom.

3.2.1.1 Static testing

Plate surface stresses along a radial line at the hot-spot location are shown in Figure 24. These stresses have been normalized with respect to the hot-spot stress. The hot-spot stress was obtained by linearly extrapolating the radial stresses, from the two strain gauge positions closest to the weld toe, to the actual weld toe. These two gauges were positioned following UKOSRP recommendations assuming a ficticious chord diameter of 914 mm. This chord diameter was selected as being typical of joint sizes tested in the European programmes. From Figure 24 it can be seen that the stresses increase linearly within about three plate thicknesses from the weld toe. Therefore, the calculated hot-spot stress is relatively insensitive to the assumed gauge locations.

The stress concentration factor (SCF) is defined as the ratio of the hot-spot stress to the nominal stress in the brace (or pipe). This nominal stress is the outer fiber stress in the brace obtained from the applied loading using the simple beam formula. In this case the SCF is about 6. Various conditions of plate constraint yielded SCF's in a narrow range from 6 to 8. Transverse stresses, as measured 13 mm from the hot-spot, were from 40-50% of the corresponding radial stress. The membrane component of stress was always less than 10% of the total at the hot-spot location. Membrane/bending proportions were significantly influenced by changes in plate end constraints. Changes in lateral support were relatively unimportant. The results for several conditions of plate constraint are given in Table 11.

Plate surface stresses along a circumferential line, 60 mm from the weld toe, are shown in Figure 25. The radial stress is maximum at 0°, and decreases gradually within 45° of the hot-spot. Thereafter, it decreases sharply to zero at ± 90° from the hot-spot, corresponding to the neutral axis for pipe bending.

The stresses at the hot-spot location on the surface of the pipe are shown in Figure 26. For this specimen geometry, for all conditions of plate constraint, the surface stresses in the pipe, extrapolated to the weld toe, were of similar magnitude to the hot-spot stress in the plate. There was concern that this similarity between the hot-spot stresses in the pipe and in the plate might lead to toe cracks in the pipe in subsequent fatigue testing. To avoid this, an artificial defect was introduced into the plate at the hot-spot location. A 44.5 mm diameter by 0.5 mm thick slitting saw was used to cut a semi-circular scallop at, and aligned with, the weld toe to a depth of about 3 mm. All subsequent specimens were fabricated using a thicker wall (30 mm) pipe, and the pipe weld toe was blended in to eliminate the possibility of pipe cracking.

3.2.1.2 Fatigue testing

Specimen PP0 was loaded with a constant amplitude sine wave giving a hot-spot stress

range of 175 MPa at an R-ratio of 0.05. After 417890 cycles the stress range was increased to 225 MPa to accelerate the test. At several points throughout the test the fracture surface was marked for subsequent comparison with DCPD predictions. At 321120 cycles the weld toe was wet with ink. Later, at 517890, 676160 and 768130 cycles, beachmarks were left on the fracture surface by reducing the stress range by 50% and increasing the mean stress to maintain the same maximum stress level. This loading was applied for about 30000 cycles in each case.

The measured saw cut, ink stain and beachmarks are shown in Figure 27 along with DCPD predictions. The vertical (depth) axis in this figure has been expanded about four times for clarity, and therefore the cracks appear to have an abnormally high aspect ratio. An extensive examination of the DCPD system and its calibration was undertaken to explain the obvious discrepancy between the actual and predicted crack depth. A more uniform current distribution was obtained in subsequent specimens by forming 25 mm square current input bars into semi-circular arcs, as opposed to the discrete point sources distributed along an arc for PP0. The effective input current was also doubled by switching the current polarity instead of pulsing between zero and maximum current. In addition, local reference probes were introduced to try to account for any local current redistribution as the growing crack approached the back face of the specimen.

One explanation for the underprediction of crack depth in Figure 27 is that current is redistributing around the relatively high aspect ratio crack which grew from the artificial defect. Although some of the errors could be attributed to the high aspect ratio of the crack which grew in this specimen from the original artificial defect, the source of the remaining errors is unknown. In subsequent tests, natural crack growth led to a more flat-fronted, low aspect ratio crack, and the DCPD predictions were much improved.

Figure 28 shows the potential drop calibration curve for PP0 obtained from an aluminum foil analogue, along with a plot of measured normalized potential drop versus corresponding measured crack depths at the hot-spot location for the saw cut, ink stain and beachmarks. These actual results were used to obtain a corrected calibration curve (shown with a dotted line in the figure), which was then applied along the entire crack front. This calibration curve was obtained by fitting a least squares cubic polynomial to the actual data. With this new calibration curve, which has been used only for this specimen, further analysis of the potential drop data was possible. Figure 29 illustrates the revised crack profile comparison with beachmarks. The solid lines represent the measured beachmarks and the symbols the potential drop predictions. As expected, the results are much improved over Figure 27, and are obviously exact at the hot-spot location from which the calibration has been derived. There is still, however, an over-estimation of the crack surface length; most likely due to the three dimensional nature of the potential field.

To assist in subsequent analysis of this data, non-linear regression techniques were applied to fit semi-ellipses to the potential drop data. Basically, the procedure involves the fitting of a semi-ellipse to successive sets of DCPD results. The results from this procedure are shown as dotted lines in Figure 29. This analysis was performed for PP0 using the saw-

cut information as a starting point, and continued until more than 80% wall penetration. This analysis provides an estimate of the crack depth and surface length, from which the aspect ratio may be determined.

The aspect ratio development for PP0 is shown in Figure 30. Here the crack aspect ratio is plotted versus the centre line depth. The symbols represent measurements from the actual saw cut, ink stain, and beachmarks while the solid line represents the results from the semi-elliptic curve fitting routine mentioned above. There is good agreement between the curve fit data and the direct measurements. The crack started with an aspect ratio of about 0.12 at a depth of 3.5 mm as a result of the saw cut. The aspect ratio increased to a maximum of about 0.21 at 7.5 mm and decreased thereafter. This data provides an opportunity for comparison with analytical predictions of crack growth behavior of a single crack at the toe of a fillet weld, since the initial saw cut probably precluded any large influence of crack coalescence. However, the experimental crack growth along the surface may still be faster than analytical predictions, due to the damage that may be caused at the weld toe as a result of the stress concentration.

Figure 31 shows the crack growth behaviour versus cycles at the hot-spot location, i.e. probe 26. The maximum crack depth was about 3.5 mm after the saw cut and increased steadily until about 418k cycles, at which point the applied load was increased to accelerate the test. It must be remembered that the potential drop calibration curve used to obtain this plot was based on actual data to about 19 mm, see Figure 28. As the crack approaches through thickness, the normalized potential drop does not increase as dramatically for the corrected calibration curve as it does for the foil results. This means that the results for very deep crack depths are unreliable and therefore are not shown in Figure 31. If a realistic calibration curve were used, a significant falling off of crack growth rates would be evident beyond 80% wall penetration. This decrease in crack growth rates beyond 80% wall penetration is associated with a curvature of the actual crack growth plane, Figure 32. The crack front begins to curve beyond about 21 mm and by about 23 mm penetration is travelling parallel to the back face of the plate. Final breakthrough occurs by a shearing of the remaining ligament. Examination of the microstructure of the plate through the thickness revealed no material faults or discontinuities at the 23 mm position and therefore this phenomenon is attributed to the stress distribution and the geometry of the cracked joint. All subsequent pipe-plate specimens cracked in a similar manner. Therefore the life of these pipe-plate specimens will be quoted as the life to 80% wall penetration.

Instantaneous crack growth rates were obtained by differentiating the crack growth curve in Figure 31. This was performed by fitting a least-squares parabola to successive sets of 7 points as per the recommendations in ASTM 647. The resulting crack growth rates from this analysis are shown in Figures 33a and 33b versus cycles and crack depth, respectively. Note that data for crack depths greater than about 19 mm are not shown. There is a more-or-less steady crack growth rate to about 420k cycles (8 mm), at which point the load was increased. This resulted in a discontinuity in the crack growth rate curves and thereafter the crack growth rate increased steadily. This change from steady to

accelerated crack growth is not necessarily directly related to the change in load levels. A more direct relationship is likely between the crack growth rates and the change in aspect ratio behaviour as evident in Figure 30. It is unclear whether the change in load level influenced the aspect ratio development.

This crack growth rate information can be used to provide information on the stress intensity factor history for this specimen. The procedure is based on the assumptions that there is a unique relationship between the stress intensity factor range and the ensuing crack growth rate, and that this relationship is known. For our purposes, it is assumed that this relationship is adequately described by the Paris-Erdogan equation with material constants, C and m, obtained from a review by Booth and Dobbs[9], i.e. $C = 7.14 \times 10^{-13}$ and $m = 3.66$. These are mean values and correspond to crack growth rates in m/cycle and stress intensity factors in MPa$\sqrt{\text{m}}$. The results from this procedure are shown in Figure 34 where the stress intensity factor range is plotted versus the crack depth. The dotted and dashed lines represent calculations based on ($m = 3.66$) and upper ($C = 14.7 \times 10^{-13}$) and lower ($C = 3.46 \times 10^{-13}$) bound (95% confidence levels) crack growth rates reported for air. These result in lower and upper limit estimates to the stress intensity factors, respectively. Since the results in [9] were based on data obtained from several sources, the limits are likely to be quite generous.

It is useful to plot this empirical stress intensity factor information in normalized form to remove the dependence on load level, and hence to remove the discontinuity when the load level was increased during this test. In Figure 35 this empirical stress intensity factor data has been normalized with respect to the stress intensity factor for a slit in an infinite plate, subjected to an alternating uniform stress field equivalent to the range in hot-spot stress, $\Delta\sigma_{hs}$. This stress intensity factor is $\Delta\sigma_{hs}\sqrt{\pi a}$, where a is the crack depth in our case. Again, upper and lower limits are shown.

Figures 36 and 37 present the redistribution in plate surface stresses during cracking. Figure 36a shows a significant reduction in radial stresses at the hot-spot location with increasing crack depth. A much less significant decrease in tangential stresses occurs, Figure 36b. Figure 37 illustrates the stress redistribution along the weld at a distance of 60 mm from the weld toe. Again, the radial component of stress changed more significantly (Figure 37a), than did the tangential component (Figure 37b).

3.2.2 Results for PP1 - Tested In Air

The first true fatigue specimen, PP1, was prepared with strain gauges as shown in Figure 38. As with PP0, strain gauges were mounted on both the top and bottom of the plate in pairs. In addition, some gauges were mounted on the outside surface of the pipe to check that, as a result of the increase in pipe wall thickness, the hot spot stress was lower than in the plate. The specimen was then bolted to the base of the loading frame as shown in Figure 39. For this, and all subsequent specimens, the loading was such that the ram pulled on the top of the specimen to produce a tensile local bending in the plate on the

side away from the reaction support, Figure 20. Due to the welding operation the plate was distorted, concave upwards. This distortion was more severe than that for PP0 and was about 13 mm from the centre of the plate to the edge. To avoid a buildup of reaction stresses when bolting the plate to the load fixture, shims were used at each bolting location and strain gauges were monitored. In general, strains induced as a result of clamping the specimen to the base were less than about 60 μ strain.

The specimen was loaded through the brace and strain gauges were monitored. Initial tests indicated that the plate surface stresses were maximum approximately 45° on either side of the desired hot-spot location (0°). To rectify this situation, a girder was positioned across the tension side of the plate and about 75 mm above the plate surface. Two bolts contacted the top surface of the plate, through a 13 mm thick plate, as shown in Figure 39. The position of these bearing points was selected to achieve a suitable stress distribution along the weld toe, i.e. maximum at the hot-spot location and decreasing (by about 25%) at 45° from the hot-spot. This stress distribution was selected to ensure that cracking initiated towards the centre of the specimen, near the 0° line, and that subsequent crack growth was symmetric.

Potential drop probes were spot-welded to the plate surface and weld reinforcement as shown in Figure 40. As with PP0, active probes were mounted straddling the weld toe with a 6.35 mm span. They were grouped within a region ± 200 mm from the hot-spot (± 45°). In addition, far-field reference probes were positioned about 100 mm from the weld toe within the same ± 45° region. Unlike PP0 however, these reference probes had a 25 mm span. Also, local reference probes were used; one for every four active probes, approximately. These shared one common probe connection with the corresponding active probe and had a span of 25 mm, see Figure 40. Potential drop probe locations are given in Table 12. The current input arrangement was also altered for this, and all succeeding specimens, in an attempt to ensure a more uniform radial current field. The input and output connections were part-circular 25 mm square copper bars bolted securely to the plate surface, concentric with the pipe, Figure 40.

Plate surface stresses along the zero degree line (at the hot-spot) are shown in Figure 41. These have been normalized with respect to the hot-spot stress. As with PP0, the stresses are linear within about three plate thicknesses from the weld toe. Therefore, the extrapolation used to obtain the hot-spot stress is relatively insensitive to the selected strain gauge positions. These positions were again chosen using UKOSRP recommendations with a ficticious chord diameter of 914 mm. As with PP0, the stresses at the hot-spot are mainly bending with a small membrane component. The membrane stress is lower than for PP0. In fact, the membrane component for this specimen is slightly compressive. This may be a result of the reduced in-plane restraint on the ends of this specimen compared with PP0. The stress concentration factor for this specimen, is considerably higher, about 14, than that for PP0. This can be attributed largely to the thicker brace wall thickness, which produces a reduced nominal bending stress in the pipe for a given load.

Plate surface stresses along the weld, at a distance of 40 mm radially out from the weld

toe, are shown in Figure 42. The radial stress is maximum at the hot-spot location and decreases gradually by about 25% at positions 45° from the hot-spot. Thereafter the radial stress decreases to zero at ± 90°, at the neutral axis for pipe bending. The stresses on the outside surface of the brace are shown in Figure 43. The stresses have been normalized with respect to the corresponding hot-spot stress in the plate and it can be clearly seen that the stresses in the brace, extrapolated to the weld toe, are about one half those in the plate. This, in conjunction with the brace weld toe grinding that was performed, eliminated the possibility of brace weld toe cracking.

PP1 was fatigue tested at a hot-spot stress range of 240 MPa at an R-ratio of 0.05. At 126380 cycles there was some indication of crack growth from the potential drop system so the weld toe was wet with ink to mark the crack depth. Subsequently, at 269680, 384240, 467780, and 593810 cycles, beachmarks were left on the fracture surface. These beachmarks were achieved by reducing the stress range by a factor of two while maintaining the same maximum stress level for approximately 30000 cycles. After final fracture the ink stains and beachmarks were measured with a travelling microscope and compared with potential drop predictions. The fourth beachmark was placed after it was suspected that the crack plane had curved parallel to the backface of the plate; this proved to be correct so no detailed measurements will be presented. have been taken.

The comparison between the predicted and actual crack depths is shown in Figure 44. The solid line represents the measured beachmarks and the symbols the predicted crack depth. The calibration curve was obtained from a two-dimensional foil analogue, with an idealized 45° weld profile, with no corrections whatsoever. The results are clearly much improved over PP0. The dotted lines shown in Figure 44 correspond to ±5% tolerance on the measured beachmarks. Most of the predicted crack depths are within this range.

An analysis of this data using either local or far-field reference probes gave the same results. This indicates that there was no significant current redistribution for deeper cracks in this specimen.

The crack shape development for PP1 is summarized in Figure 45 in terms of crack aspect ratio versus crack depth. This figure is more complicated than that for PP0 due to the presence of multiple cracks and the ensuing coalescence of these cracks. At least two cracks were evident when the weld toe was stained with ink. These cracks grew and coalesced to form a single crack at about the time of the first beachmark. Beyond this the single crack grew with an aspect ratio which remained essentially constant at about 0.05. In Figure 45, the symbols represent measurements from the ink stains or beachmarks and the lines represent results from fitting semi-ellipses to the potential drop data using least squares regression. The results for PP0 are also shown in Figure 45. As a result of the dominance of the single crack growing from the initial saw cut, coalescence was not a factor for PP0 so the aspect ratio remained higher for PP0 throughout its life. There is a tendency for the aspect ratios for these two specimens to converge at very deep crack depths.

The ink stain on PP1 indicated the presence of two distinct cracks at 126280 cycles;

one 25 mm to the right of the hot-spot (probe 27) and a second, smaller one 102 mm to the left of the hot-spot (probe 8). The crack growth behaviour at these locations and at the hot-spot (probe 24) is shown in Figure 46. A more detailed look at these results shows that the two cracks initiated at approximately the same time, at 58000 and 55000 cycles respectively. Thus the crack on the left initiated first, but because it initiated in a lower global stress region, the crack closer to the hot-spot grew faster and subsequently dominated. For all three probe locations illustrated in Figure 46, the crack growth began to decrease after about 50% wall penetration and at about 90% wall penetration the growth through the wall had almost stopped. After final fracture an examination of the crack front showed that the crack had begun to curve in the direction under the weld reinforcement at about 0.8T and that by 0.9T was growing parallel to the plate back surface. Breakthrough occurred by shearing of this ligament and was first noticed at about 600000 cycles, at which point the crack was about 40 mm long on the underside. As with PP0, the useful life of this specimen is defined as the time for the crack to grow to 0.8T, i.e. at the onset of crack front curvature. Note that in Figure 46 the crack growth curves have been modified by eliminating the cycles corresponding to the placement of the beachmarks. Otherwise, short (30000 cycle) discontinuities would be present.

Before the specimen was instrumented and tested, a plaster of Paris mold was taken of the weld reinforcement profile. After completion of the test, and the determination of the initiation locations, the mold was sectioned and the weld profile measured at the three locations corresponding to the crack growth data in Figure 46. These shapes are shown in Figure 47. There is little macroscopic evidence to suggest why initiation occurred first at these locations.

Crack growth rates have been obtained by differentiating the crack growth curves in Figure 46 using the procedure outlined in the previous section. These crack growth rates, expressed in microns per cycle, are presented versus cycles and crack depth in Figures 48a and 48b respectively. After initiation the crack growth rate increases rapidly to a steady value representing the growth of single cracks in relative isolation. At about 300k cycles, coalescence occurs and the growth rates of all cracks increases markedly to a maximum of about 0.13 microns per cycle at about 350k cycles and 12 mm crack depth. Thereafter the crack growth rates decrease for all probes illustrated.

This crack growth rate information has been used to obtain empirical stress intensity factors. These are plotted in Figure 49 and in normalized form in Figure 50. For crack depths greater than about 5 mm, the indicated stress intensity factor range is between 20 and 30 MPa$\sqrt{\text{m}}$. Figures 51 and 52 present the same type of information as Figures 49 and 50; however, in these figures, results for a single probe are illustrated with lines corresponding to the mean and 95% confidence limits for the Paris rule constants obtained from the review by Booth and Dobbs [9]. These lines therefore represent confidence limits on the value of the stress intensity factors obtained using this procedure.

In Figure 52, the stress intensity correction factors are compared with corresponding mean data for PP0. There is a noticeable difference in the stress intensity correction factors

over the range from 5 to 20 mm which can be attributed largely to differences in aspect ratio development over this same range as a result of coalescence in PP1. The results converge for very deep crack depths as the measured aspect ratios tend to similar values. It must also be remembered that the geometry of these two specimens, specifically the brace wall thickness and the weld reinforcement detail, were different.

The stress redistribution for PP1 with crack growth is illustrated in Figures 53 and 54. The stress redistribution at the hot-spot location is broadly similar to that for PP0. Along the weld, however, there is a more extensive redistribution resulting from the lower aspect ratio crack that developed in PP1.

3.2.3 Results for PP2 - Tested in Air

The next pipe-plate specimen, PP2, was tested in air with strain gauges and potential drop probes. The potential drop probes were spot-welded to the specimen as for PP1 with the exception that far field reference probes were no longer used, Figure 55. The positions of the potential drop probes are given in Table 13.

The measured initial plate surface stress distribution was similar to that for PP1 and is shown in Figures 56 and 57. PP2 was tested at a hot-spot stress range of 160 MPa at an R-ratio of 0.05. At 360000 cycles the weld toe was wet with ink to mark the crack surface. Subsequently, at 700000, 900000, 1300000, and 1600000 cycles, beachmarks were left on the fracture surface. This was achieved by reducing the applied load range by a factor of two and increasing the mean load to maintain the same maximum load level. The specimen was loaded in this manner for 70000 cycles for each beachmark. The fifth beachmark, at 1600000 cycles, was placed after the crack front had curved parallel to the backface of the plate.

A comparison between the ink stain and beachmark results, with the potential drop predictions is shown in Figure 58. The solid line represents the measured beachmarks and the symbols the DCPD predictions. The dotted lines represent $\pm 5\%$ ranges on the measured beachmarks. The deepest ink stain occurred at probe 19, 32 mm to the left of the hot-spot. The depth at this point is about 3 mm and, as expected, due to the semi-elliptic shape, the depth is underestimated by the PD system. For the first beachmark which, at its maximum depth, (again at probe 19) is about 7.5 mm, the prediction is much improved. This is largely due to the more flat-fronted shape. For the deeper cracks the predictions are generally within 5%, since the flat-fronted shape better approximates the two-dimensional geometry from which the calibrations were derived.

The aspect ratio development for PP2 is illustrated in Figure 59, along with data shown previously for PP1. Very many more distinct initiation sites were visible when the fracture surface was stained with ink than were evident for PP1. These cracks were quite small, less than about 3 mm, and had a wide range of aspect ratios from 0.2 to 0.5. As these cracks grew they coalesced with neighboring cracks while other cracks initiated. Thus it is difficult to follow the progression of any particular crack. For cracks less than about 10 mm, there

is a general tendency for the aspect ratio to decrease as the crack depth increases; this is largely due to the process of coalescence. A dominant crack emerged at about 10 mm, and the aspect ratio remained approximately constant thereafter at about 0.05. This behaviour for deeper cracks is the same as for PP1. Thus, despite very different early crack shape development, many more cracks being evident for PP2, there is a tendency toward the same aspect ratio development late in the fatigue life.

An examination of the PD results and the ink stains indicates the presence of multiple initiation sites near probes 16 and 17, 19, 25 and 26, and 29 and 30. Unfortunately, the actual cycles to initiation is impossible to establish accurately due to excessive noise in the instrumentation. This problem was diagnosed and corrected at 200000 cycles. Since the actual crack depths were still quite small at 200000 cycles, the error in the measurement of larger cracks is minimal.

All of the above mentioned sites showed some indication of initiation by 200000 cycles. The crack at probe 19, 32 mm to the left of the hot-spot, appears to have initiated first at between 100000 and 150000 cycles. The crack growth characteristics for three locations, at probes 17, 19, and 24, are shown in Figure 60. The useful life of this specimen is approximately 1.2 million cycles, with coalescence occurring between 500000 and 800000 cycles. The crack had not broken through the wall, however, until after about 2.5 million cycles. By this time a large crack had initiated and grown on the compressive side of the specimen, 180° from the hot-spot. While this crack was not monitored and was only detected late in the test, it is believed that this crack initiated late in the fatigue life and grew relatively slowly. Thus having an insignificant effect on the crack growth behaviour of the cracks on the tension side. An examination of PP1, and all subsequent specimens, indicated no such cracking.

The stroke of the loading actuator was measured at intervals during the fatigue life and is plotted versus cycles in Figure 61a and versus crack depth in Figure 61b. In these figures, the stroke has been normalized with respect to the initial deflection for the uncracked specimen and hence represents the relative change in overall specimen compliance with fatigue cracking. The compliance has remained essentially unchanged for 75% of the useful fatigue life, and then increases by about 20% by 1.2 million cycles. Thereafter the compliance increases more gradually until near the end of the test, at which point the compliance again increases more sharply. This increase in compliance very late in the life may be associated with the advent of the large crack on the compression side of the specimen.

The crack growth rates for the three probes presented in Figure 60 are shown in Figure 62. Although there is considerable scatter in these results, there is a steady increase in crack growth rates after initiation to a maximum of about 0.4 microns/cycle at about 1.0 million cycles and about 0.5T. These maximum measured crack growth rates, excluding 'spikes' caused by discontinuities resulting from the beachmarking process and the higher rates at the hot-spot where it was trying to catch-up with neighbouring cracks, were about one third those for PP1.

The crack growth information for PP2 has been used to obtain the empirical stress intensity factor plots, Figures 63 and 64. These are broadly similar to the corresponding graphs for PP1, Figures 49 and 50. Confidence limits are illustrated in Figures 65 and 66 based on the Booth and Dobbs data discussed previously. In Figure 66, mean data for PP1, probe 24, are superimposed on results for PP2. In general, the values for PP1 were somewhat lower than for PP2 but there is no appreciable difference for the probes illustrated in Figure 66.

The stress redistribution for PP2 along the radial line through the hot-spot is illustrated in Figures 67a and 67b. The radial stress decreases monotonically with a rapid decrease during coalescence, between the first and second beachmarks. The transverse stress, like PP1, is affected less with evidence of a slight recovery for very deep cracks. The radial stress redistribution along the weld, Figure 68a, is significantly influenced by cracking and is slightly asymmetric. There is evidence of a slight increase in stress at the $\pm$ 45° locations for the deeper cracks. There is little significant redistribution of the transverse stresses, Figure 68b.

3.2.4 Results for PP3 - Free Corrosion

The remaining specimens were tested in a seawater environment. Therefore, a less extensive array of strain gauges were mounted on each specimen, Figure 69. These were used only at the beginning of each test to aid in bolting the specimen to the base of the test rig with minimal distortion and to establish the loading level. All strain gauges were removed before the test section was filled with seawater and the test begun. Potential drop probes were mounted to specimen PP3 in a pattern similar to that in PP2, Figure 55. The actual positions are listed in Table 14. For PP3, the probes were much longer (about 200 mm) so that the solder connections to the wires leading to the multiplexers could be made above the level of the seawater. The technique for potential drop measurements in a seawater environment had been developed for earlier testing of plate-plate welded joints.

PP3 was tested at a hot-spot stress range of 240 MPa at an R ratio of 0.05, at a frequency of 0.2 Hz, in a freely corroding seawater environment. The seawater was cooled to maintained the specimen in a temperature range from 2-8 °C. Unfortunately, problems with the refrigeration unit occurred shortly after start-up, and the temperature was allowed to rise to about 10 °C until 85000 cycles. The seawater was circulated in the moat-like test section surrounding the weld and the remainder of the specimen was insulated with fiberglas. Due to the corrosive action of the seawater on the fracture surface, no attempt was made to leave beachmarks.

Figure 70 shows the crack shape development for PP3. First indication of initiation appears at about 20000 cycles at probe 17, about 65 mm to the left of the hot-spot. Probe 37, about 65 mm to the right of the hot-spot, has initiated at about 36000 cycles. A number of probes, specifically 5, 12, 24, and 27, initiated soon thereafter at about 40000 cycles. These initiation sites grew and coalesced to form a single, long, shallow crack at

about 90000 cycles. Thereafter the crack grew relatively quickly through the thickness.

The aspect ratio development of the cracks in this specimen has been estimated from the DCPD results. These are presented in Figure 71 along with results for PP1 and PP2. No information is available for aspect ratios less than about 5 mm since no beachmarking was possible in the seawater environment. For cracks between about 5 and 15 mm deep, the observed aspect ratios were lower than those observed in air as a result of earlier coalescence. The aspect ratio just after coalescence, at about 7 mm maximum crack depth, was about 0.025. This increased to about 0.04 at 80% wall penetration and is about 20% lower than those in air.

The crack growth for probes 17, 27 (at the hot-spot) and 37 are shown in Figure 72 along with the early part of the growth curve for probe 27 of PP1. This plot indicates very slow growth for probe 17 until about 80000–90000 cycles. At this point, the crack coalesced with its neighbours, and the resulting long shallow crack grew rapidly. The crack growth tapered off at about 160000 cycles, as the crack front approached the backface of the plate. Here, the crack front curves slightly. This curvature, however, was not as pronounced as that for the corresponding air test, and final breakthrough occurs shortly thereafter at about 195000 cycles. By comparison, probe 27 of PP1 illustrates much slower growth over the range illustrated in Figure 72. Coalescence did not occur for PP1 until well after 200k cycles and 5 mm crack depth.

Crack growth rates for probes 17, 27 and 37 are shown in Figure 73. The crack growth rates increase monotonically after initiation to reach a maximum of about 0.30 microns/cycle at about 125000 cycles. This corresponds to a 10–15 mm deep crack. The crack growth rate diminishes after this steadily until the practical end of the test at 160000 cycles. For comparison, results for probe 27 of PP1 are superimposed on Figure 73b. The crack growth rates are consistently higher for the seawater environment except for very deep crack depths, where results tend to converge.

Overall, the fatigue life of this specimen, in a freely corroding seawater environment, was one third that in air. This can be attributed to several factors. First, the time to initiation was reduced from about 60000 to 20000 cycles. Second, the crack shape development in the seawater test tended toward more initiation sites and more rapid coalescence to form a single long shallow crack. This rapid coalescence into a low aspect ratio crack, combined with any acceleration in crack growth rates due to the presence of the seawater, resulted in maximum crack growth rates about three times those in air.

3.2.5 Results for PP4 - Free Corrosion

The fourth pipe-plate specimen, PP4, was instrumented with strain gauges as for PP3, Figure 69. These strain gauges were used to assist in bolting the specimen to the base of the test rig and to establish the applied load level. Potential drop probes were mounted as shown in Figure 55. The actual positions are given in Table 15. This layout was used for all subsequent specimens.

PP4 was tested at a hot-spot stress level of 160 MPa, at a frequency of 0.2 Hz, in a freely corroding seawater environment. The seawater was cooled to maintain a specimen temperature within the range 2-8 °C.

The potential drop results were particularly noisy at the beginning of the test. At about 120k cycles a different averaging scheme was implemented which significantly reduced the noise. This noise was attributed to a low frequency (about 0.05 Hz) fluctuation superimposed on the amplifier output, which was unrelated to the loading frequency. At about 410k cycles, the source of this oscillation was traced to a beating phenomenon within the amplifier. It was eliminated by adjusting the pulse frequency of the amplifier slightly to avoid the critical frequency.

As a result of the initial excessive noise, the readings to 120k cycles were eliminated and those at 122k cycles were used as initial readings for subsequent calculation of normalized potential drop. Since the cracks, if any, were quite small at 120k cycles the deletion of this early data will have little detrimental effect on the accuracy of subsequent readings. The results between 122k and 410k cycles are still quite noisy. After 410k cycles the noise was essentially eliminated.

Figure 74 shows the crack shape development for this specimen. A close examination of all the data indicates that initiation was first detected at, or slightly before, 120k cycles. This initiation occurred very near the hot-spot at probe 27. Coalescence occurred between 300k and 400k cycles with the crack depth increasing from about 2 to 5 mm during this period. Crack growth was very rapid from this point until it slowed again as the crack began to curve under the weld toe. At 648k cycles the seawater was drained and the specimen left for two days to dry. Cycling was continued in air, with an increase in load level at 760k cycles, to break open the specimen.

The aspect ratio development, as determined from DCPD data, is illustrated for PP4 in Figure 75 with results for PP1 and PP2. As with PP3, also tested in seawater with free corrosion, early coalescence led to very low aspect ratios early in the life of the specimen. The aspect ratio was about 0.02 at 5 mm and increased to 0.045 by about 10 mm and remained essentially constant thereafter. Aside from an earlier indicated coalescence (in terms of crack depth), PP4 showed similar aspect ratio development for deeper cracks as the previous specimens.

The crack growth behaviour for three probes near the hot-spot is illustrated in Figure 76. Following initiation at about 120k cycles, there is a period of slow crack growth to 350k cycles and a rapid increase thereafter as a result of coalescence. The effective end of test, 0.8T, is about 600k cycles. Also shown in Figure 76 are partial results for PP2, probe 17. Although initiation occurred at about the same time, early coalescence and the seawater environment accelerated crack growth in PP4.

These curves have been differentiated to produce the crack growth rate information shown in Figures 77a and 77b. The rapid increase in crack growth rate with coalescence is clear with a maximum of about 0.18 occurring at about 7 mm crack depth at 450k cycles, at the end of coalescence. These crack growth rates decreases steadily after about 10 mm.

The results for PP2 (probe 17) have been added to Figure 77b. As with the higher stress results (PP3), the peak crack growth rates in seawater are consistently higher than in air, by a factor of at least three.

3.2.6 Results for PP5 - Optimum Cathodic Protection

The fifth pipe-plate specimen, PP5, was prepared as for PP4.

Specimen PP5 was tested at a hot-spot stress level of 240 MPa and cycled at a frequency of 0.2 Hz in seawater. The seawater was cooled to maintain a specimen temperature in the range 2-8 °C. An impressed current cathodic protection system was used to maintain a specimen potential of -0.870 volts with respect to a calomel reference electrode. This corresponds to -0.850 volts with respect to a Ag/AgCl electrode, and represents the optimum level of cathodic protection.

The fatigue crack shape development is shown in Figure 78. The crack growth is asymmetric with an indication of a very early initiation at about 5k cycles, 120 mm to the left of the hot-spot, near probe 6. In addition, the crack initiated and grew behind the potential drop probes, i.e. on the weld reinforcement, in the area just to the right of the hot-spot. Thus no crack depth information is available in this region. The end of the specimen useful life was taken to be 225k cycles, when the crack had reached 0.8T. The seawater was removed shortly thereafter at about 250k cycles and cycling continued in air to 488k cycles, at which point the specimen was broken open.

An examination of the silicone rubber cast of the weld profile, made prior to testing, indicates the presence of a severe weld toe profile at the initiation site near probe 6, see Figure 79. This early initiation resulted in a different aspect ratio development, Figure 80, than for earlier tests in seawater with free corrosion. The early portion of the fatigue life for PP5 was dominated by a single, high aspect ratio crack. Thus, although there was an early initiation, the subsequent growth was relatively slow. The observed aspect ratio development for PP5 was comparable to that for air, with the exception that the crack in PP5 was centered away from the specimen hot-spot.

The crack growth behaviour for probes 6, 24, and 40 is shown in Figure 81 with representative data for PP1 and PP3, also tested at 240 MPa. The early initiation at probe 6, 120 mm to the left of the hot spot location, is clear. The crack growth behaviour for this specimen lies between that for specimens tested in air (PP1) and in seawater with free corrosion (PP3) at the same stress level. The free corrosion results, despite a later initiation than for PP5, had a shorter life. This is mainly a result of the different aspect ratio development. The results for air, with roughly similar aspect ratio development and a longer initiation period, show a propagation life somewhat shorter than in seawater with cathodic protection. The differences in crack propagation behaviour are more clearly seen by considering observed crack growth rates.

The crack growth rates for probes 6, 24 and 40 are shown versus cycles in Figure 82a. The early initiation at probe 6 is again quite clear. At probe 6, there is a constant crack

growth rate until coalescence with cracks initiating toward the centre of the specimen at about 110k cycles. Thereafter the crack growth rate peaks at 0.15 microns/cycle at 180k cycles and then decreases. Higher crack growth rates occur for probes which "initiated" later since they are in a higher stress region (probe 24) and/or they are forced to 'catch up' following coalescence, probe 40 for example (about 0.28 microns/cycle).

The crack growth rates for PP5 are plotted versus crack depth in Figure 82b and compared with representative data for PP1 and PP3. The maximum crack growth rates shown here for probe 6 are somewhat higher, and the crack growth rates near the hot-spot (probe 24) are significantly higher, than those shown for PP1. The crack in PP5 initiated well away from the maximum stress (hot-spot) region but had a similar aspect ratio development later in the life. This indicates a higher basic crack growth rate in seawater with cathodic protection than in air. The crack growth rate for probe 6 is significantly less than for seawater with free corrosion (PP3). The crack growth rate for probe 24, near the hot-spot, is also less. The aspect ratio development in these two specimens was similar from 10–20 mm, although the crack in PP5 was somewhat off-center. It is possible that there was a lower enhancement in crack growth rates in seawater with cathodic protection than with free corrosion. No crack closure measurements were taken to determine whether this benefit with cathodic protection could be attributed to crack plugging with calcareous deposits.

Overall the life of this specimen was one half that in air (PP1 - 450k) and about 50% longer than that in seawater with free corrosion (PP3 - 160k). Thus, despite a very early initiation in this specimen at 5k cycles versus about 20k for PP3, cathodic protection appears to have had a significant benefit over free corrosion. This benefit stems from the differences in crack shape development early in the life of the specimen, and from slightly lower observed crack growth rates (compared with free corrosion).

3.2.7 Results for PP6 - Optimum Cathodic Protection

The sixth pipe-plate specimen, PP6, was prepared as for PP4.

Specimen PP6 was tested at a hot-spot stress level of 160 MPa and cycled at a frequency of 0.2 Hz in seawater. The seawater was cooled to maintain the specimen in the range 5 $\pm$ 3 °C, and an impressed current cathodic protection system was used to maintain a specimen potential of -0.870 Volts with respect to a calomel reference electrode.

The crack shape development is shown in Figure 83. The crack grew symmetrically with the first indication of initiation occurring at probe 24, about 13 mm to the left of the hot-spot, at about 180k cycles. This first crack grew and coalesced with a separate crack centered near probe 33, 45 mm to the right of the hot-spot, at about 600k cycles. The resulting crack grew to eventually coalesce with cracks that had initiated separately near to the edge of the monitored sector of the specimen ($\pm$ 45° from the hot-spot).

The aspect ratio development for PP6 is shown in Figure 84 along with data for specimens tested at the same stress level in air (PP2) and in seawater with free corrosion (PP4).

The early stage of fatigue life is dominated by a few high aspect ratio cracks which persist until beyond about 15 mm crack depth. Unlike PP5, also tested with cathodic protection, these cracks maintained an aspect ratio higher than in air until late in the fatigue life. There is a significant difference again between the results for free corrosion and with cathodic protection; the free corrosion results leading to a very low aspect ratio crack early in the fatigue life. This is reflected in the crack growth behaviour.

The crack growth behaviour at probes 5, 24, 33 and 50 is shown in Figure 85 along with data for PP2 and PP4. The useful life of this specimen can be seen to be 1070k cycles. This is comparable to that in air and twice that in seawater with free corrosion. The improvement over free corrosion is largely due to differences in aspect ratio development. The aspect ratio development in PP6 was also different from that in air. This may have partially offset any acceleration in crack growth rates due to the seawater environment.

There are slight undulations in the crack growth curves for PP5, which represent variations in the crack growth rates during crack coalescence. This is shown more clearly in Figures 86a and 86b, where the crack growth rates for the above mentioned probes are plotted versus cycles and crack depth respectively. Similar undulations in crack growth rate occurred during coalescence in PP3. The crack growth rates for PP4, in seawater with free corrosion, are significantly higher throughout the life than those for PP6. The results in air (PP2) are on the lower bound of the results shown for PP6.

Overall, the life of this specimen was about the same as that tested in air and twice that in seawater with free corrosion. This can be attributed to a slightly delayed crack initiation compared with air and the presence of a relatively high aspect ratio crack through most of the life of the specimen. The peak measured crack growth rates for PP6 were about 50% higher than those measured in air, and about one-third those with free corrosion.

3.2.8 Results for PP7 - Cathodic Over-Protection

The seventh pipe-plate specimen, PP7, was prepared as for PP4. Specimen PP7 was tested at a hot-spot stress level of 240 MPa and cycled at 0.2 Hz in seawater. The seawater was cooled to maintain the specimen at 5 $\pm$ 3 °C, and an impressed current cathodic protection system was used to maintain the specimen at a potential of -1.070 Volts with respect to a calomel reference electrode. This corresponds to -1.050 Volts with respect to a Ag/AgCl electrode, and constitutes over-protection.

The crack shape development for this specimen is shown in Figure 87. Initiation occurred at several points along the weld toe and coalescence occurred by about 60k cycles. Eighty percent wall penetration was achieved by about 100k cycles for this specimen and through cracking occurred slightly thereafter at 125k cycles.

The aspect ratio development for this specimen, and for specimens tested in air (PP1 and PP2), in seawater with free corrosion (PP3), and in seawater with cathodic protection (PP5), is shown in Figure 88. The benefits of optimum cathodic protection, observed for PP5 and PP6, are not evident here since coalescence occurred relatively early in PP7 (by

about 8 mm crack depth), and the aspect ratio development thereafter was similar to PP3 (free corrosion).

The crack growth behaviour for probes 11, 30 and 39 is shown in Figure 89 along with data for PP1, PP3 and PP5, all tested at a hot-spot stress of 240 MPa. Initiation was first indicated at 20k cycles at probe 47, about 133 mm to the right of the hot-spot. All of the illustrated probes indicated initiation before 30k cycles. This initiation behaviour was earlier than for all other specimens except for PP5. Unlike PP5, crack initiation occurred at several locations at about the same time, and there was no indication of a particularly severe weld toe profile. The crack growth in PP7 outpaced that for PP5 and PP1. The differences between PP7 and PP3 (free corrosion) are largely a result of earlier initiation in PP7.

Crack crack growth rate information is illustrated in Figure 90a and 90b, versus cycles and crack depth respectively. All lines for PP7 are relatively smooth and well behaved with peak crack growth rates of about 0.4 microns/cycle occurring for probe 30, the probe closest to the hot-spot location. For comparison, crack growth rates for the other specimens tested at 240 MPa hot-spot stress are illustrated in Figure 90b. The crack growth rates for PP7 are somewhat higher than those for PP3 (free corrosion), despite similar aspect ratio development after about 8 mm crack depth. This may indicate an acceleration in crack growth rates over free corrosion as has been observed for small specimen tests in some studies. The results for PP7 are significantly higher than for air (PP1). This acceleration over air may be attributed to the crack shape development and an acceleration due to the environment. The higher crack growth rates with cathodic over-protection (PP7) compared with optimum cathodic protection (PP5) may be attributed to a combination of differences in crack shape development, and accelerations in crack growth rates, possibly the result of higher hydrogen evolution and uptake with cathodic over-protection.

The useful life of this specimen was the shortest of all those specimens tested. It had one quarter the life recorded in air and 60% that in seawater with free corrosion. This can be attributed in part to a relatively uniform and early initiation of cracks along the weld toe which coalesced relatively quickly. Thus the benefit in initiation (in the absence of severe defects) and in subsequent crack shape development observed for optimum cathodic protection, was not present here. This was coupled with the highest crack growth rates observed in this series of tests, about twice those observed in air at this stress level and 30% higher than those in seawater with free corrosion.

3.2.9 Results for PP8 - Cathodic Over-Protection

The eighth pipe-plate specimen, PP8, was prepared as for PP4. Specimen PP8 was tested at a hot-spot stress level of 160 MPa at 0.2 Hz in seawater. The seawater was cooled to maintain the specimen at 2-8 °C and an impressed current cathodic protection system was used to maintain a specimen potential of -1.070 Volts with respect to a calomel reference electrode. At 234.7k cycles, when the crack was about 17 mm deep, a leak in the stainless

steel coils immersed in the seawater reservoir allowed some of the glycol working fluid into the seawater. The leak was repaired, a fresh batch of seawater was prepared, and the cycling was continued four days later. At the same time, the remainder of the glycol circuit was flushed with warm water and the glycol was replaced with a 50-50 glycol-water solution. This greatly improved the circulation efficiency of the coolant, but led to excess cooling capacity. As a result, throughout the remainder of the test the temperature varied outside the above stated limits to between 0 and 10 °C as the refrigeration was alternatively turned on and off once or twice a day instead of running continuously.

The crack shape development for PP8 is shown in Figure 91. The crack was first observed to initiate 45 mm to the right of the hot-spot near probe 33 at about 50k cycles. This crack grew and appears to have coalesced with a neighbouring crack to its right at about 150k cycles. The resulting crack grew without further significant coalescence through to the end of the test (0.8T) at 340k cycles. At 350k cycles the seawater was drained, the load increased by 50% and the specimen was cycled at about 0.5 Hz until the test was stopped and the specimen broken open at 420k cycles.

The aspect ratio development for PP8 is illustrated in Figure 92 along with data for air (PP1 and PP2), for seawater with free corrosion (PP4), and for seawater with optimum cathodic protection (PP6). Unlike PP7, also tested with cathodic over-protection, there is a relatively high aspect ratio crack present for most of the life of this specimen. This crack had a higher aspect ratio than that observed for PP4, tested with free corrosion, and for PP2, tested in air. Similar high aspect ratio cracks were observed for both specimens tested with optimum levels of cathodic protection (PP5 and PP6). The aspect ratio tends to the same value for all specimens for crack depths greater than about 15 mm.

The crack growth behaviour for probes 26 and 33 (PP8), and for representative probes for PP2, PP4 and PP6, are presented in Figure 93. Initiation occurred earlier for PP8 compared with all other tests at this same stress level. The weld profile was not significantly worse than the other specimens. The subsequent crack growth outpaced all other specimens except PP4 (free corrosion) despite the relatively high aspect ratio crack that developed in PP8.

The crack growth rates for PP8 are shown versus cycles in Figure 94a. An undulation is apparent in the crack growth rates at probe 33 when coalescence occurred at 150k cycles. The crack growth rate for probe 33 reaches a peak of about 0.12 at about 150k cycles after which it falls off toward the end of the test. The maximum observed crack growth rate occurs away from the initiation site for a probe located between two coalescing cracks. This maximum rate is about 0.20 microns/cycle.

These crack growth rates are compared in Figure 94b with those for the other specimens tested at 160 MPa. The crack growth rates at probe 33 are comparable to those in free corrosion (PP4) and therefore higher than those observed in air (PP2) and in seawater with optimum cathodic protection (PP6).

The life of this specimen, as in the other specimen tested with over-protection, was about one quarter that in air and about one half that with free corrosion. This is a result

of early initiation and a high peak crack growth rate despite the presence of a relatively high aspect ratio crack through most of the specimen life.

4 DISCUSSIONS AND CONCLUSIONS

4.1 Thickness Effect

In these tests of welded plate-to-plate T-joints, usually between 20 to 40 % of the fatigue life had gone before small cracks, about .5mm deep, were detected by the potential drop systems.

Using this detection level as the boundary betwen initiation life (N_i) and propagation life (N_p), it was possible to statistically assess the influence of plate thickness on N_i an d N_p. All of the data indicates that increasing plate thickness reduces N_p. Except for a difference between CANMET and Waterloo data for 103 mm specimens, the data indicates that increasing plate thickness also decreases initiation life.

In this test program and most studies of thickness effect, see review by Berge and Webster [10], the thickness of the attachment plate (t) and size of the weldment were scaled in proportion to the thickness of the base plate (T). However, geometric similarity was not maintained because the notch root radius at a weld toe (ρ), see Figure 95, does not increase with weld size/plate thickness. This radius is largely determined by the pass at the weld toe. Since this very local stress concentration is a function of T/ρ, it increases with base plate thickness. This implies that in thicker specimens, fatigue cracks are likely to initiate sooner and crack growth rates may be faster at smaller values of a/T.

Stress concentrations from the overall weld and toe profiles and the general state of stress in the base plate combine to produce a stress gradient in the plane of crack growth. In a tubular joint, the fatigue cracks usually propagate into the chord plate, where the general stress state is a combination of membrane and bending. The bending component is high in tubulars and bending has been the usual mode of loading in plate-to-plate joints used to study the thickness effect. The combined effect of a general bending stress field plus a stress concentration introduced by a weld is shown schematically in Figure 95. First consider the case, Figures 95(a) and (b), where the radius at the weld toe (r_2) is the same when the plate thickness is increased from T_2 to T_1, and both plates are subjected to the same hot spot stress (σ_{HS}). In this case, the maximum stress (σ_{MAX}) in the thinner plate and the fatigue crack growth rate (da/dN), at small values of a/T, should be lower in the thinner plate. If much of the fatigue life is spent initiating and propagating cracks in the region of steep stress gradient, then this simple geometric comparison gives a possible explanation of the thickness effect. Figure 95(c) illustrates the effect of increasing the toe radius from r_2 to r_1 as the base plate thickness is increased T_2 to T_1. If the stress concentration is a linear function of r/T and $r_1 = (T_1/T_2)r_2$, the maximum stress will be the same in both plates and the differences in the stress fields initiating and propagating the fatigue cracks will be reduced; hence the rationale for the 1986 AWS D1.1 Code

requirements for weld profiles which vary from flat fillet-like profiles for thin members to concave, radius controlled profiles for thick members [11].

4.1.1 Effect of Specimen Width On Fatigue Life

In our tests, the specimen width was held constant at 203 mm. In some studies of thickness effects, the width of plate-to-plate joints was increased with plate thickness. A comparison of experimental data (N_T) from these tests with our data revealed no significant differences in thickness effect; hence suggesting that the thickness effect is not dependent on specimen width. This result may be fortuitous since specimen width is likely to have a different effect on N, and N_p. The applied stress field does not vary across the specimen width in this type of plate-to-plate joint so increasing the specimen width will tend to increase the "highly stressed volume" and according to a well known size effect theory , this will reduce fatigue life. In other words, increasing the weld length increases the number of initiation sites and this will tend to reduce N_i. However, increasing the specimen width will tend to reduce the chance of a dominant crack developing near a free edge so edge cracking will be less likely to reduce Np. Figures 12-16 show that a dominant semi-elliptic crack was likely to be present in thicker specimens for a much larger percentage of the propagation life. For example, a dominant semi-elliptic crack with a depth of about 8mm, and an aspect ratio of 0.1 already has a surface length of 80 mm compared to the plate width of 203 mm. By definition, the propagation life is finished for a 16 mm specimen (a/T =.5) whereas for a 103 mm specimen, a/T is only .08 and Figure 14 shows that about 75% of N_p remains. Clearly, the chance of free edge cracking must and did increase with plate thickness in our tests.

In an interim paper [12] an attempt was made to estimate the effect that edge cracking had on the Waterloo and CANMET test results. Beachmark data obtained in the CANMET tests were used to identify the crack depth and percentage of N_p at which edge cracking occurred. An LEFM analysis, using a K_1 solution for a semi-elliptic crack in a flat plate [13], was then used to estimate the number of cycles that would be required to propagate the crack to a/T equal to .5 if the plate had been wider and edge cracking had not occurred. These simple calculations, see Table 16, indicated that without the edge cracking, the ratio of N_p/N_T would only increase four to six percentage points above the experimental ratios of 68 to 80%.

In Norwegian tests in which the specimen widths were scaled with plate thickness and crack initiation detected with soap water [14] cracks with surface lengths of the order 1-3 mm were detected. Assuming an aspect ratio of .3 to .5, this implies a detection level of .3 to 1.5 mm. The corresponding ratios of N_P/N_T varied from 75 to 90% which compares very well with our adjusted bounds of 73 to 85%. However, our more recent LEFM analyses in which coalescence and edge cracking in a T-joint were modelled suggests that the effect of edge cracking may be more significant.

Another factor to consider is the effect of specimen width on the residual stress state

in the specimens, which were tested in the as-welded condition. In the direction transverse to the weld, residual stresses are tensile near the centre of the specimen width but are low near the free edges. Therefore, crack initiation tends to occur along the weld toe away from the free edges. Below some width, the magnitude of the residual stresses decreases due to lower stiffness and thermal gradients before and after welding. Accordingly, it has been argued that specimen width may have to be scaled with plate thickness to avoid distortion of the residual stress states, which would confuse the interpretation of the thickness effect.

4.1.2 Fracture Mechanics Models For Predicting Propagation Life

Some LEFM models for predicting the growth of fatigue cracks at weld toes are reviewed in detail in a previous paper [15]. All except one of those models consider the development of a semi- elliptic crack, with some mechanism that allows for aspect ratio changes produced by crack growth or by crack growth plus coalescence.

One approach for estimating N_p is to use the Paris equation to predict a change in crack depth (δ_a) and a change in crack surface length (δ_c), for a small cycle increment (Δ N). This defines a new crack shape and size, and the calculation is repeated until the crack depth is half the plate thickness. This so-called natural growth of a single crack is illustrated on Figure 96 for a plate-to-plate T-joint with a base and attachment plate thickness of 78 mm and with a hot spot stress range of 150 MPa. An initial crack size of 0.5 mm was used in these calculations because this is the size we have used to define the boundary between initiation and propagation. It also happens to be the size at which crack closure effects are not very significant [19]. Crack tip stress intensity factors at the surface and deepest point were obtained by Bell with finite element analysis [5,6]. Crack shape development is shown for initial aspect ratios of 0.1, 0.2, 0.3, 0.4 and 0.5 . These values were chosen because experimental observations (see Figure 14) lie in this range when a/T is small (i.e. $a/T < .05$).

Figure 96 shows that all of these initial defects develop the same shape and Table 17 shows that the initial shape has almost no effect on the propagation life predicted by this single crack model. This has been reported by others but many have not given sufficient attention to the differences in shape development between this single crack model (SC) and real cracks in welds. For example, Figure 17 compares the shape development of a single crack from an initial aspect ratio of 0.5 (SC1 model) with the shape development observed in our experiments. Crack coalescence produces cracks with aspect ratios smaller than those developed in the SC model. Also when edge cracking occurs (illustrated by cases ① and ② on Figure 17, the aspect ratio quickly tends to zero.

These differences between LEFM models for the natural growth of a single crack (e.g. SC1) and real behaviour led to the development of a so-called multi-crack model [17]. In this model, the Paris equation is still used to predict a change in crack depth (δ_a) for a semi-elliptic defect of initial size (a_i, $2c_i$). However, a forcing function for changes in aspect ratio is used to determine the new surface length ($2c + \delta_c$). Cases ①,② and ①,② on Figure

17 show how this forcing function relates to experimental behaviour. Case (1,2) is model MC1 which accounts for coalescence but ignores the possibility that the dominant semi-elliptic crack will reach a free edge. Cases (1) and (2) are for model MC2 which accounts for coalescence but assumes that edge cracking (which occurred in our specimens) is highly likely when the aspect ratio reaches 0.1. Both models, MC1 and MC2, assume an initial crack with an aspect ratio of 0.5 and that a higher stress range will lead to a more rapid reduction in aspect ratio.

A simplification that merits consideration is to assume that the semi-elliptic defect has a fixed aspect ratio of 0.1 throughout the propagation phase. To illustrate the differences between this model (SC2) and those (SC1,MC1 and MC2) discussed earlier, Table 18 shows predictions of N_p for each plate thickness for a hot spot stress range of 150 MPa. As discussed earlier, statistical methods have been used to analyse our experimental results. Statistical predictions of mean life for the Waterloo and CANMET data sets and for the combined data set are also shown in Table 18.

In general, the N_p predictions of model SC1 are always too high compared to the statistical means of the experimental data. In general, models MC1 and MC2 are a better fit than model SC1 to the experimental data while model SC2 lies between models MC1 and MC2. Model MC2 gives a remarkably close prediction to the combined data sets.

Another and better way to compare the model predictions and experimental data, and at the same time illustrate the thickness effect, is to normalize with respect to the predictions for the 16 mm data (see Table 19). The data for the 16mm specimens is used as the reference because it is known that edge cracking did not occur in these tests.

In all cases, models which do not account for edge cracking (i.e. SC1, SC2 and MC1) underestimate the thickness effect observed in our experiments. For example, models SC1 and MC1 indicate that increasing the plate thickness from 16 to 103 mm is likely to decrease N_p by a factor of 2.5 and 4.6 respectively. Although both values are significantly less than the experimental mean value of about 7, the underestimation may be due in part to the brittle pop-ins that occurred in the 103 mm specimens. Nevertheless, the reduction factor predicted by the MC1 model is nearly twice that predicted by the SC1 model. As mentioned earlier in section 3.2.2, our experimental data indicates that crack coalescence forms a smaller percentage of N_P as plate thickness decreases. The differences between the single work model, SC1, and the MC1 model, which accounts for coalescence, suggest that coalescence may be a significant factor contributing to the thickness effect observed in our and previous experiments.

In comparison, the MC2 model which accounts for coalescence and edge cracking, overestimates the thickness effect in most cases. One interpretation of the differences between the MC2 and MC1 models is that edge cracking has exaggerated the thickness effect in our experiments but the correction in model MC2 is too severe.

In these models, the crack tip stress intensity factors, K_1, were obtained by finite element analysis [6] using a mesh that assumed a weld angle (θ) of 45° and ignored the weld toe radius (ρ). Table 20 shows that for a sample of fifteen of the CANMET specimens,

the actual values of ρ varied between 0.2 and 3.3 mm and that θ varied between 30° and 72°. An indication of the effect of θ on K_1 (at deepest point with $\rho = 0$) was presented in Bell's papers [5,6]. An indication of the effect of θ and ρ on K_1 (deepest point) was obtained by Niu and Glinka [18] and by Dijkstra et al. for an edge crack [19]. In all three cases, the effect of θ on K_1 (deepest point) was small when a/T was larger than about 0.1. In the two studies of the effect of ρ on K_1 (deepest point), the effect was insignificant when a/T was larger than about 0.03.

Our experimental data, indicate that as much as 40-50% of the propagation life is spent propagating a crack to a/T of 0.1. Obviously, variations of θ and ρ must be the cause of some of the experimental scatter. Since θ and ρ vary along the weld front, it is difficult to believe that LEFM models can be used to estimate the effect on life of such variations, particularly when one also considers the problems encountered when predicting K_1 at small values of 'a' in steep stress gradients. These difficulties must also be considered when evaluating theoretical studies that have been done to support the new AWS profile codes. Hopefully, the experimental programs underway or scheduled to start this year will give a clear indication of the effect of overall weld profile on life.

4.2 Pipe-Plate Discussion

A DCPD crack monitoring system has been developed to monitor the initiation and growth of fatigue cracks in a pipe-to-plate welded specimen. Based on an examination of the analytical calibration available for semi-elliptic surface cracks in a semi-infinite flat plate, and an assumed system resolution of 0.5%, it is estimated that cracks 0.5 to 1.5 mm were detected. The actual size of the detected crack will depend on the crack shape and on its position relative to the potential drop probes. As the cracks grow and coalesce, estimates may be made of the crack size and shape. In these pipe-plate specimens, cracks tend to an aspect ratio of between 0.1 and 0.02 after coalescence. Such coalesced cracks may be measured to a tolerance within about 5% with the present system. This error represents the random variability in weld toe profiles and probe spacing. The development of this DCPD system has allowed crack shape development and crack growth rates to be monitored in tests of pipe-plate specimens in air and seawater environments. This information permits quantitative comparisons of the results in these different environments.

The pipe-plate data will also be compared with some of the T-plate data and with data obtained in a test of an unstiffened tubular joint [20]. For the purposes of this discussion, only results from 26 mm T-joints will be presented since these were manufactured from the same plate as the base plate for the pipe-plate specimen.

The T-tubular joint result discussed forms part of a program to investigate the effect of chord ring-stiffening on fatigue behaviour. Twelve specimens are being tested with constant amplitude loading; six at Memorial University in Newfoundland and six at the University of Waterloo. The specimens consist of a 417 mm diameter brace welded at right angles to a 914 mm diameter chord. Both brace and chord have 19 mm wall thickness.

The first specimen in each test series was unstiffened. S. Lambert assisted J. Forbes in the testing of the unstiffened joint at the University of Waterloo. Full details of this test will appear in another report and in the PhD thesis of J. Forbes, but some details will be discussed herein.

The tubular joint testing fixture at the University of Waterloo was designed to allow In-Plane Bending (IPB), axial, and Out-of-Plane Bending (OPB) loading modes. As a result, uncracked stress distributions are available for the unstiffened specimen, TB1, for each of these loading modes. The fatigue test for TB1 was conducted in air using in-plane bending at a hot-spot stress range of 260 MPa. The static and fatigue testing of this specimen had three purposes: to provide stress distributions for comparison with those in the pipe-plate, to confirm the accuracy of the DC potential drop crack monitoring system for tubular joints, and to provide a benchmark for comparison with subsequent tests by J. Forbes on stiffened joints.

4.2.1 Results in Air

The results for the pipe-plate specimen, tested in air, will be discussed and compared with T-plate and tubular joint data in terms of the initial stress distribution, crack shape development, and crack growth rate behaviour. This crack growth rate behaviour will then be discussed in LEFM terms.

4.2.1.1 Initial stress distribution

The initial radial stress distribution along the zero degree line (at the hot-spot) is illustrated in Figure 97 for the pipe-plate and the unstiffened T-tubular joint, TB1. In both cases the stresses have been normalized with respect to the corresponding hot-spot stress. The illustrated stress distributions are in general similar, but a more important comparison, in terms of the growth of fatigue cracks, is the ratio of membrane to bending stress in the chord (or plate) through the thickness. In the pipe-plate specimen, the stresses were predominantly bending with no significant membrane component. This is consistent with results reported by Clayton [21] for tubular joints. His finite element analyses indicated that for the in-plane bending case, as the brace/chord diameter ratio (β) was reduced, the membrane component became less significant; tending toward 10% at a β-ratio of 0.25. For in-plane bending for TB1, which has a β-ratio of 0.5, the membrane component was 27% of the total. This difference between the pipe-plate and this tubular influenced the crack growth of larger cracks.

Another important characteristic of the stress field in a welded joint is the stress distribution along the weld toe. In Figure 98, the radial stress distribution along the weld toe, obtained by extrapolation from strain gauges mounted on the chord surface, is shown for the pipe-plate and for three modes of loading for TB1. Similar results for tubular joints have been presented by Dover [22]. Note that the zero degree line for the tubular joint may refer to the crown or saddle position, depending on the mode of loading. The stress

distribution for the pipe-plate is determined by the constraint conditions on the edge of the plate; a symmetric stress profile with a maximum at the hot-spot location was selected. A very flat profile was avoided to encourage crack initiation near the centre of the specimen near to the hot-spot. The resulting stress distribution lies between the tubular results for the various loading modes. Therefore, while the pipe-plate cannot be considered a model of a particular tubular joint, it has an initial stress distribution representative of that seen in some tubular joints. It is not the purpose of this program to generate S-N data for the design of specific tubular joints. The benefits result from the study and analysis of the fatigue crack growth behaviour, and from comparisons which may be drawn between the results for this specimen in the different environments.

4.2.1.2 Crack shape development

Figure 99 compares the crack aspect ratio development for the two pipe-plate specimens tested in air, PP1 and PP2, with TB1. As with the pipe-plate, many small semi-elliptic cracks were evident in the tubular joint when the weld toe was stained with ink during the fatigue test. These cracks had a wide range of aspect ratios from about 0.1 to semi-circular ($a/2c = 0.5$) for crack depths to 10% of the wall thickness. As these cracks grew they coalesced, so that by $0.2T$ a single long shallow crack of very low aspect ratio was present. The aspect ratio of this crack increased steadily to about 0.05 at through-thickness cracking. The crack aspect ratio development may be explained by considering the initial stress distribution in the tubular joint, Figure 98. A very flat stress profile encouraged initiation of cracks over a relatively long length of weld which, upon coalescence, led to a low aspect ratio crack. After coalescence the ends of the crack did no extend significantly since they were in a region of rapidly decaying stress along the weld toe. This effectively pinned the crack ends, and the aspect ratio increased therafter, as the crack grew through the plate thickness. In the pipe-plate, the stress distribution along the weld toe did not decay as abruptly, and the crack grew both in depth and surface length following coalescence, resulting in an almost constant crack aspect ratio.

Comparisons may also be drawn between the pipe-plate and some T-plate results obtained in this study, Figure 100. Here the aspect ratio development for T-plates tested at CANMET, as measured from ink stains and beachmarks, is illustrated. As for the pipe-plate and tubular results, aspect ratios for the T-plate for shallow cracks vary over a wide range, and there is a consistent tendency toward lower observed aspect ratios with increasing crack depth. In addition, there appears to be a consistent effect of applied stress range in the T-plate results. Higher applied stresses led to earlier coalescence as a result of an increase in the number of initiation sites. This was not as clear from the two pipe-plate results.

In the T-plate specimens, the stress distribution is constant across the width of the specimen (203 mm). However, due to the welding operation, there are higher residual stresses in the plate centre than at the edges. There is a tendency, therefore, for cracks to initiate away from the free edges of the specimen. In addition, as the cracks grow and

coalesce, the growth at the edges seems to be slowed, perhaps because of the plane stress conditions. Therefore, the ensuing crack has a relatively high aspect ratio. As the crack reaches the free edges of the specimen, the aspect ratio moves quickly toward zero. The life thereafter is very short, due to an increase in the stress intensity factor. For the results from CANMET presented in Figure 100, the crack had not reached the free edges and become flat-fronted, before the cenerline crack depth was 50% or more of the thickness. For the T-plate work, $0.5T$ was considered the end of the useful life of the specimen.

4.2.1.3 Crack growth behaviour

The crack growth behaviour for pipe-plate, T-plate, and T-tubular joint specimens, tested at similar hot-spot stress ranges, at the University of Waterloo, are illustrated in Figure 101. All results are from DCPD measurements. The differences in crack growth behaviour may be related to the initial stress distribution and aspect ratio development, in each specimen. Crack growth was slower for the pipe-plate than for the tubular joint. The aspect ratio of the crack in the pipe-plate was consistently higher than that for the tubular joint throughout the life. This, in combination with a somewhat higher applied stress and a higher membrane component of stress in the tubular joint, resulted in higher crack growth rates in the tubular joint.

In the pipe-plate joint, the crack begins to slow down beyond about $0.6T$, and begins to curve toward the specimen centerline, under the weld toe, by about $0.8T$. Similar, but less severe crack curvature has been observed in fatigue tests of T-tubular joints, tested in axial loading, see van Delft, Dijkstra and Snijder [23]. It is believed that this slowing and eventual curving of the crack plane is due to a build-up of compressive stresses in the ligament as a result of the cracked geometry. This may be particularly severe in the pipe-plate geometry due to the absence of significant tensile membrane stress. Since this crack front curvature unnecessarily complicates fracture mechanics analyses, the useful life of the pipe-plate specimen was defined as $0.8T$, i.e. at the onset of crack front curvature.

Also shown in Figure 101 is the crack growth behaviour for a 26 mm T-plate specimen, tested at 250 MPa. Crack coalescence in this T-plate was such that an edge crack formed at about $0.2T$. This, in addition to an earlier initiation, gave it the shortest life of the specimens shown. By comparison, in the tubular joint, as a result of the initial stress distribution, the crack coalesced into a very long shallow crack very quickly and hence the crack growth rates were high. The propagation behaviour in the T-plate was actually very similar to that in the T-tubular joint. In the T-plate, edge cracking accelerated crack growth after about $0.2T$, whereas in the tubular joint a very low aspect ratio crack was present by about the same time (in terms of normalized crack depth). These quite different mechanisms have lead to similar crack propagation behaviour.

4.2.1.4 Stress intensity factors

This crack propagation data has been used to prepare Figure 102. Stress intensity factors have been derived from the measured crack growth rates, assuming a Paris rule

relationship with $C = 7.14 \times 10^{-13}$ and $m = 3.66$ [9]. These stress intensity factors have been normalized with respect to that for a through-thickness centre crack, length $2a$, in an infinite plate, subjected to a uniform stress field. This stress corresponds to the hot-spot stress in each case. Figure 102 illustrates the resulting stress intensity correction factors for PP1 and PP2, along with data for the T-tubular joint (TB1), a T-plate joint (not the same joint shown in Figure 101), and a scatterband for data reported by Dover and Dharmavasan [24]. This presentation allows direct comparison of tests performed at different stress levels. However, the stress distribution along the weld and through the plate thickness are not considered in the normalization; this may influence the results. In particular, membrane and bending components of through-thickness stress are not distinguished. The stress distribution, in combination with the density and distribution of weld toe defects, will influence the crack shape development. Differences in crack shape development will influence the inferred stress intensity factors.

The data presented for the tubular joint, TB1, was taken near the crown of the joint. In fact, cracks initiated to either side of this location and the increase in stress intensity factor after a small dip in the curve shown in Figure 102 is most likely a result of the crack coalescing with neighbouring cracks which initiated sooner. The resulting stress intensity correction factor for the tubular joint is consistently higher than those for the pipe-plate specimen. At shallow crack depths, this is likely a result of the lower aspect ratio crack that occurred in TB1. As the crack depth increased, the aspect ratios tended toward similar values. However, at the same time, the influence of the significantly higher membrane stress in the tubular becomes more important, keeping the stress intensity higher.

The results for the T-plate clearly show the influence of edge cracking. The PD results indicated that cracks had reached at least one edge by about 0.2T.

Also shown in Figure 102 are bounds for results presented by Dover and Dharmavasan [22] for several types of tubular joints tested under variable amplitude loading in air. The lower bound corresponds to a T-joint tested in out-of-plane bending, while the upper bound corresponds to either Y- or K-joints in axial loading. No results for a simple T-joint in in-plane bending were presented in [22]. The trends in the pipe-plate joints agree very well with Dover's results. Direct comparisons are not appropriate due to the differences in specimen geometry and loading, and without more information regarding initial stress distributions. The large differences evident between the results for TB1 and the results from Dover and Dharmavasan are similarly difficult to assess without more information. A major factor could be the development of the low aspect ratio crack early in the life of TB1.

These comparisons serve to illustrate the suitability of the pipe-plate specimen for the study of the growth of fatigue cracks in tubular welded joints. The initial stress distribution along the weld toe, and the resulting fatigue crack propagation behaviour in the pipe-plate specimen, are consistent with of those observed in tubular welded joints.

Results for T-plate specimens have clearly shown a free edge effect. When the crack reaches the free edges of the specimen there is a rapid increase in the crack growth rate,

and a rapid end to the specimen life. The crack will contact the free edge sooner if the dominant semi-elliptic crack forms away from the centreline. In a freely corroding seawater environment there are far more initiation sites, crack coalescence occurs faster so the crack reaches the edges sooner. Thus the T-plate joints may tend to show an exaggerated influence of seawater on fatigue life. The absence of free edges makes the pipe-plate particularly attractive for studying the influence of seawater on fatigue crack growth behaviour.

4.2.2 Influence of Seawater

The hot-spot stress range for eight pipe-plate specimens has been plotted versus the specimen endurance (i.e. life to $0.8T$) in Figure 103, i.e. a conventional S-N plot. The results have been grouped according to the environment. Also shown are DoE recommended design lines [24] for 26 mm tubular joints in air and seawater with free corrosion. These design lines have been obtained by applying the thickness correction to the design 32 mm curves; this results in a small benefit, a 5.3% increase in the allowable stress range for a given life. A mean fatigue line for air has also been shown, calculated from the 32 mm mean line and the same thickness correction.

The pipe-plate results in air fall on the calculated mean air line for 26 mm wall thickness tubular joints. The influence of seawater environment on endurance is clearly shown, with increasing degradation for cathodic protection, free corrosion, and cathodic over-protection. All data lies above the design line for free corrosion, but the results with cathodic over-protection fall below the corresponding air design curve.

The observed influence of seawater on the fatigue behaviour of the pipe-plate specimen is illustrated in Figure 104, and summarized in Table 21. In the figure, the fatigue lives of all eight specimens are plotted on a bar chart, grouped according to the applied hot-spot stress range. The overall length of each bar represents the number of cycles required to produce a crack $0.8T$ deep, and hence represents the useful life of each specimen. The solid line within each bar represents the first indication of cracking, i.e. crack initiation. This corresponds to a semi-elliptic surface crack of from 0.5 to 1.5 mm depth. Two bars are shown for PP2 to express the uncertainty regarding the initiation life as a result of excessive noise in the instrumentation. The small tick-marks along the bottom of each bar represent the number of cycles required to produce a crack $0.1T$, $0.2T$, $0.3T$, $0.4T$, $0.5T$, $0.6T$, and then $0.7T$ deep. This therefore gives an impression of the crack propagation behaviour. The broken line hanging from the top of the bar represents the number of cycles to form a single, but irregular, dominant crack, i.e. crack coalescence.

The influence of seawater on the fatigue behaviour of the pipe-plate joints is summarized in Table 21. The total fatigue lives (i.e. to $0.8T$) and the estimated initiation lives (i.e. 0.5 to 1.5 mm) are presented for each specimen. Crack propagation lives have been calculated by subtracting the initiation lives from the total fatigue lives. Conventional S-N plots have been presented in Figures 103, 105 and 106, for total, initiation, and propagation

fatigue lives, respectively. In each figure, results are grouped according to the environment. Results from the Canadian T-plate program are included in Figures 105, for comparison since initiations were not influenced by the edge effect.

Fatigue life reduction factors were calculated by dividing the fatigue life in air by the corresponding fatigue life in seawater at the same hot-spot stress level. These are presented for total, initiation and propagation lives in Table 21. There was some uncertainty in the prediction of the initiation life of specimen PP2, tested in air. For the purposes of this calculation, a value of 125k cycles was assumed.

Total fatigue life reduction factors of 2.8 and 1.8 were obtained in seawater with *free corrosion* in pipe-plate specimen testing. This is consistent with values for plate/plate and tubular studies reviewed by Vosikovsky and Tyson [25]. In their review, seawater with free corrosion was reported to reduce the fatigue life by from 2 to 3 times. There was an observed tendency in the T-plate results for the seawater to have a greater degradation for lower stress testing, reflecting the longer exposure to seawater.

Although it is impossible to infer trends from just two pipe-plate specimens, the freely corroding seawater environment had a larger influence on the more highly loaded specimen. In specimen PP3, tested at 240 MPa hot-spot stress, initiation and propagation lives were uniformly affected. For specimen PP4, tested at 160 MPa, there was no significant difference in initiation life compared with air, and the reduction in total life was accounted for entirely in the propagation life.

For both specimens in free corrosion, there was a noticeable acceleration of coalescence as a result of more initiation sites compared with air. Coalescence occurred at between 4 and 5 mm in seawater with free corrosion compared with about 7 and 8.5 mm in air. Such differences in crack shape development between air and seawater with free corrosion were also observed in the T-plate tests In these T-plate specimens, there was a tendency for cracks to coalesce in a freely corroding seawater environment by about 5 mm crack depth. Thereafter, the cracks usually reached the edges of the T-plate specimens, and the remaining lives were short. This edge cracking is analogous to, but more severe than, the formation of a very low aspect ratio crack in the pipe-plate specimens.

In seawater with optimum *cathodic protection*, the pipe-plate specimens had total life reduction factors of 1.65 and 1.07. The poor result for specimen PP5, tested at 240 MPa in seawater with cathodic protection, was a result of a very early initiation due to a poor local weld profile, and a 30% decrease in the crack propagation life. For Specimen PP6, tested at 160 MPa, initiation, propagation and total lives were all comparable to corresponding lives in air.

The fatigue lives for plate and tubular joints in seawater with cathodic protection, reviewed by Vosikovsky and Tyson [25], showed considerable more scatter than free corrosion results. There was a general tendency for cathodic protection to be more beneficial for lower stressed plate results, while the tubular results reviewed showed a consistent fatigue life reduction factor of about 1.8. In the pipe-plate specimen, there was a more severe reduction in fatigue life for the more highly stressed specimen, although this was in part

due to a very early initiation. Despite this early initiation, the fatigue life reduction factors for both pipe-plate joints were not quite as severe as for the average behaviour for tubular joints reviewed in [25].

In a seawater environment with *cathodic over-protection*, fatigue life reduction factors for the pipe-plate specimen were 4.2 and 3.3, Table 21. This degradation was a combination of reduced initiation lives and of a large reduction in fatigue crack propagation lives. For specimen PP8, tested at 160 MPa, the aspect ratio development was more favourable (i.e. the cracks had a higher aspect ratio) than for PP7, tested at a higher stress level (240 MPa) in the same environment, and for PP2, the corresponding test in air. This more favourable crack shape development may be responsible for the reduced degradation in fatigue performance for PP8. However, both PP7 and PP8 had significantly shorter crack propagation lives than in air. This is most likely due to hydrogen embrittlement.

4.2.2.1 Crack growth rates

Another way of assessing the influence of the environment on fatigue crack growth is to consider the measured crack growth rates. Early in the life, fatigue crack growth is complicated by crack coalescence. Therefore, to determine the influence of seawater on crack growth rates, it is necessary to consider deeper cracks. Measured fatigue crack growth rates at the deepest point of cracks $0.5T$, $0.6T$ and $0.7T$ deep, for eight pipe-plate specimens, are given in Table 22. Since crack growth rates are significantly influenced by crack shape, crack aspect ratios are also given. Unfortunately, in only a few cases were crack shapes sufficiently similar to allow direct comparison of crack growth rates in the different environments.

One way of accounting for these differences in crack aspect ratios, and in the applied stress ranges, is to calculate the range of crack tip stress intensity factor, ΔK. Finite element analyses of semi-elliptic surface cracks at the toes of T-plate welded specimens by Bell [6] indicate that the influence of the weld toe stress concentration diminishes for a/T greater than 0.5. Therefore, the crack growth rates in Table 22 are been presented in Table 23 along with stress intensity factor ranges calculated from equations presented by Newman and Raju [13] for semi-elliptic surface cracks in flat plates subject to bending. The hot-spot stress range has been used in this calculation. This data has been plotted in Figure 107 in standard $\mathrm{d}a/\mathrm{d}N$ versus ΔK format. Data at $0.8T$ has been omitted since this corresponds to the onset of crack plane curvature. This $0.8T$ data fell on the lower bound to all data, for all environments. For reference, mean (solid line) and 95% confidence limit (dotted lines) crack growth rate information for edge cracked specimens, reported in a review by Booth and Dobbs [9], are also included.

Most of the pipe-plate data lie considerably below the data for edge cracked specimens. Such an offset is not unexpected, due to the flat plate assumption used in this calculation of the crack tip stress intensity factor range for the pipe-plate. There is considerable scatter in the observed pipe-plate crack growth rates. Although some trends regarding the influence of seawater environments on crack growth rates may be inferred, the results are

not conclusive.

Discussions of the benefits of cathodic protection usually cite the improvement in initiation behaviour, counterbalanced by acceleration in crack growth rates of larger cracks. Although this is partly true, a significant benefit of cathodic protection is the resulting influence on crack shape development as a consequence of this initiation behaviour. This is very apparent as a result of this careful monitoring of the crack shape development in cathodically protected T-plates and these pipe-plate joints. Under free corrosion conditions, there is a tendency toward more initiation sites than are observed in air. This has a significant influence on crack shape development and hence on fatigue life as discussed above. Cathodic protection tends to restore the crack initiation behaviour to that in air, and in some cases may lead to improvements over air results as a result of calcareous deposits plugging small cracks. This may delay coalescence, resulting in the growth over a longer period of higher aspect ratio cracks, and hence prolonged life in welded joints. This potential improvement in crack shape development should be considered in any modelling of fatigue crack growth in welded joints. In design applications, however, it is inappropriate to rely on this beneficial effect of calcareous deposits, and more conservative assumptions regarding crack shape development should be made.

4.3 CONCLUSIONS

1. In these tests of welded plate-to-plate T-joints, usually between 20 to 40% of the fatigue life had gone before small cracks, about .5 mm deep, were detected by the potential drop systems

2. Using this detection level as the boundary between initiation life (N_i) and propagation life (N_p), it was possible to statistically assess the influence of plate thickness on N_i and N_p. All of the data indicates that increasing plate thickness reduces N_p. Except for a difference between CANMET and Waterloo data for 103 mm specimens, the data indicates that increasing plate thickness also decreases initiation life.

3. For most of the propagation life, the maximum crack depth (a) is less than 20% of the plate thickness (T). For 40% of the propagation life, the ratio a/T is less than 0.1; in this range crack coalescence is a dominant factor. Ignoring crack coalescence in LEFM models leads to overestimation of fatigue life.

4. There is some evidence that edge cracking tended to exaggerate the thickness effect observed in these experiments. An LEFM model (MC1), that accounts for coalescence and ignores edge cracking, indicates that increasing plate thickness from 16 to 103 mm is likely to reduce fatigue life by a factor of 4.6, which is significantly less than the experimental mean value of about 7 but is still very large.

5. A pipe-plate specimen has been developed to study the influence of seawater on fatigue crack growth in tubular welded joints. This simplified specimen is less ex-

pensive to test and easier to analyze than tubular joints. At the same time, it has no free edges which complicate the interpretation of plate-plate joint tests. Comparisons with tubular joints indicate that this specimen has an initial stress distribution along the weld which is representative of tubular joints. The stress distribution through the thickness is predominantly bending, with no membrane component. This leads to crack front curvature for very deep cracks, as has been observed in some testing of tubular joints. The useful fatigue life has therefore been defined as a 0.8T crack, at the onset of this crack curvature.

6. The fatigue life of two pipe-plate specimens in air were comparable to mean experimental lives from European testing of tubular joints, corrected for thickness. The initiation lives were comparable to results in the T-plate test program. Initiation is defined here as the first detectable crack using the DCPD crack monitoring system. The early crack shape development in the pipe-plate, during coalescence, is similar to that observed in T-plate and tubular joints. Multiple cracks initiate, grow and coalesce with neighbouring cracks to form a dominant semi-elliptic surface crack.

7. Total fatigue life reduction factors of 2.8 and 1.8 were obtained in seawater with *free corrosion* in two pipe-plate tests. This is consistent with values for plate-plate and tubular specimens, see review by Vosikovsky and Tyson. In their review, seawater with free corrosion was reported to reduce the fatigue life by from 2 to 3 times.

   For both specimens in free corrosion, there was a noticeable acceleration of coalescence as a result of more initiation sites compared with air. Coalescence occurred at between 4 and 5 mm in seawater, with free corrosion, compared with about 7 and 8.5 mm in air. Such differences in crack shape development between air and seawater with free corrosion were also observed in the T-plate tests. In the T-plate specimens, there was a tendency for cracks to coalesce in a freely corroding seaawater environment by about 5 mm crack depth. Thereafter, the cracks usually reached the edges of the T-plate specimens, and the remaining lives were short. This edge cracking is analogous to, but more severe than, the formation of a very low aspect ratio crack in the pipe-plate specimens.

8. In seawater with optimum *cathodic protection*, the pipe-plate specimens had total life reduction factors of 1.65 and 1.07. The poor result for specimen PP5, tested at 240 MPa in seawater with cathodic protection, was a result of a very early initiation due to a poor local weld profile, and a 30% decrease in the crack propagation life. For Specimen PP6, tested at 160 MPa, initiation, propagation and total lives were all comparable to corresponding lives in air.

   In a seawater environment with *cathodic over-protection*, fatigue life reduction factors for the pipe-plate specimen were 4.2 and 3.3. This degradation was a combination of

reduced initiation lives, and of a large reduction in fatigue crack propagation lives. Both specimens, had significantly shorter crack propagation lives than in air. This is most likely due to hydrogen embrittlement.

9. Discussions of the benefits of optimum cathodic protection usually cite the improvement in initiation behaviour, counterbalanced by acceleration in crack growth rates of larger cracks. Although this is true, a significant effect of cathodic protection is a change in crack shape development because of a reduction in initiation sites. This has only become apparent as a result of careful monitoring of the crack shape development in cathodically protected T-plates and these pipe-plate joints. Under free corrosion conditions, there is a tendency toward more initiation sites than are observed in air. This has a significant influence on crack shape development and hence on fatigue life. Cathodic protection tends to restore the crack initiation behaviour to that in air, and in some cases may lead to improvements over air results as a result of calcareous deposits plugging small cracks. This may delay coalescence, resulting in the growth over a longer period of higher aspect ratio cracks. This prolongs life. In design applications, it is inappropriate to rely on this beneficial effect of calcareous deposits; also all tests indicate that cathodic over-protection significantly reduces fatigue life.

5 ACKNOWLEDGEMENTS

The authors wish to thank G. Proulx, formerly of AMCA International, presently of Transarc Pulse Systems, for his contribution. Also, earlier or ancilliary studies at Waterloo by M. Rayman, R. Yee and S. Lambert highlighted or solved many of the problems of using DCPD crack monitoring systems. Grants or Scholarships from the Natural Sciences and Engineering Research Council of Canada have supported these students.

References

[1] D.S.S. Contract - "Fabrication and Fatigue Evaluation of Welded Tubular Joints For Structures In A Marine Environment - Phase II)", D.S.S. File 23SQ.23440-4-9276.

[2] Lambert, S., "Fatigue Crack Growth in Pipe-Plate Welded Joints in Seawater", Ph.D. Thesis submitted March 1988, University of Waterloo.

[3] Vosikovsky, O., Bell, R., Burns, D.J. and Mohaupt, U.H., "Fracture Mechanics Assessment of Fatigue Life of Welded Plate T-joints Including Thickness Effect", Proc. of 4th Int. Conf. On Behaviour of Offshore Structures (BOSS '85), J.A. Battjes (editor), Elsevier Science Publisher, Amsterdam, 1985, pp. 453-464.

[4] Bell, R., Vosikovsky, O., Burns, D.J. and Mohaupt, U.H., "A Fracture Mechanics Model For Life Prediction of Welded Plate Joints", Proc. of 3rd Int. Offshore Conf. - Steel in Marine Structures (SIMS'87), C. Noordhoek and J. de Back (editors), Elsevier Science Publisher, Amsterdam,1987.

[5] Bell, R. and Kirkhope, J., "Determination of Stress Intensity Factors For Weld Toe Defects", Final Report D.S.S. Contract OSU82-00233, Carleton University, April 1984.

[6] Bell, R., "Determination of Stress Intensity Factors For Weld Toe Defects - Phase II", Final Report D.S.S. Contract OST84-00125, Carleton University, Oct. 1985.

[7] Tyson, W.R., Vosikovsky, O., Faucher, B. and Burns, D.J., "Brittle Fracture in Heavy Section Welded T-Joints: Correlation Between Stress Intensity at Fracture and Small-Specimen Toughness Tests", Proc. 7th Int. Conf. Offshore Mechanics and Arctic Engineering (OMAE '88), Vol. III, Houston, pp.219-220.

[8] Gangloff, R.P., "Electrical Potential Monitoring of Crack Formation and Sub-Critical Crack Growth From Small Defects", J. Fatigue of Engineering Materials and Structures, Vol.4, No.1 (1981), pp.15-33.

[9] Booth, G.S. and Dobbs, S.J., "Corrosion Fatigue Crack Growth In BS4360 Grade 50D Steel - An Analysis", The Welding Institute Research Bulletin", Sept. 1986.

[10] Berge, S. and Webster, S.E., "The Size Effect On Fatigue of Welded Joints", Paper PS8, Ibid 4.

[11] American Welding Society, "Structural Welding Code - Steel", AWS D1.1-86, Miami.

[12] Mohaupt, U.H., Burns, D.J., Kalbfleisch, J.G., Vosikovsky, O. and Bell, R., "Fatigue Crack Development, Thickness and Corrosion Effects In Welded Plate T-Joints", Paper TS3, Ibid 4.

[13] Newman, J.C. and Raju, I.S., "An Empirical Stress Intensity Factor Equation For The Surface Crack", Engineering Fracture Mechanics, Vol. 15, No.2, 1981, pp.185-192.

[14] Berge, S., "Effect of Plate Thickness in Fatigue of Cruciform Joints", The Norwegian Institute of Technology, Department of Marine Technology, Report MKIR167, March 1983.

[15] Burns, D.J., Lambert, S. and Mohaupt, U.H., "Crack Growth Behaviour and Fracture Mechanics Approach", Paper PS6, Ibid 4.

[16] Verreman, Y., Bailon, J.P. and Masonauve, J., "Fatigue Short Crack Propagation and Plasticity-Induced Closure At The Toe of Fillet Welded Joint", 1st Int. Symp. on the Behaviour of Short Fatigue Cracks, University of Sheffield, Sept. 1985.

[17] Yee, R., Burns, D.J., Mohaupt, U.H., Bell, R. and Vosikovsky, O., "Thickness Effect and Crack Shape Development In Welded Plate T-Joints", Ibid 7.

[18] Niu, X. and Glinka, G., "The Effect of Weld Geometry On Stress Intensity Factors and Fatigue Crack Growth", Int. Conf. on Fatigue of Welded Constructions, Brighton, U.K., April, 1987.

[19] Dijkstra, O.D., Snijder, H.H. and Overbeeke, J.L. and Wildschut, H., "Prediction of Fatigue Crack Growth For Welded Joints Using Stress Intensity Factors Determined By FEM Calculations", Paper TS52, Ibid 4.

[20] Forbes, J., Private Communication, University of Waterloo.

[21] Clayton, A.M., "Stress In Tubular Joints", Interim Technical Report UKOSRP2/04, May 1978.

[22] Dover, W.D. and Dharmavasan,S., "Fatigue Fracture Mechanics Analysis of Y-Joints", OTC 4404, Houston, Texas,1982.

[23] Dijkstra, O.D. and Noordhoek, C., "The Effect of Grinding and Special Weld Profile On The Fatigue Behaviour of Large-Scale Tubular Joints", OTC 4866, Offshore Technology Conference, Houston, Texas, 1985.

[24] Department of Energy, U.K., Offshore Installations:Guidance On Design and Construction, New Fatigue Design Guidance For Steel Welded Joints In Offshore Structures. HMSO, 1984.

[25] Tyson, W.R. and Vosikovsky, O., "Effects of Cathodic Protection On Fatigue Life of Steel Welded Joints", Proc. of Workshop on Cathodic Protection: A + or - In Corrosion Fatigue. Halifax, Nova Scotia, Sept.86. Ministry of Supply and Services, Canada ISBN-0-660-12546-3.

TABLES

Table 1
Specimen dimensions for T-plates

JOINT	T (mm)	l (mm)	L (mm)	A (mm)
A	16	8–12	300	406
B	26	14–18	442	406
C	52	26–30	442	406
D	78	38–42	584	457
E	103	52–56	726	457

Table 2(a)
In-air fatigue data from Waterloo tests
(N_i based on $a_i = .5mm$)

T (mm)	$\Delta\sigma$ (MPa)	N_i (kcycles)	N_T (kcycles)	N_i/N_T (%)
16	100	2340	8986	26.0
	125	1013	4430	22.9
	175	860	2082	41.3
	225	75	280	26.8
	300	80	158	50.5
26	90	1575	5682	27.7
	100	2470	6815	34.1
	150	268	976	27.4
	187	104	265	39.0
	250	20	126	15.8
52	110	430	1650	25.8
	125	131	751	17.5
	175	89	308	28.9
	225	15	92	16.3
	300	8	49	16.3
78	90	1135	3405	33.3
	125	116	750	15.4
	300	5	64	7.8
103	80	1400	4036	34.7
	125	180	658	27.3
	175	83	220	37.8
	200	19	96	19.7
	250	17	59	28.8

Table 2(b)
In-air fatigue data from CANMET tests
(N_i based on $a_i = .5mm$)

T (mm)	$\Delta\sigma$ (MPa)	N_i (kcycles)	N_T (kcycles)	N_i/N_T (%)
16	150	320	1270	26.0
	200	147	460	32.0
26	100	1130	3910	28.9
	150	390	1125	34.7
	200	88	336	26.2
52	100	380	1210	31.4
	150	90	370	24.3
	200	37	137	27.0
78	100	260	1257	20.4
	150	70	282	24.8
	200	25	97	25.8
103	100	160	660	24.2
	150	45	167	26.9

Table 3
Corrosion fatigue data
(N_i based on $a_i = .5mm$)

T (mm)	Potential (volts)	$\Delta\sigma$ (MPa)	N_i (kcycles)	N_T (kcycles)	N_i/N_T (%)
26	f.c.	100	760	1660	45.8
		110*	325	932	34.9
		150	130	318	40.9
		150	146	312	46.8
		200	39	106	36.8
26	-0.85	100	750	2950	25.4
		110*	370	1006	36.8
		150	155	355	43.7
		200	175	404	43.3
		200	26	131	19.8
26	-1.05	110*	220	837	26.3
		150	630	910	69.2
		150	232	420	55.2
		200	27	90	30.0
78	f.c.	80	150	1033	14.5
		100	150	490	30.6
		110*	97	398	24.4
		150	44	167	26.3
		200	17	66	25.8
78	-0.85	80	200	962	20.8
		100	385	924	41.2
		110*	67	340	19.7
		150	30	165	19.4
		200	18	81	22.2
78	-1.05	80	800	1975	40.5
		100	220	692	31.8
		110*	151	420	36.0
		150	33	123	26.9
		200	8	54	15.0

f.c. free corrosion

* Waterloo test data

Table 4
Predicted initiation life (kcycles) based on equation (4)

T (mm)	Environment	Predicted Life	Actual Life	Actual Life/ Predicted Life
16 - #2*	air	25	80	3.19
16 - #4	air	243	860	3.54
26 - #6	seawater (f.c.)	820	325	.396
26 - #7	seawater (o.c.p.)	820	370	.451
26 - #8	seawater (c.o.)	820	220	.269
78 - #4	seawater (f.c.)	372	97	.260
78 - #5	seawater (o.p.c)	372	67	.179
78 - #6	seawater (c.o.)	372	151	.404

* Experimental problems
f.c. free corrosion
o.c.p. optimum cathodic protection
c.o. cathodic over-protection

Table 5
Predicted propagation life (kcycles) based on equation (5)

T (mm)	Environment	Predicted Life	Actual Life	Actual Life/ Predicted Life
16 -#2*	air	135	89	.659
26 -#6	seawater (f.c.)	2267	607	.268
26 - #7	seawater (o.c.p.)	2267	636	.280
26 - #8	seawater (c.o.)	2267	617	.272
78 - #4	seawater (f.c.)	977	300	.308
78 - #5	seawater (o.p.c)	977	273	.280
78 - #6	seawater (c.o.)	372	269	.276

* Experimental problems
f.c. free corrosion
o.c.p. optimum cathodic protection
c.o. cathodic over-protection

Table 6
Predicted total life (kcycles) based on equation (6)

T (mm)	Environment	Predicted Life	Actual Life	Actual Life/ Predicted Life
26 - #6	seawater (f.c.)	3183	932	.293
26 - #7	seawater (o.c.p.)	3183	1006	.316
26 - #8	seawater (c.o.)	3183	837	.263
78 - #4	seawater (f.c.)	1353	397	.294
78 - #5	seawater (o.p.c)	1353	340	.251
78 - #6	seawater (c.o.)	1353	420	.310

* Experimental problems
f.c. free corrosion
o.c.p. optimum cathodic protection
c.o. cathodic over-protection

Table 7
Predicted life (kcycles) for in-air tests at $\Delta\sigma = 150$ MPa

		T (mm)				
		16	26	52	78	103
Initiation	W*	607	254	107	87	103
Life	O*	364	298	94	66	35
	O and W*	515	283	97	72	68
Propagation	W*	1732	715	393	408	248
Life	O*	894	588	249	257	130
	O and W *	1388	676	326	318	195
Total	W	2330	997	505	510	355
Life	O	1265	905	344	311	164
	O and W	1905	992	427	386	266

* - omit 16 mm #2 data
W - Waterloo data
O - CANMET data

Table 8
Estimates of correction factors for seawater tests

		Slope β	Correction Factors			Error Variance Δ^2(df)
			f.c.	o.p.	c.o.	
Initiation Life	W	-4.124	.333	.295	.342	.2132 (19)
	O	-3.598	.481	.608	.685	.2704 (28)
	O and W	-3.652	.456	.537	.598	.2900 (56)
Propagation Life	W	-3.595	.259	.253	.248	0.0895 (19)
	O	-3.436	.368	.561	.405	0.0766 (28)
	O and W	-3.395	.312	.434	.331	.1145 (56)
Total Life	W	-3.705	.270	.260	.263	0.0877 (20)
	O	-3.501	.407	.586	.511	.1006 (28)
	O and W	3.445	.348	.462	.409	.1332 (57)

f.c. - free corrosion
o.p.- optimum protection
c.o. - cathodic over-protection
W - Waterloo data
O - CANMET data

Table 9
Pipe-Plate Test Matrix

Specimen	Hot-spot Stress Range (MPa)	Environment
PP0[1]	175/225[2]	Air
PP1	240	Air
PP2	160	Air
PP3	240	Sea/FC[3]
PP4	160	Sea/FC[3]
PP5	240	Sea/CP[4]
PP6	160	Sea/CP[4]
PP7	240	Sea/OP[5]
PP8	160	Sea/OP[5]

[1]PP0 had a different geometry than all subsequent specimen
[2]Stress was increased during test
[3]Seawater with Free Corrosion
[4]Seawater with Optimum Cathodic Protection (-0.850 V Ag/AgCl)
[5]Seawater with Cathodic Over-Protection (-1.10 V Ag/Cl)

Table 10
PP0 - PD probe locations

Probe	Position[1]	Type[2]	Probe	Position	Type	Probe	Position	Type
3	-165.1	a	22	25.4	a	39	82.5	a
4	-152.4	a	23	-19.0	a	40	88.9	a
5	-139.7	a	24	-12.7	a	41	95.3	a
6	-127.0	a	25	- 6.3	a	42	101.6	a
8	-114.3	a	26	0.0	a	44	114.3	a
10	-101.6	a	27	6.3	a	46	127.0	a
11	-95.3	a	28	12.7	a	47	139.7	a
12	-88.9	a	29	19.0	a	48	152.4	a
13	-82.5	a	30	25.4	a	49	165.1	a
14	-76.2	a	31	31.8	a	52	-190.5	r
15	-69.8	a	32	38.1	a	53	-127.0	r
16	-63.5	a	33	44.5	a	54	-63.5	r
17	-57.1	a	34	50.8	a	55	0.0	r
18	-50.8	a	35	57.1	a	56	63.5	r
19	-44.5	a	36	63.5	a	57	127.0	r
20	-38.1	a	37	69.8	a	58	190.5	r
21	-31.8	a	38	76.2	a			

Position[1] - distance from hot-spot (mm)
Type[2] (a) - active probe
Type[2] (b) - local reference probe
Type[2] (c) - far-field reference

Table 11
PP0 - Summary of Constraints CONT'D

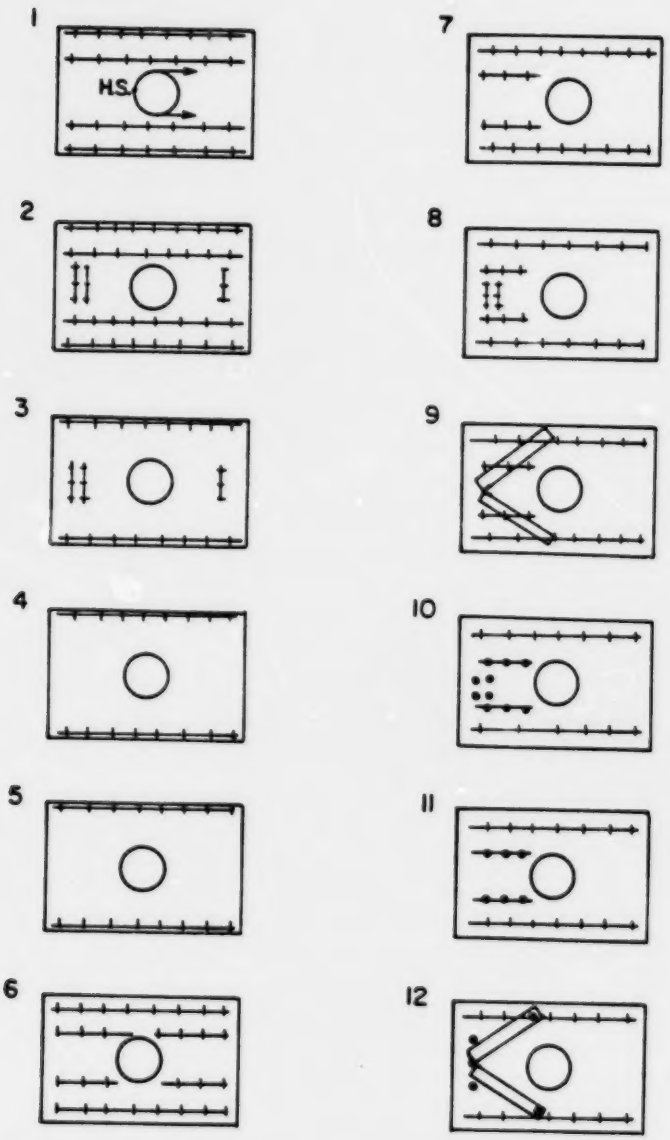

Table 11
PP0 - Summary of Constraints

Constraint Condition	Stresses - extrapolated to weld toe - σ_r and σ_t					SCF	
	Plate				Brace	Plate	Brace
	Top	Bottom	Membrane	Bending	Surface		
1	138.3 66.0	-122.1 - 71.8	8.1 -2.9	130.2 68.9	137.6 84.7	6.52	6.49
2	145.5 68.1	-128.9 - 73.8	8.3 -2.9	137.2 71.0	143.4 87.6	6.86	6.47
3	166.2 74.6	-148.2 - 80.8	9.0 -3.1	157.2 77.7	154.2 92.3	7.84	7.27
4	143.0 67.9	-124.9 - 73.9	9.1 -2.8	134.0 70.7	138.3 86.3	6.74	6.52
5	165.4 77.4	-145.0 - 84.7	10.2 -3.7	155.2 81.1	154.7 95.7	7.80	7.29
6	136.2 65.1	-120.5 - 71.3	7.9 -3.1	128.4 68.2	138.3 84.2	6.42	6.52
7	134.0 64.6	-114.3 - 68.7	9.9 -2.1	124.2 66.7	134.2 84.2	6.32	6.33
8	138.1 66.2	-119.1 -70.8	9.5 -1.8	128.6 68.5	137.9 84.8	6.51	6.50
9	138.5 66.5	-118.1 - 70.1	10.2 -1.8	128.3 68.3	138.8 84.6	6.53	6.54
10	130.4 63.4	-110.7 - 66.8	9.9 -1.7	120.6 65.1	132.2 81.1	6.15	6.23
11	125.0 62.1	-108.0 - 66.0	8.5 -2.0	116.5 64.1	128.3 79.3	5.89	6.05
12	133.7 63.8	-116.7 - 69.5	8.5 -2.9	125.2 66.7	135.0 83.4	6.30	6.36

Table 12
PP1 - PD probe locations

Probe	Position[1]	Type[2]	Probe	Position	Type	Probe	Position	Type
2	-177.8	a	26	12.7	a	53	-107.9	lr
3	-152.4	a	27	19.0	a	54	-88.9	lr
4	-127.0	a	28	25.4	a	55	-69.8	lr
6	-114.3	a	29	31.8	a	56	-44.5	lr
8	-101.6	a	30	38.1	a	57	0.0	lr
9	-95.3	a	31	44.5	a	58	25.4	lr
10	-88.9	a	32	50.8	a	59	44.5	lr
11	-82.5	a	33	57.1	a	60	69.8	lr
12	-76.2	a	34	63.5	a	61	88.9	lr
13	-69.8	a	35	69.8	a	62	107.9	lr
14	-63.5	a	36	76.2	a	63	127.0	lr
15	-57.1	a	37	82.5	a	64	152.4	lr
16	-50.8	a	38	88.9	a	65	177.8	lr
17	-44.5	a	39	95.3	a	67	-190.5	r
18	-38.1	a	40	101.6	a	68	-127.0	r
19	-31.8	a	42	114.3	a	69	-63.5	r
20	-25.4	a	44	127.0	a	70	0.0	r
21	-19.0	a	45	152.4	a	71	63.5	r
22	-12.7	a	46	177.8	a	72	127.0	r
23	-6.3	a	50	-177.8	lr	73	190.5	r
24	0.0	a	51	-152.4	lr			
25	6.3	a	52	-127.0	lr			

Position[1] - distance from hot-spot (mm)
Type[2] (a) - active probe
Type[2] (b) - local reference probe
Type[2] (c) - far-field reference

Table 13
PP2 - PD probe locations

Probe	Position[1]	Type[2]	Probe	Position	Type	Probe	Position	Type
1	-177.8	a	22	-12.7	a	43	120.7	a
2	-152.4	a	23	-6.3	a	44	127.0	a
3	-139.7	a	24	0.0	a	45	139.7	a
4	-127.0	a	25	6.3	a	46	152.4	a
5	-120.7	a	26	12.7	a	47	177.8	a
6	-114.3	a	27	19.0	a	48	-177.8	lr
7	-107.9	a	28	25.4	a	49	-152.4	lr
8	-101.6	a	29	31.8	a	50	-127.0	lr
9	-95.3	a	30	38.1	a	51	-101.6	lr
10	-88.9	a	31	44.5	a	52	-76.2	lr
11	-82.5	a	32	50.8	a	53	-50.8	lr
12	-76.2	a	33	57.1	a	54	-25.4	lr
13	-69.8	a	34	63.5	a	55	0.0	lr
14	-63.5	a	35	69.8	a	56	25.4	lr
15	-57.1	a	36	76.2	a	57	50.8	lr
16	-50.8	a	37	82.5	a	58	76.2	lr
17	-44.5	a	38	88.9	a	59	101.6	lr
18	-38.1	a	39	95.3	a	60	127.0	lr
19	-31.8	a	40	101.6	a	61	152.4	lr
20	-25.4	a	41	107.9	a	62	177.8	lr
21	-19.0	a	42	114.3	a			

Position[1] - distance from hot-spot (mm)
Type[2] (a) - active probe
Type[2] (b) - local reference probe
Type[2] (c) - far-field reference

Table 14
PP3 - PD probe locations

Probe	Position[1]	Type[2]	Probe	Position	Type	Probe	Position	Type
1	-196.8	a	24	-19.0	a	47	127.0	a
2	-171.4	a	25	-12.7	a	48	133.3	a
3	-158.8	a	26	-6.3	a	49	139.7	a
4	-146.1	a	27	0.0	a	50	146.1	a
5	-139.7	a	28	6.3	a	51	158.8	a
6	-133.3	a	29	12.7	a	52	171.4	a
7	-127.0	a	30	19.0	a	53	196.8	a
8	-120.7	a	31	25.4	a	54	-158.8	lr
10	-107.9	a	32	31.8	a	55	-127.0	lr
11	-101.6	a	33	38.1	a	56	-101.6	lr
12	-95.3	a	34	44.5	a	57	-76.2	lr
13	-88.9	a	35	50.8	a	58	-50.8	lr
14	-82.5	a	36	57.1	a	59	-25.4	lr
15	-76.2	a	37	63.5	a	60	0.0	lr
16	-69.8	a	38	69.8	a	61	25.4	lr
17	-63.5	a	39	76.2	a	62	50.8	lr
18	-57.1	a	40	82.5	a	63	76.2	lr
19	-50.8	a	41	88.9	a	64	101.6	lr
20	-44.5	a	42	95.3	a	65	127.0	lr
21	-38.1	a	43	101.6	a	66	158.8	lr
22	-31.8	a	44	107.9	a			
23	-25.4	a	46	120.7	a			

Position[1] - distance from hot-spot (mm)
Type[2] (a) - active probe
Type[2] (b) - local reference probe
Type[2] (c) - far-field reference

Table 15
PP4 - PP8 - PD probe locations

Probe	Position[1]	Type[2]	Probe	Position	Type	Probe	Position	Type
1	-190.5	a	23	-19.0	a	45	120.7	a
2	-177.8	a	24	-12.7	a	46	127.0	a
3	-165.1	a	25	-6.3	a	47	139.7	a
4	-152.4	a	26	0.0	a	48	152.4	a
5	-139.7	a	27	6.3	a	49	165.1	a
6	-127.0	a	28	12.7	a	50	177.8	a
7	-120.7	a	29	19.0	a	51	190.5	a
8	-114.3	a	30	25.4	a	52	-165.1	lr
9	-107.9	a	31	31.8	a	53	-127.0	lr
10	-101.6	a	32	38.1	a	54	-101.6	lr
11	-95.3	a	33	44.5	a	55	-76.2	lr
12	-88.9	a	34	50.8	a	56	-50.8	lr
13	-82.5	a	35	57.1	a	57	-25.4	lr
14	-76.2	a	36	63.5	a	58	0.0	lr
15	-69.8	a	37	69.8	a	59	25.4	lr
16	-63.5	a	38	76.2	a	60	50.8	lr
17	-57.1	a	39	82.5	a	61	76.2	lr
18	-50.8	a	40	88.9	a	62	101.6	lr
19	-44.5	a	41	95.3	a	63	127.0	lr
20	-38.1	a	42	101.6	a	64	165.1	lr
21	-31.8	a	43	107.9	a			
22	-25.4	a	44	114.3	a			

Position[1] - distance from hot-spot (mm)
Type[2] (a) - active probe
Type[2] (b) - local reference probe
Type[2] (c) - far-field reference

Table 16
Incidence of edge cracking

T (mm)	$\Delta\sigma$ (MPa)	a_E (mm)	N_E (kcycles)	N_E/N_T (%)
16	200	10 (s)	475	103
16	150	10 (a.s.)	1320	104
26	200	12 (a.s.)	330	98
26	150	15 (a.s.)	1140	101
26	100	15 (s)	4140	106
52	200	5 (a.s.)	96	70
52	150	12 (a.s.)	300	81
52	100	14 (s)	1120	93
78	200	6 (a.s.)	56	58
78	150	12 (a.s.)	224	79
78	100	11 (a.s.)	1080	86
78	80	17(s)	1510	89
103	100	16(a.s.)	590	89
103	70	20(a.s.)	1860	78

s - both edges (i.e. symmetric)
a.s. - one edge (i.e. asymmetric)

Table 17
N_p (kcycles) from a_i = .5mm to a_T/T = .5 predicted with
LEFM model (SC1) for natural growth of a single semi-elliptic crack
($\Delta\sigma$ = 150 MPa)

T	a/2c				
(mm)	.1	.2	.3	.4	.5
16	1720	1800	1840	1865	1880
26	1420	1480	1505	1515	1530
52	1050	1085	1095	1110	1113
78	864	888	895	903	905
103	725	746	750	755	780

Table 18
N_p (kcycles) from a_i = .5mm to a_T/T = .5
($\Delta\sigma$ =150 MPa)

Plate Thickness (mm)	LEFM Predictions				Statistical Model of experimental data		
	SC1	SC2	MC1	MC2	CANMET	UW	Combined
16	1880	1080	1680	1397	894	1732	1388
26	1400	890	1170	768	588	715	676
52	1100	595	620	326	249	393	326
78	900	435	470	217	257	408	318
103	750	315	365	170	130*	248*	195*

Table 19
Thickness Effect Ratios Based on N_p from table 18
($\Delta\sigma$ =150 MPa)

Plate Thickness (mm)	LEFM Predictions				Statistical Model of experimental data		
	SC1	SC2	MC1	MC2	CANMET	UW	Combined
16/26	1.3	1.2	1.4	1.8	1.5	2.4	2.1
16/52	1.7	1.8	2.7	4.3	3.6	4.4	4.2
16/78	2.1	2.5	3.6	6.4	3.5	4.2	4.4
16/103	2.5	3.4	4.6	8.2	6.9*	7.0*	7.1*

* brittle pop-ins
SC1 - natural growth of single crack ($a_i/2c$ = .5)
SC2 - single crack with fixed aspect ratio (a/2c = .1)
MC1 - single crack with forcing function for a/2c to account for coalescence
MC2 - single crack with forcing function for a/2c to account for coalescence and edge cracking

Table 20
Weld toe geometry of T-plates tested at CANMET

T (mm)	θ_{min} (deg)	θ_{max} (deg)	$\overline{\theta}$ (deg)	ρ_{min} (mm)	ρ_{max} (mm)	$\overline{\rho}$ (deg)
16	34	47	40	0.4	2.0	1.2
16	30	44	38	0.4	2.4	1.5
16	31	51	40	0.4	2.0	1.2
26	35	50	42	0.2	2.2	1.3
26	32	46	38	0.3	3.2	1.3
26	33	38	36	0.7	3.0	1.6
52	33	57	39	0.5	3.3	1.3
52	33	55	41	0.5	1.8	1.1
52	33	45	39	0.2	3.0	1.1
78	39	52	46	0.2	2.0	0.9
78	40	62	46	0.3	2.5	1.8
78	36	69	46	0.8	3.0	1.9
103	31	53	40	0.3	3.0	1.5
103	30	72	45	1.0	3.0	1.7
103	36	52	43	0.5	2.4	1.5

Table 21
Summary of pipe-plate test results

Specimen	Hot-spot Stress Range (MPa)	Environment	Total Life (kcycles)	Initiation Life (kcycles)	Propagation Life (kcycles)
PP1	240	Air	413	55	358
PP2	160	Air	1130	100 – 150	985 – 1030
PP3	240	Sea/FC[3]	148	20	128
PP4	160	Sea/FC[3]	613	120	493
PP5	240	Sea/CP[4]	250	5	245
PP6	160	Sea/CP[4]	1070	160	910
PP7	240	Sea/OP[5]	99	20	79
PP8	160	Sea/OP[5]	339	50	289

Table 22
Crack growth rates for pipe-plates

Specimen (Probe)	0.5T(13m)		0.6T(15.6m)		0.7T(18.2m)	
	a/2c	da/dN	a/2c	da/dN	a/2c	da/dN
PP0	0.133	0.036	0.120	0.046	0.094	0.052
PP1 (27)	0.0491	0.114	0.055	0.120	0.056	0.082
PP2 (17)	0.057	0.035	0.057	0.037	0.046	0.026
PP3 (27)	0.030	0.280	0.037	0.295	0.038	0.230
PP4 (27)	0.041	0.101	0.043	0.085	0.044	0.051
PP5 (24)	0.043	0.217	0.041	0.200	0.037	0.145
PP6 (24)	0.084	0.030	0.073	0.037	0.039	0.036
PP7 (30)	0.029	0.380	0.035	0.360	0.041	0.300
PP8 (33)	0.083	0.096	0.054	0.070	0.050	0.066

Table 23
Empirical ΔK values corresponding to da/dN values in Table 22

Specimen	0.5T(13mm)		0.6T(15.6mm)		0.7T(18.2mm)	
	ΔK	da/dN	ΔK	da/dN	ΔK	da/dN
PP1	40.12	0.114	40.16	0.120	39.95	0.082
PP2	25.38	0.035	26.28	0.037	30.70	0.026
PP3	47.26	0.280	49.04	0.295	52.69	0.230
PP4	28.45	0.101	30.34	0.085	31.69	0.051
PP5	41.99	0.217	46.61	0.200	53.67	0.145
PP6	22.05	0.030	23.14	0.037	34.50	0.036
PP7	47.76	0.380	50.39	0.360	49.97	0.300
PP8	22.15	0.096	27.02	0.070	28.91	0.066

FIGURES

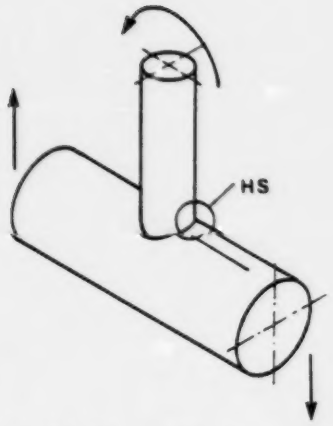

a) TUBULAR

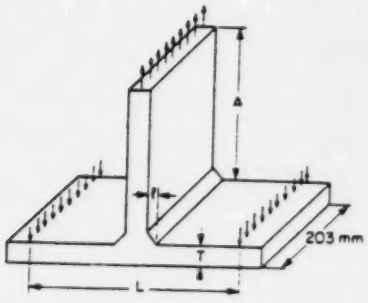

b) PLATE - PLATE

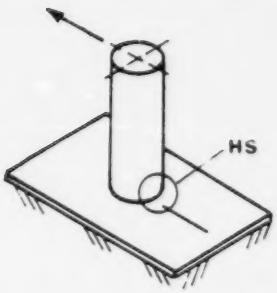

c) PIPE PLATE

Figure 1: Full penetration welded joint fatigue specimens

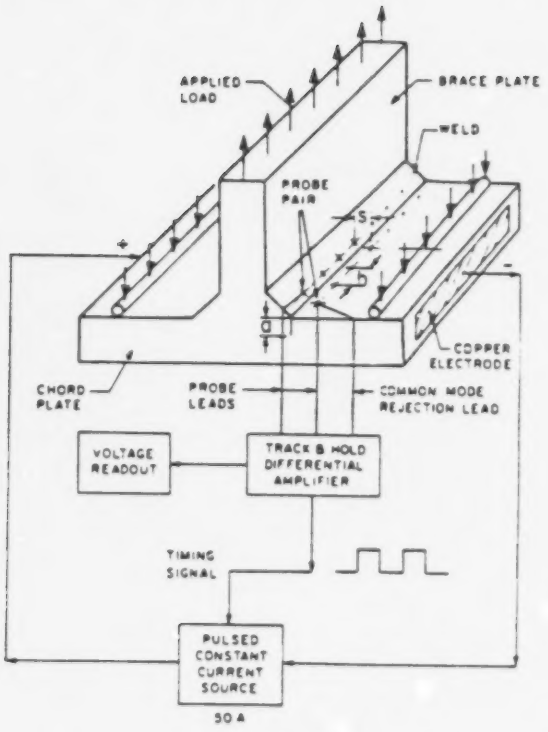

Figure 2: Pulsed DC potential drop system

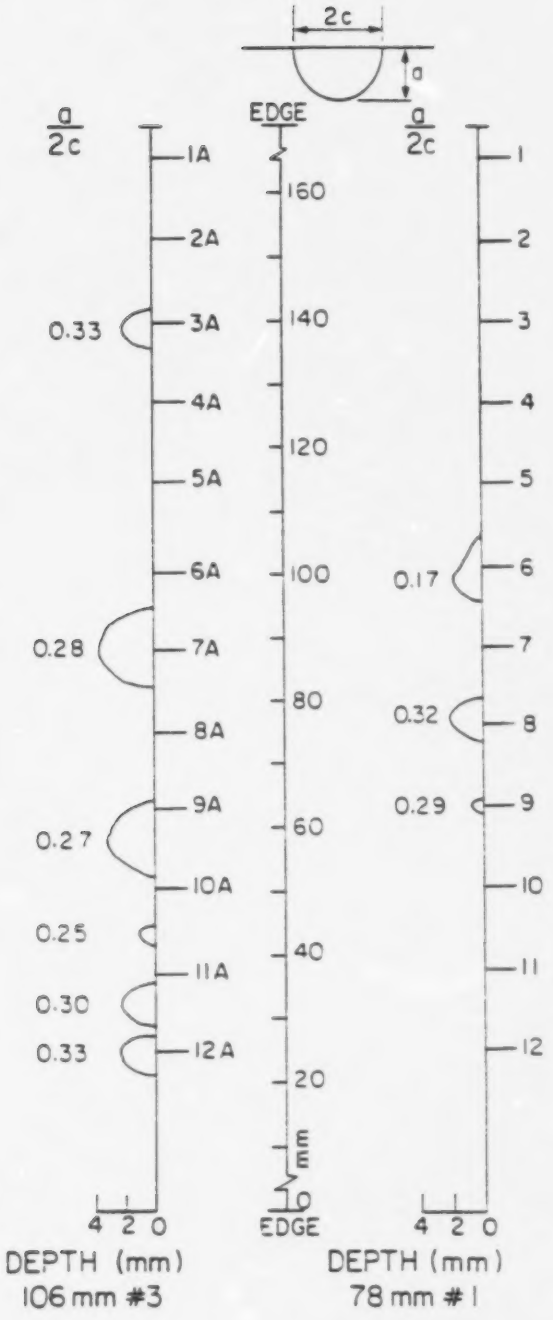

Figure 3: Cracks detected by ink staining two specimens

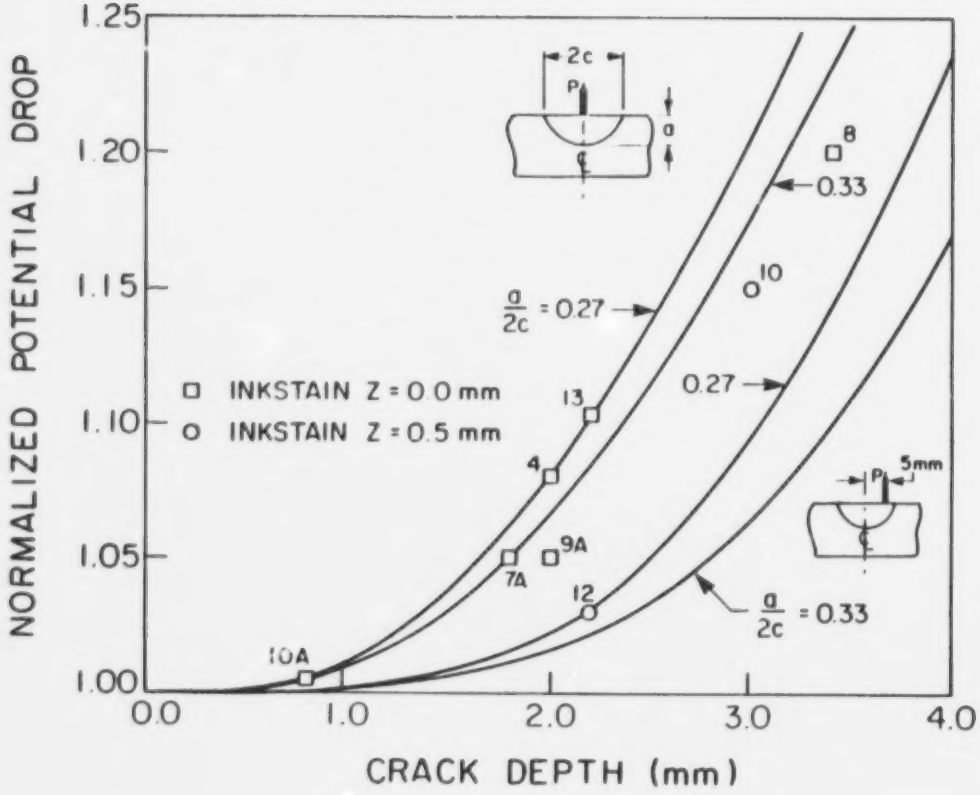

Figure 4: Experimental and theoretical relationship between normalized voltage and maximum crack depth

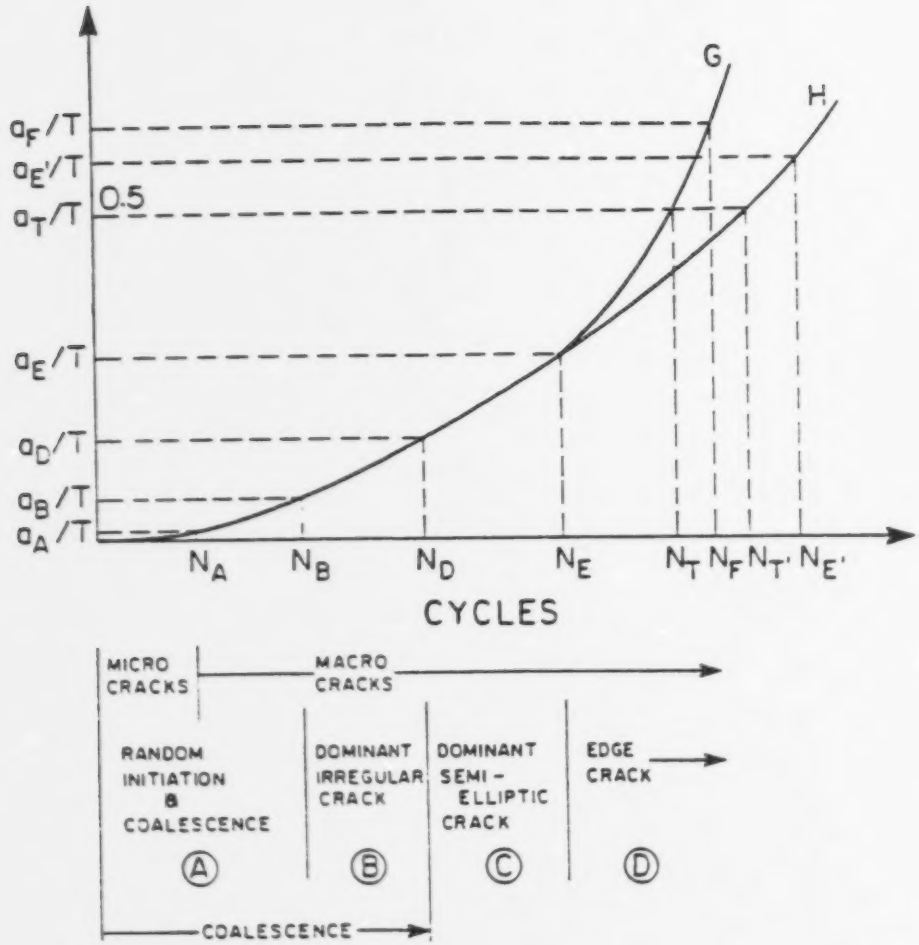

Figure 5: Crack development in T-plate joints

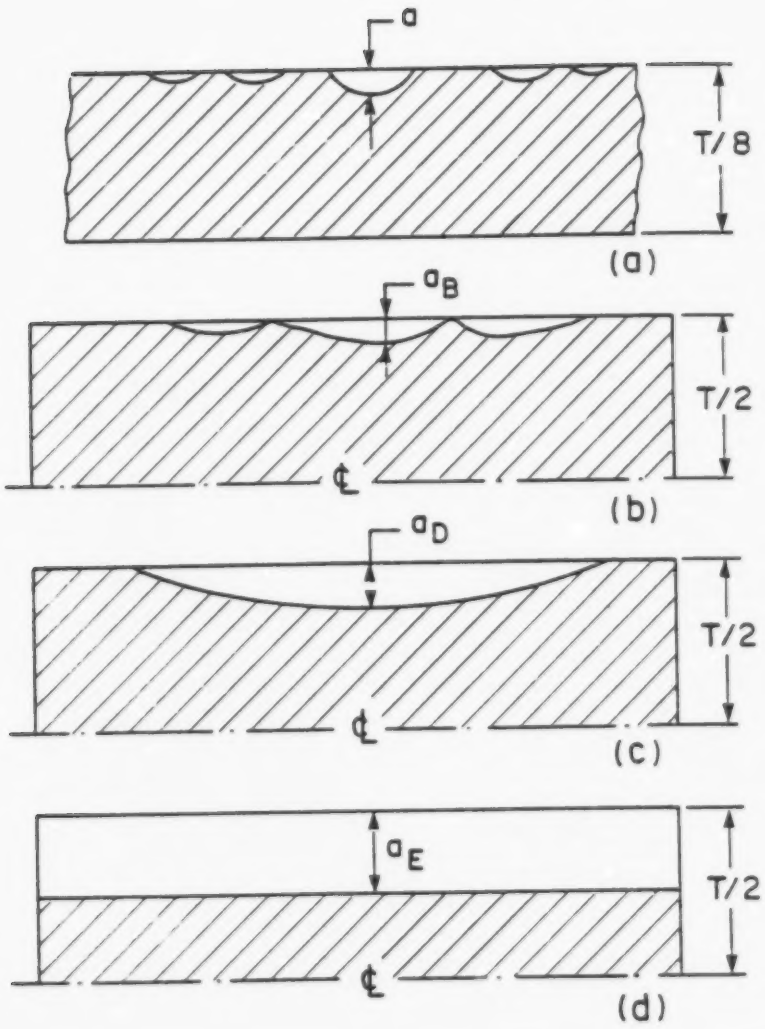

Figure 6: Schematic of crack shape development in T-plate joints

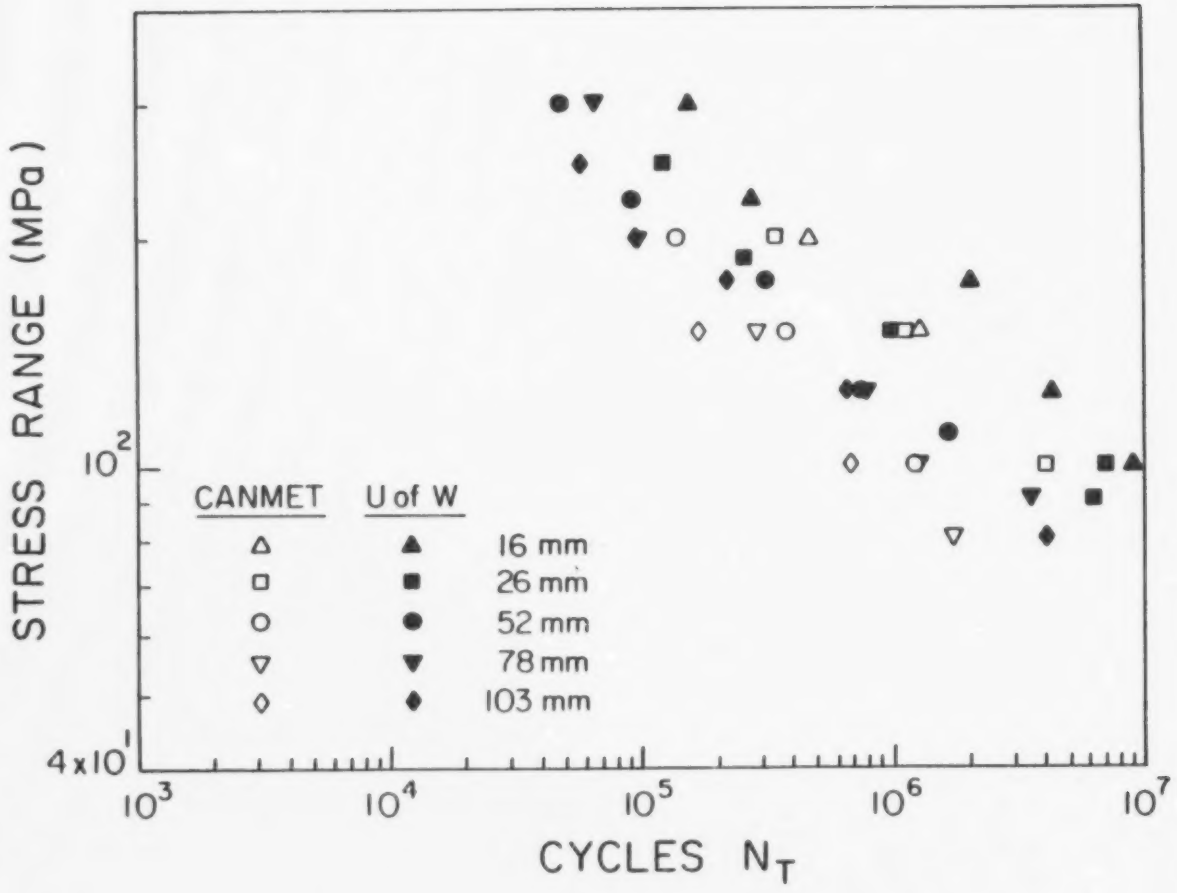

Figure 7: Hot spot stress range vs total fatigue life (N_T)

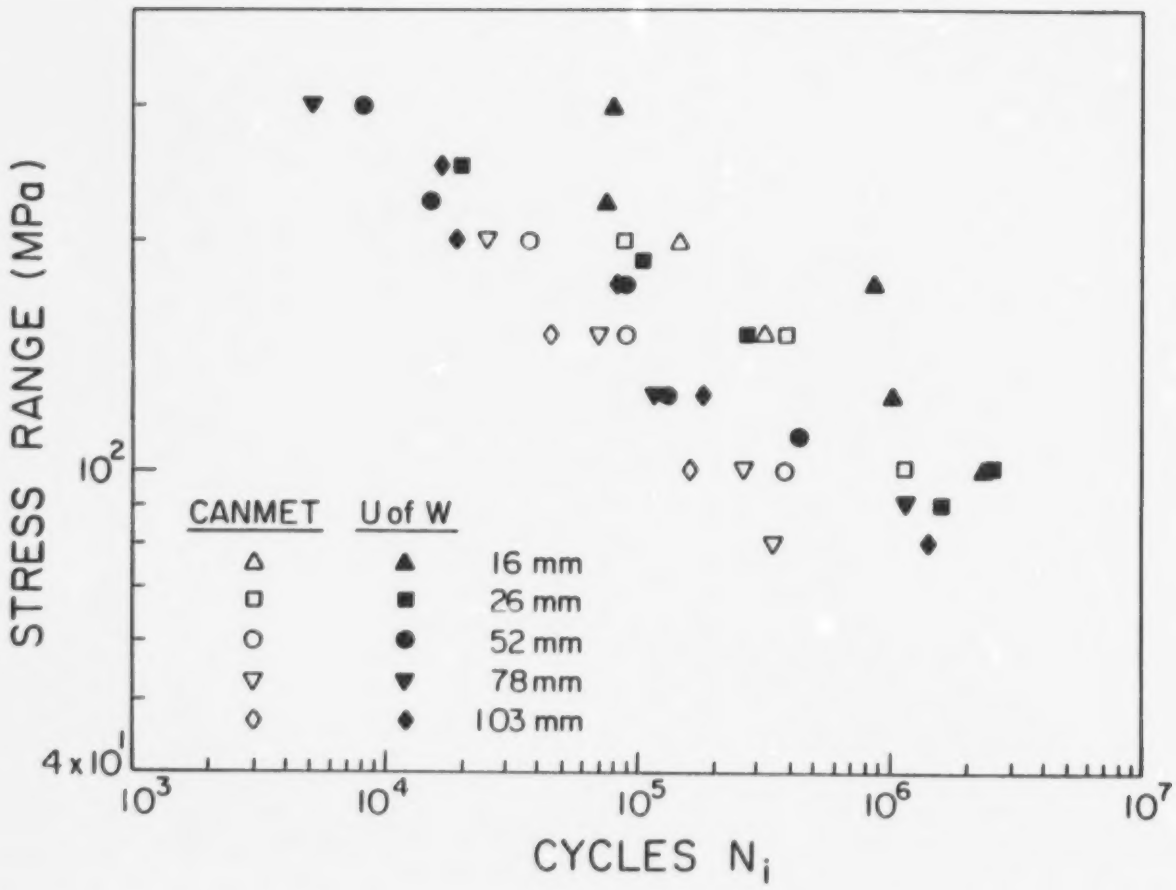

Figure 8: Hot spot stress range vs initiation life (N_i)

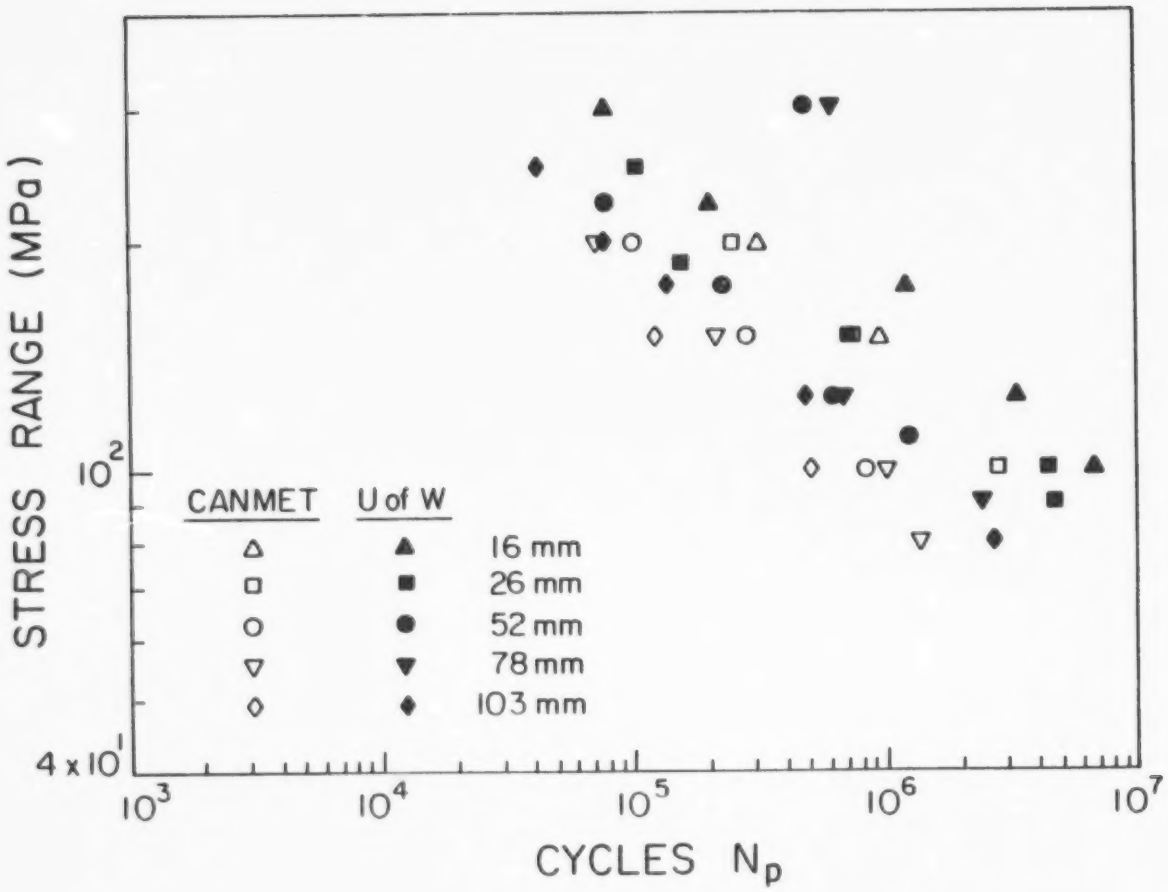

Figure 9: Hot spot stress range vs propagation life (N_p)

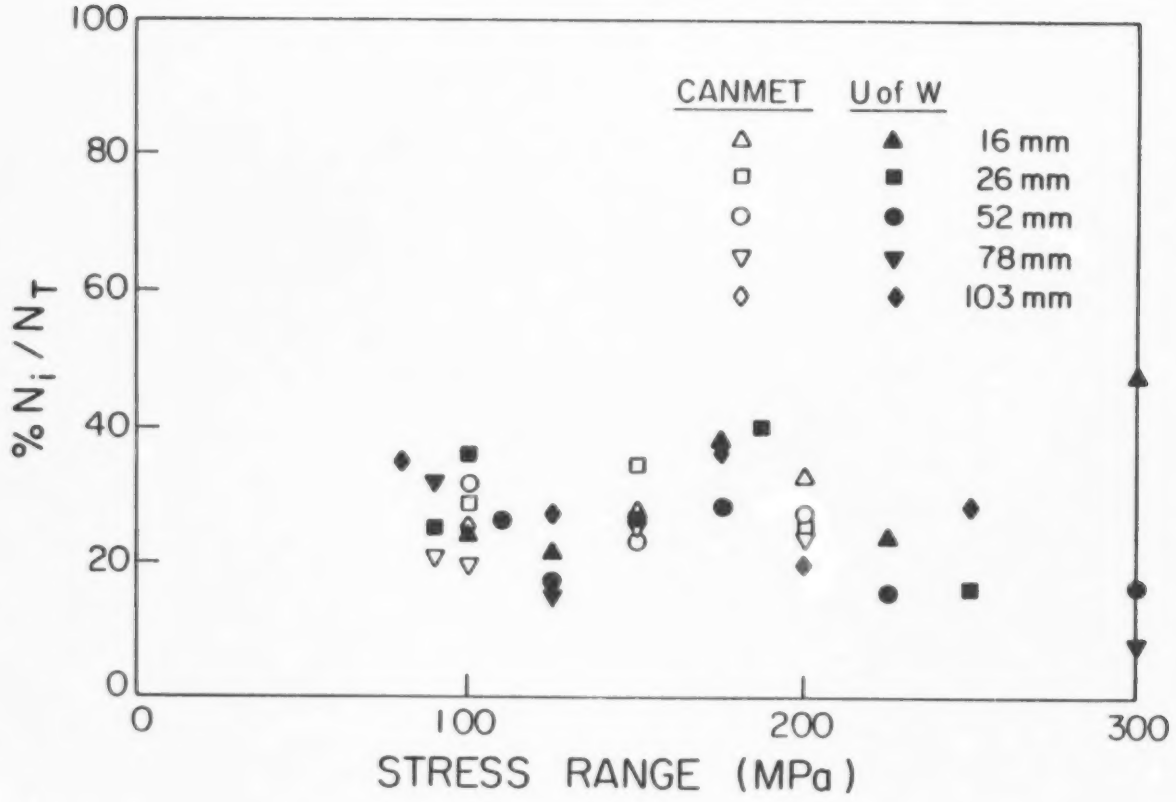

Figure 10: % N_i/N_T vs hot spot stress range

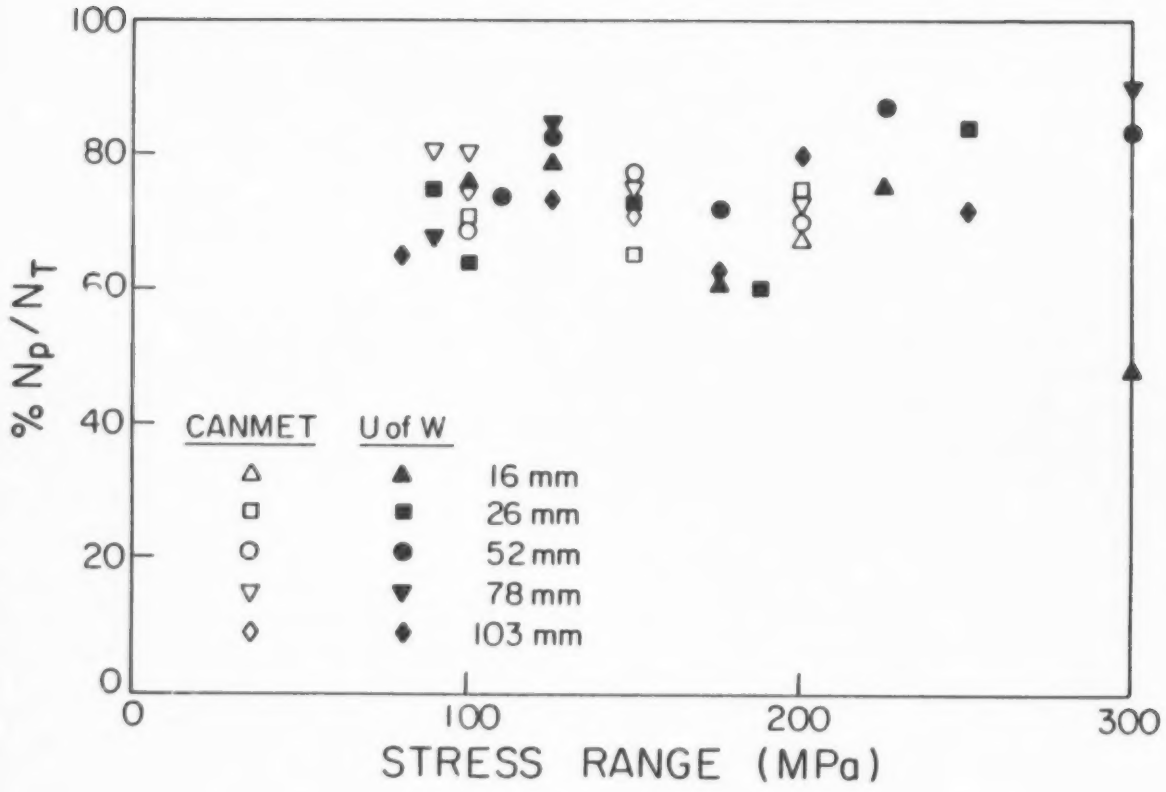

Figure 11: % N_p/N_T vs hot spot stress range

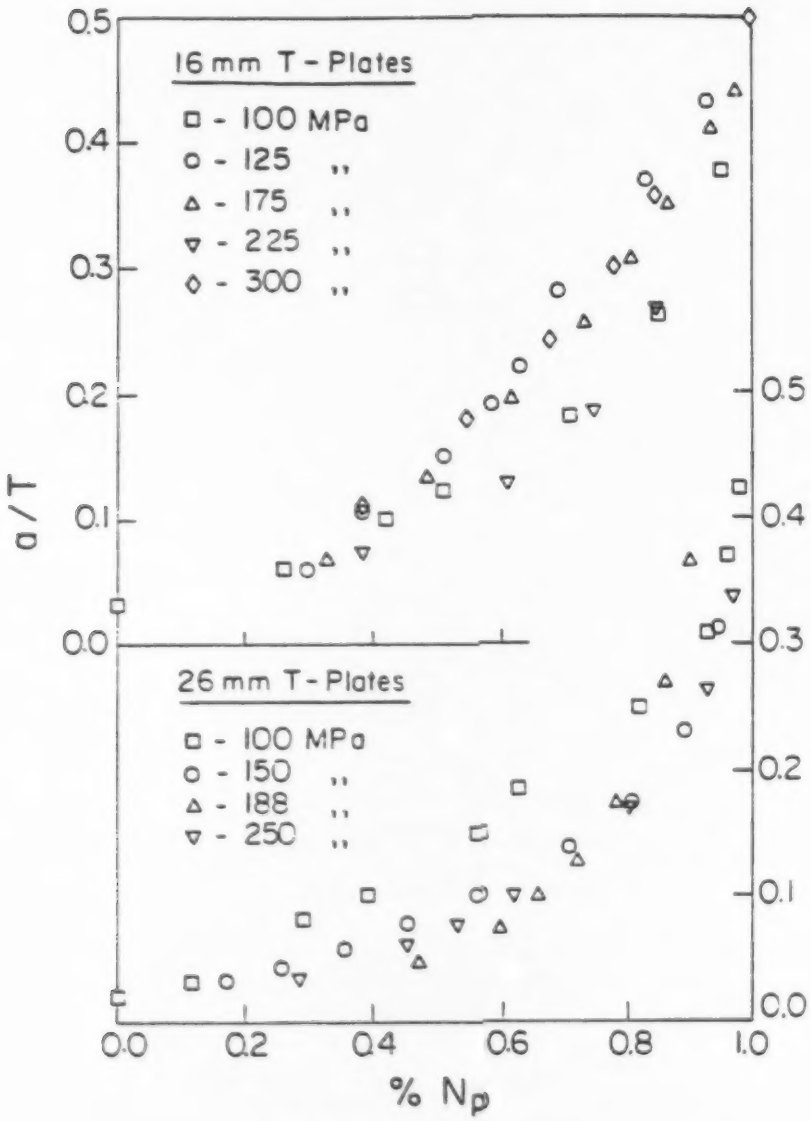

Figure 12: Normalized crack depth vs % N_p for 16 and 26 mm plates for various hot spot stress ranges

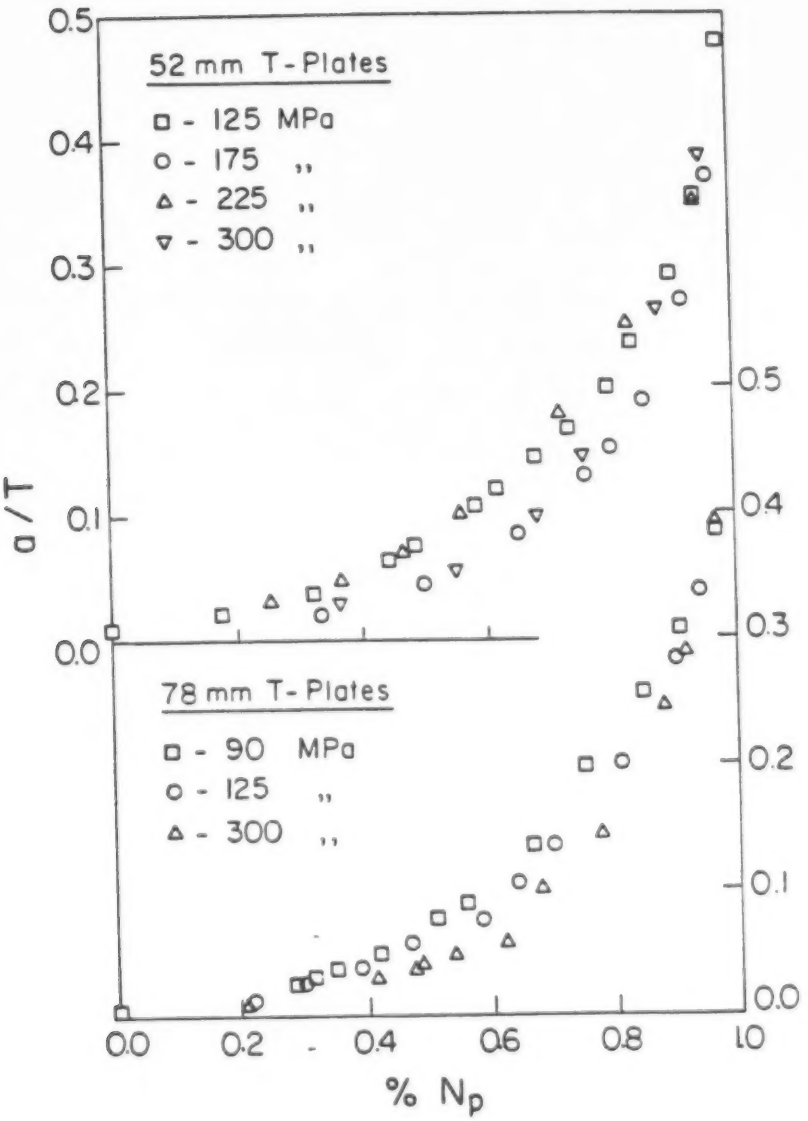

Figure 13: Normalized crack depth vs % N_p for 52 and 78 mm plates for various hot spot stress ranges

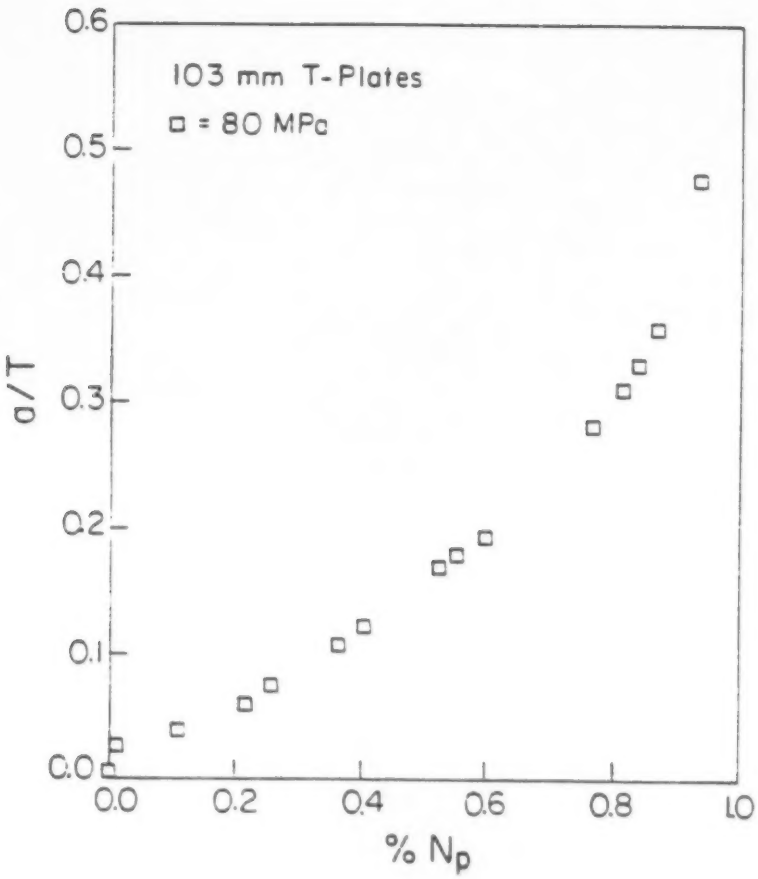

Figure 14: Normalized crack depth vs % N_p for 103 mm plates

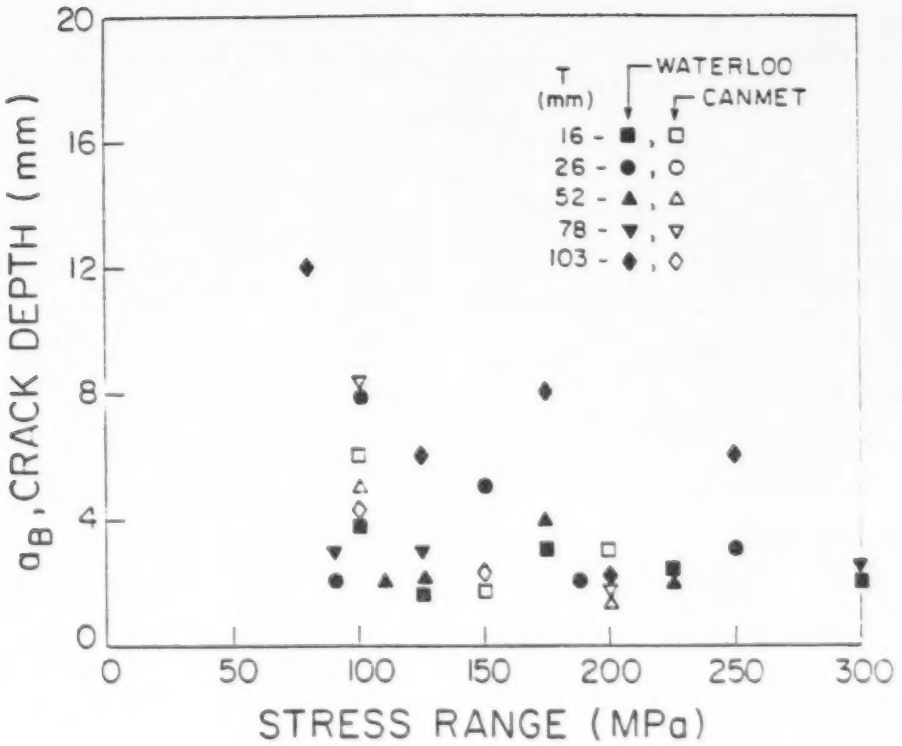

Figure 15: Maximum crack depth (a_B) when a dominant irregular crack has developed

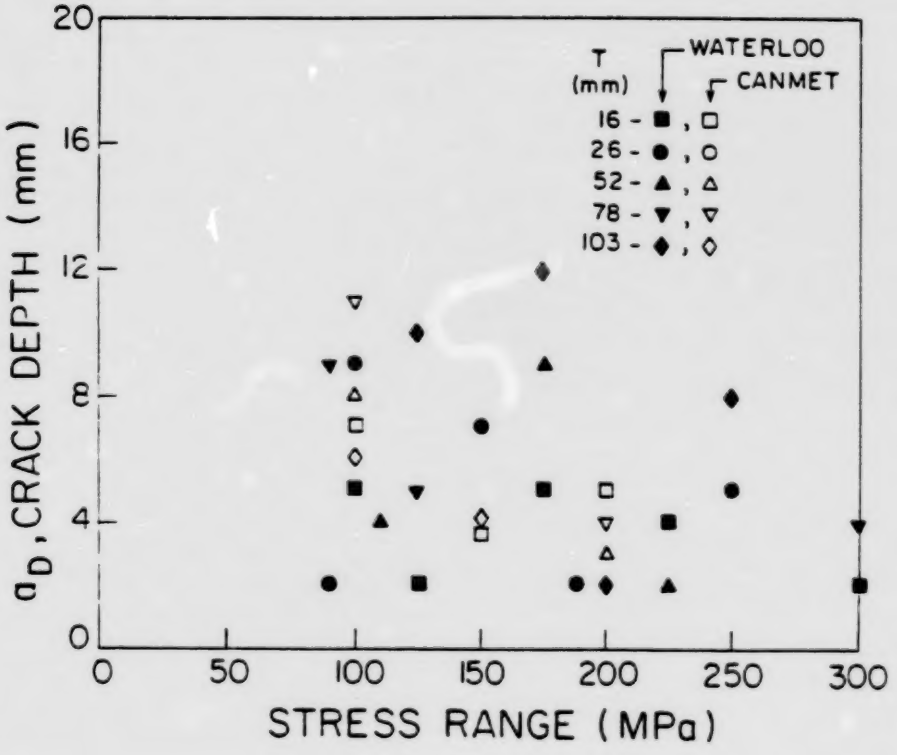

Figure 16: Maximum crack depth (a_D) when a dominant semi-elliptic crack has developed

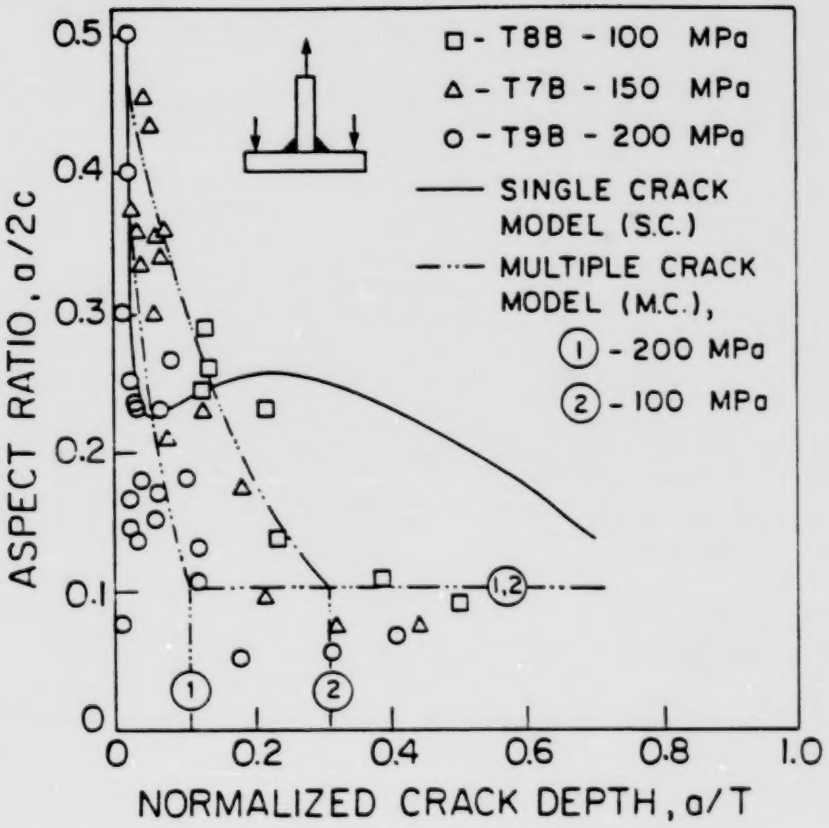

Figure 17: Measurements and models for crack shape development of a fatigue crack at weld toe

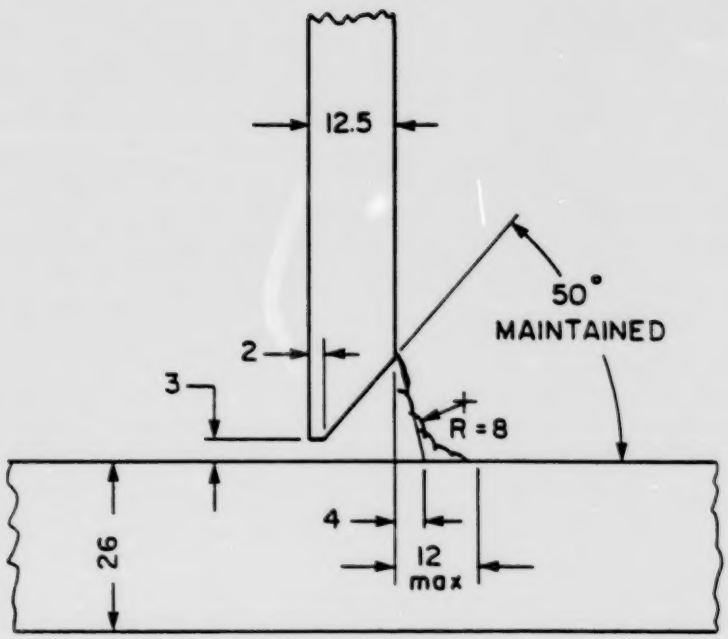

Figure 18: PP0 – test weld specification.

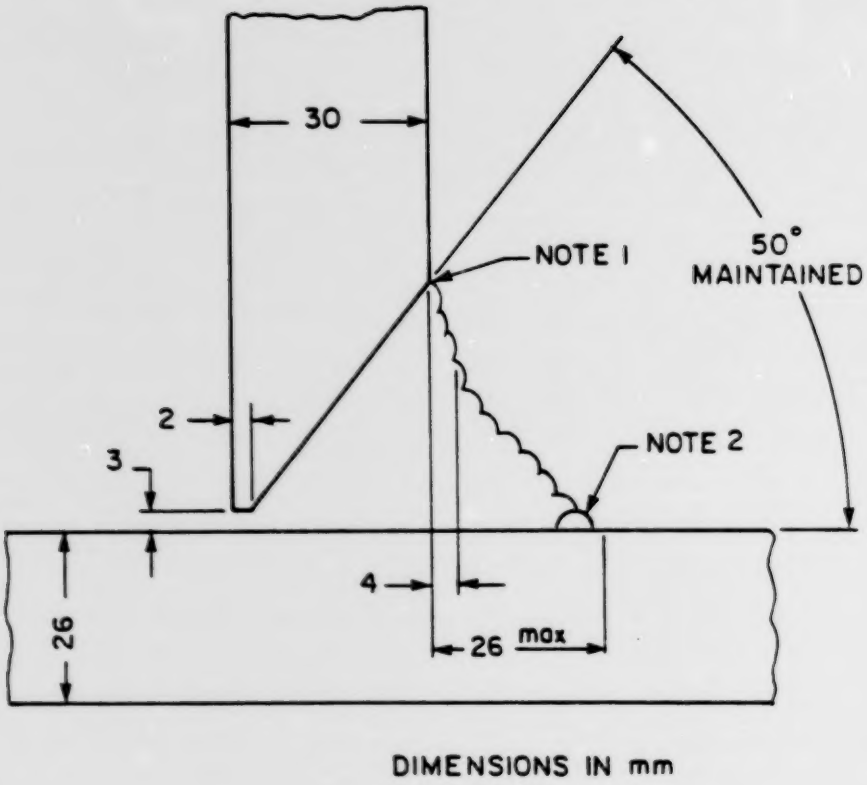

NOTE 1 : TOP PASS TO BE BLENDED IN (GRIND)
NOTE 2 : DIME TEST

Figure 19: PP1–PP8 weld specification.

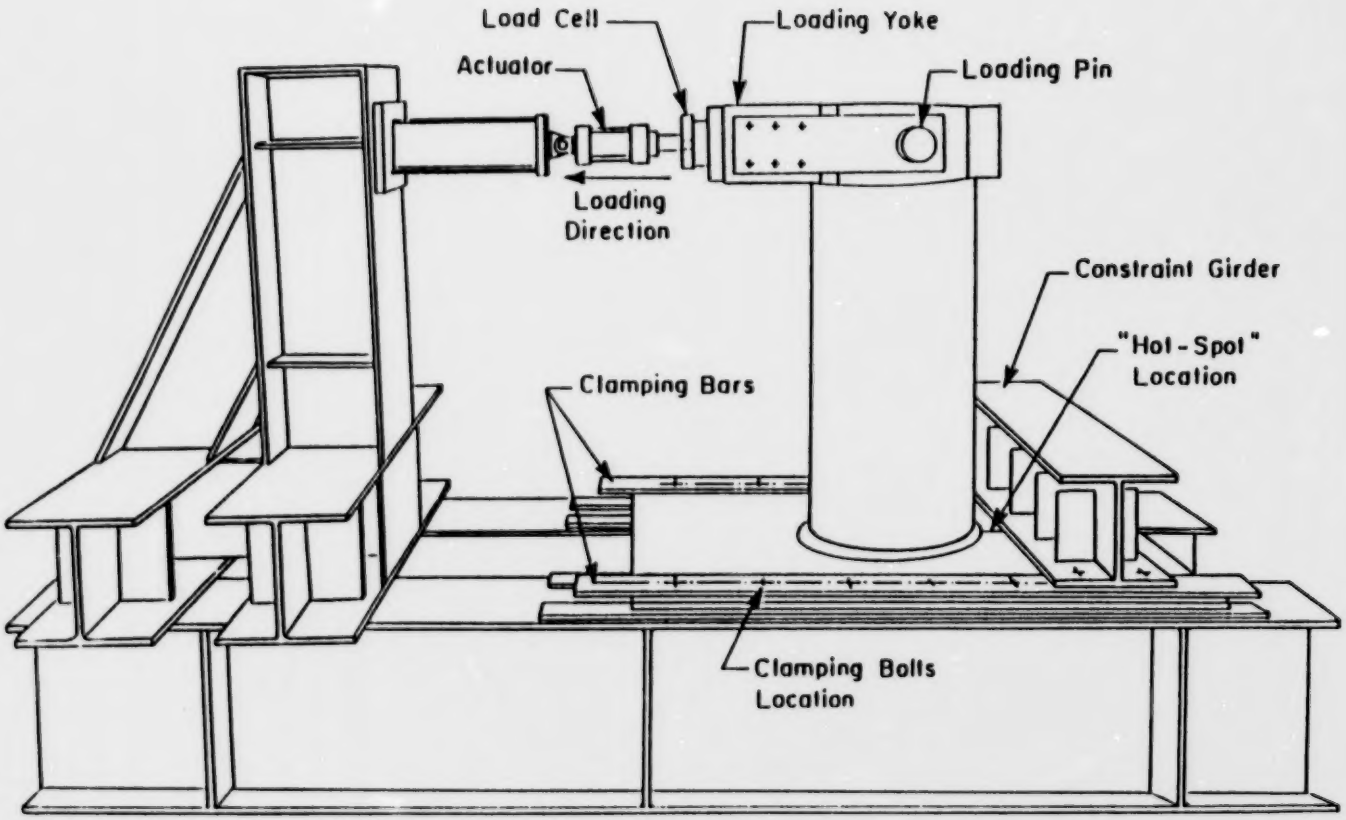

Figure 20: Pipe/plate specimen (PP1–PP8) and test fixture.

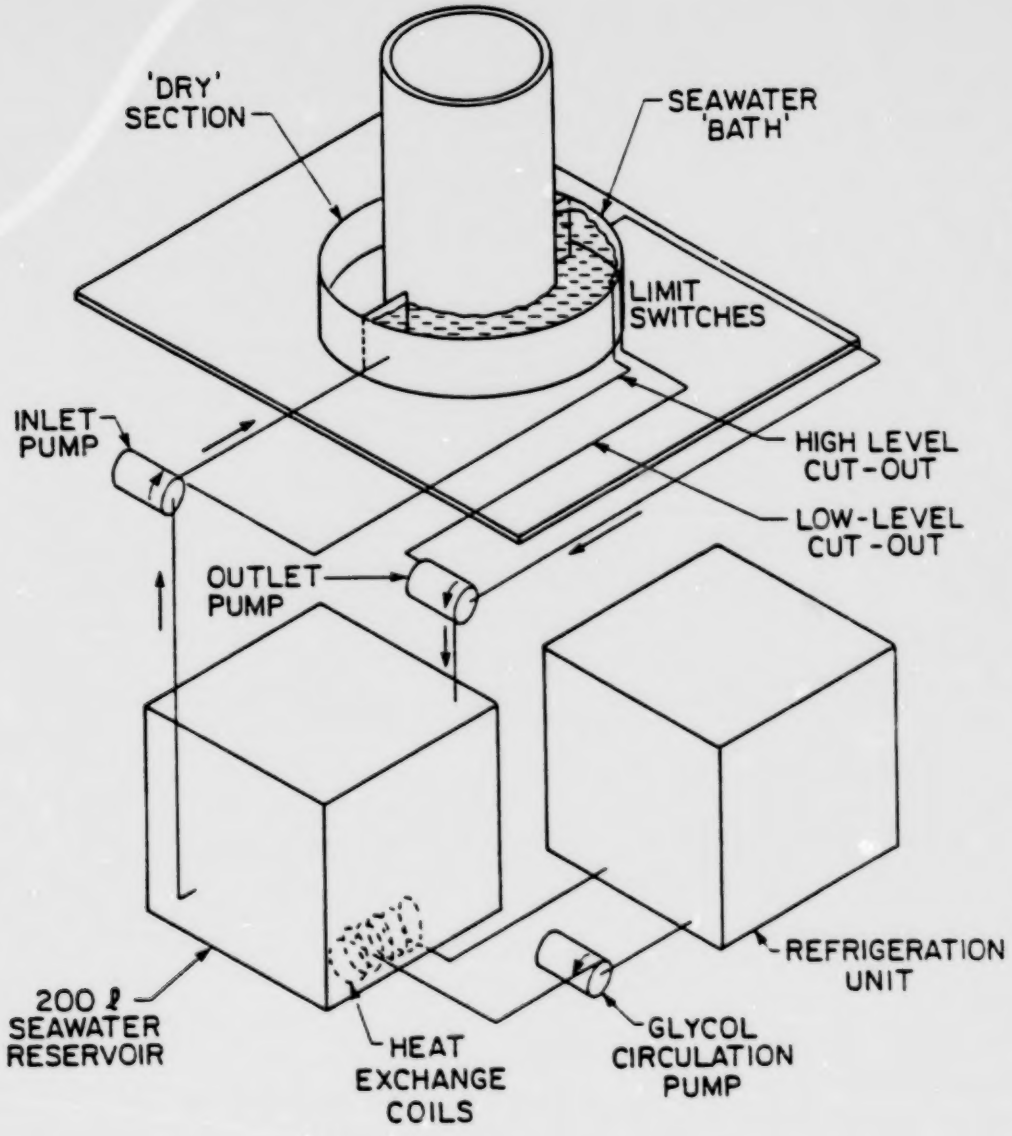

Figure 21: Seawater cooling and circulation systems.

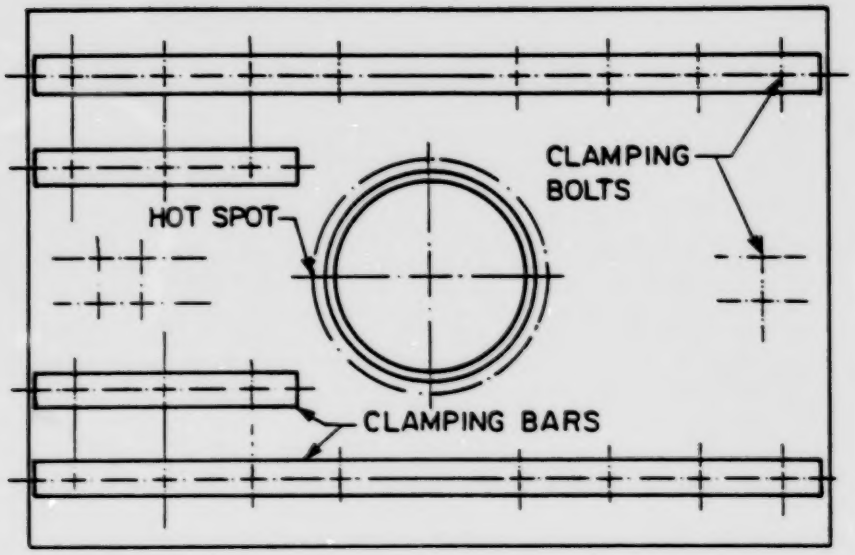

Figure 22: PP0 – typical plate constraint.

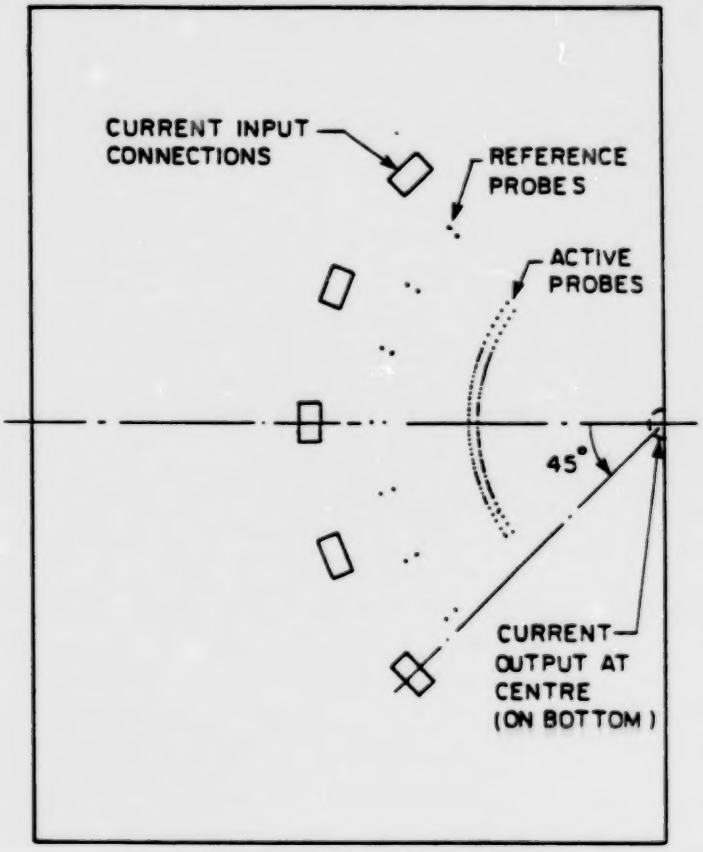

Figure 23: PP0 – PD probe locations.

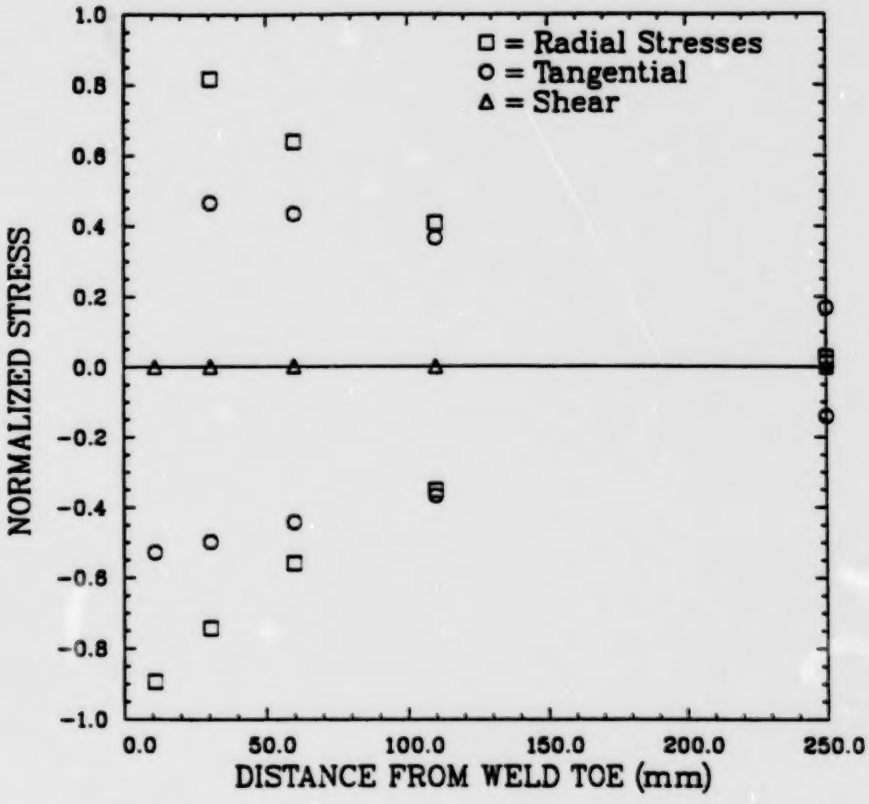

Figure 24: PP0 – plate surface stresses at the hot-spot.

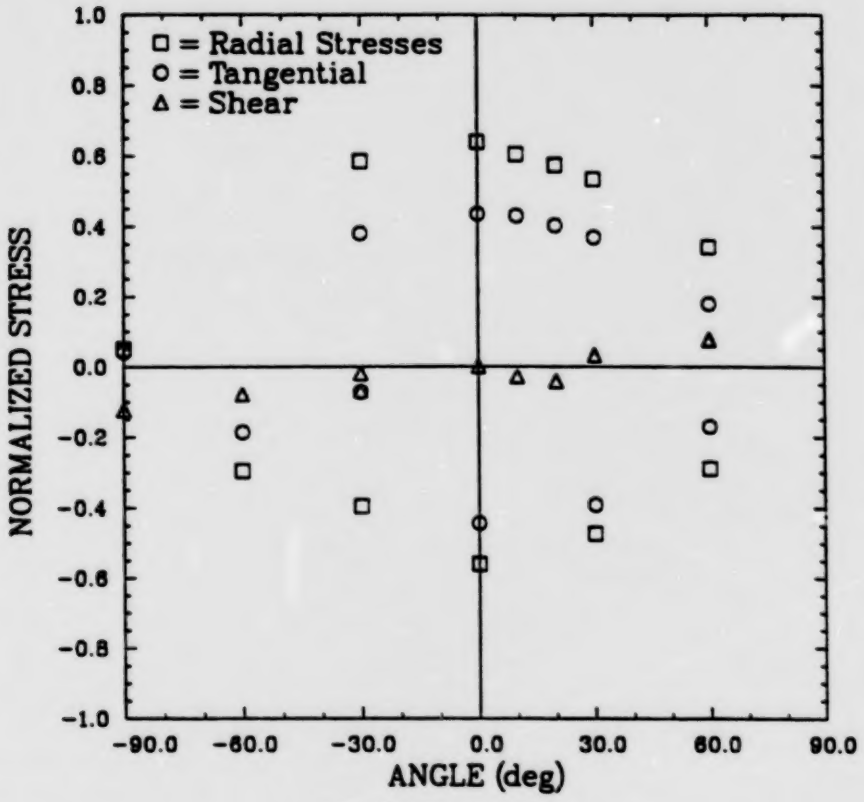

Figure 25: PP0 – plate surface stresses 60 mm from weld.

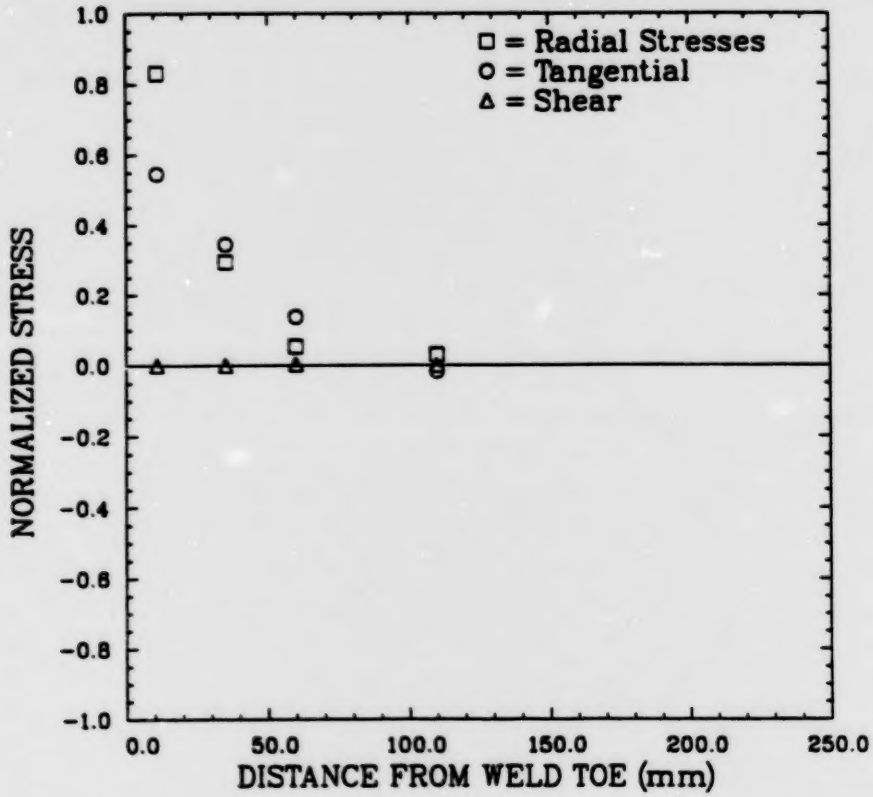

Figure 26: PP0 – pipe surface stresses at the hot-spot.

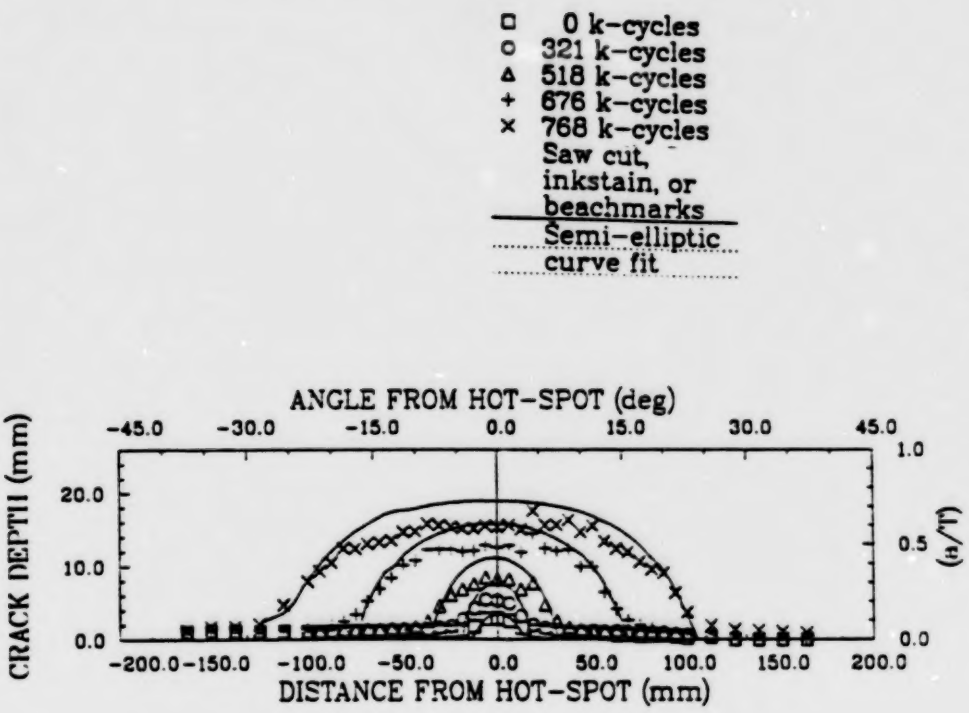

Figure 27: PP0 – PD predictions compared with beachmarks.

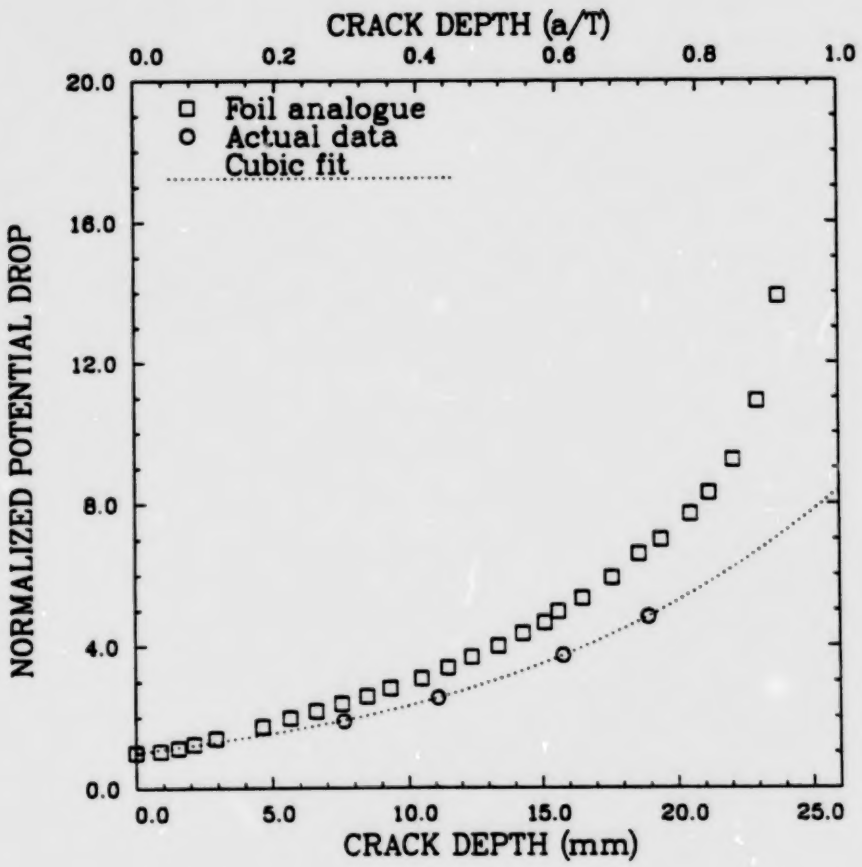

Figure 28: PP0 – PD calibration and actual results.

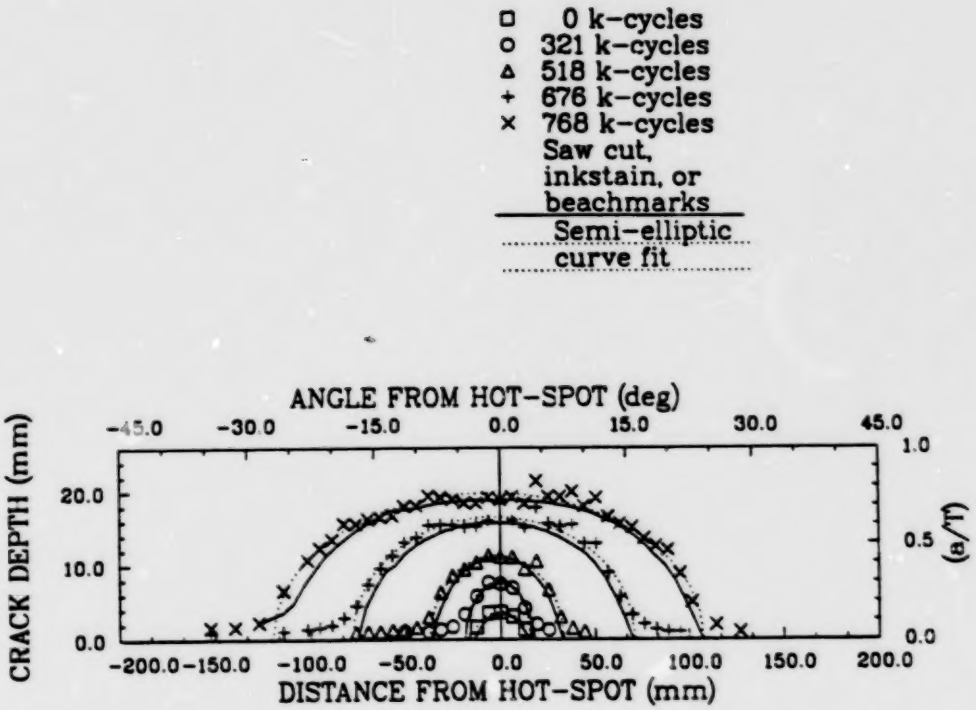

Figure 29: PP0 – corrected PD results compared with beachmarks.

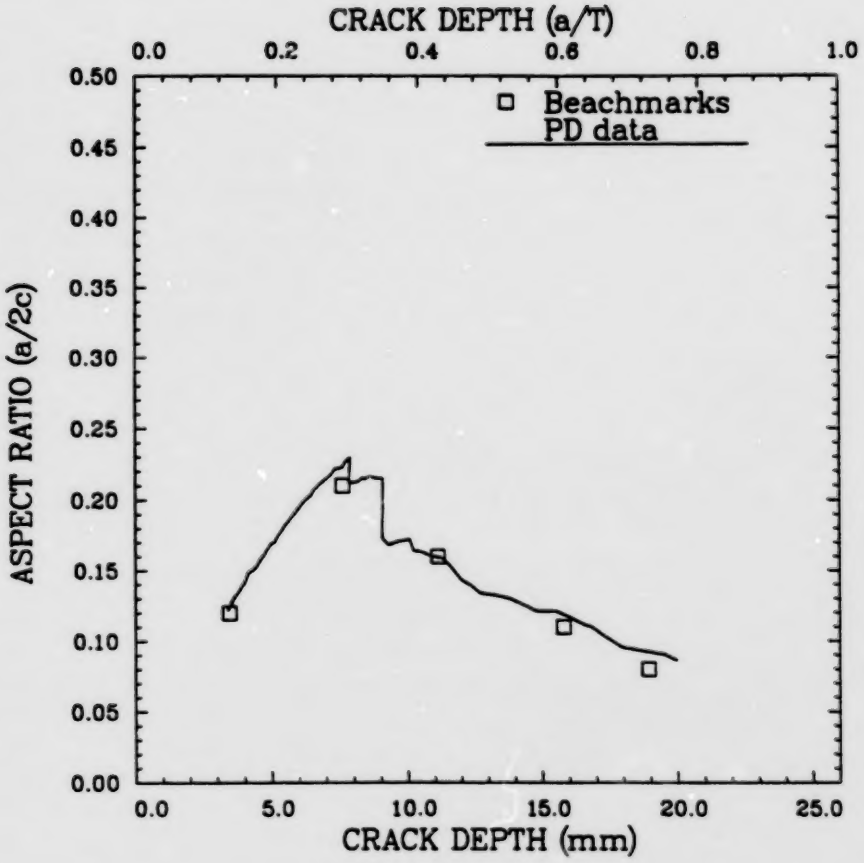

Figure 30: PP0 – aspect ratio development.

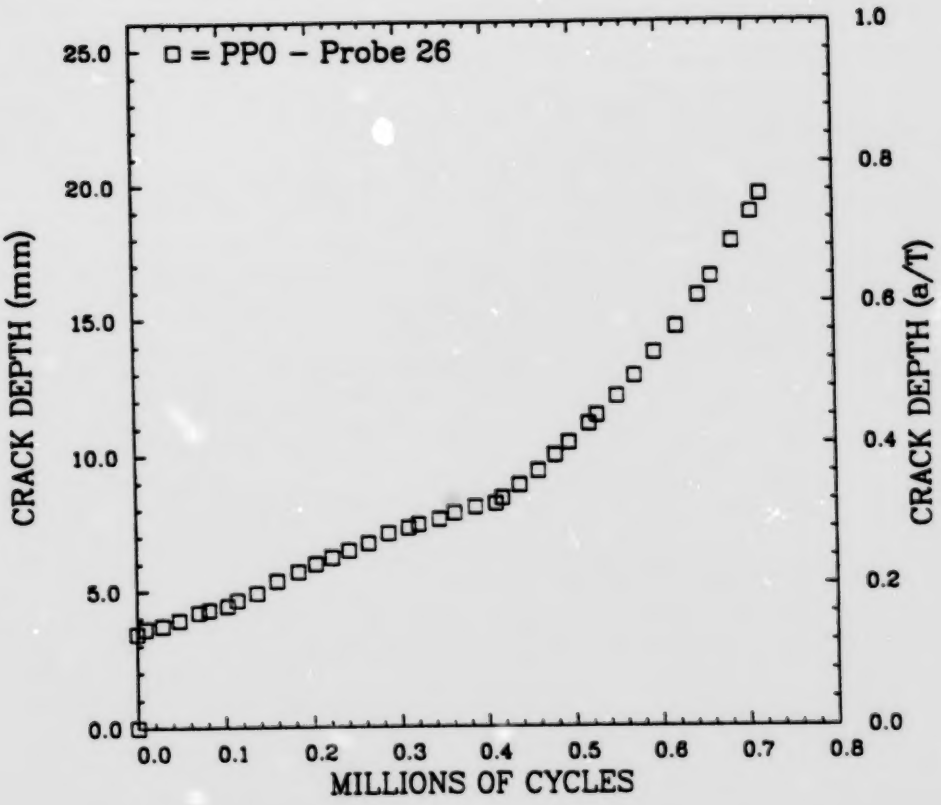

Figure 31: PP0 – crack growth at the hot-spot.

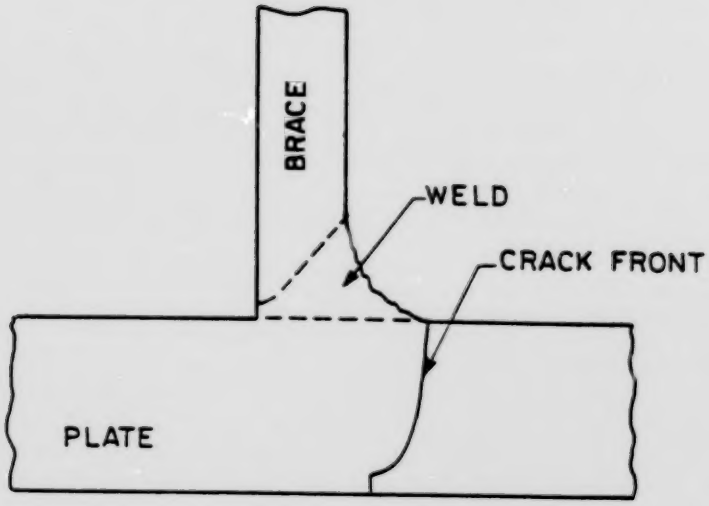

Figure 32: PP0–typical weld profile and crack propagation path

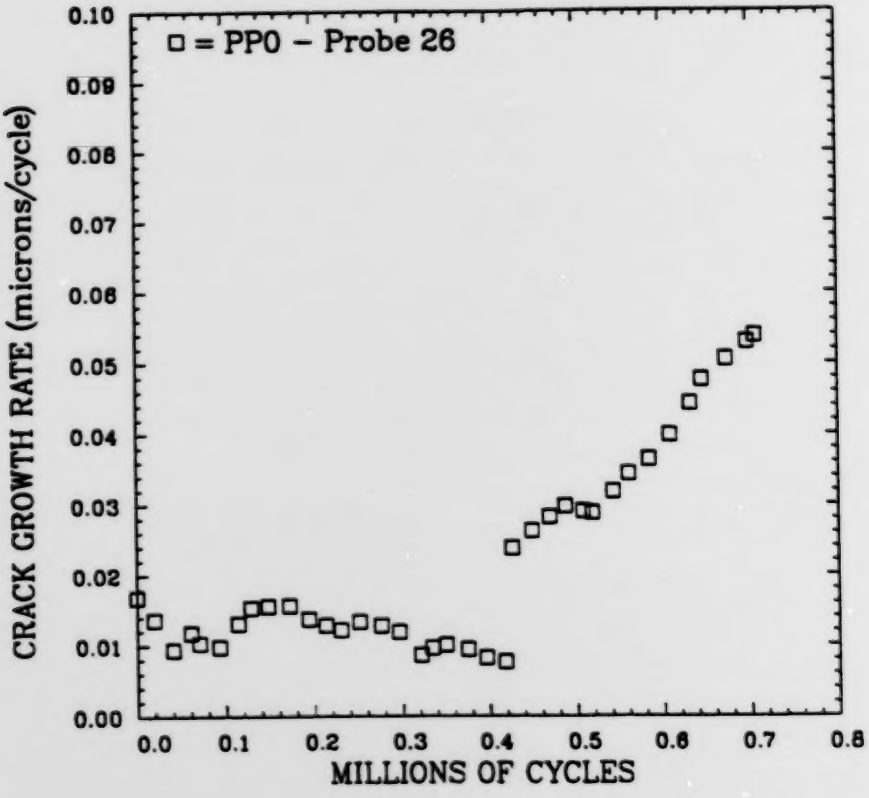

Figure 33a: PP0 – crack growth rates at hot-spot versus cycles.

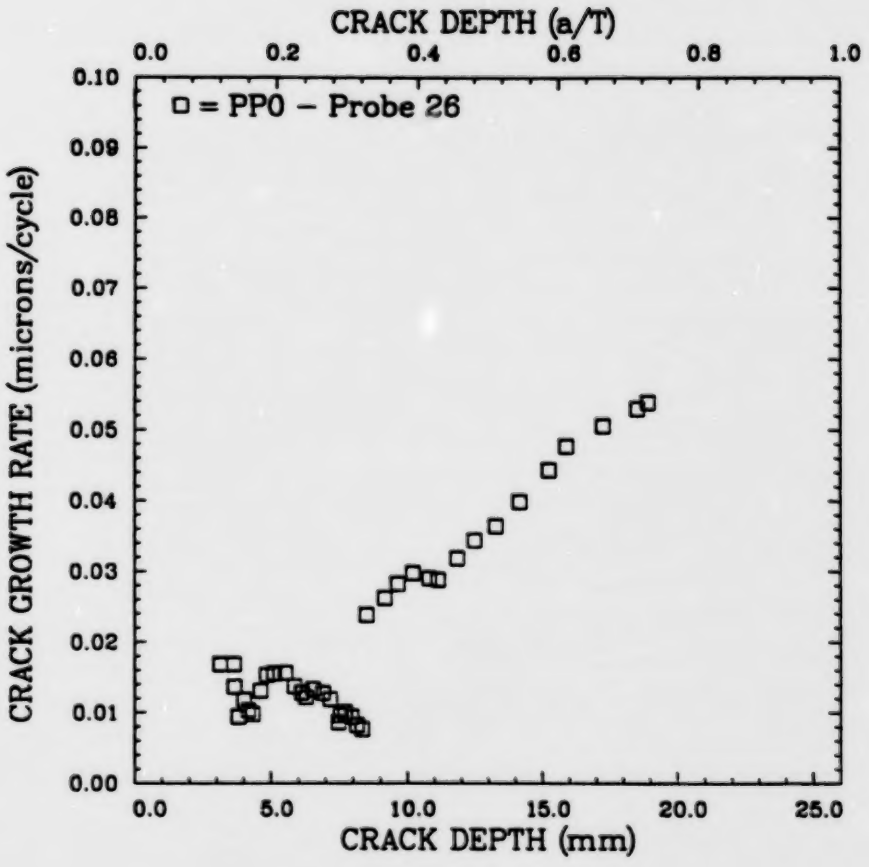

Figure 33b: PP0 – crack growth rates at hot-spot versus crack depth.

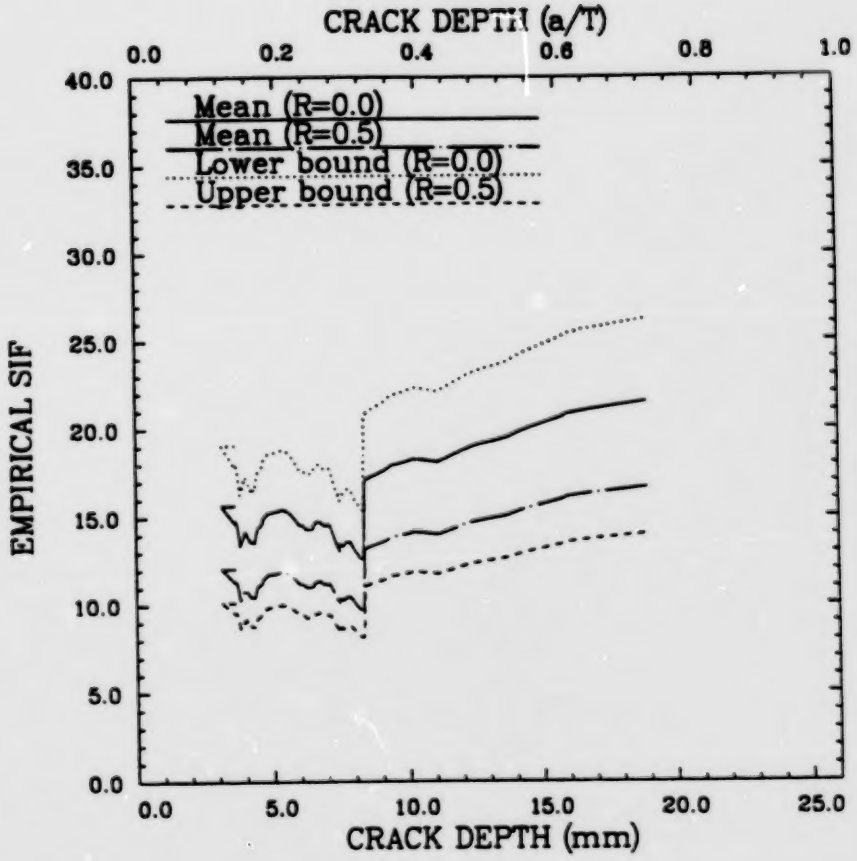

Figure 34: PP0 – empirical stress intensity factors, ΔK.

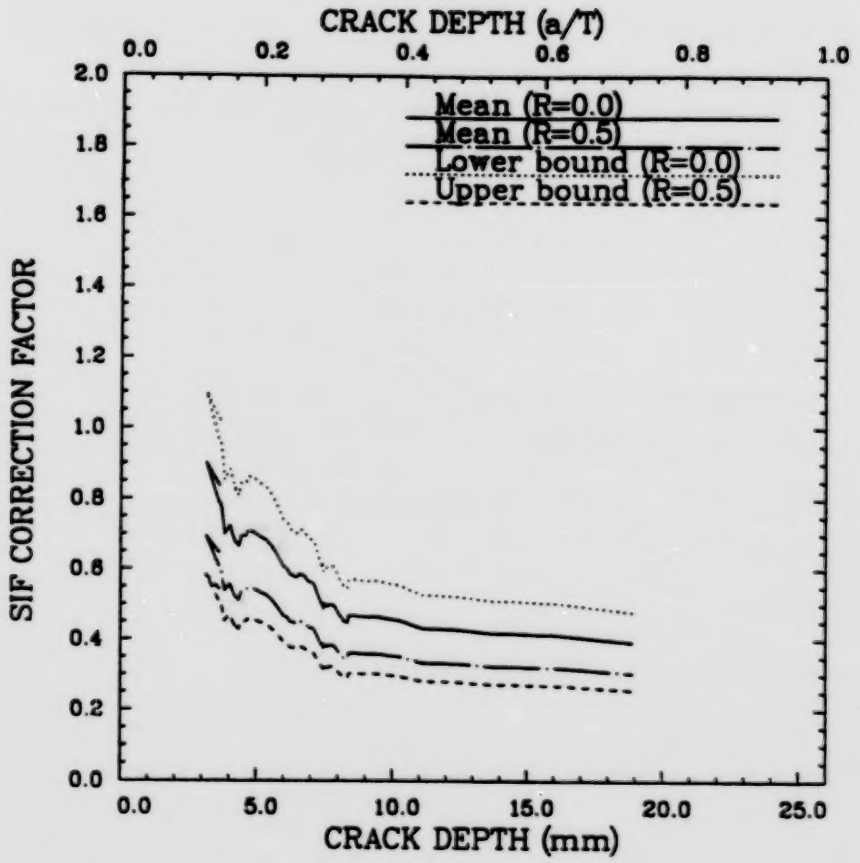

Figure 35: PP0–empirical stress intensity factors, $M_k M$.

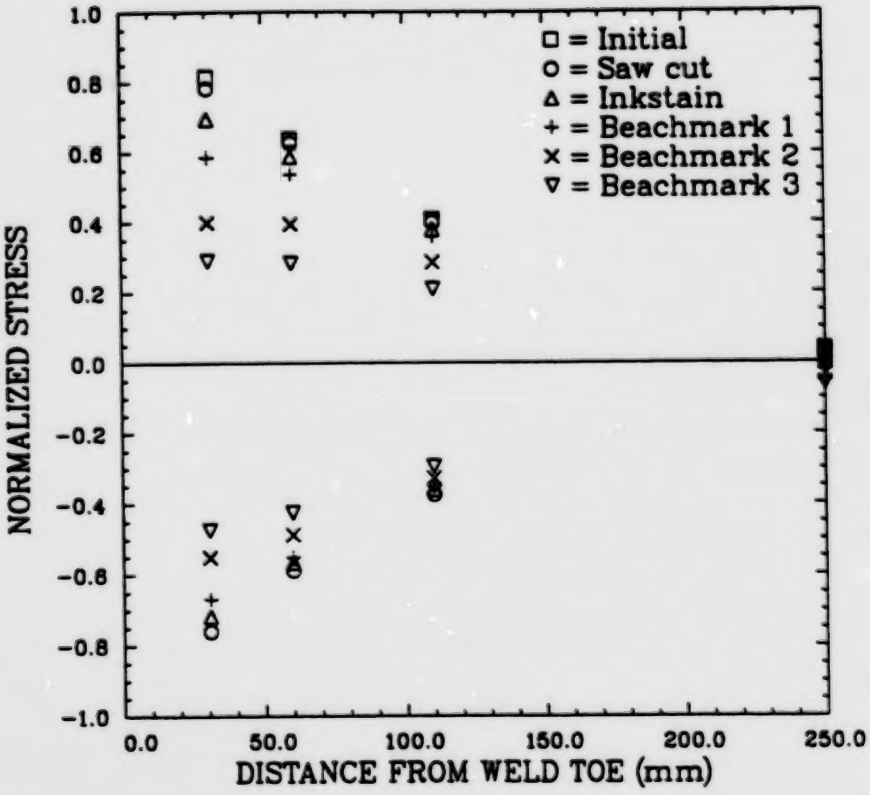

Figure 36a: PP0 – plate surface radial stress redistribution at hot-spot.

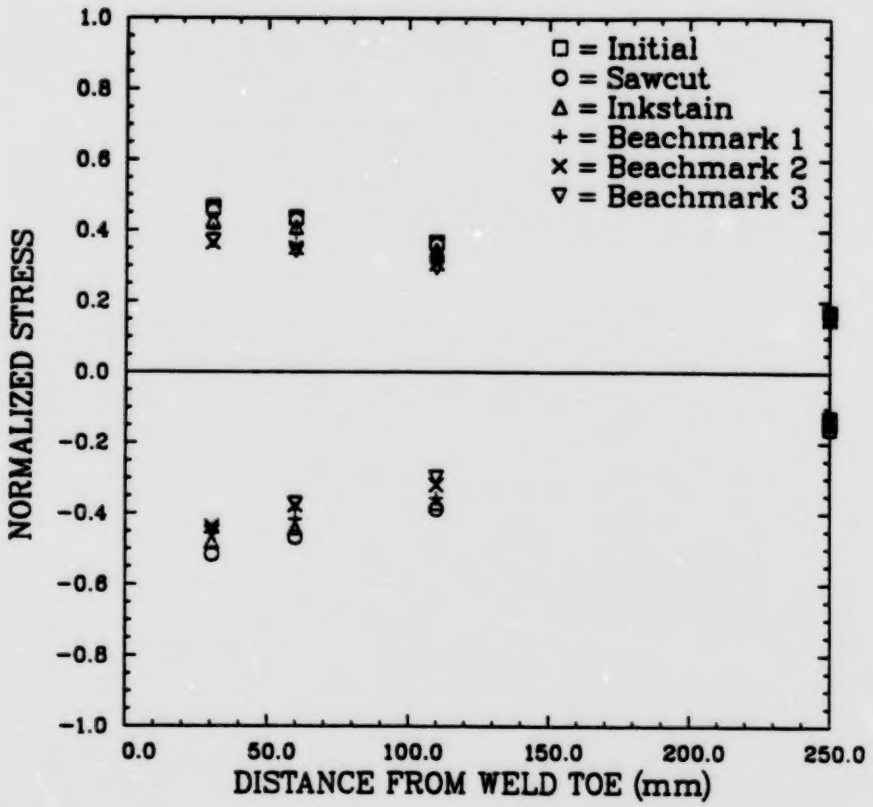

Figure 36b: PP0 – plate surface tangential stress redistribution at hot-spot.

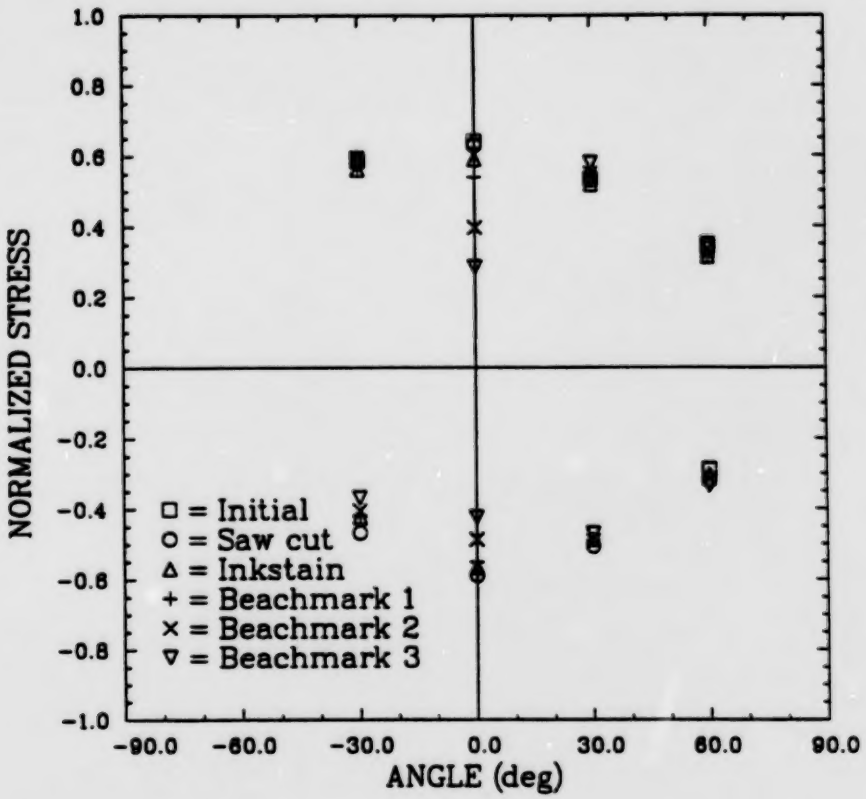

Figure 37a: PP0 – plate surface radial stress redistribution along weld.

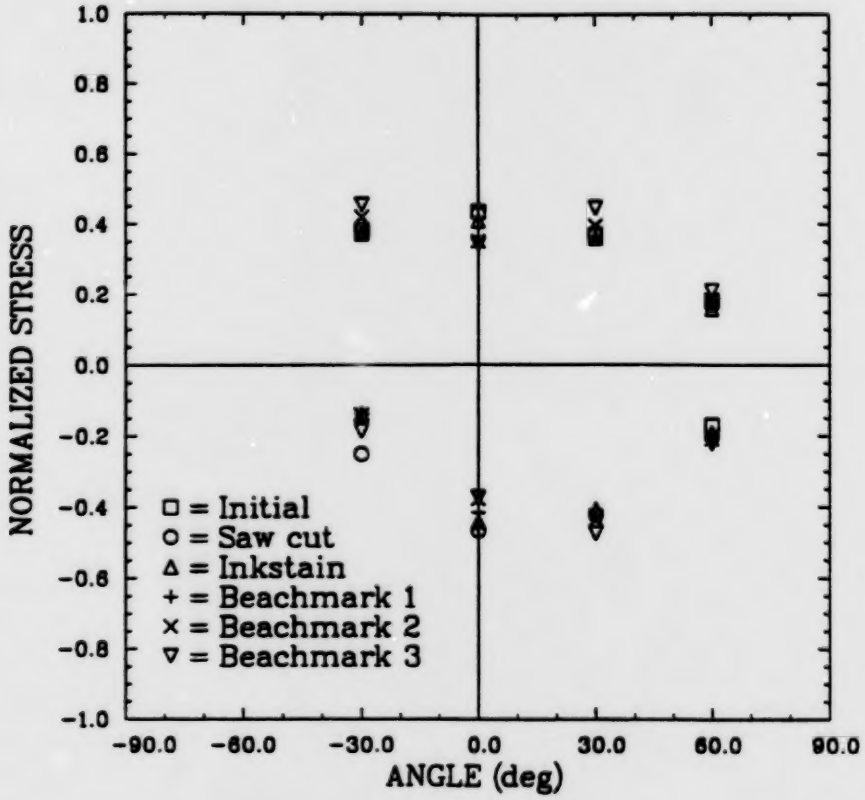

Figure 37b: PP0 – plate surface tangential stress redistribution along weld.

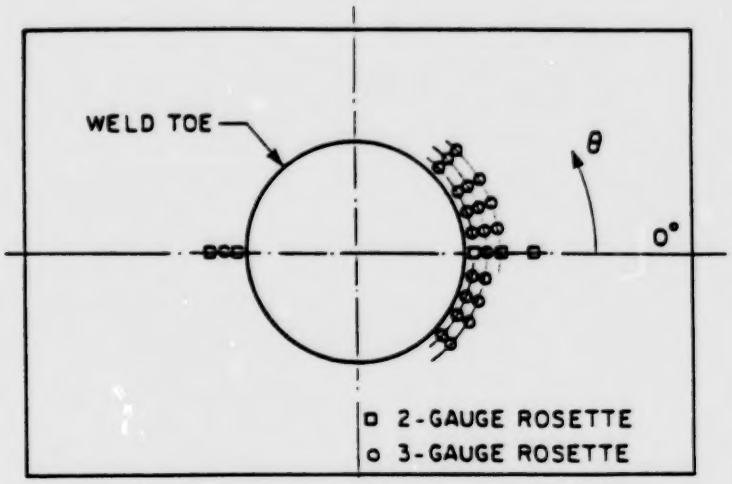

a) GAUGE POSITIONS ON TOP AND BOTTOM OF PLATE (AS SEEN FROM TOP)

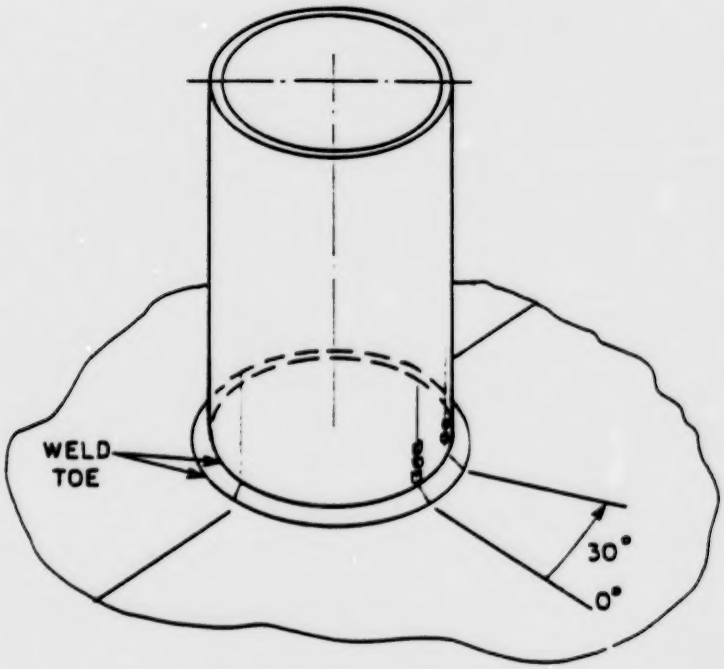

b) GAUGE LAYOUT ON PIPE

Figure 38: PP1 – strain gauge locations.

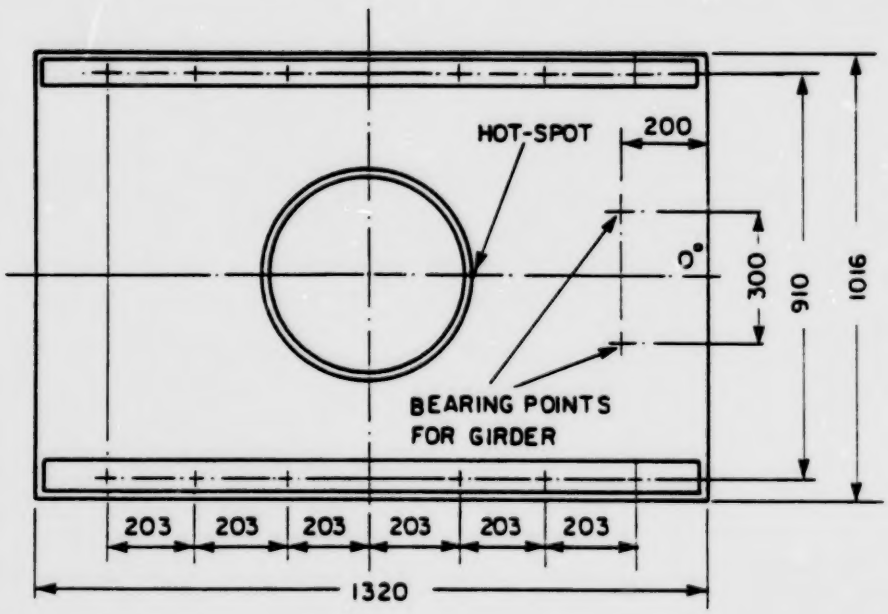

Figure 39: Plate constraint for specimens PP1 – PP8.

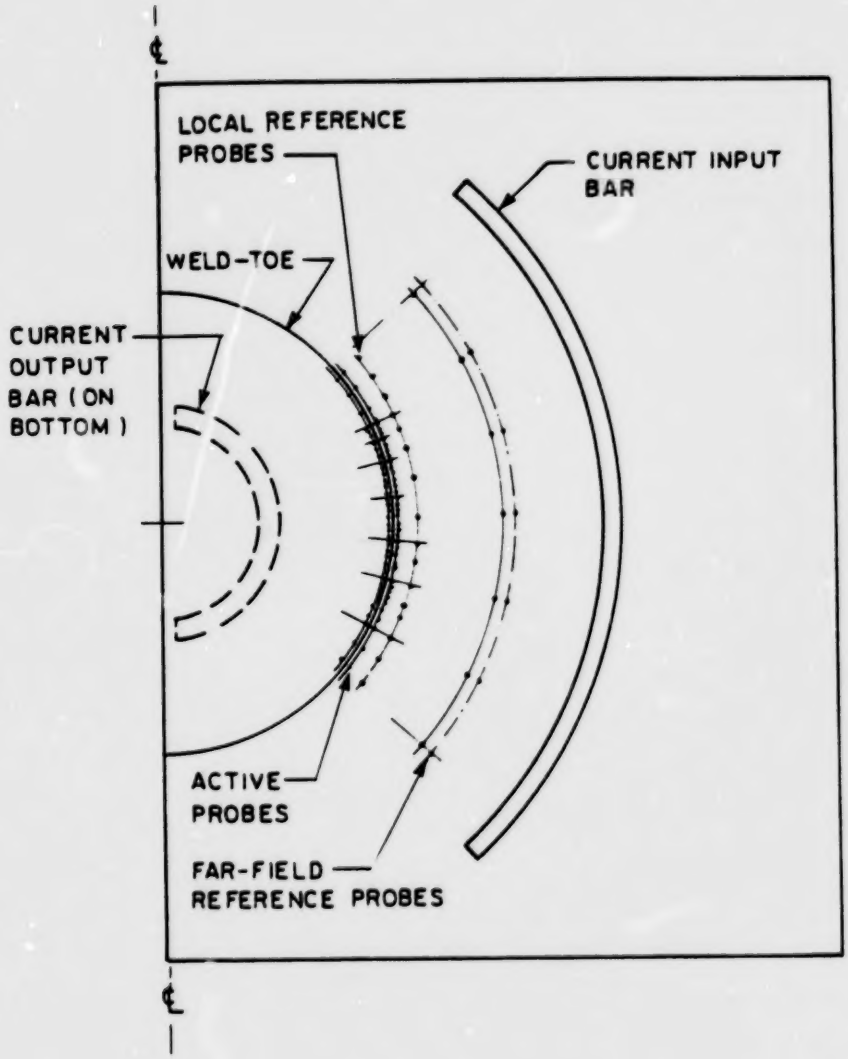

Figure 40: PP1 – PD probe locations.

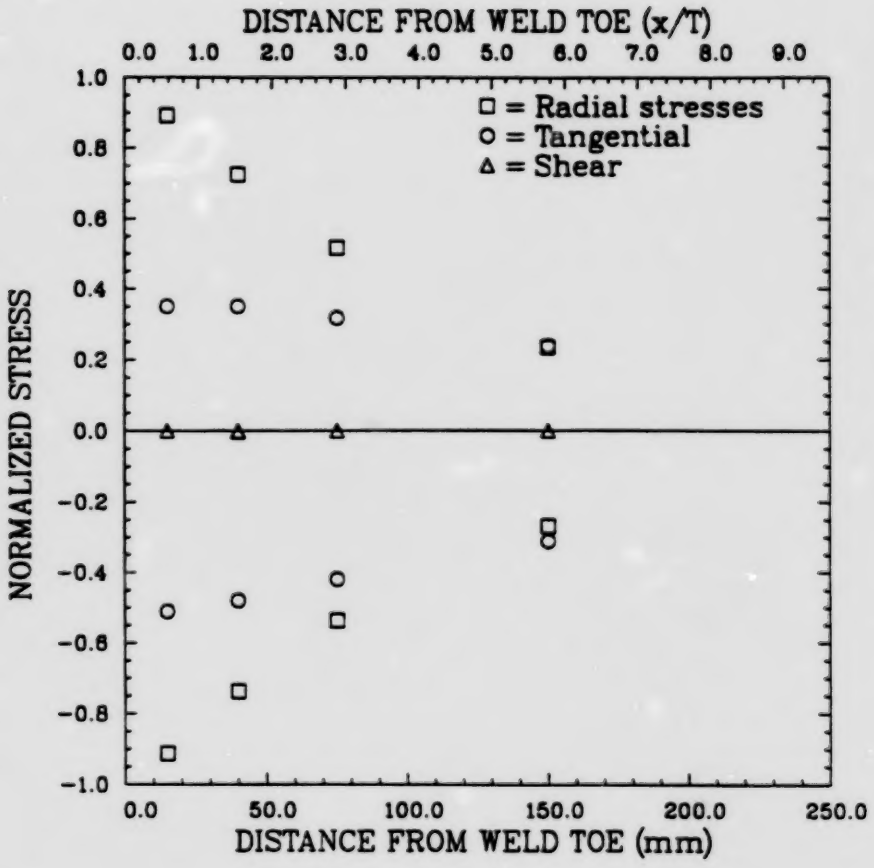

Figure 41: PP1 – plate surface stresses at hot-spot.

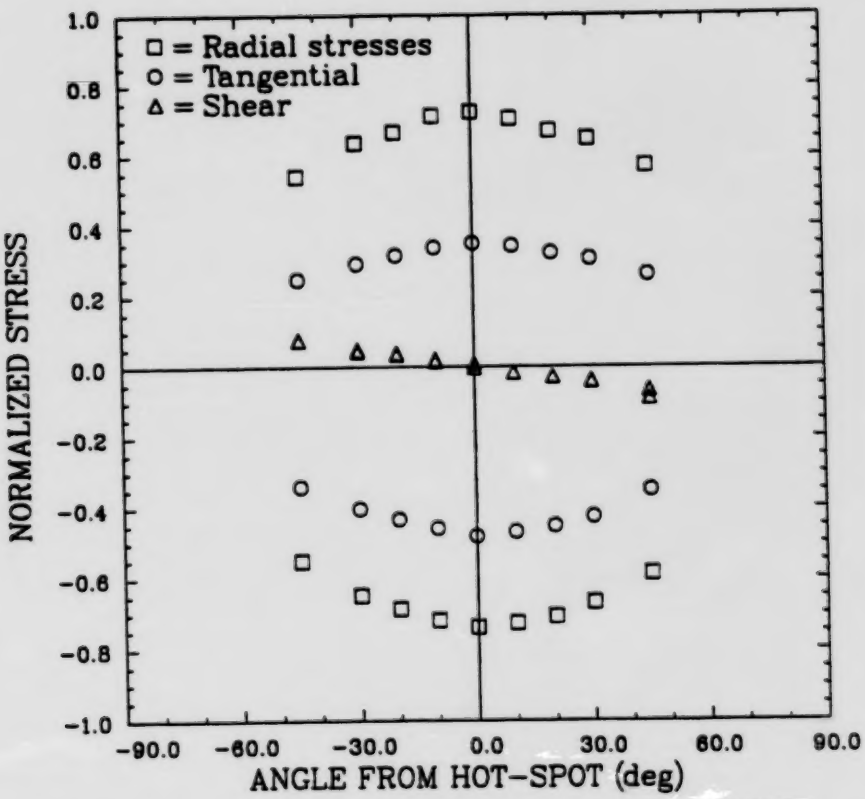

Figure 42: PP1 – plate surface stresses along weld.

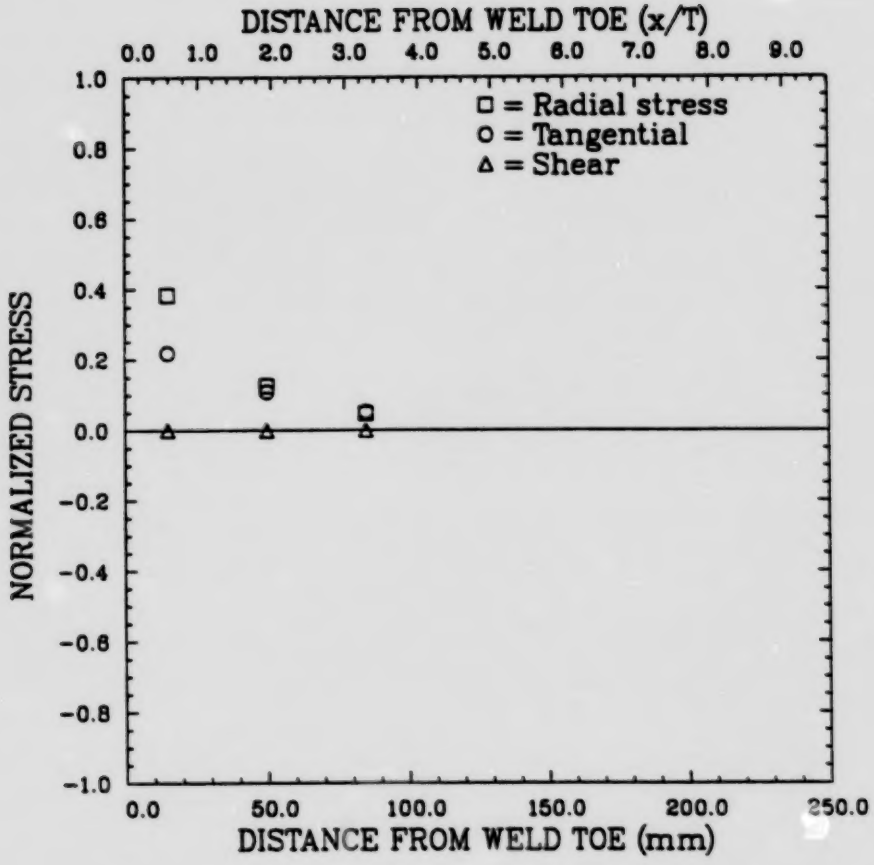

Figure 43: PP1 – pipe surface stresses at hot-spot.

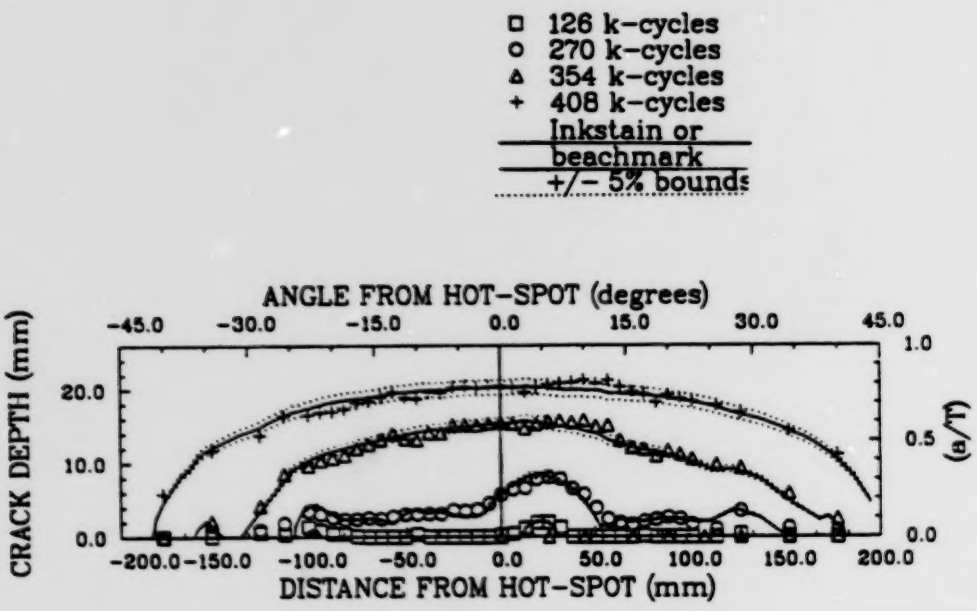

Figure 44: PP1 – PD predictions compared with beachmarks.

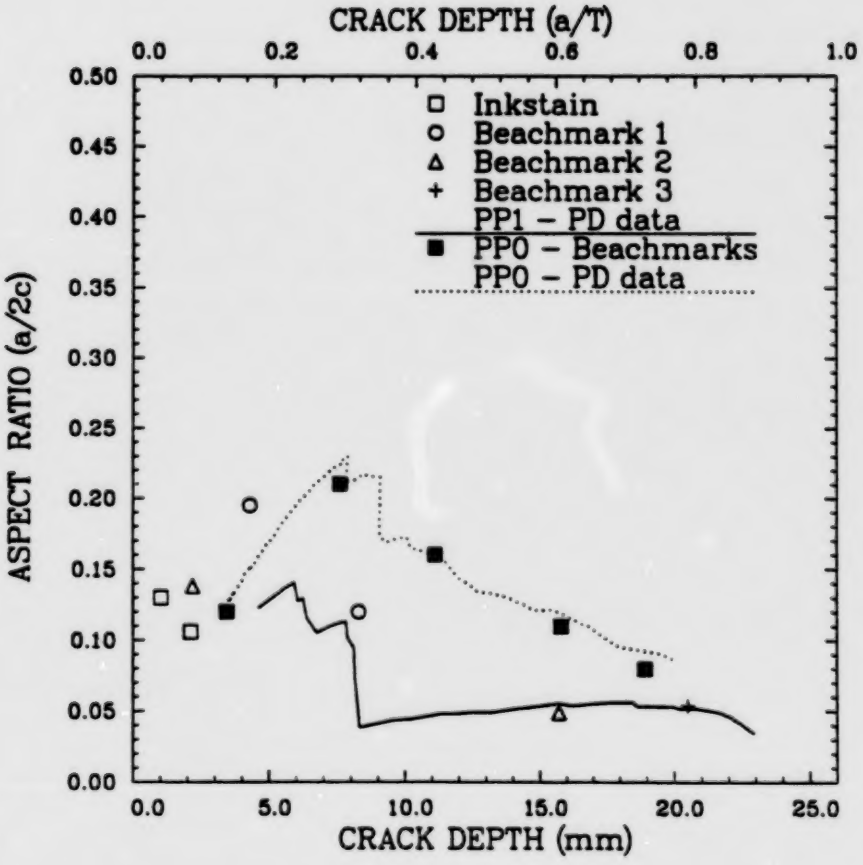

Figure 45: PP1 – aspect ratio development.

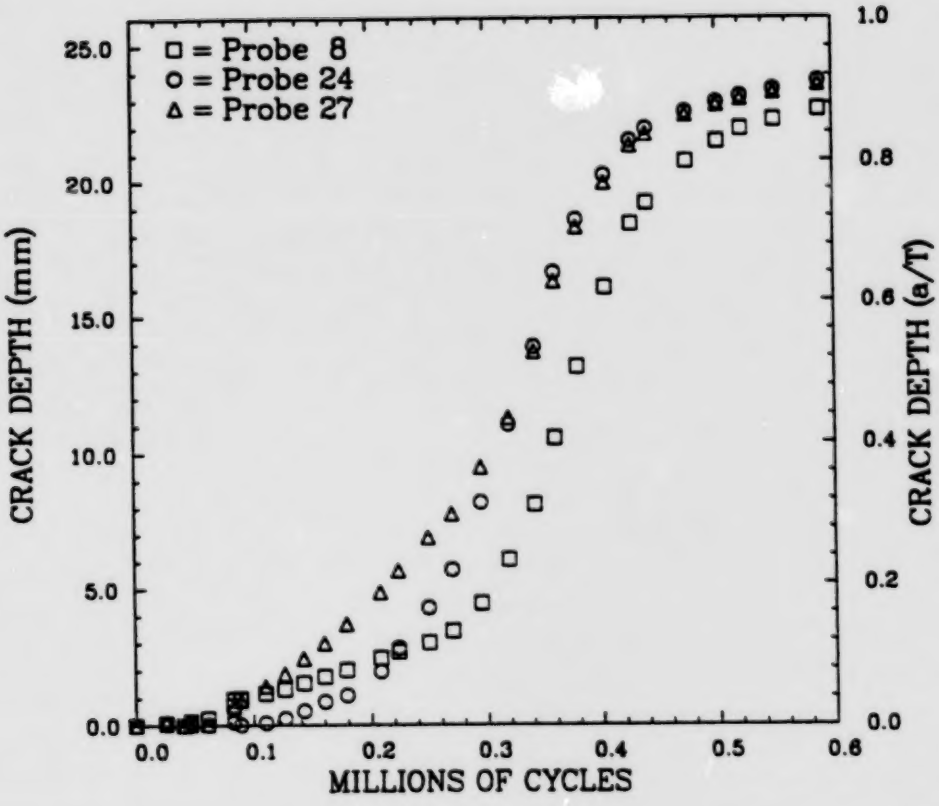

Figure 46: PP1 – crack growth behaviour.

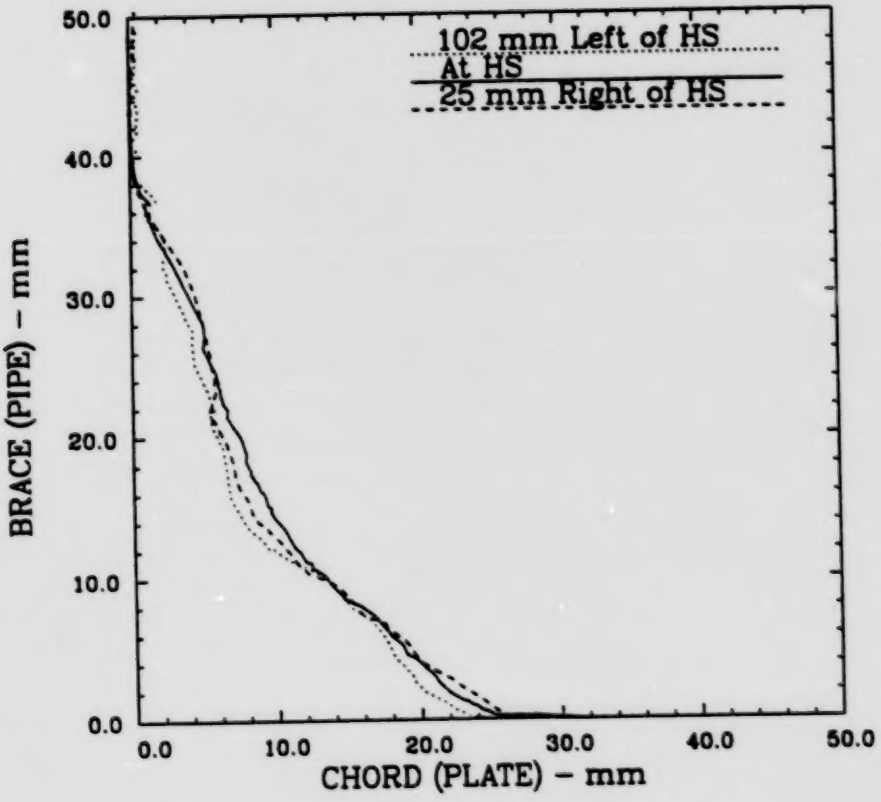

Figure 47: PP1 – measured weld reinforcement profiles.

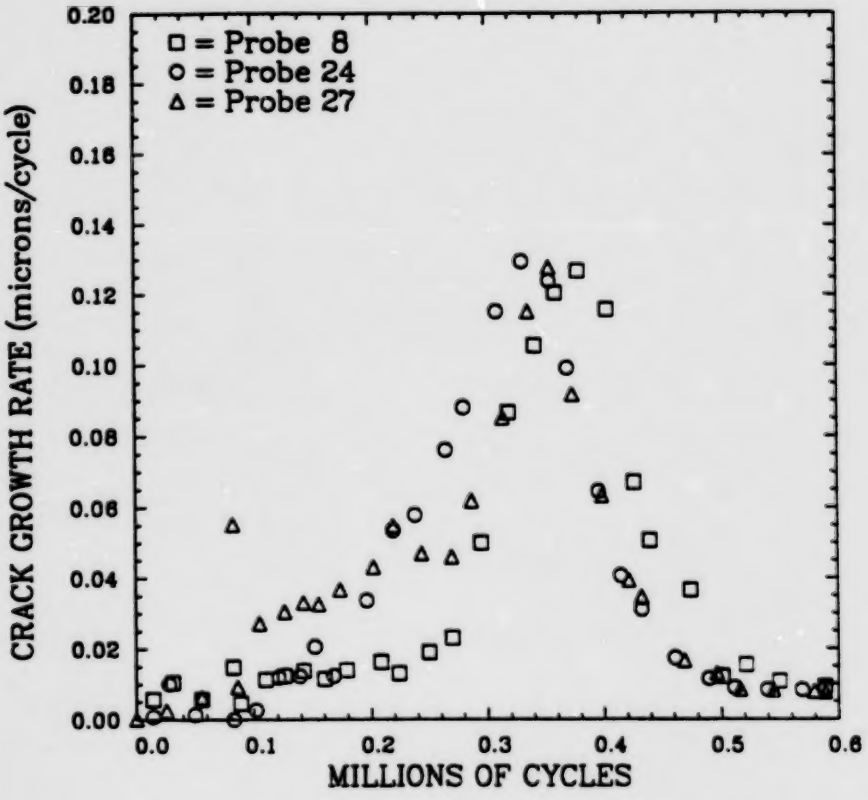

Figure 48a: PP1 – crack growth rates versus cycles.

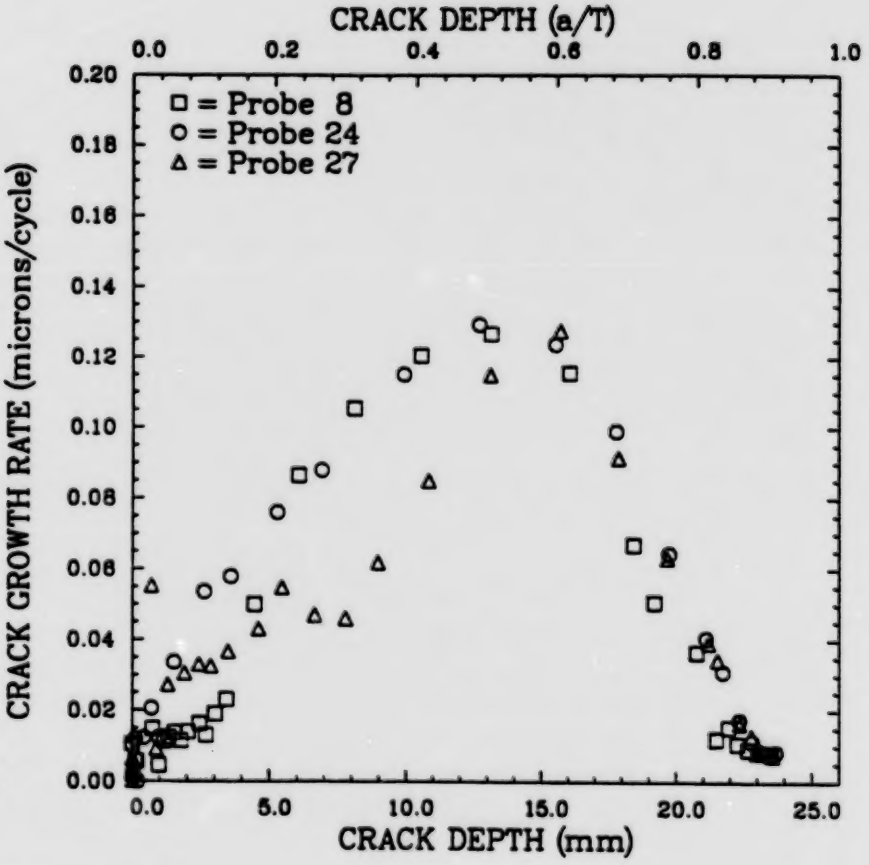

Figure 48b: PP1 – crack growth rates versus crack depth.

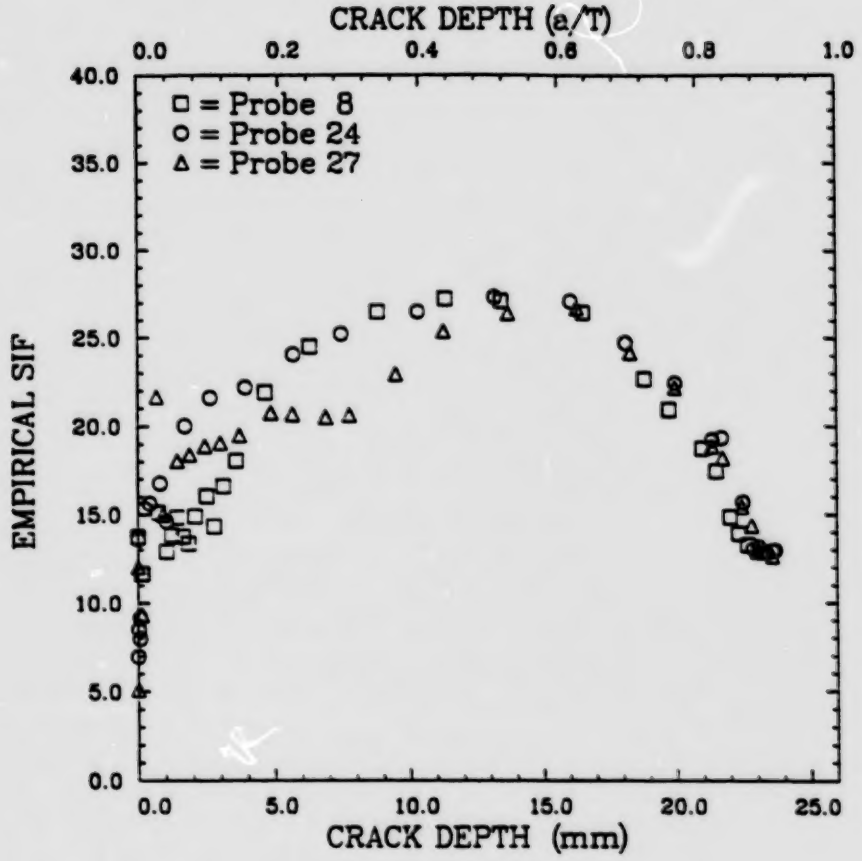

Figure 49: PP1 – empirical stress intensity factors, ΔK.

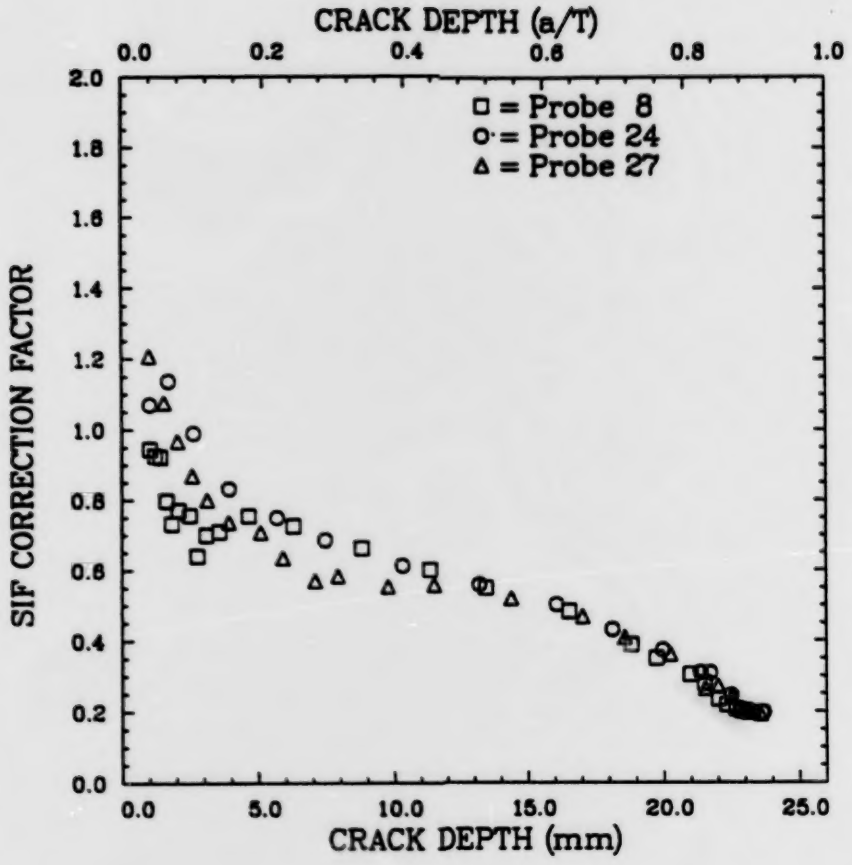

Figure 50: PP1 – empirical stress intensity correction factors, $M_k M$.

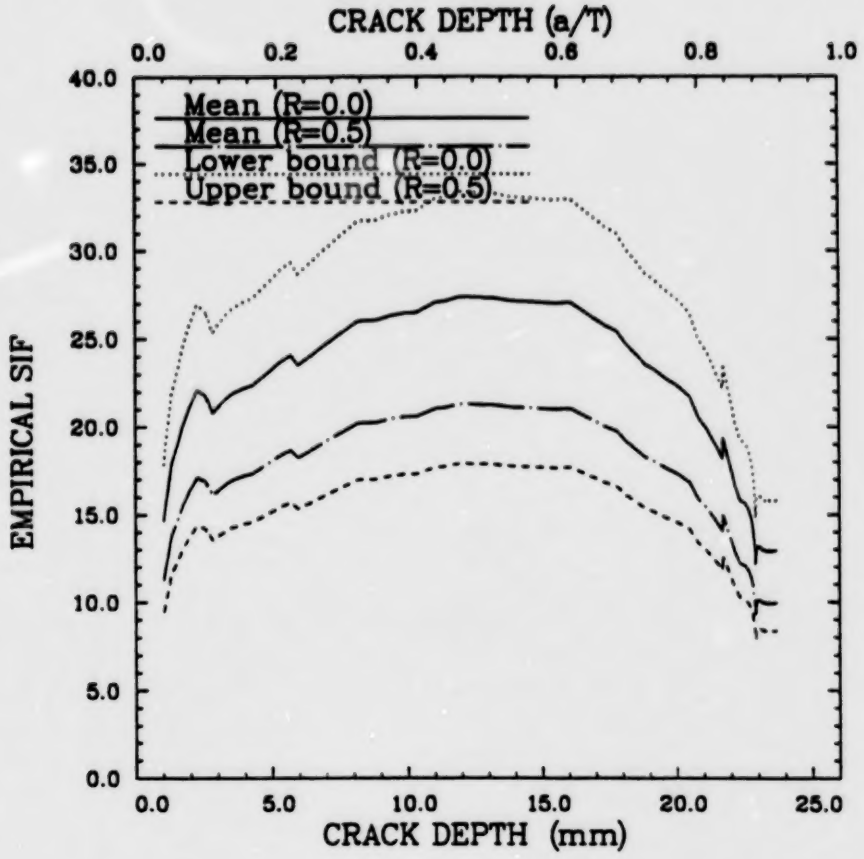

Figure 51: PP1 – empirical stress intensity factors, ΔK, near hot-spot, calculated using different C and m values.

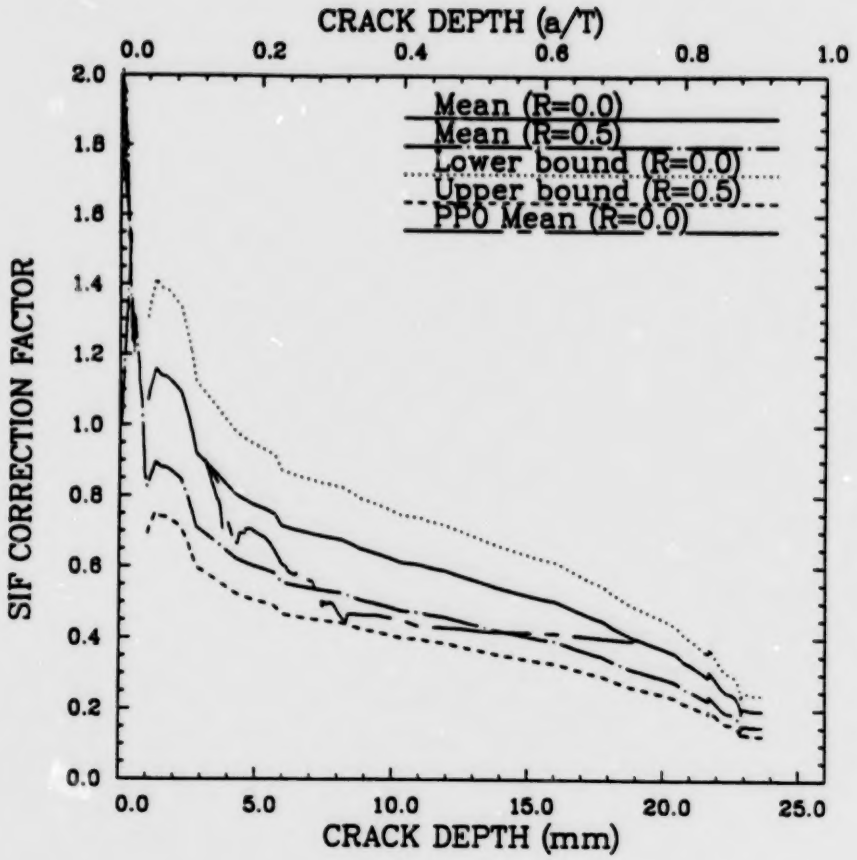

Figure 52: PP1–empirical stress intensity correction factors, $M_k M$, near hot-spot, calculated using different C and m values.

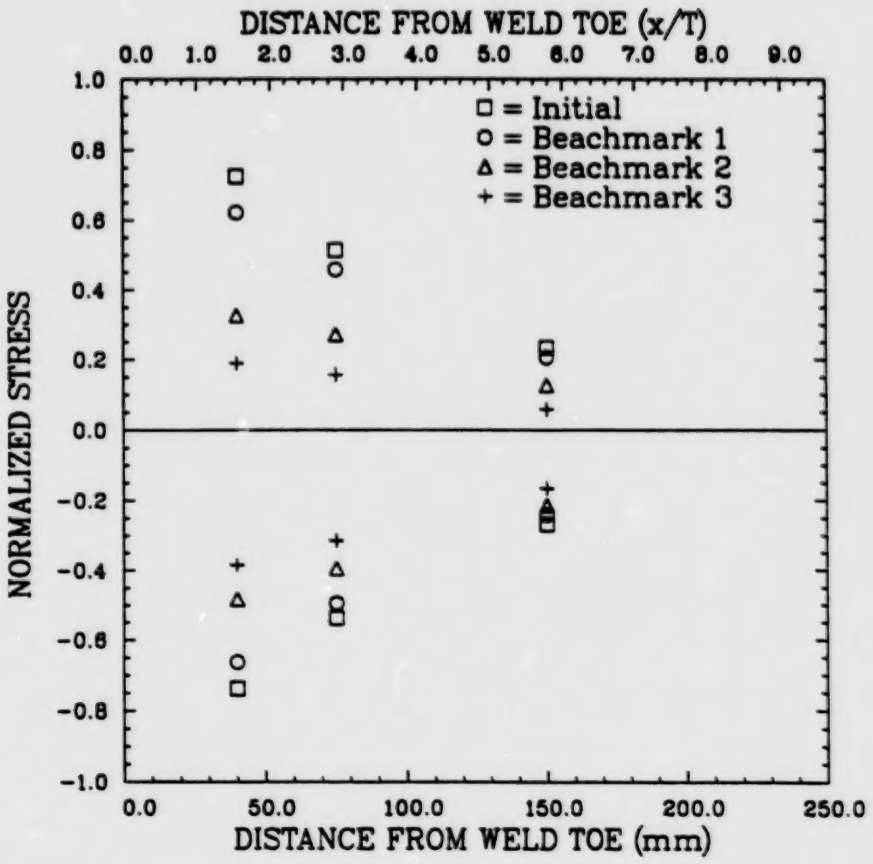
DISTANCE FROM WELD TOE (x/T)
0.0 1.0 2.0 3.0 4.0 5.0 6.0 7.0 8.0 9.0
□ = Initial
○ = Beachmark 1
△ = Beachmark 2
+ = Beachmark 3
NORMALIZED STRESS
1.0 0.8 0.6 0.4 0.2 0.0 -0.2 -0.4 -0.6 -0.8 -1.0
0.0 50.0 100.0 150.0 200.0 250.0
DISTANCE FROM WELD TOE (mm)

Figure 53a: PP1 – plate surface radial stress redistribution at hot-spot

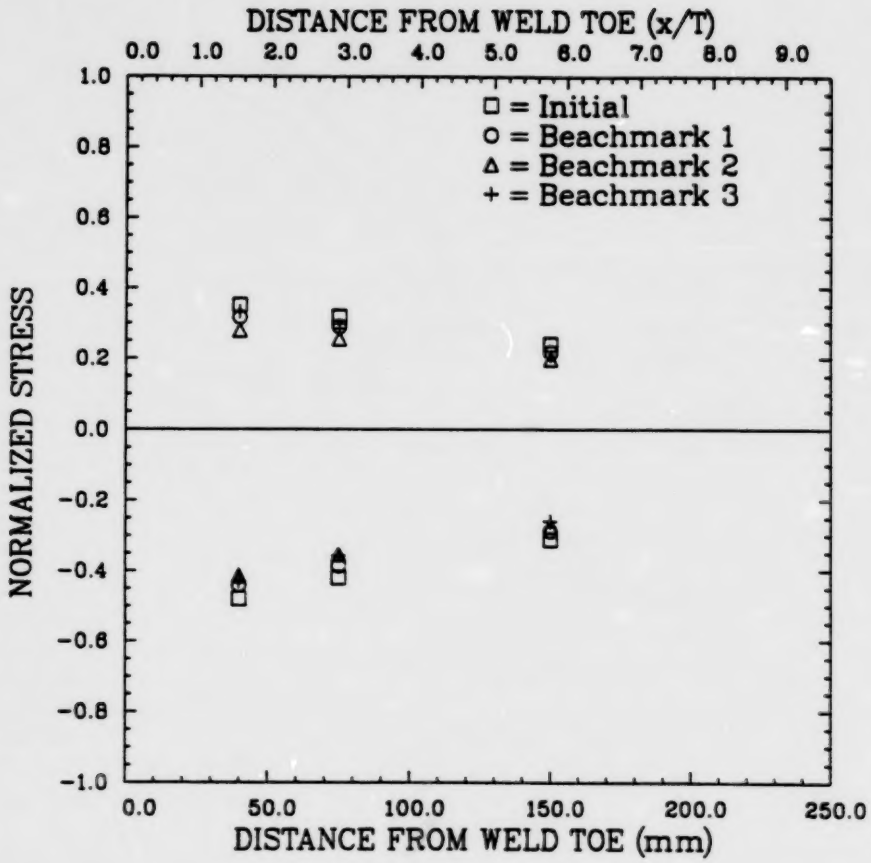

Figure 53b: PP1 – plate surface tangential stress redistribution at hot-spot

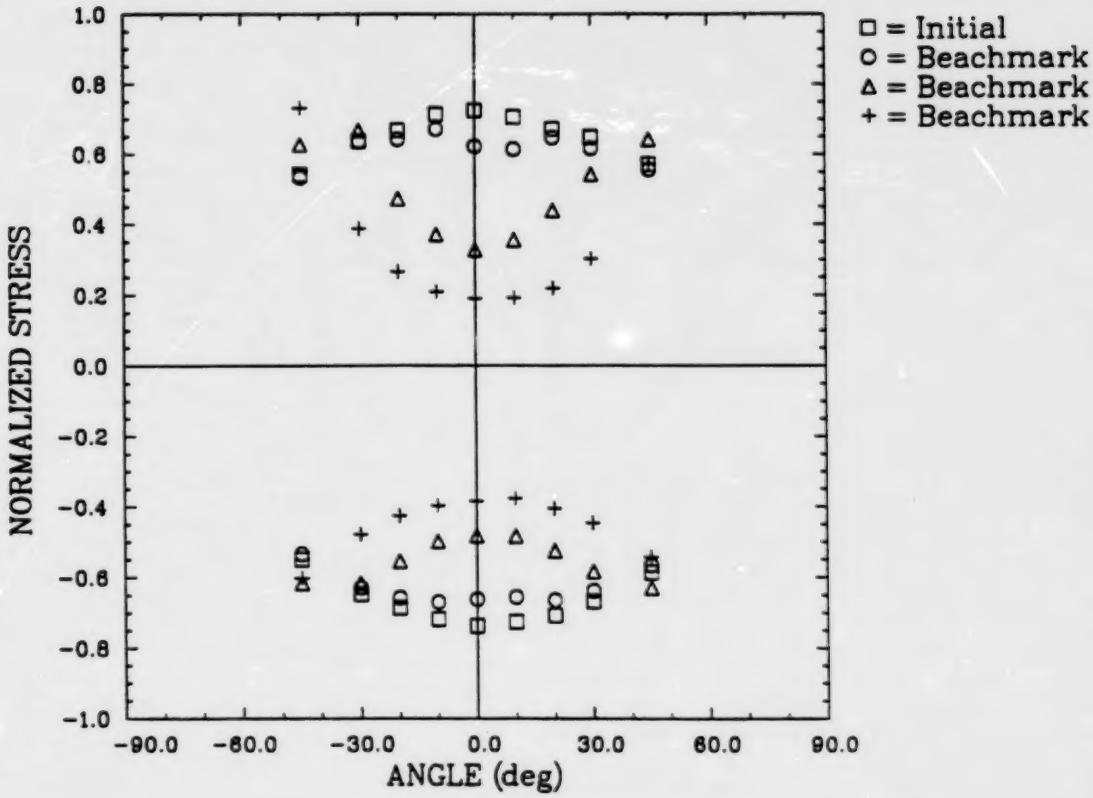

Figure 54a: PP1 – plate surface radial stress redistribution along weld

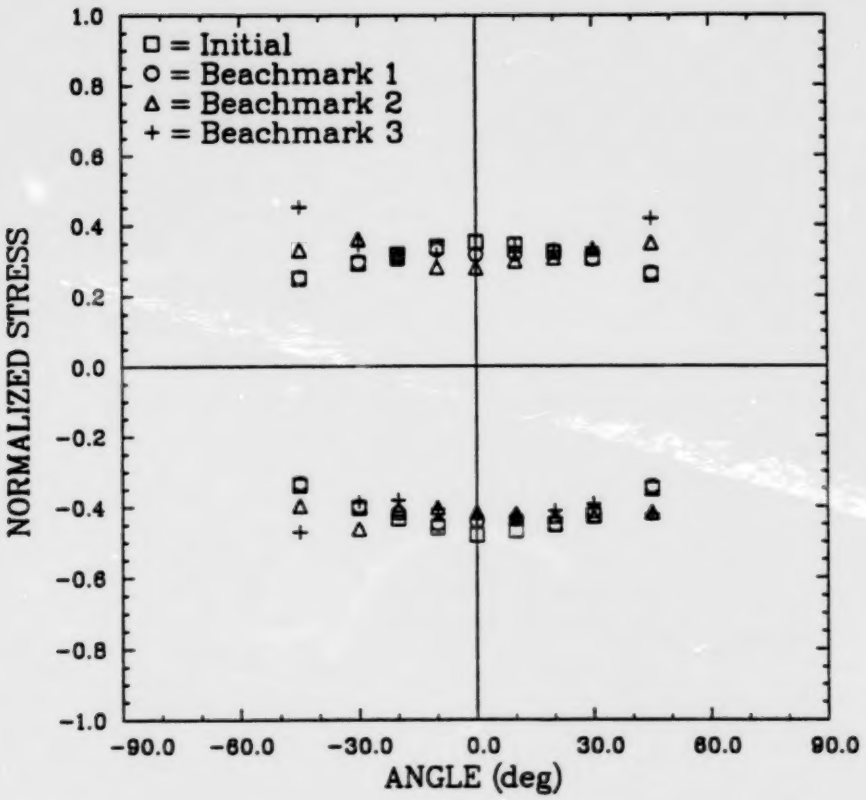

Figure 54b: PP1 – plate surface tangential stress redistribution along weld.

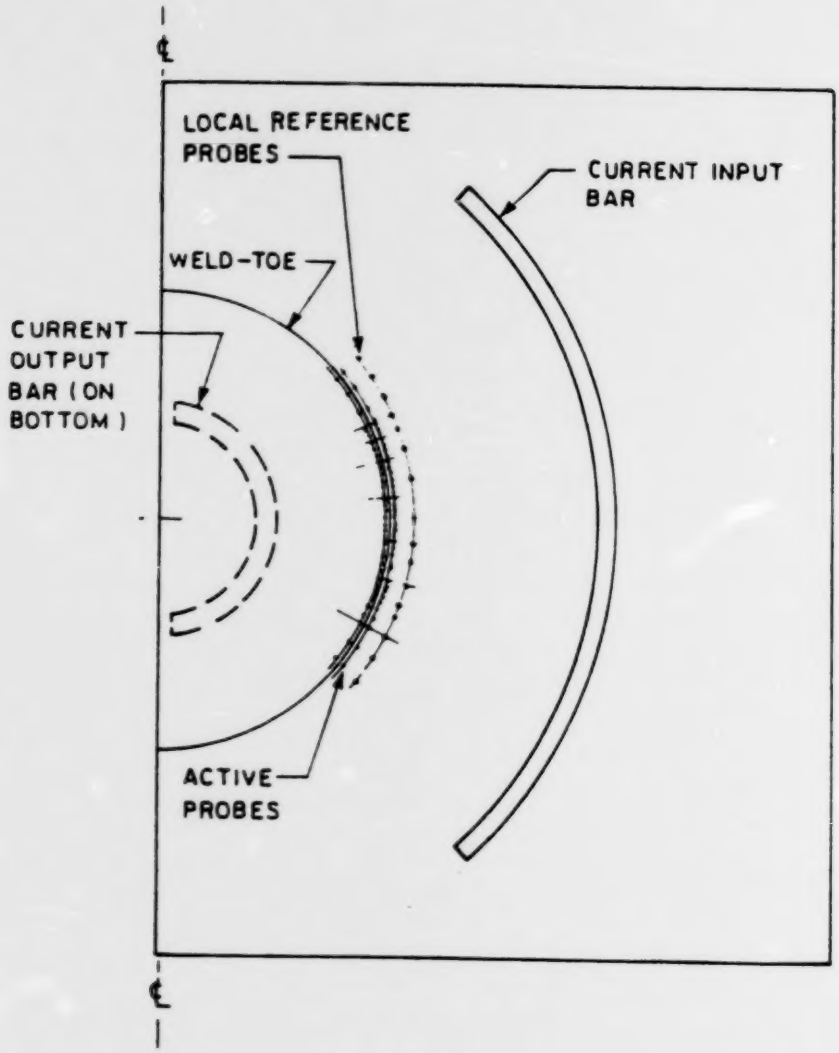

Figure 55: PP2 – PD probe locations.

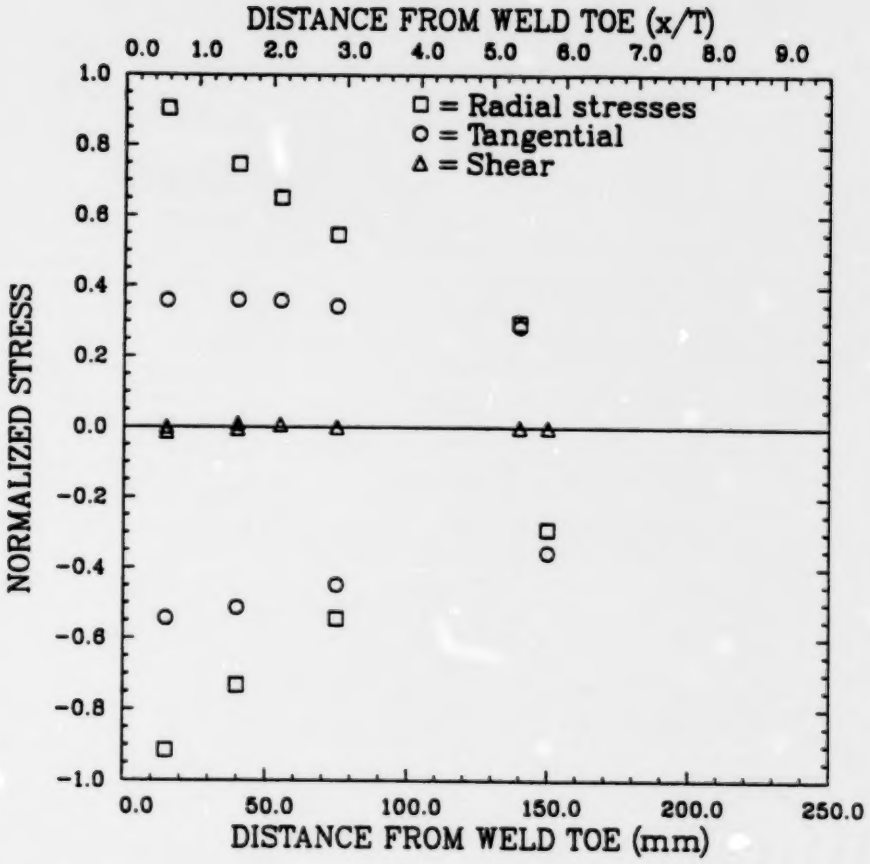

Figure 56: PP2 – plate surface stresses at hot-spot.

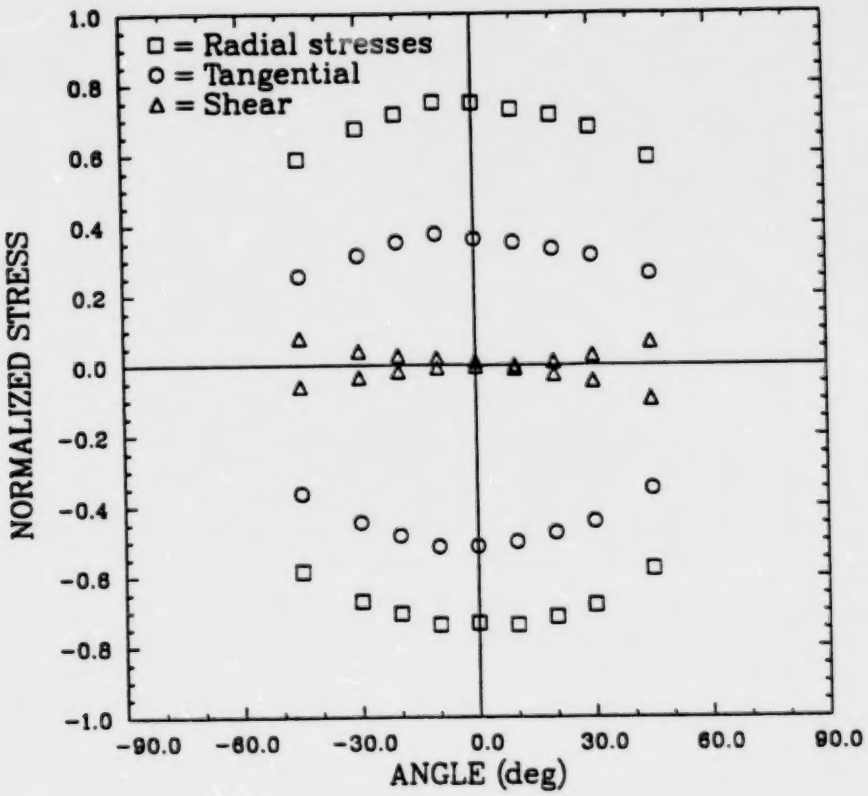

Figure 57: PP2 – plate surface stresses along weld.

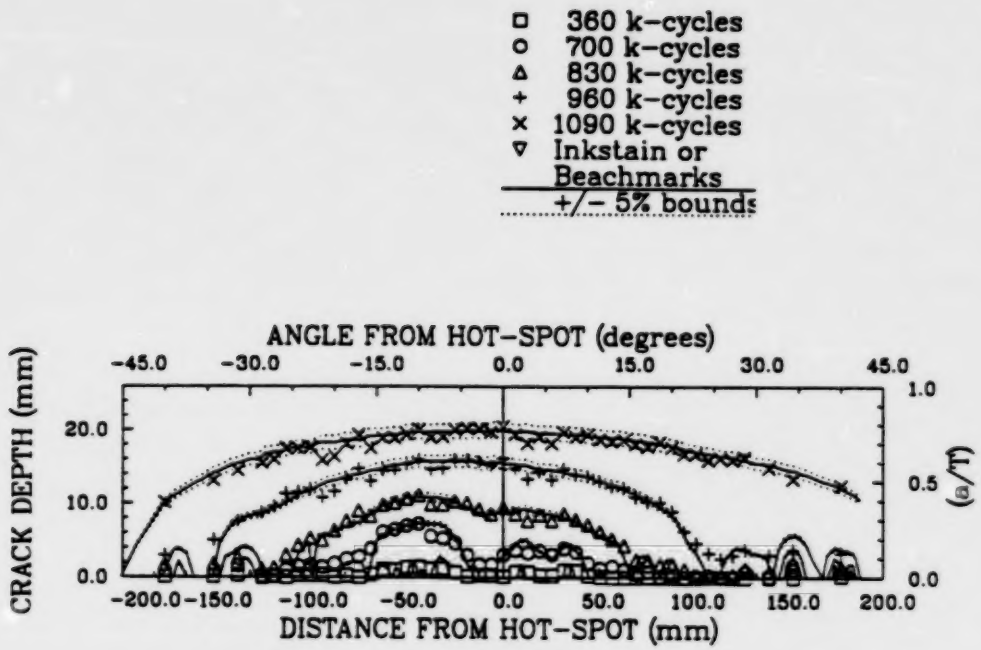

Figure 58: pp2 – PD predictions compared with beachmarks.

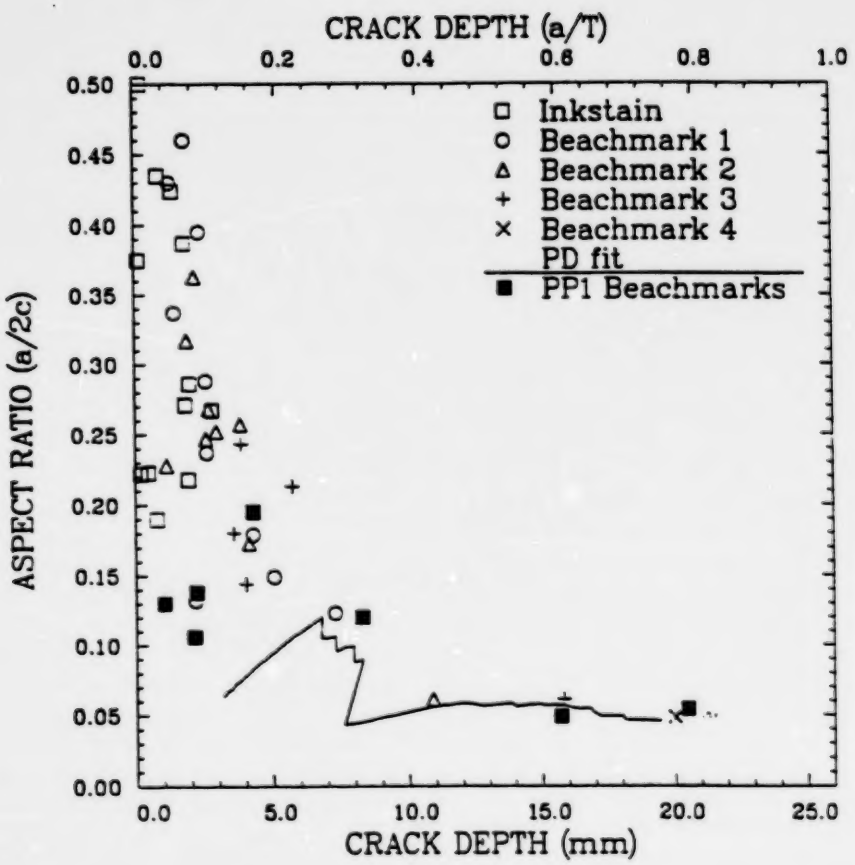

Figure 59: PP2 – aspect ratio development.

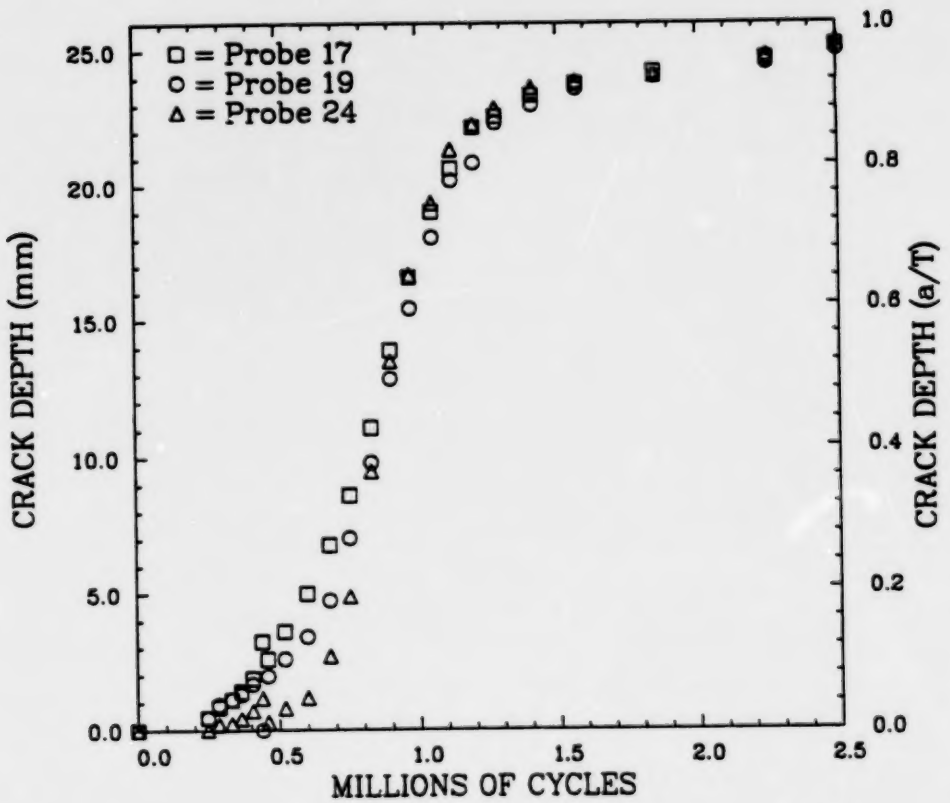

Figure 60: PP2 – crack growth behaviour.

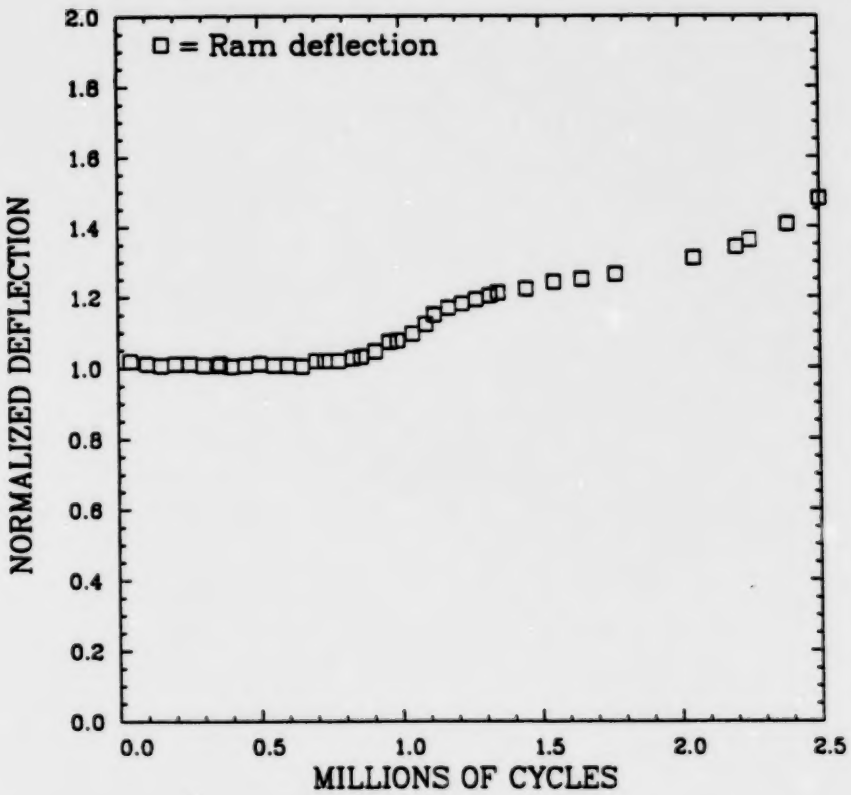

Figure 61a : PP2 – specimen compliance changes versus cycles.

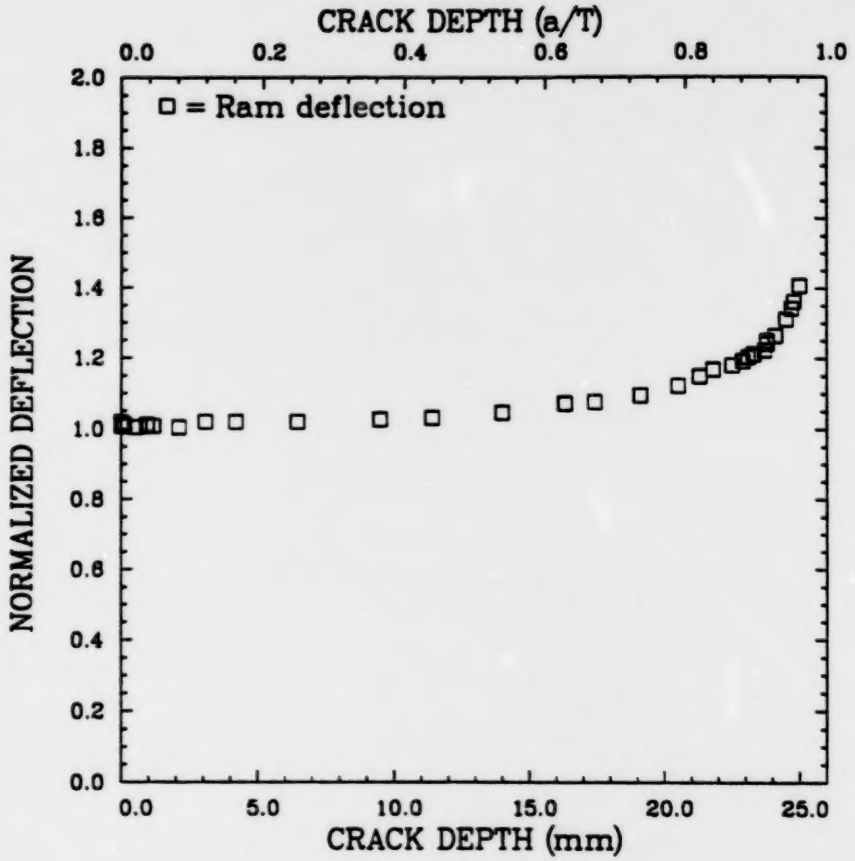

Figure 61b: PP2 – specimen compliance changes versus crack depth.

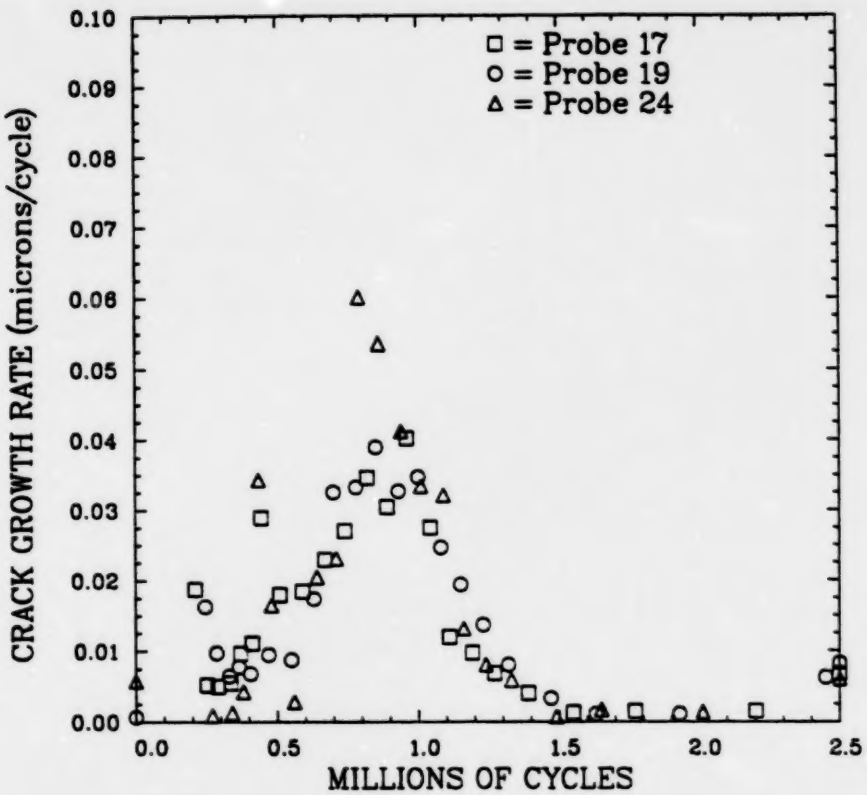

Figure 62a: PP2 – crack growth rates versus cycles.

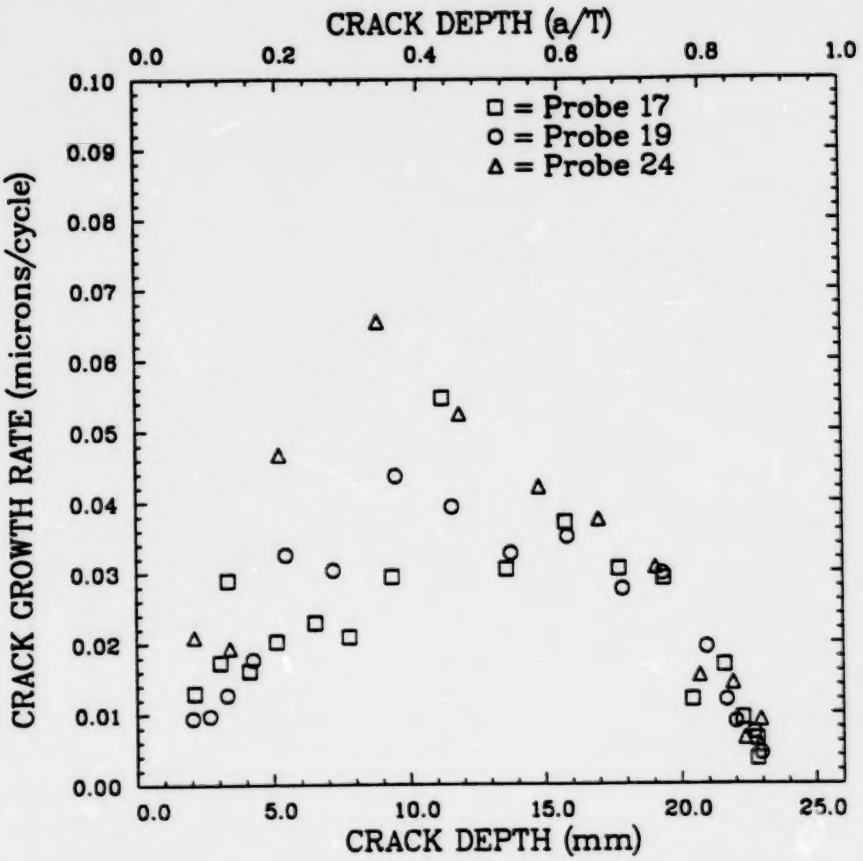

Figure 62b: PP2 – crack growth rates versus crack depth.

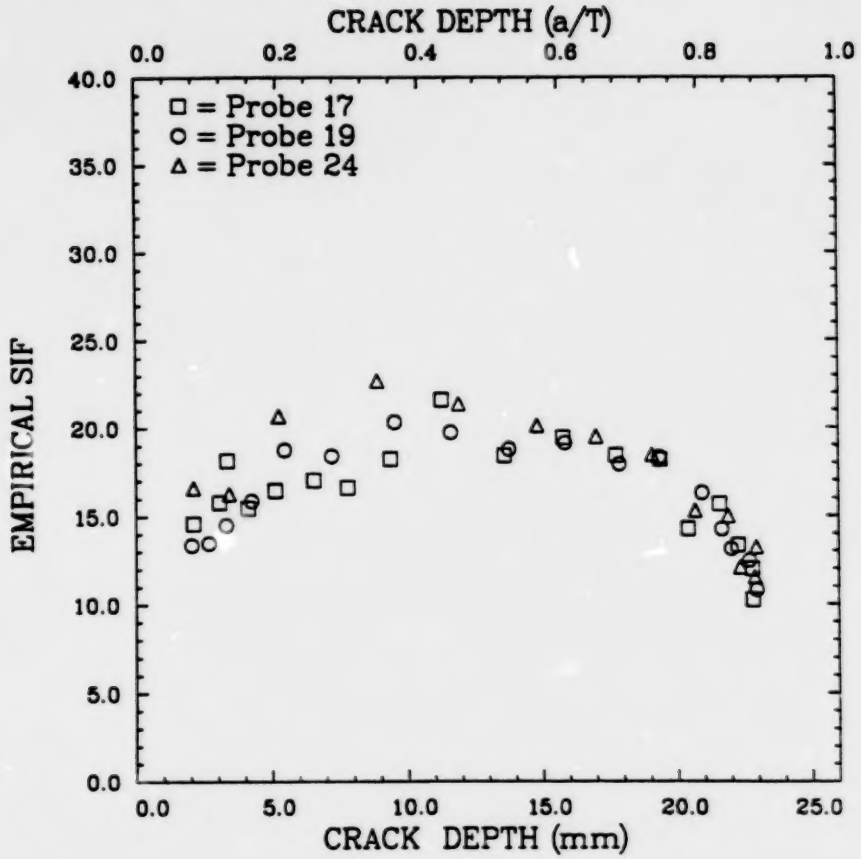

Figure 63: PP2 – empirical stress intensity factors, ΔK.

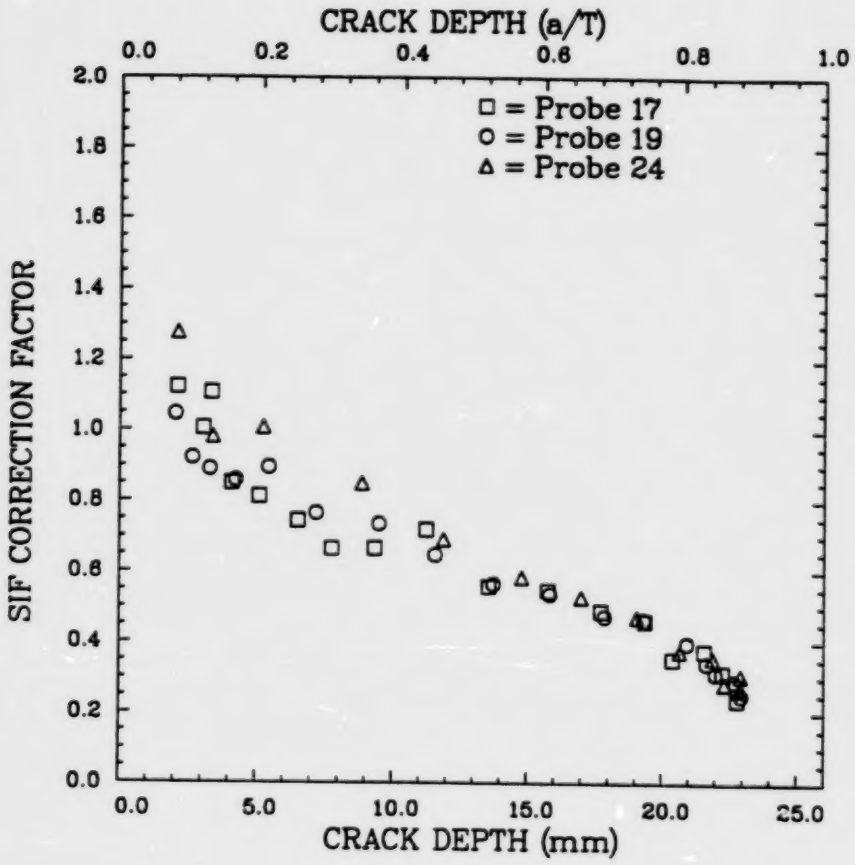

Figure 64: PP2 – empirical stress intensity correction factors, $M_k M$.

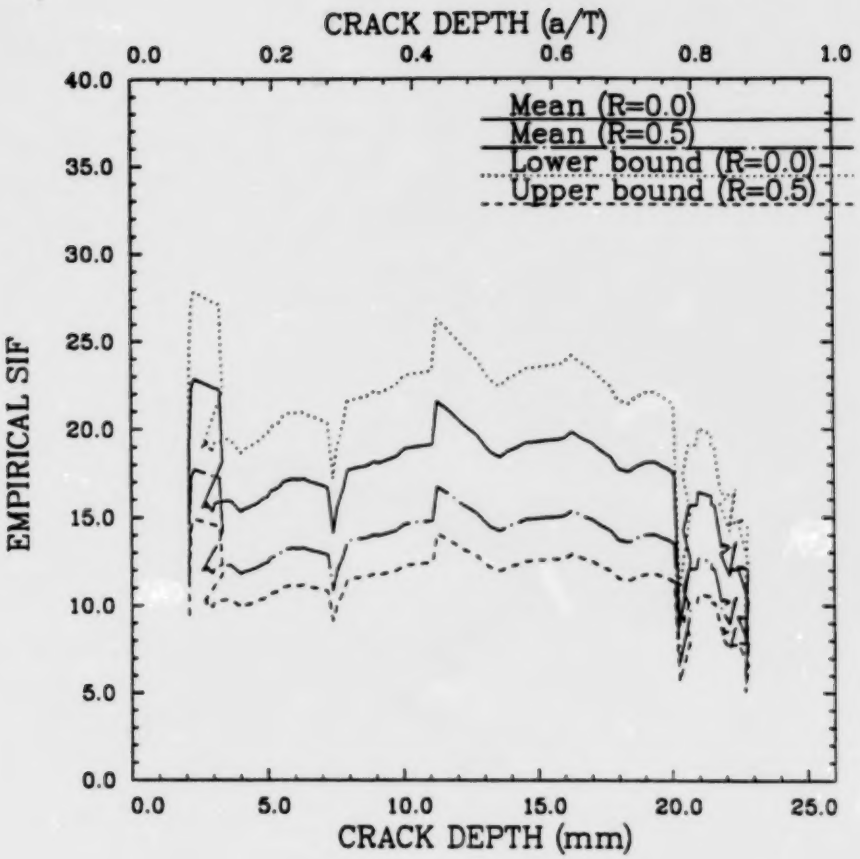

Figure 65: PP2 – empirical stress intensity factors, ΔK, calculated using different values for C and m.

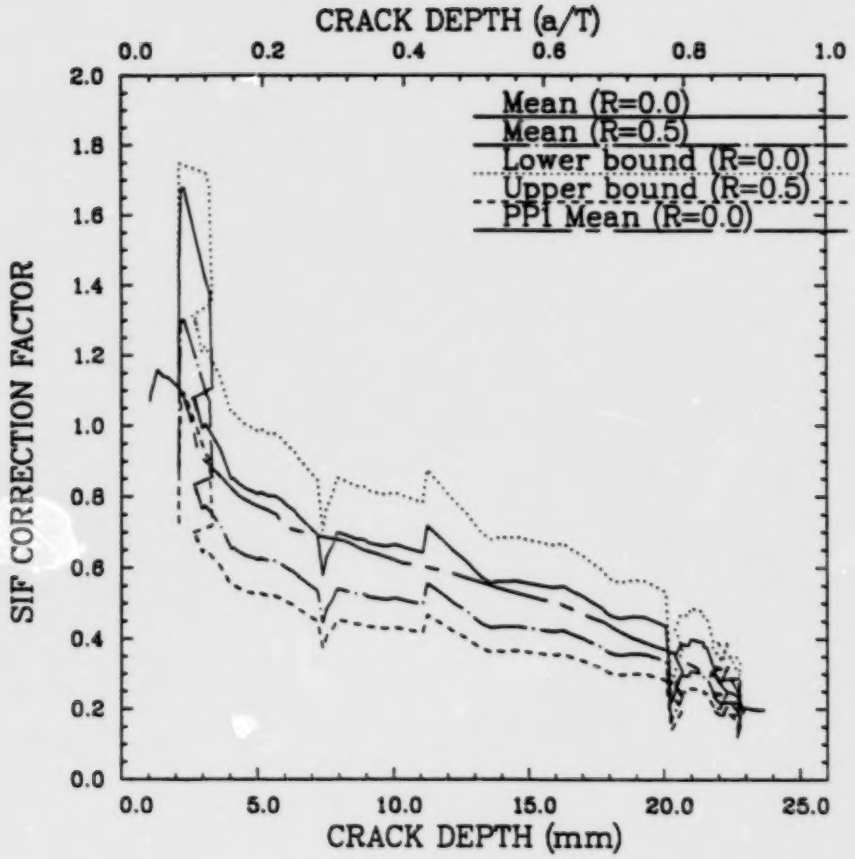

Figure 66: PP2 – empirical stress intensity correction factors, $M_k M$, calculated using different values for C and m.

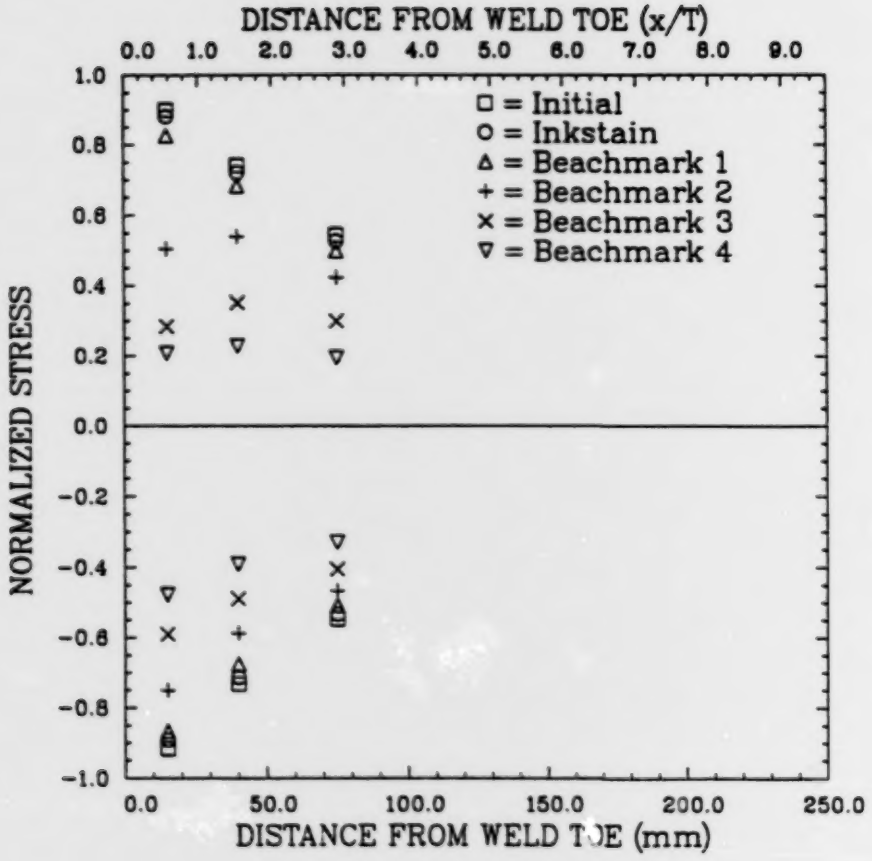

Figure 67a: PP2 – plate surface radial stress redistribution at hot-spot.

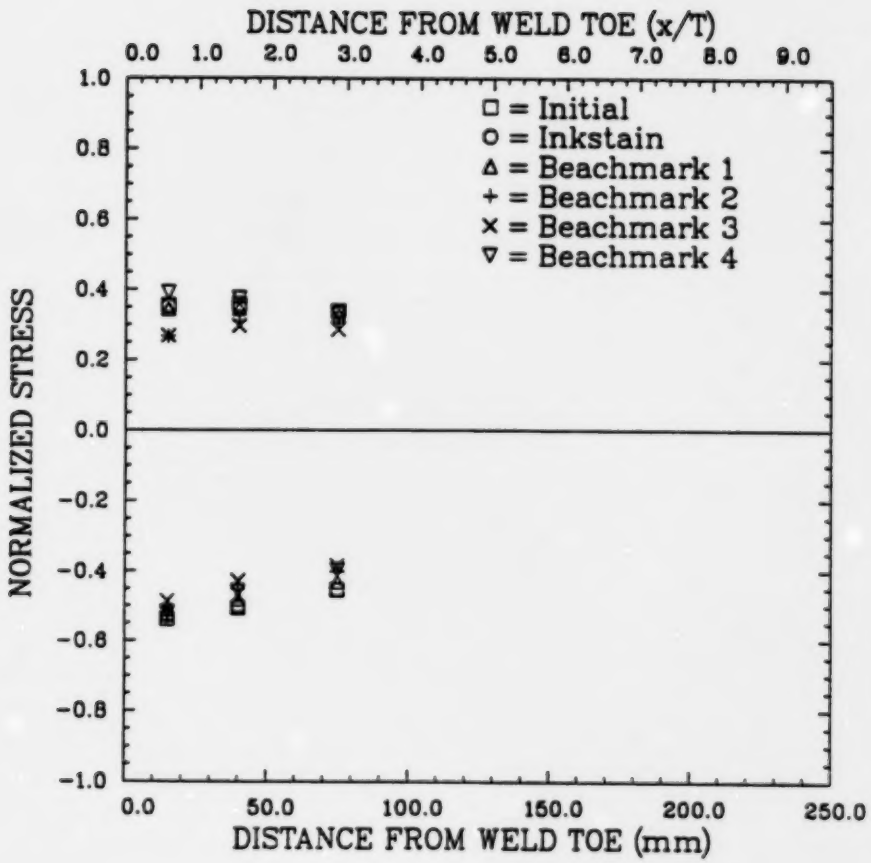
DISTANCE FROM WELD TOE (x/T)
0.0 1.0 2.0 3.0 4.0 5.0 6.0 7.0 8.0 9.0
1.0 0.8 0.6 0.4 0.2 0.0 -0.2 -0.4 -0.6 -0.8 -1.0
NORMALIZED STRESS
□ = Initial
○ = Inkstain
△ = Beachmark 1
+ = Beachmark 2
× = Beachmark 3
▽ = Beachmark 4
0.0 50.0 100.0 150.0 200.0 250.0
DISTANCE FROM WELD TOE (mm)

Figure 67b: PP2 – plate surface tangential stress redistribution at hot-spot.

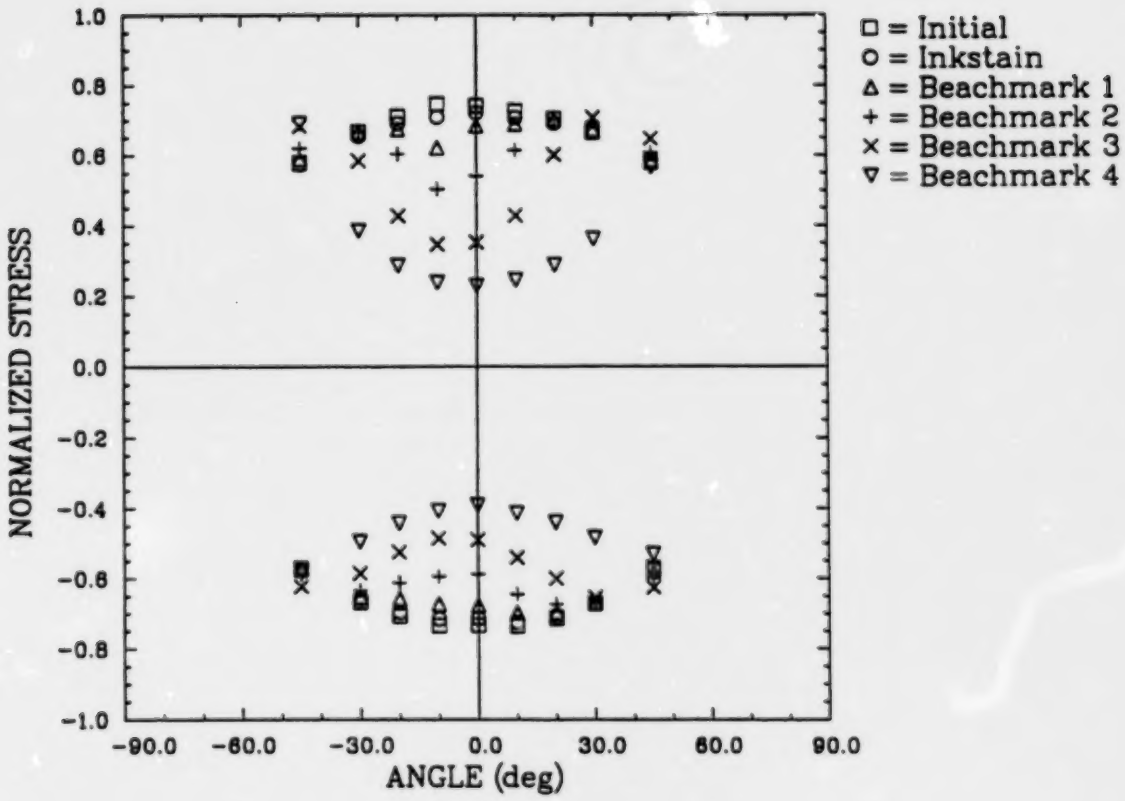

Figure 68a: PP2 – plate surface radial stress distribution along weld.

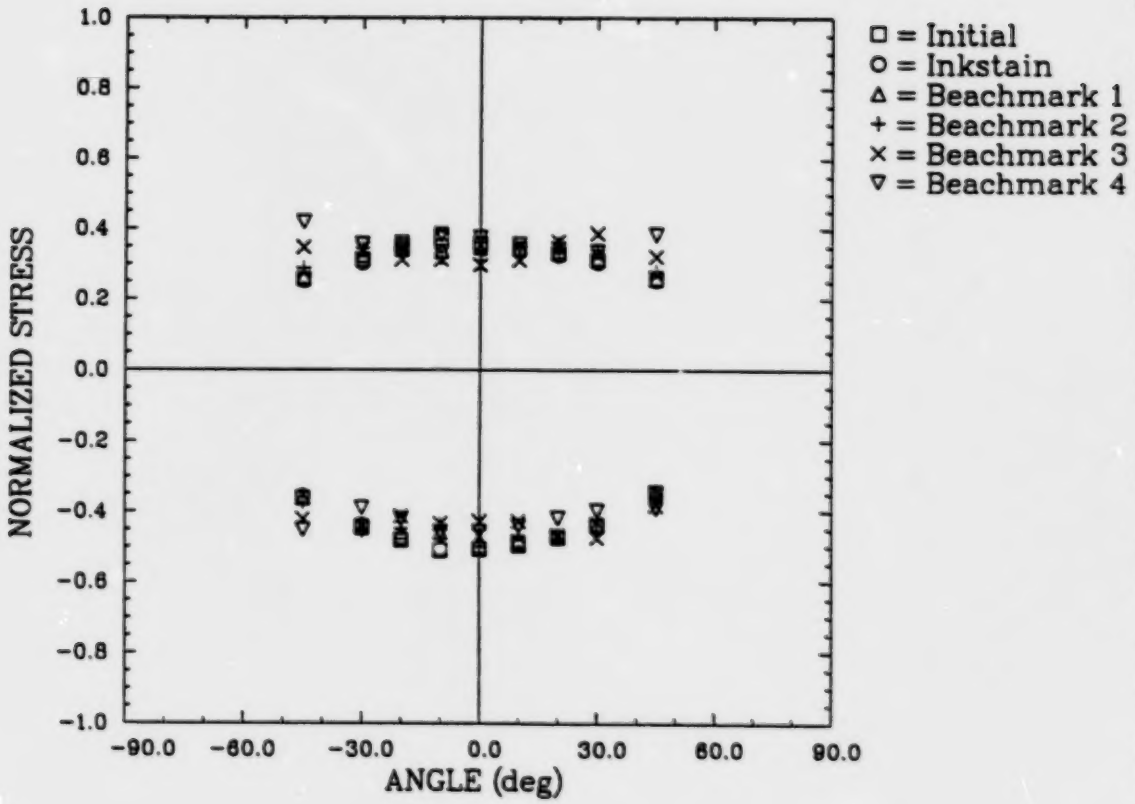

Figure 68b: PP2 – plate surface tangential stress distribution along weld.

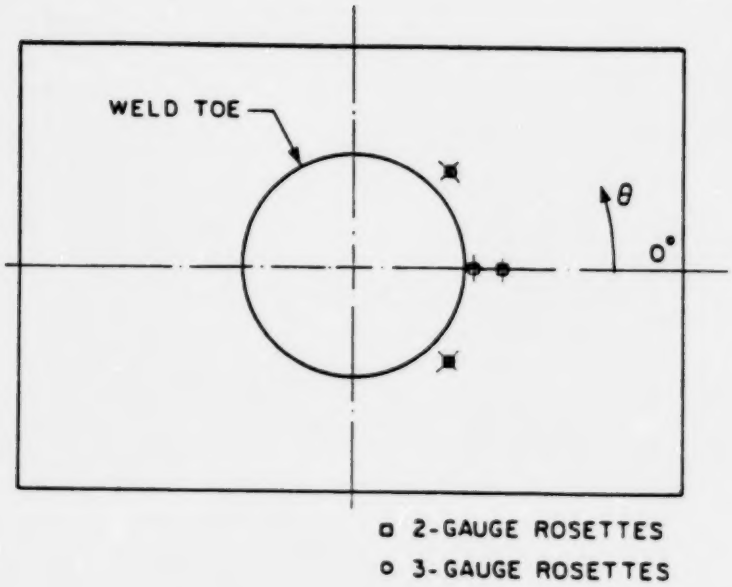

Figure 69: PP3 – PP8 – strain gauge locations.

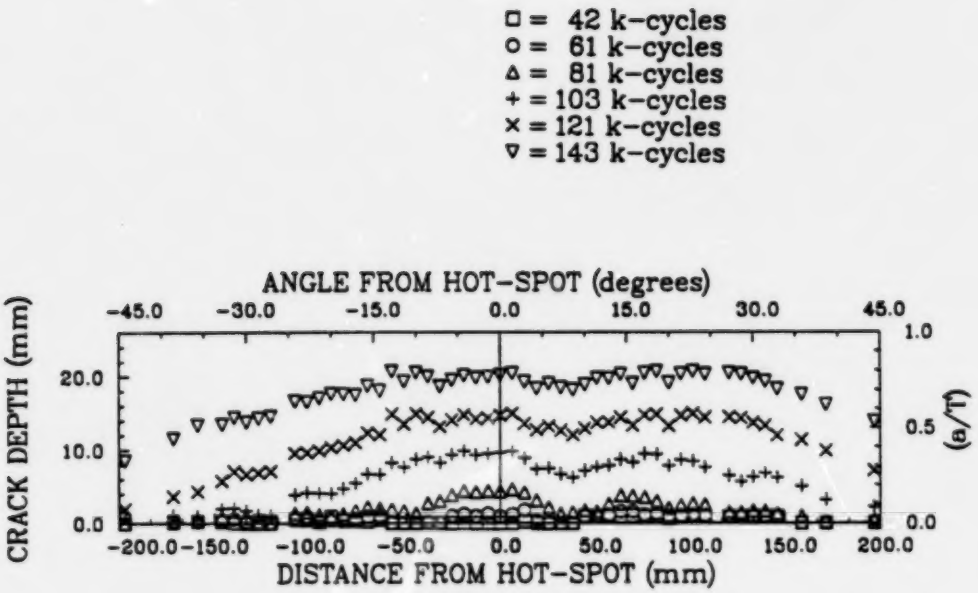

Figure 70: PP3 – crack shape development.

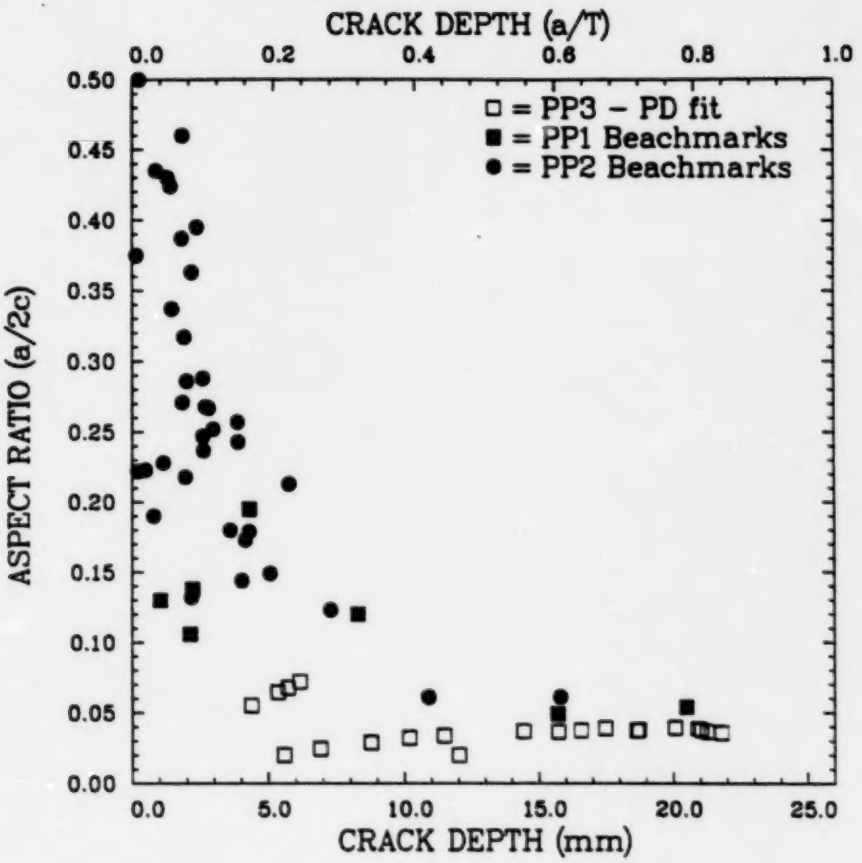

Figure 71: PP3 – aspect ratio development.

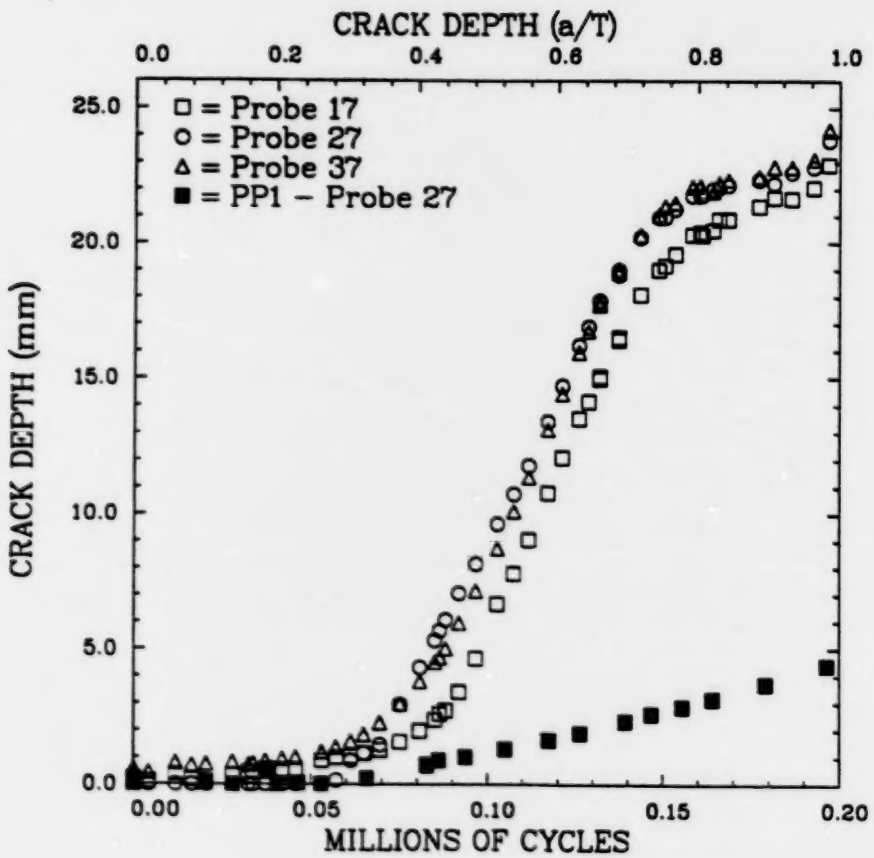

Figure 72: PP3 – crack growth behaviour.

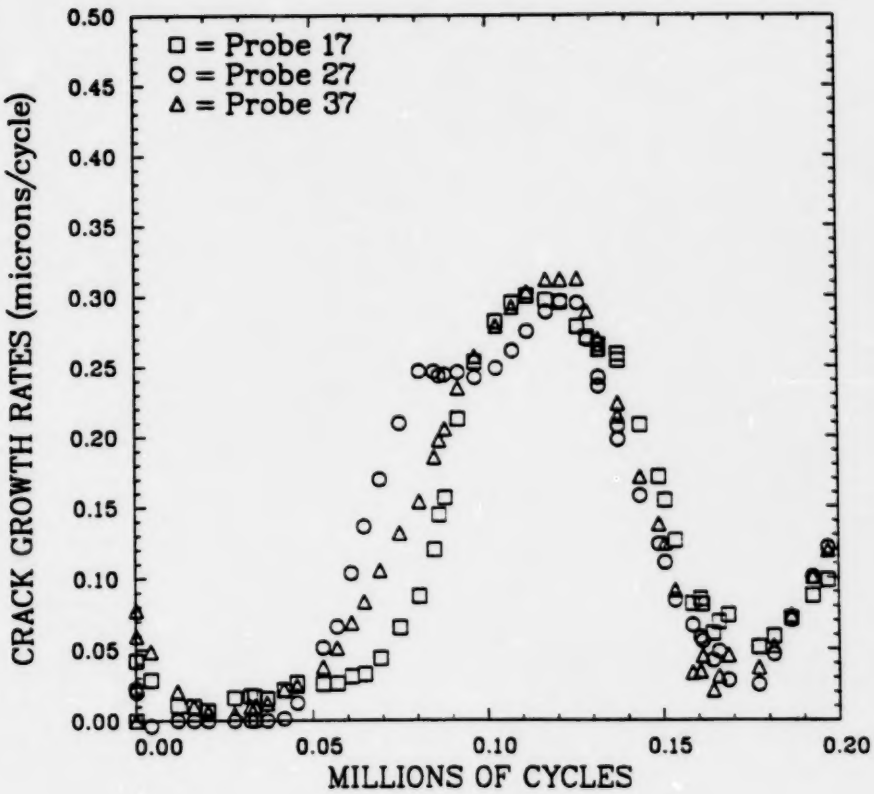

Figure 73a: PP3 – crack growth rates versus cycles.

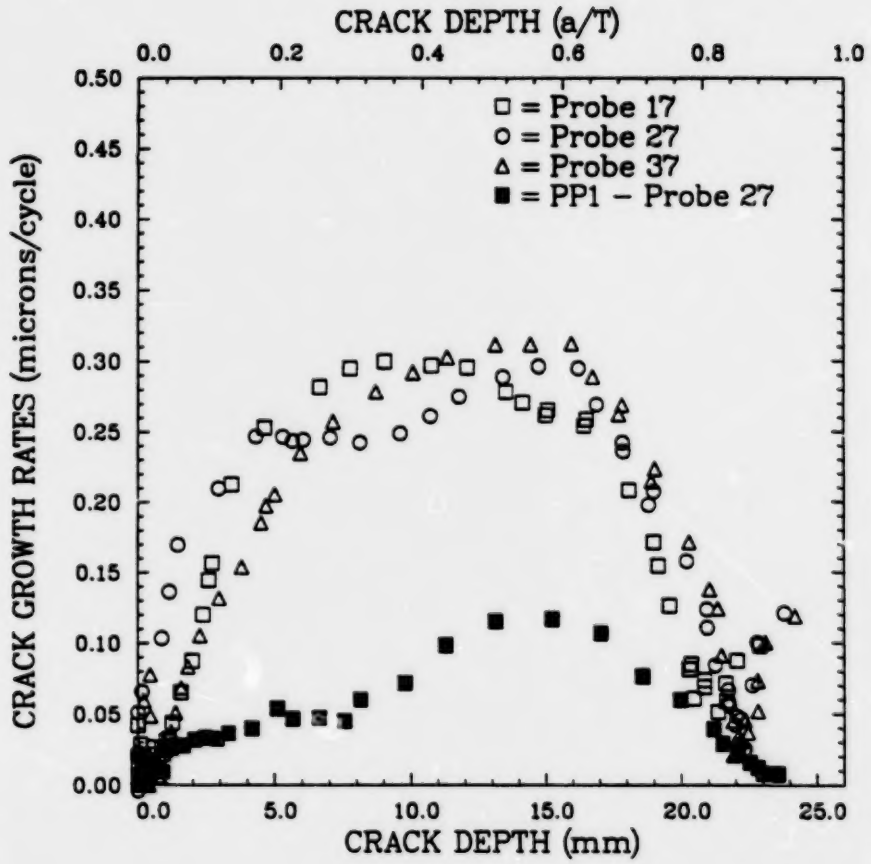

Figure 73b: PP3 – crack growth rates versus crack depth.

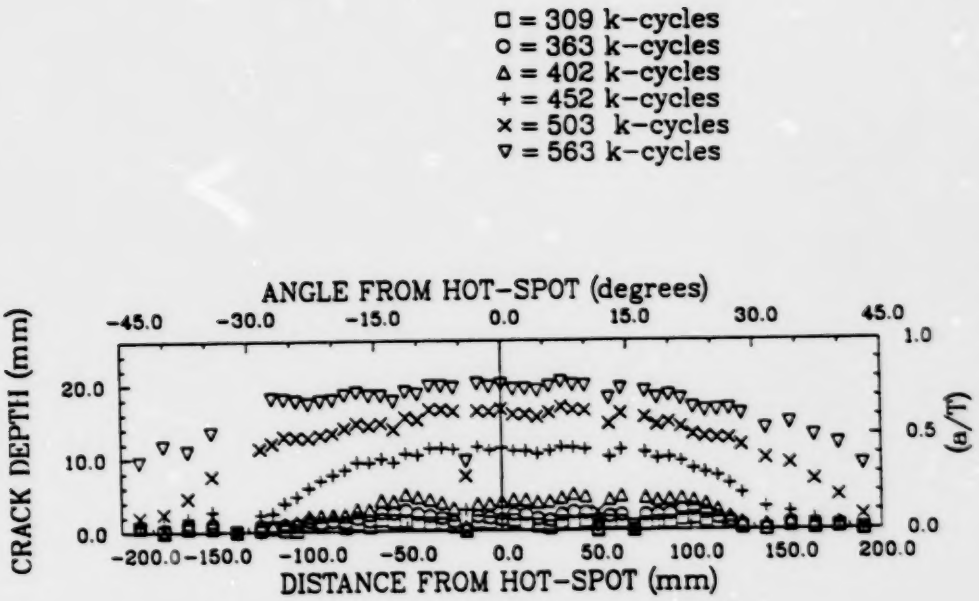

Figure 74: PP4 – crack shape development.

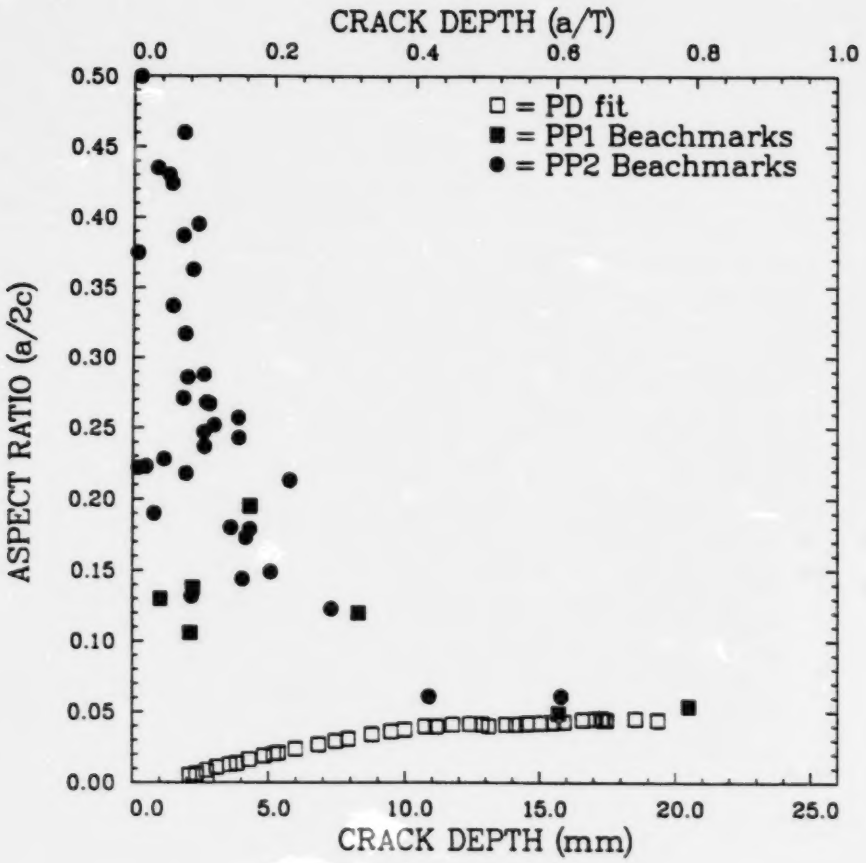

Figure 75: PP4 – aspect ratio development.

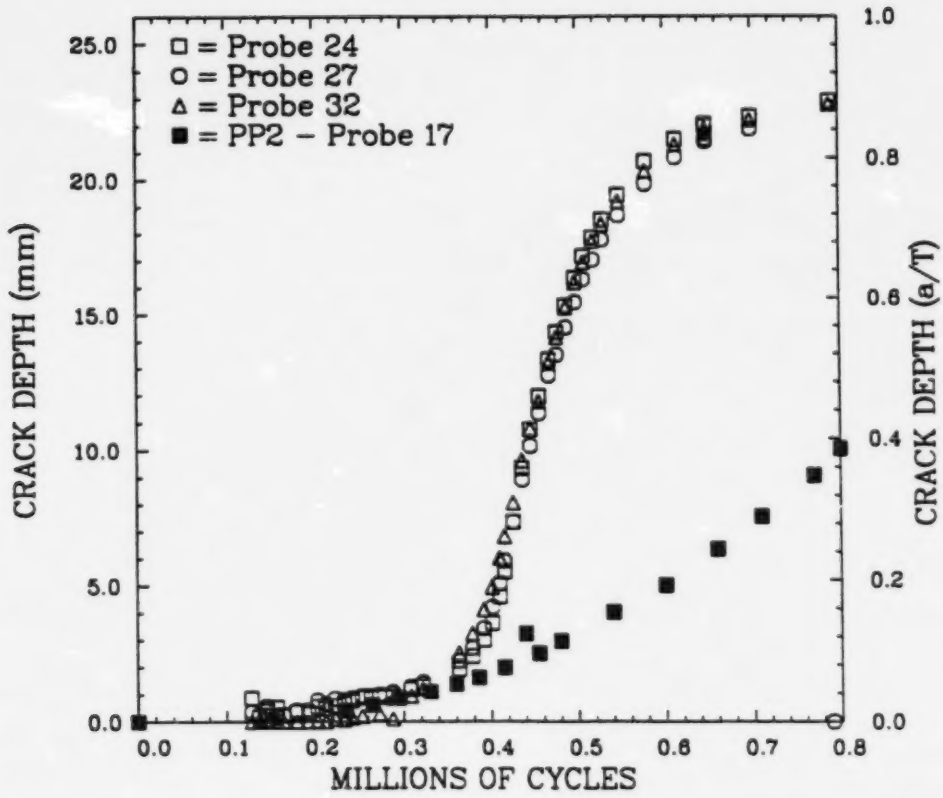

Figure 76: PP4 – crack growth behaviour.

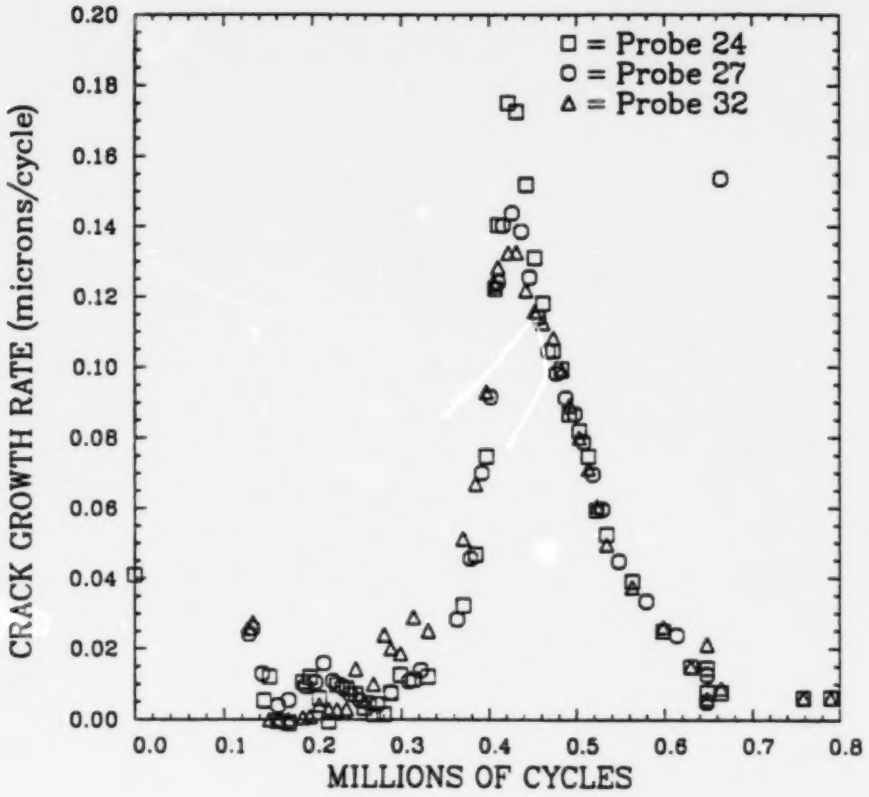

Figure 77a: PP4 – crack growth rates versus cycles.

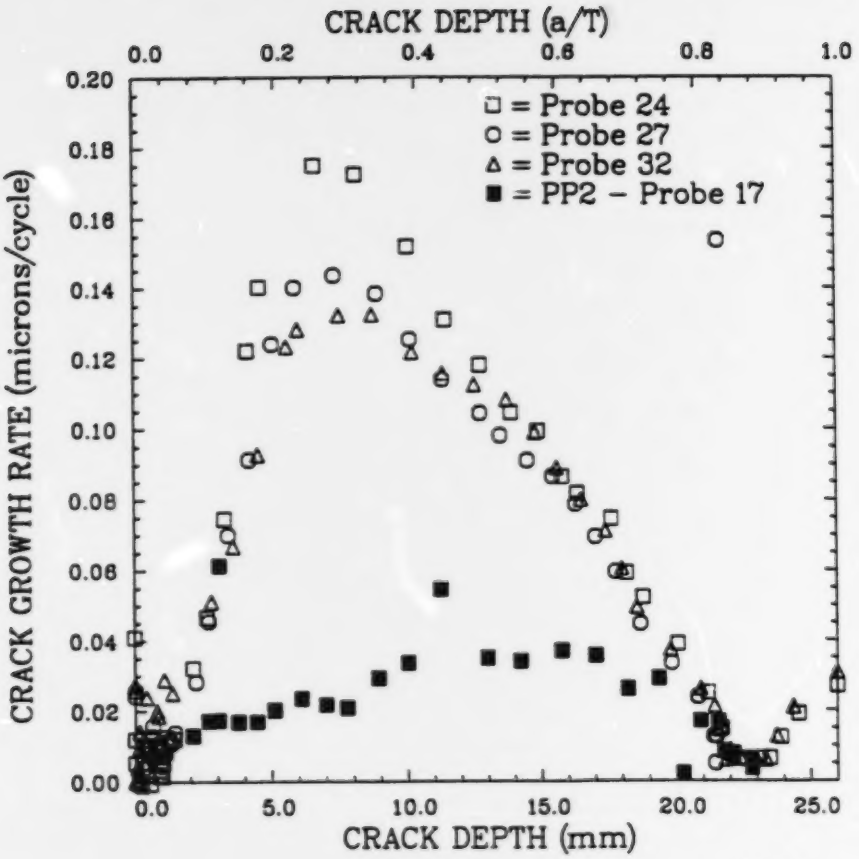

Figure 77b: PP4 – crack growth rates versus crack depth.

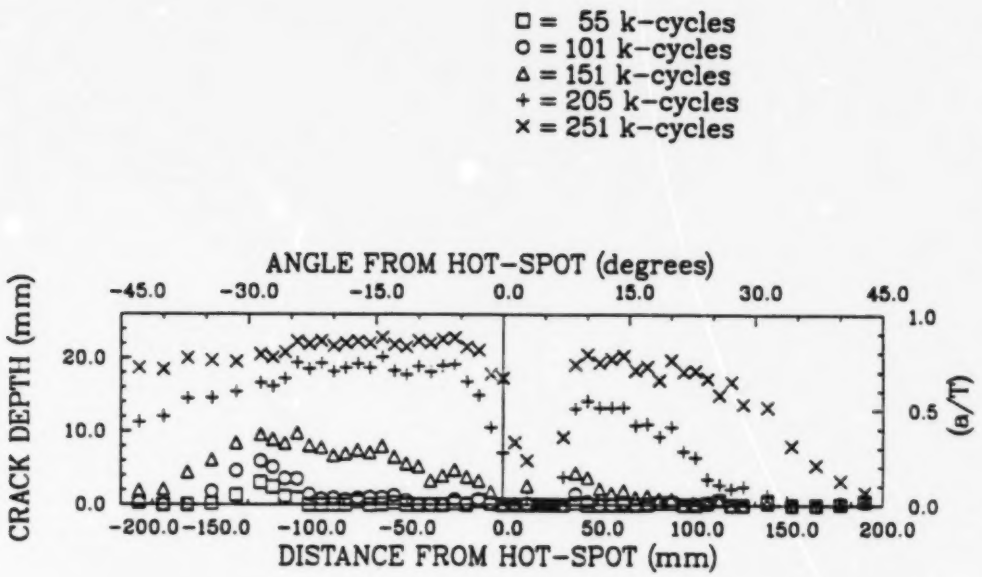

Figure 78: PP5 – crack shape development.

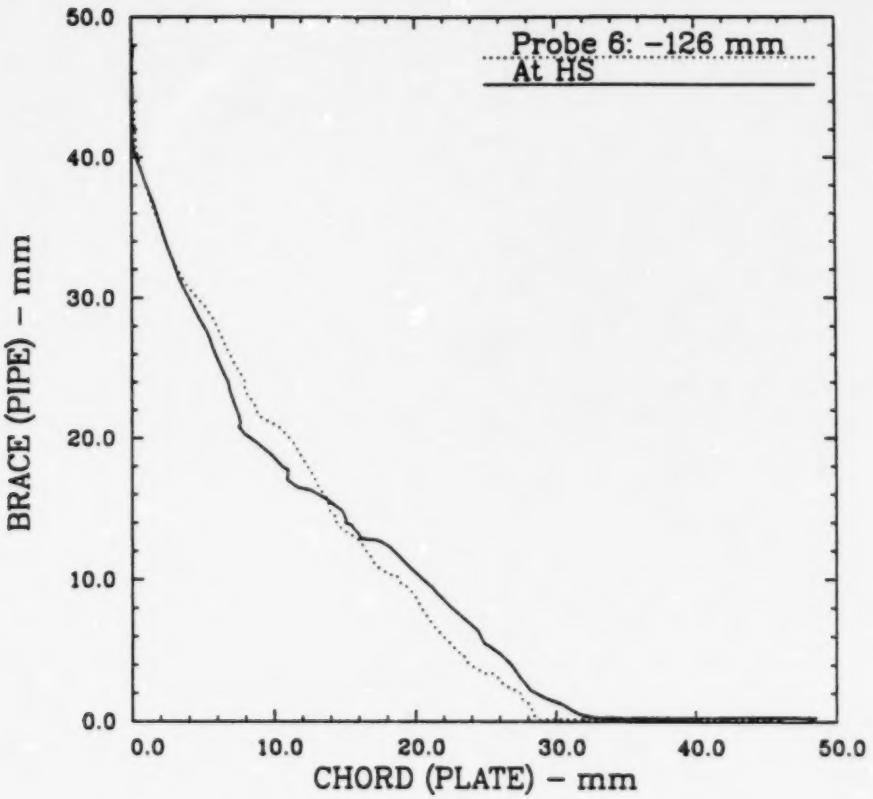

Figure 79: PP5 - weld reinforcement profiles.

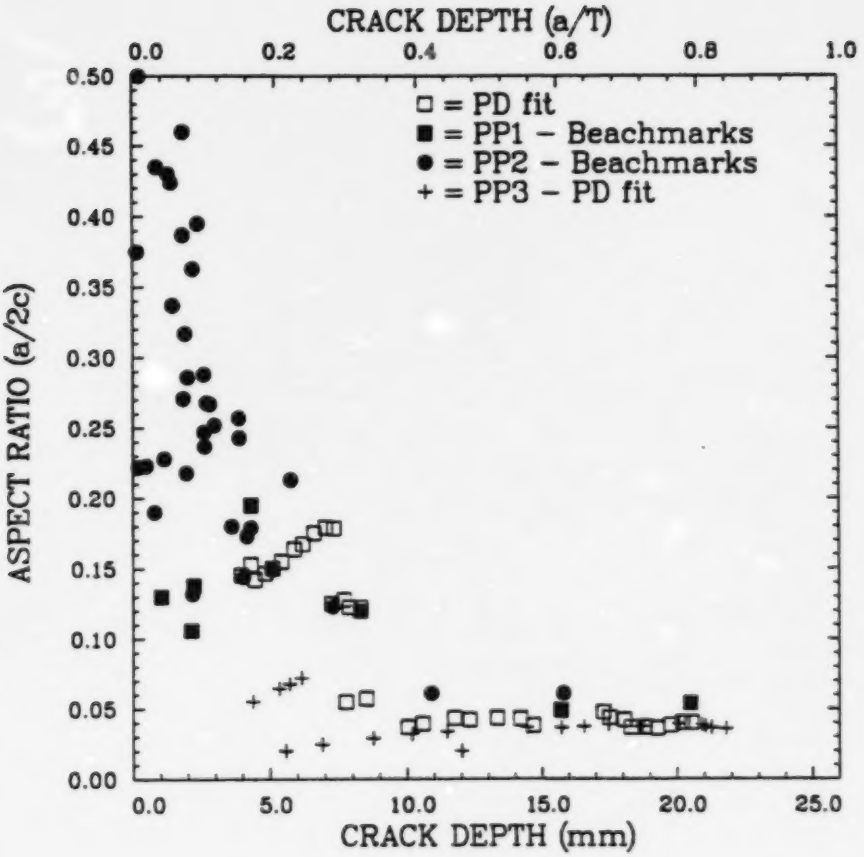

Figure 80: PP5 – aspect ratio development.

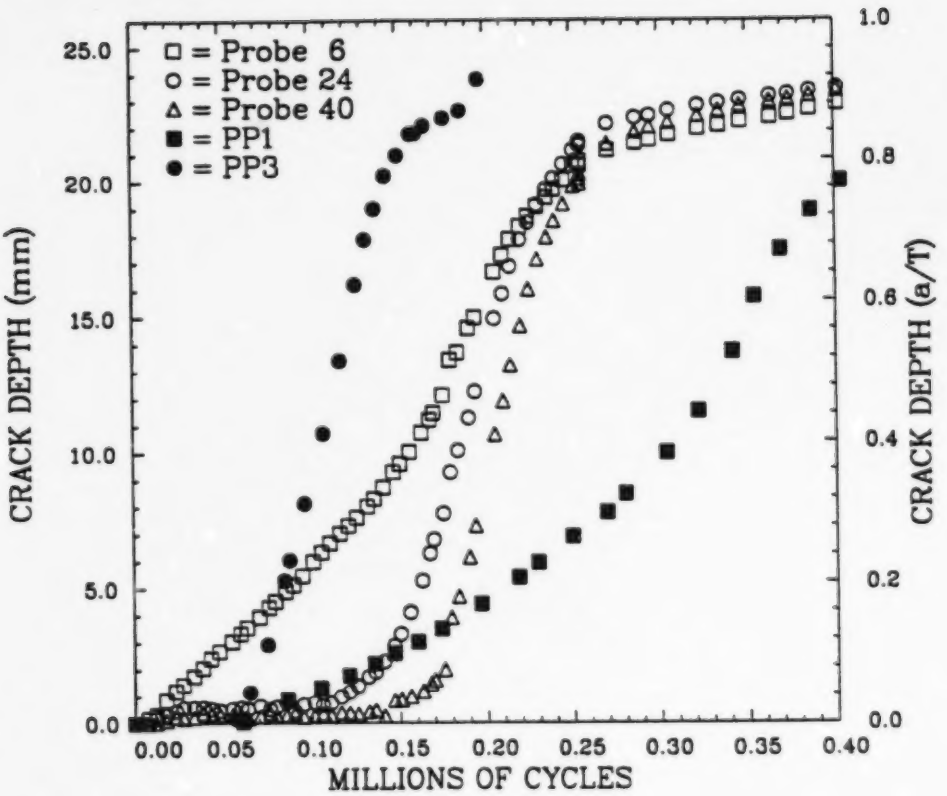

Figure 81: PP5 – crack growth behaviour.

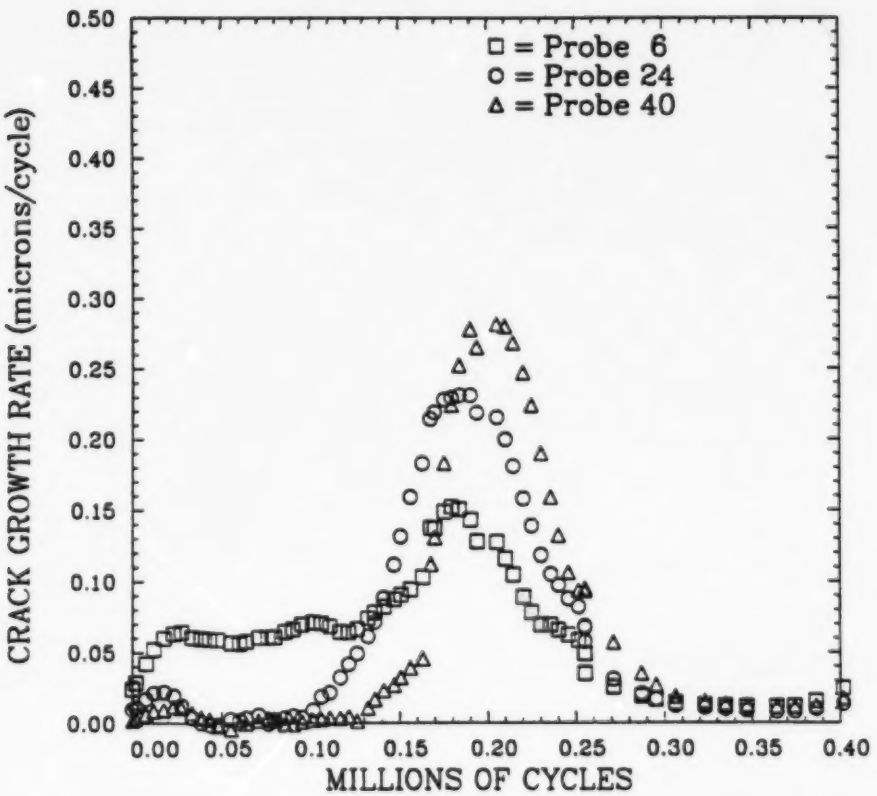

Figure 82a: PP5 – crack growth rates versus cycles.

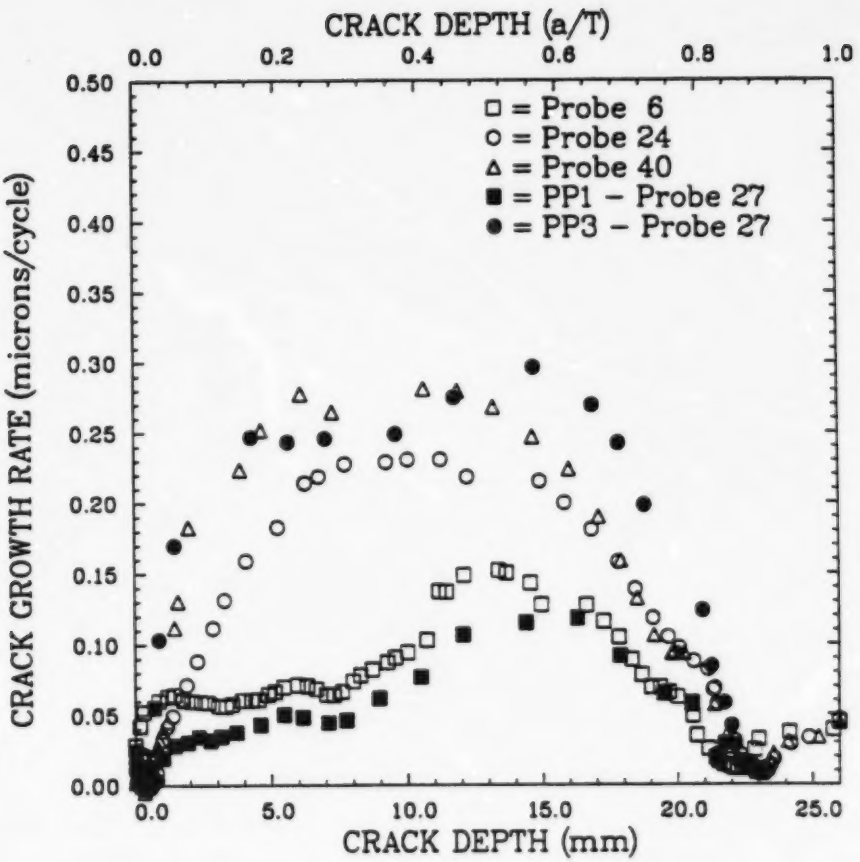

Figure 82b: PP5 – crack growth rates versus crack depth.

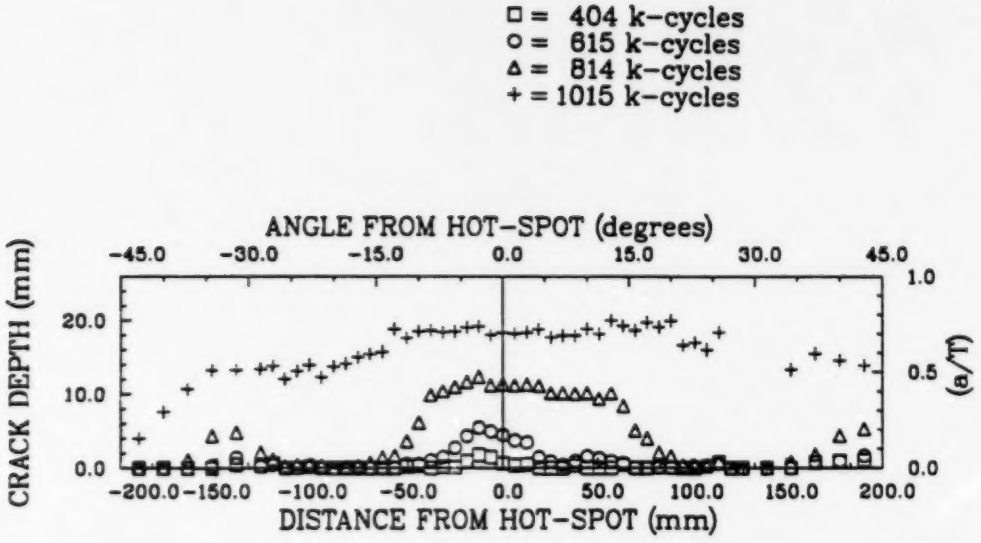

Figure 83: PP6 – crack shape development.

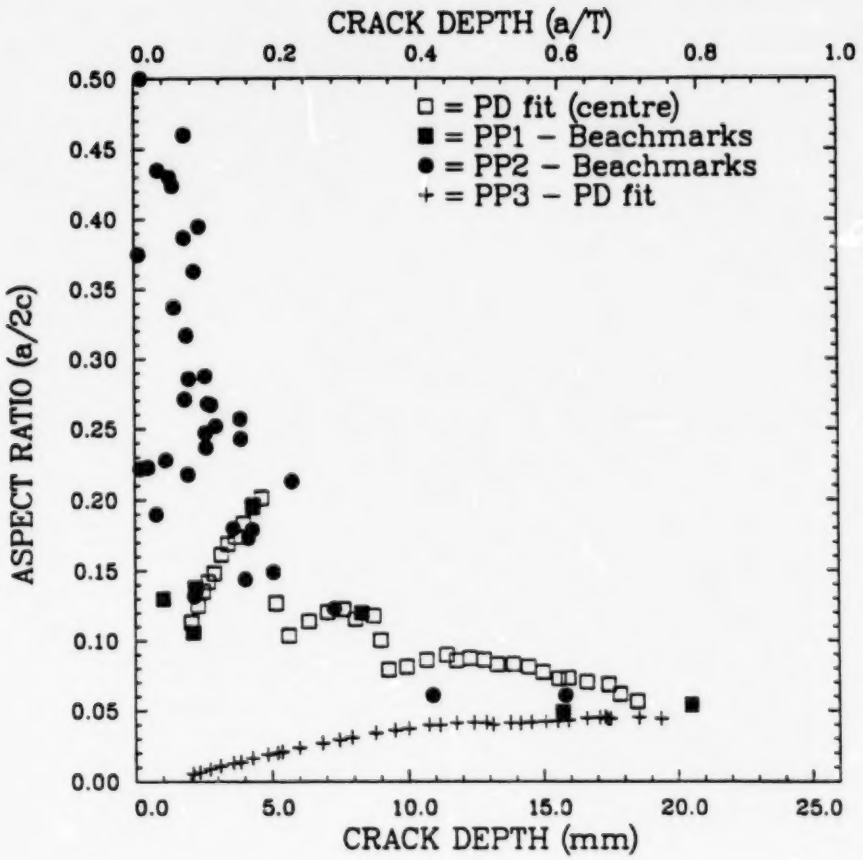

Figure 84: PP6 – aspect ratio development.

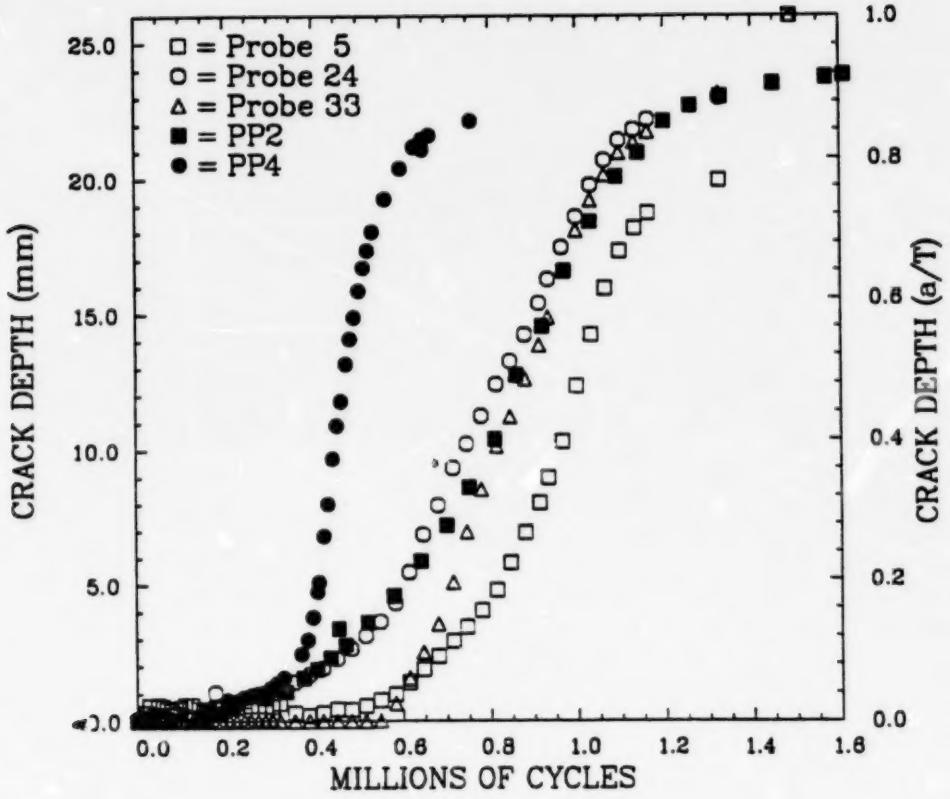

Figure 85: PP6 – crack growth behaviour.

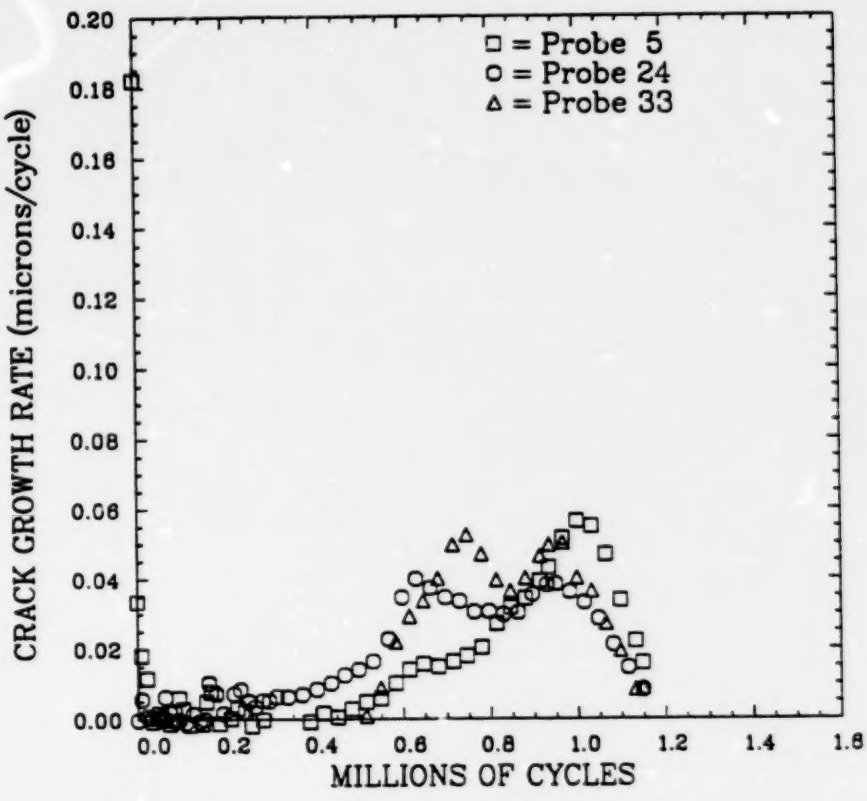

Figure 86a: PP6 – crack growth rates versus cycles.

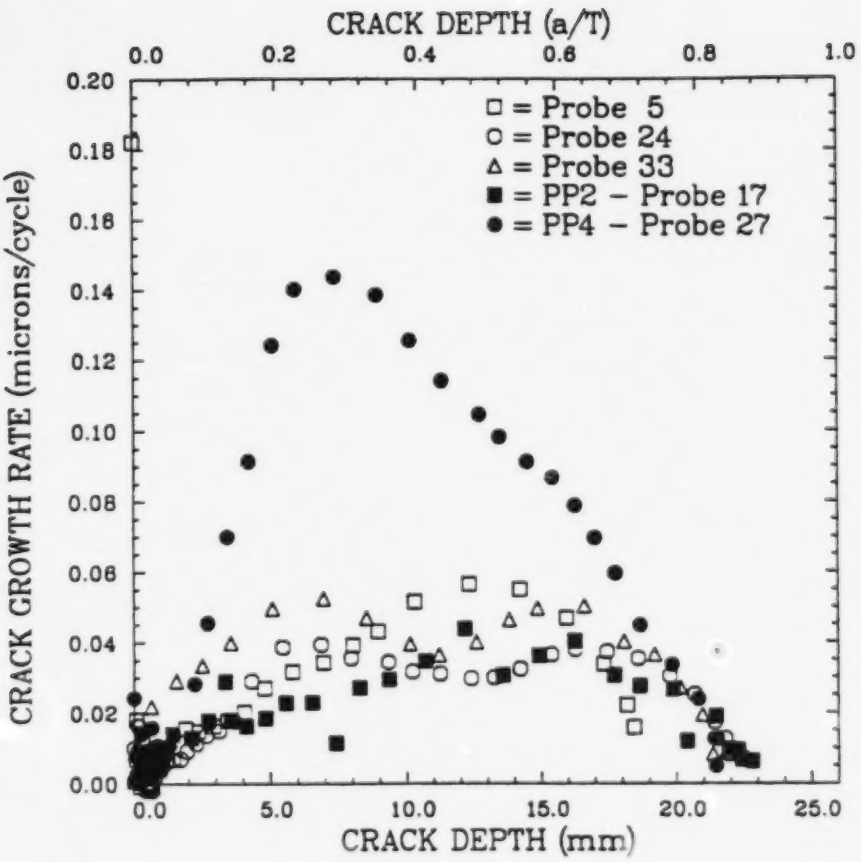

Figure 86b: PP6 – crack growth rates versus crack depth.

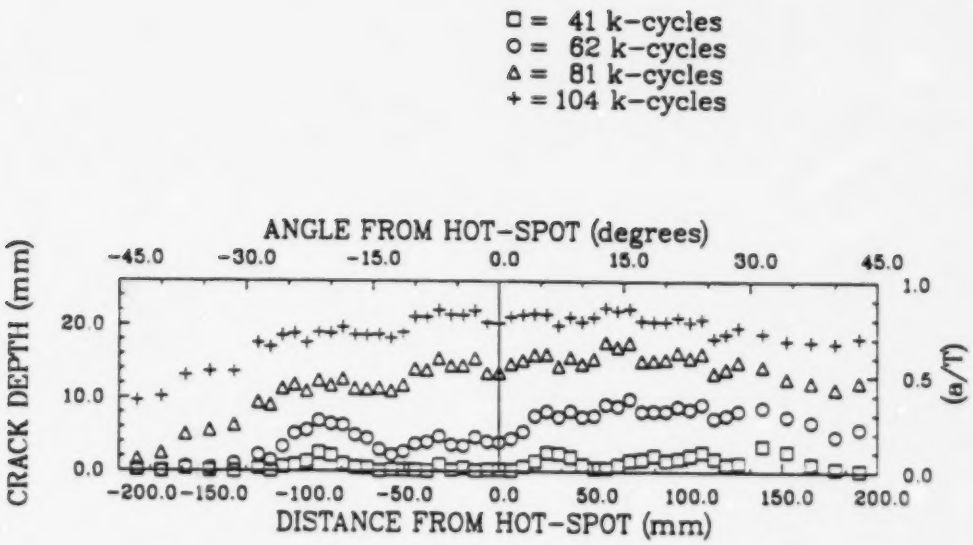

Figure 87: PP7 – crack shape development.

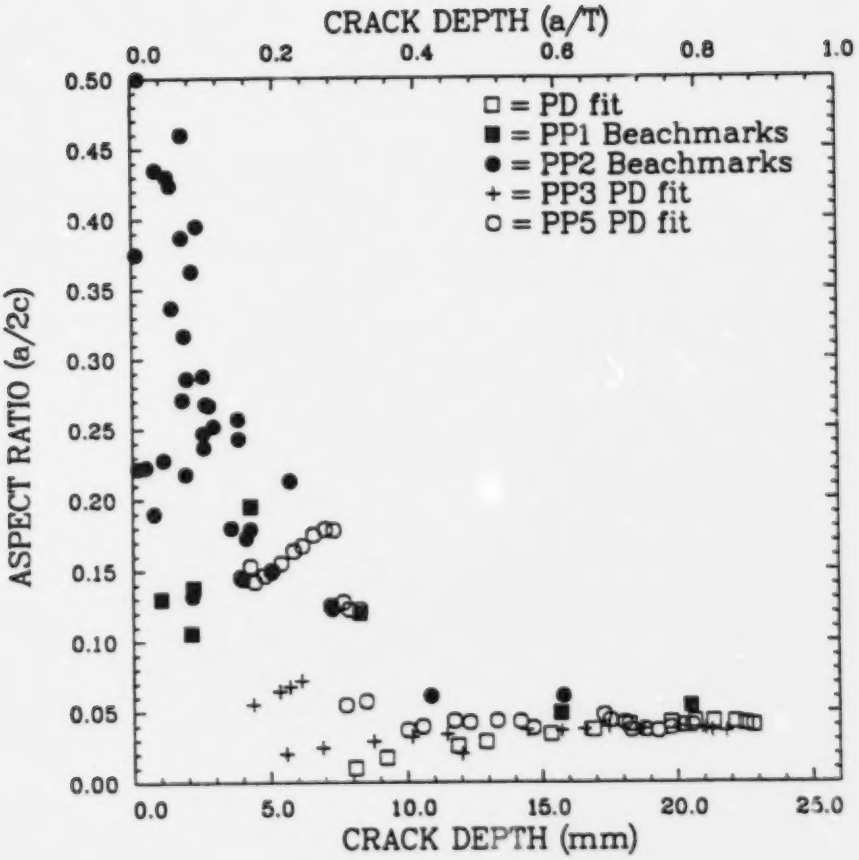

Figure 88: PP7 – aspect ratio development.

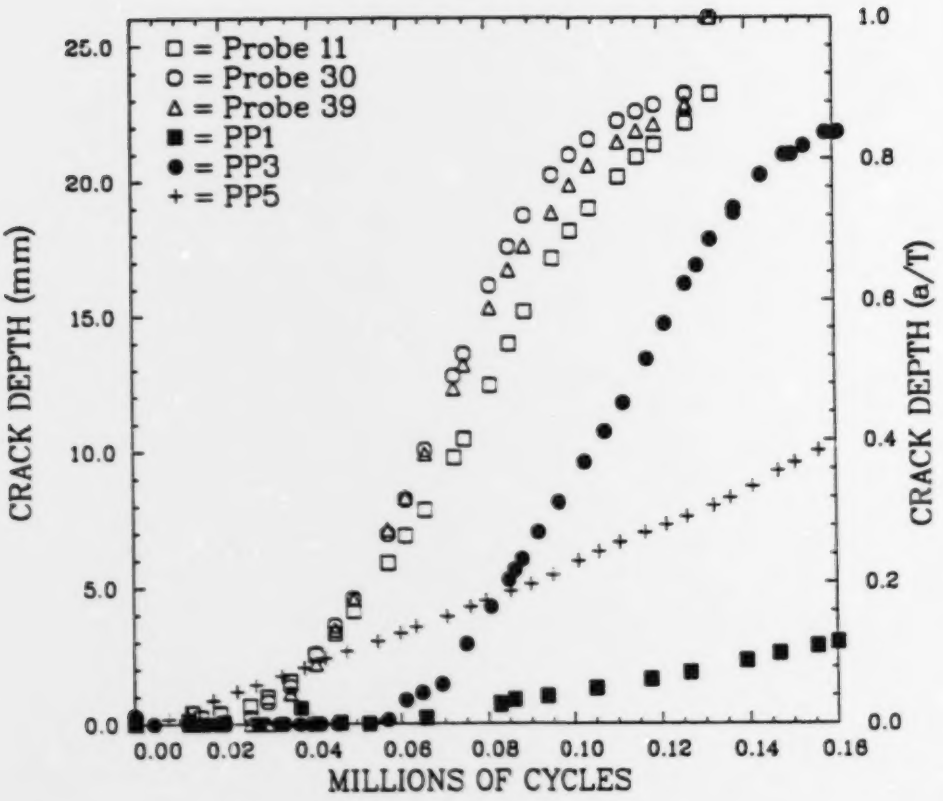

Figure 89: PP7 – crack growth behaviour.

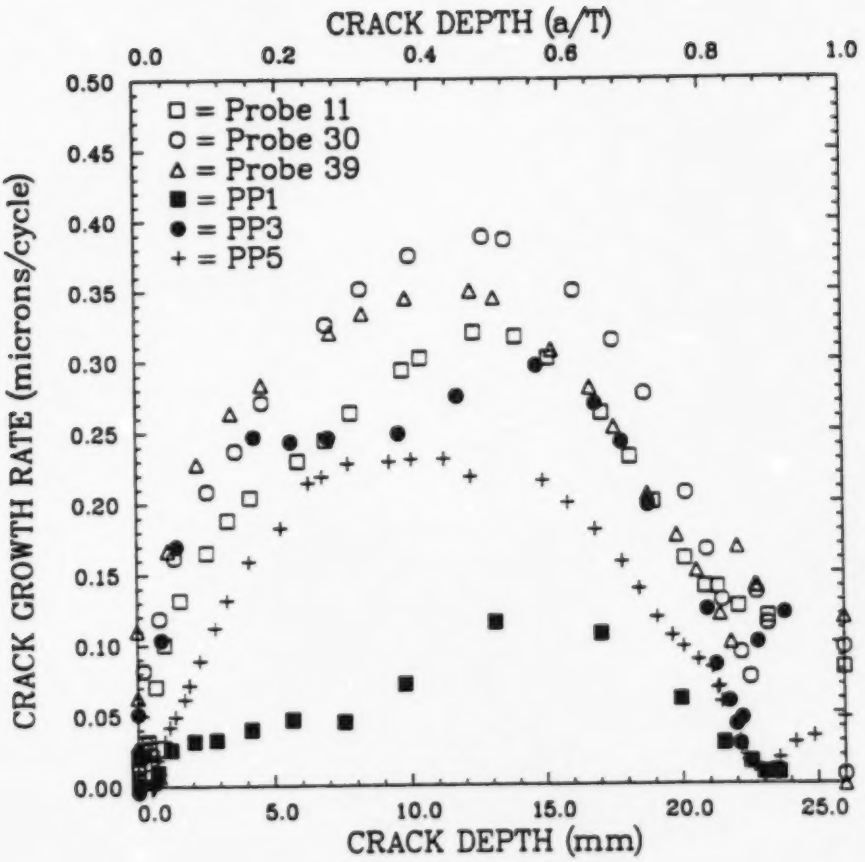

Figure 90a: PP7 – crack growth rates versus crack depth.

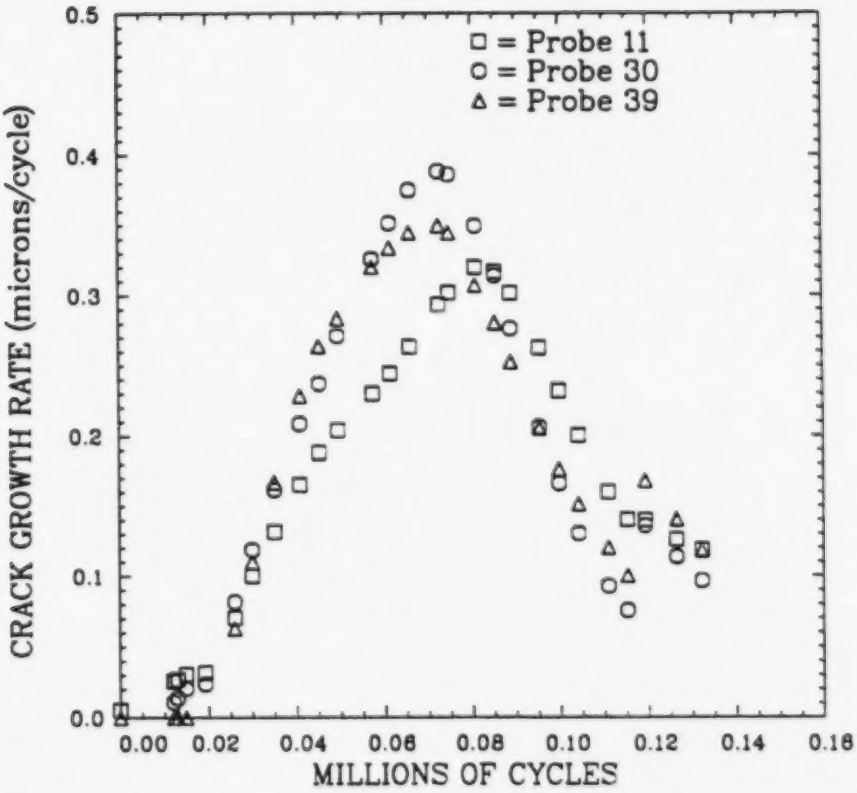

Figure 90b: PP7 – crack growth rates versus cycles.

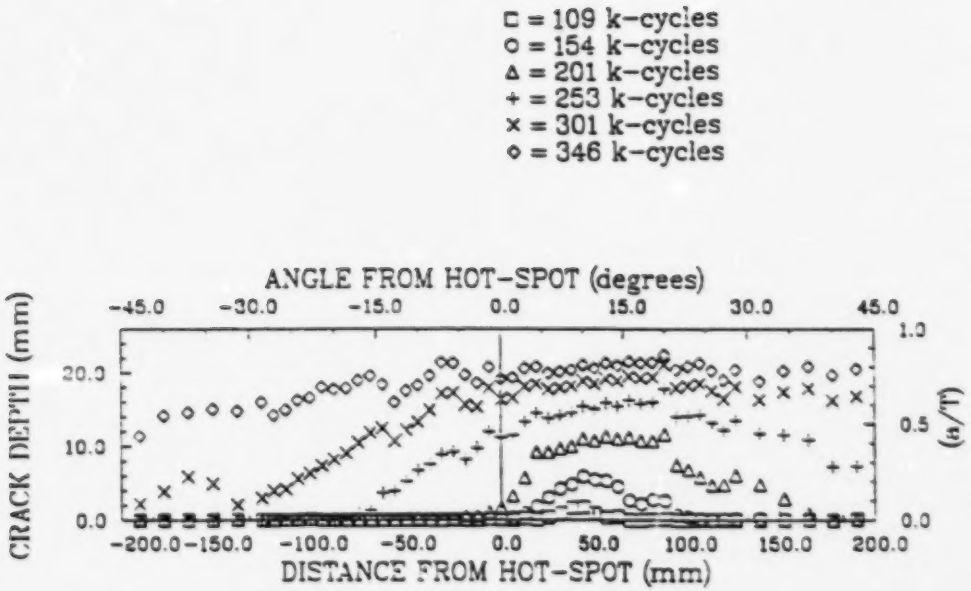

Figure 91: PP8 – crack shape development.

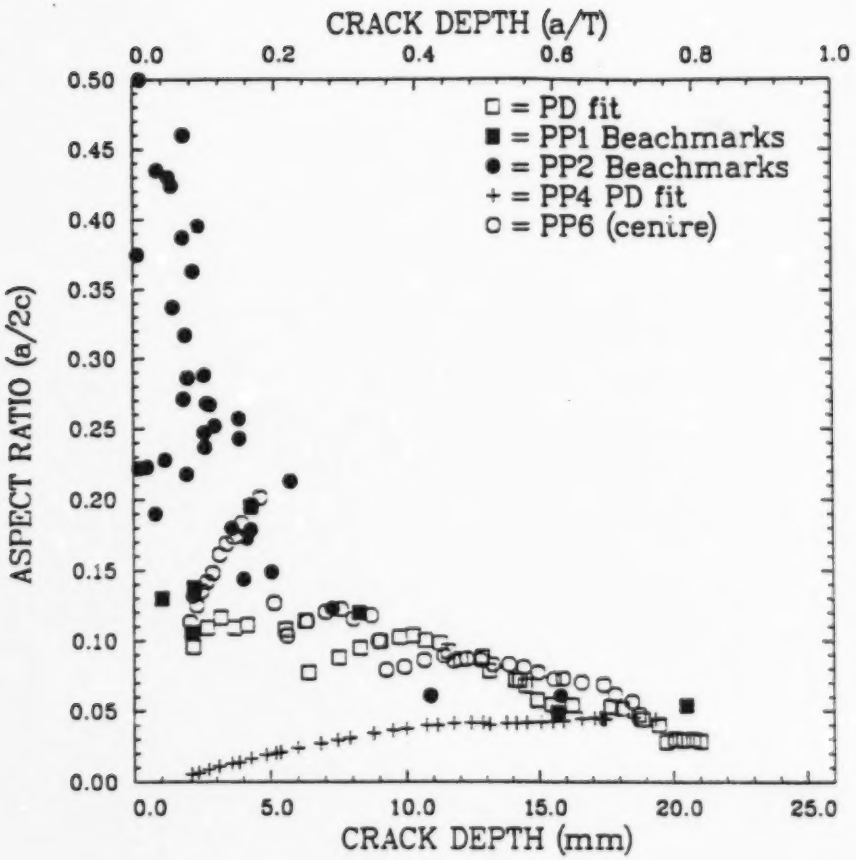

Figure 92: PP8 – aspect ratio development.

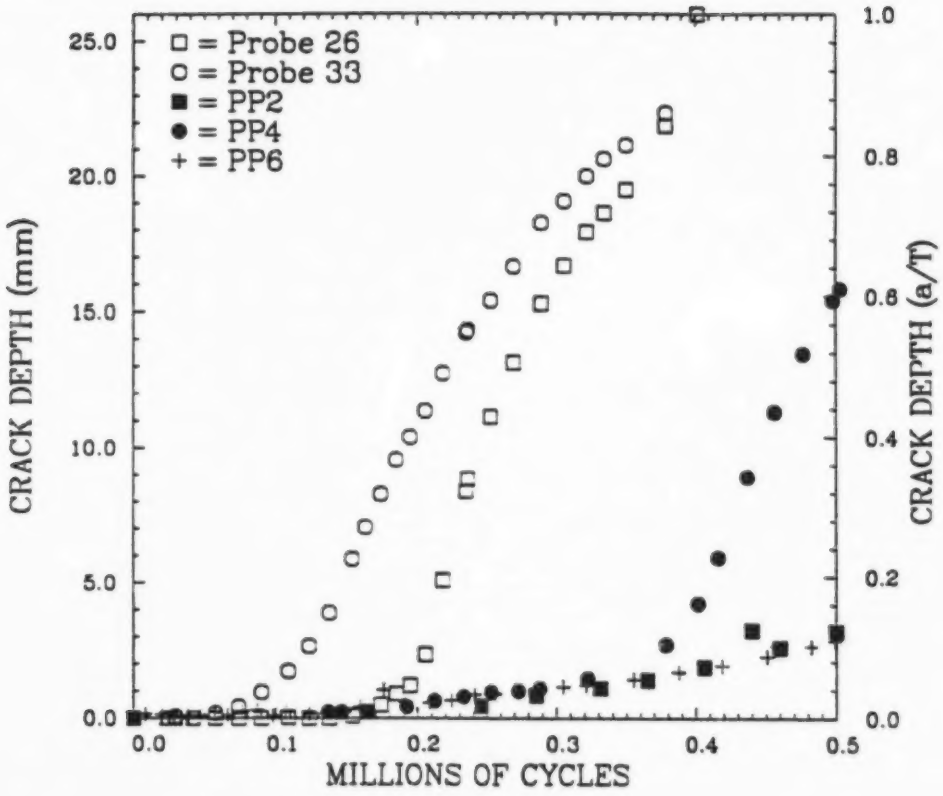

Figure 93: PP8 – crack growth behaviour.

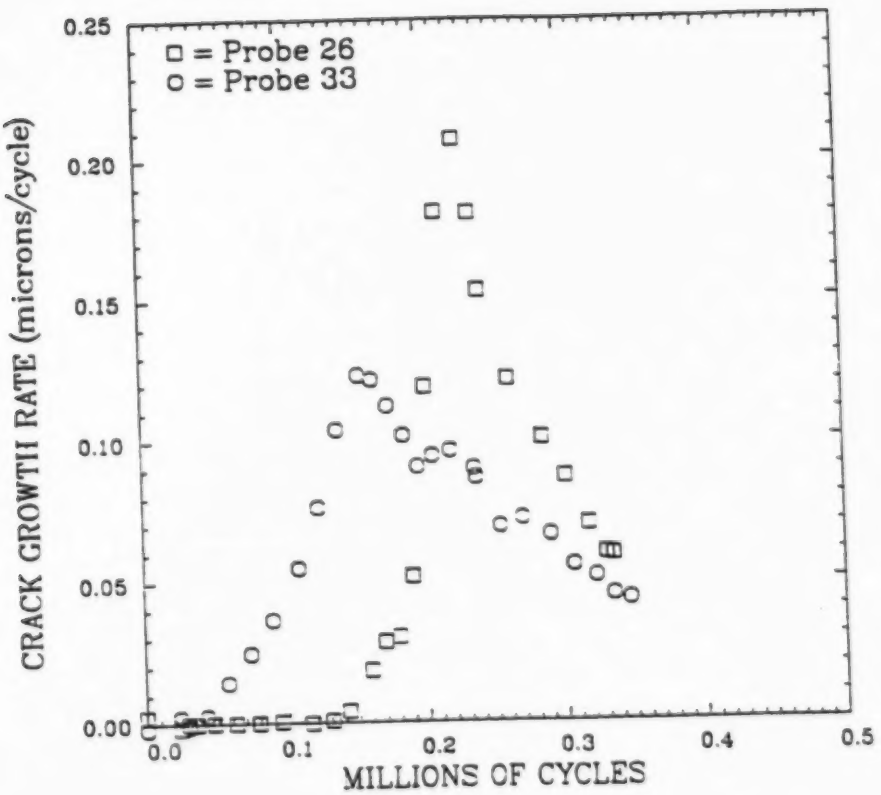

Figure 94a: PP8 – crack growth rates versus cycles.

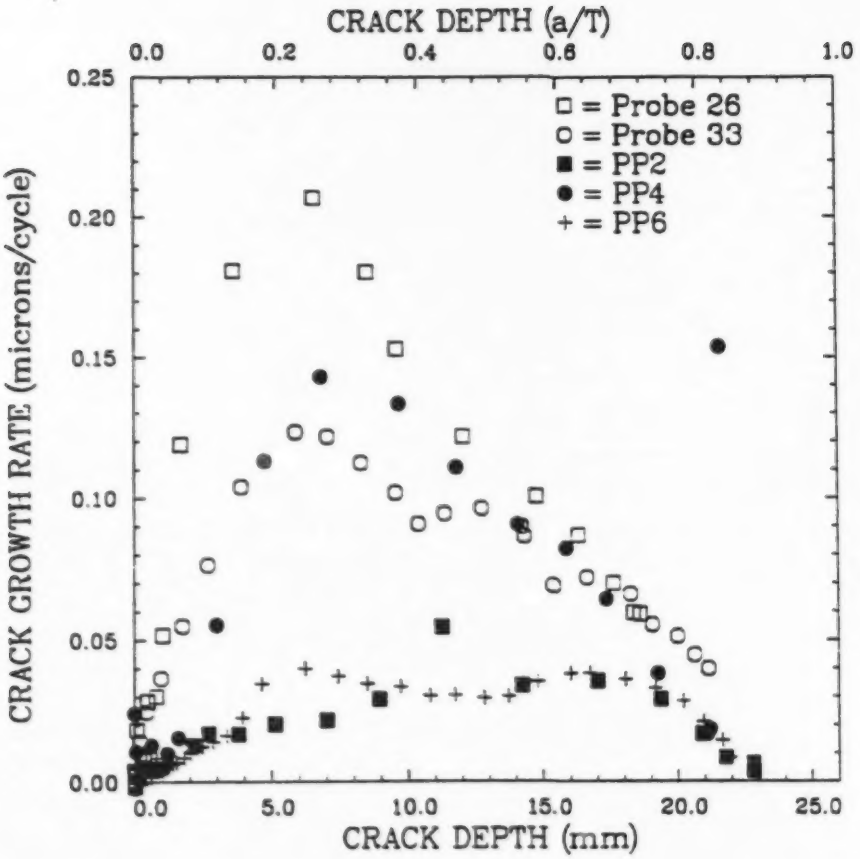

Figure 94b: PP8 – crack growth rates versus crack depth.

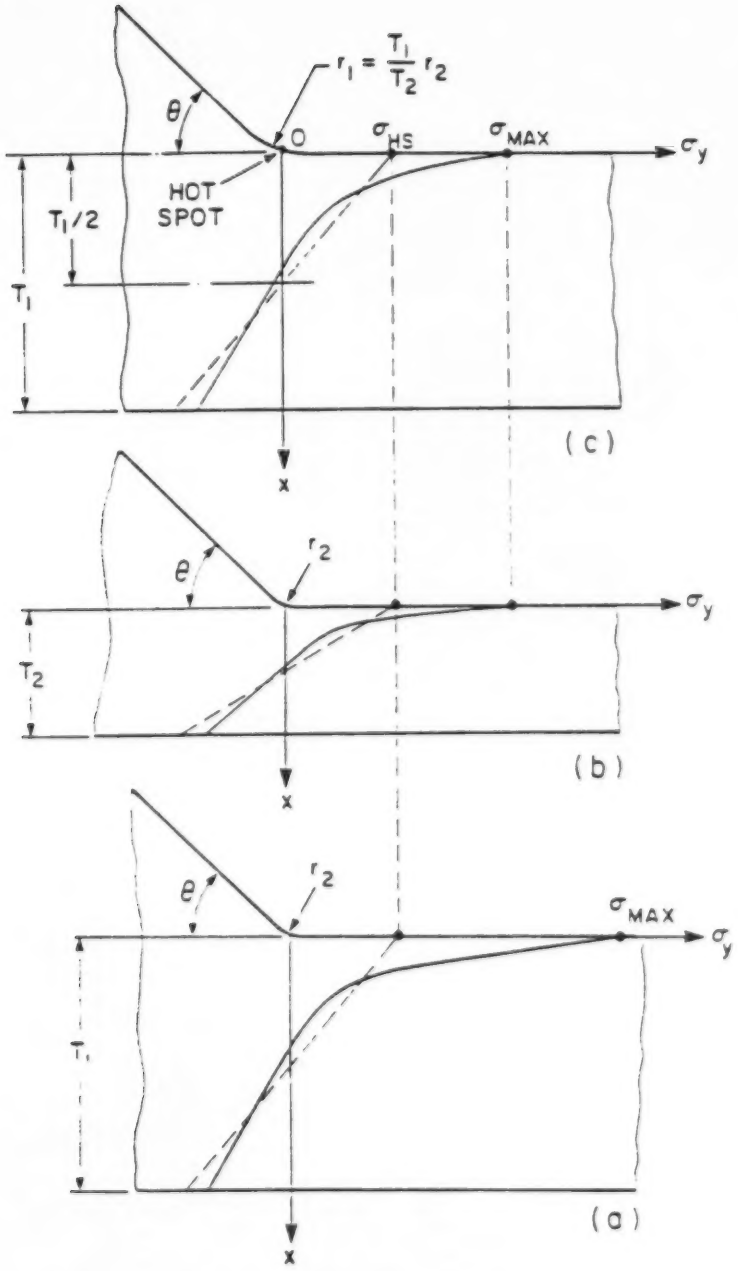

Figure 95: Stresses introduced by stress concentration and general loading

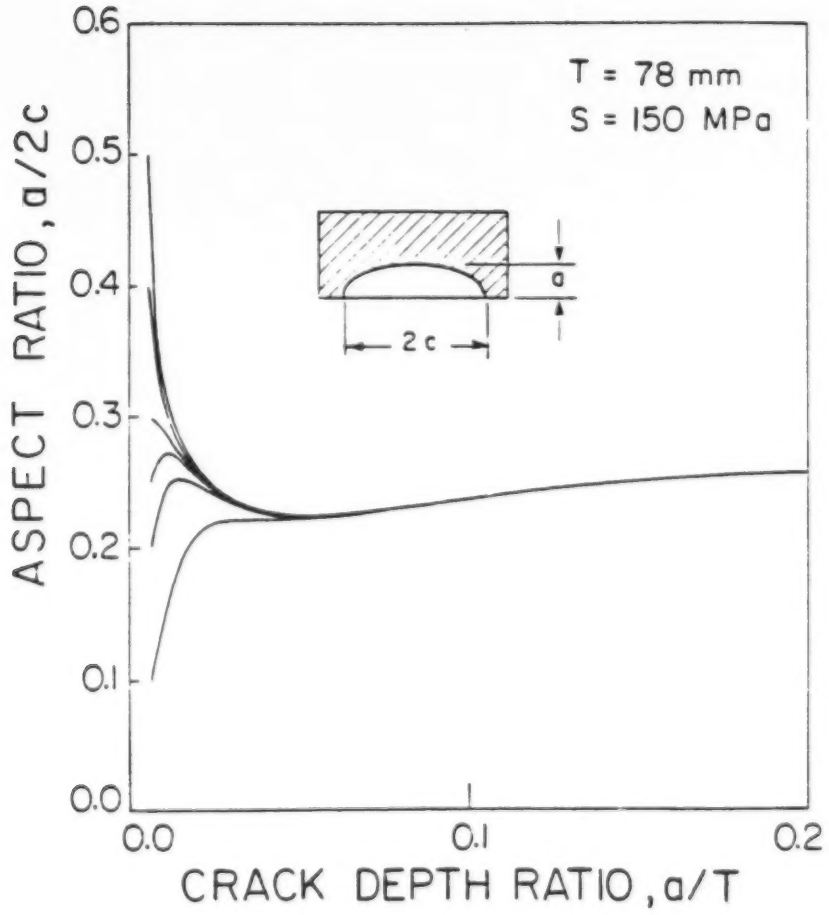

Figure 96: Predictions of crack shape development of a single fatigue crack at weld toe.

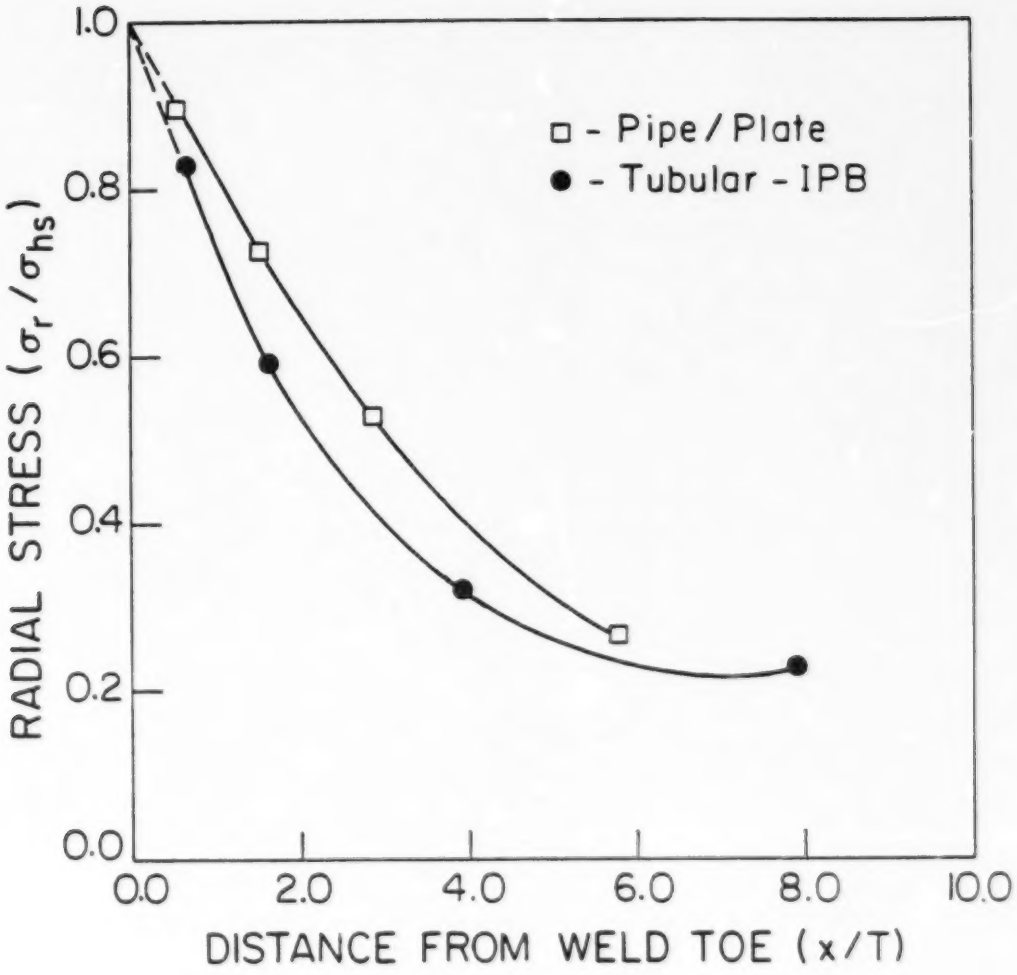

Figure 97: Radial stress distribution on plate (chord) surface – comparison with tubular joint.

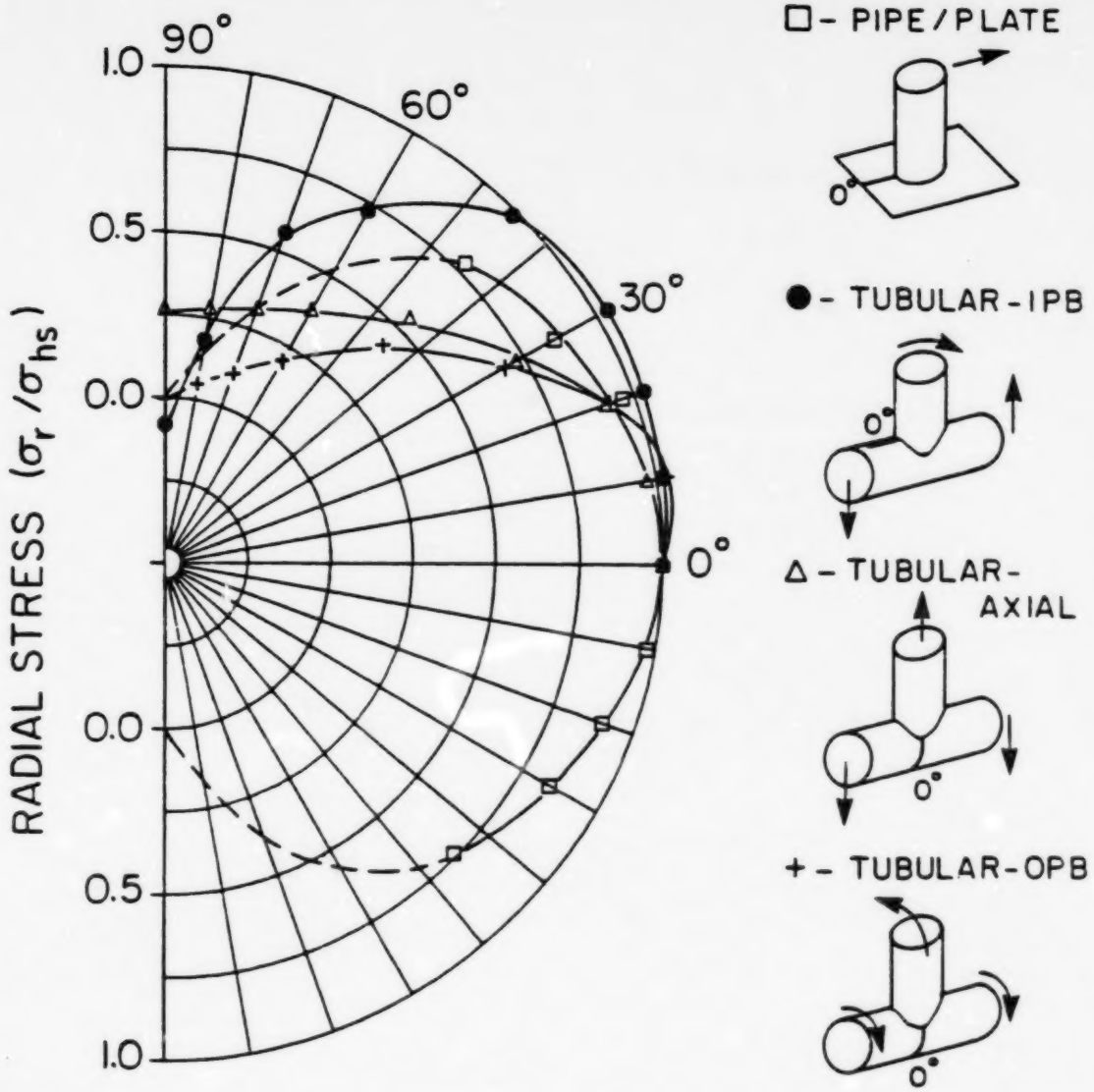

Figure 98: Radial stress distribution extrapolated to weld toe on plate (chord) surface – comparison with tubular joint.

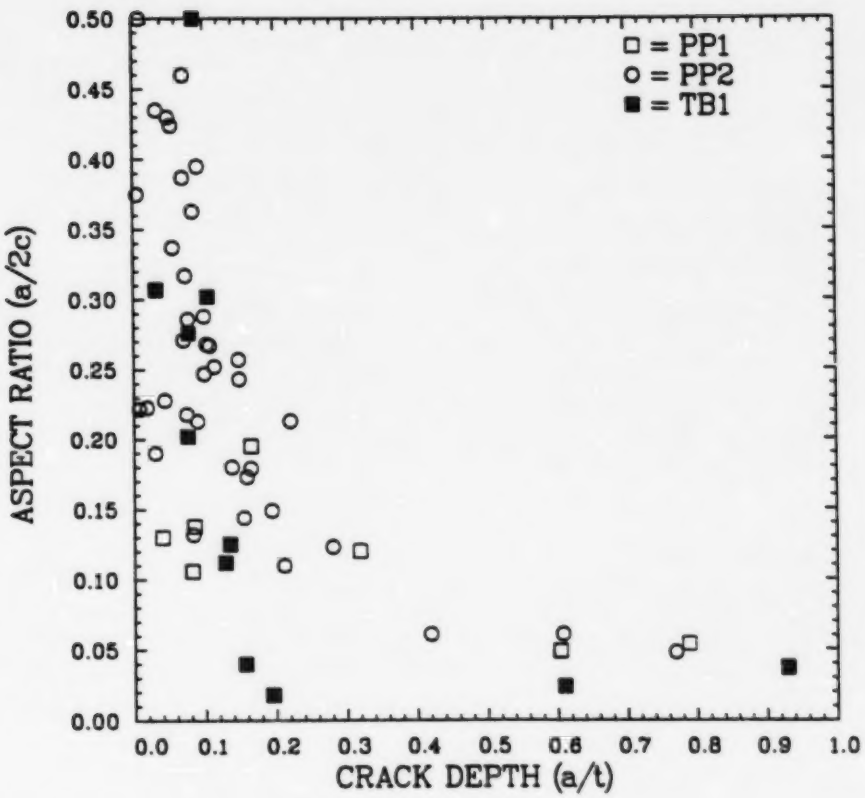

Figure 99: Aspect ratio development in pipe/plate and tubular joints.

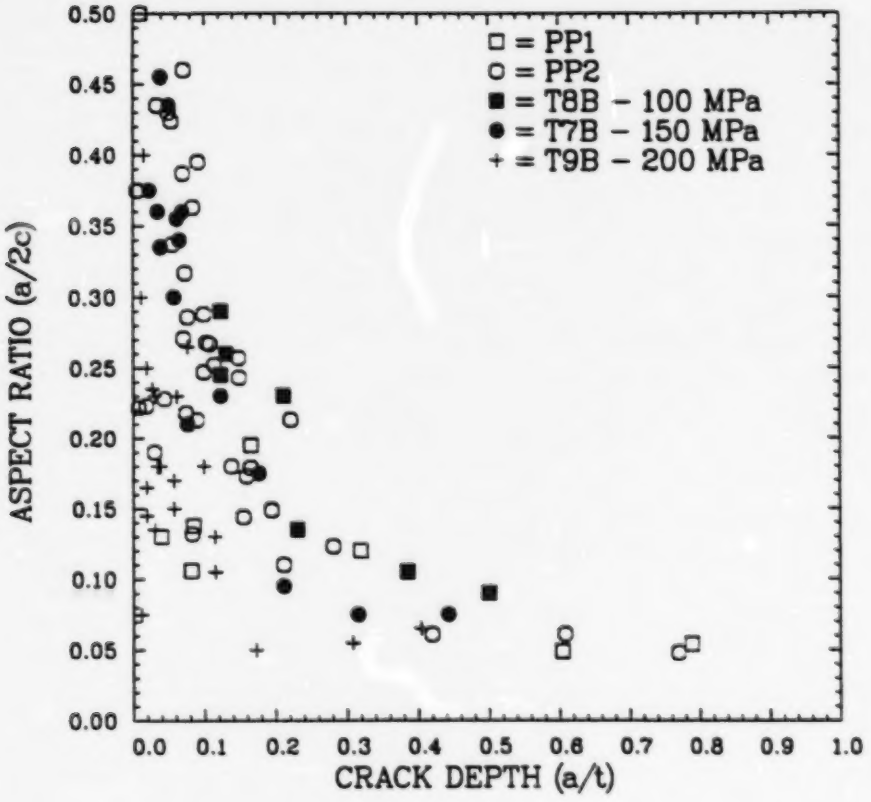

Figure 100: Aspect ratio development in pipe/plate and T-plate joints.

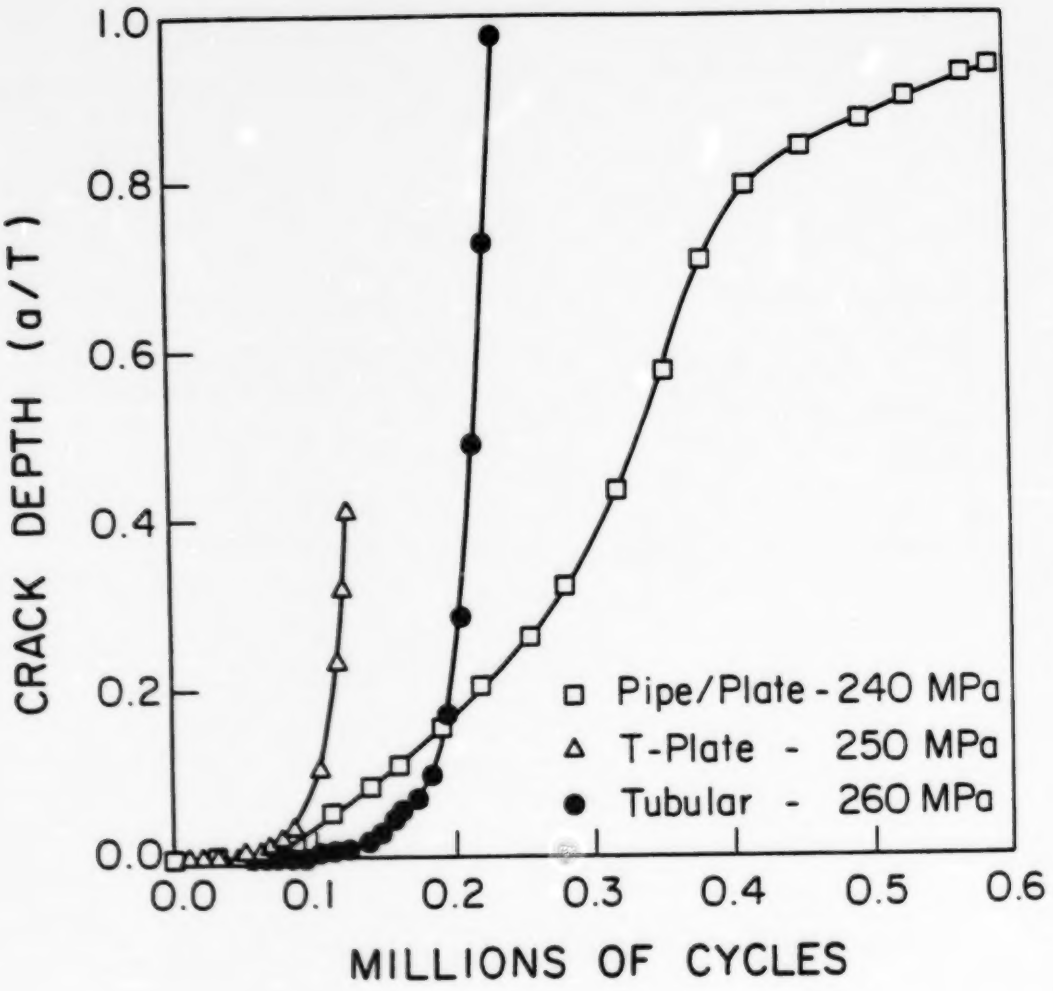

Figure 101: Crack growth in pipe/plate, T-plate and tubular joints.

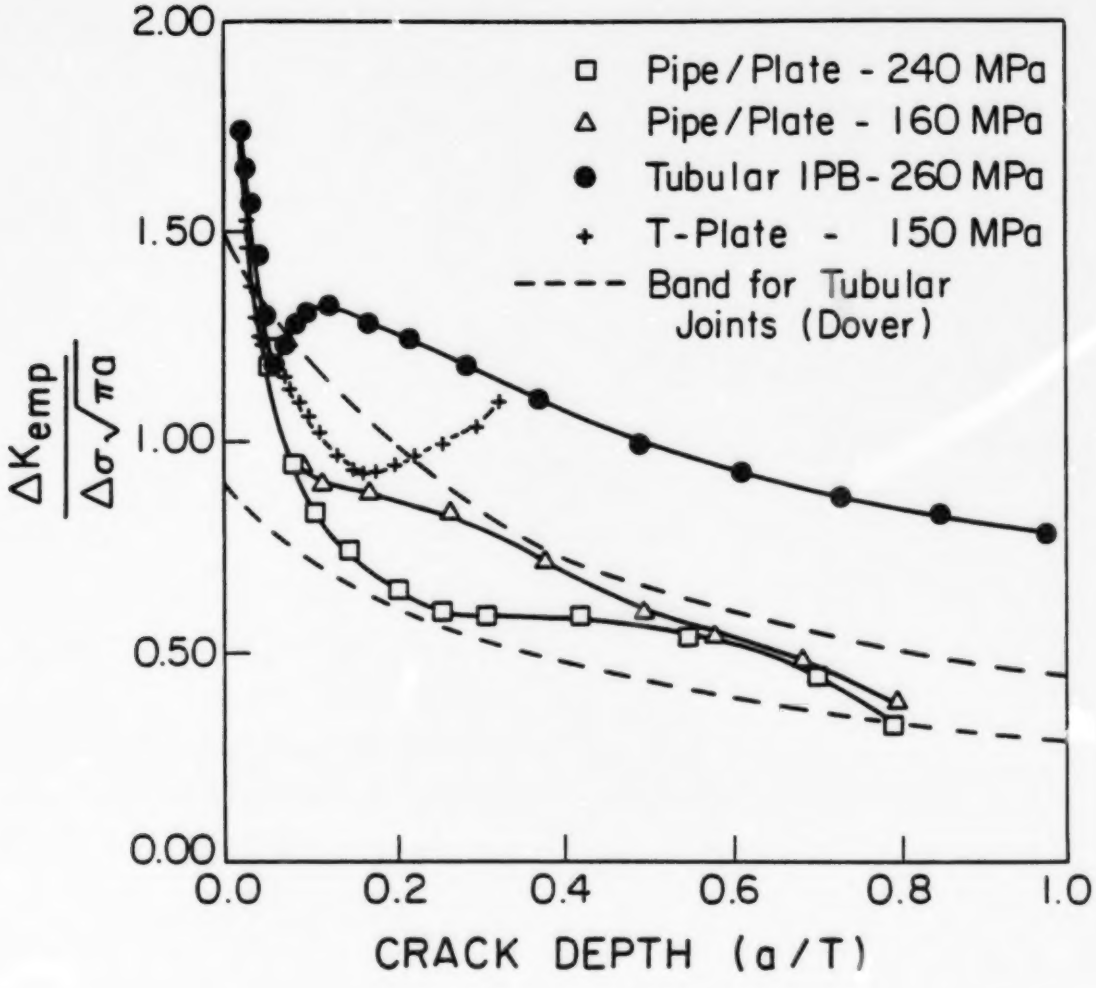

Figure 102: Empirical stress intensity correction factors, $M_k M$, in pipe/plate, T-plate and tubular joints.

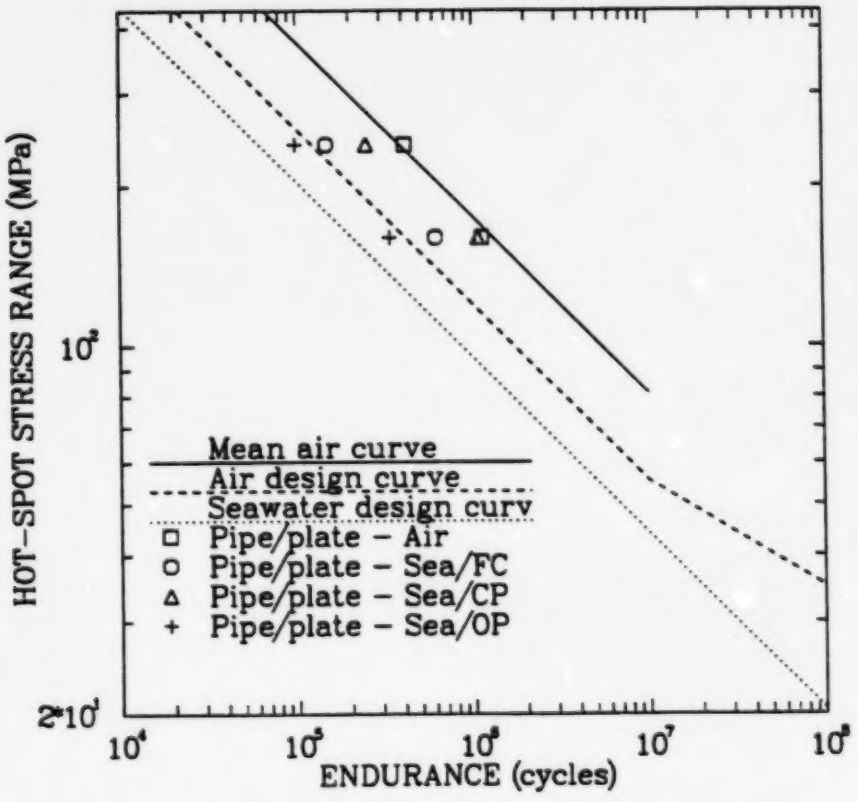

Figure 103: S-N plot of pipe/plate lives to 0.8T, i.e. fatigue life.

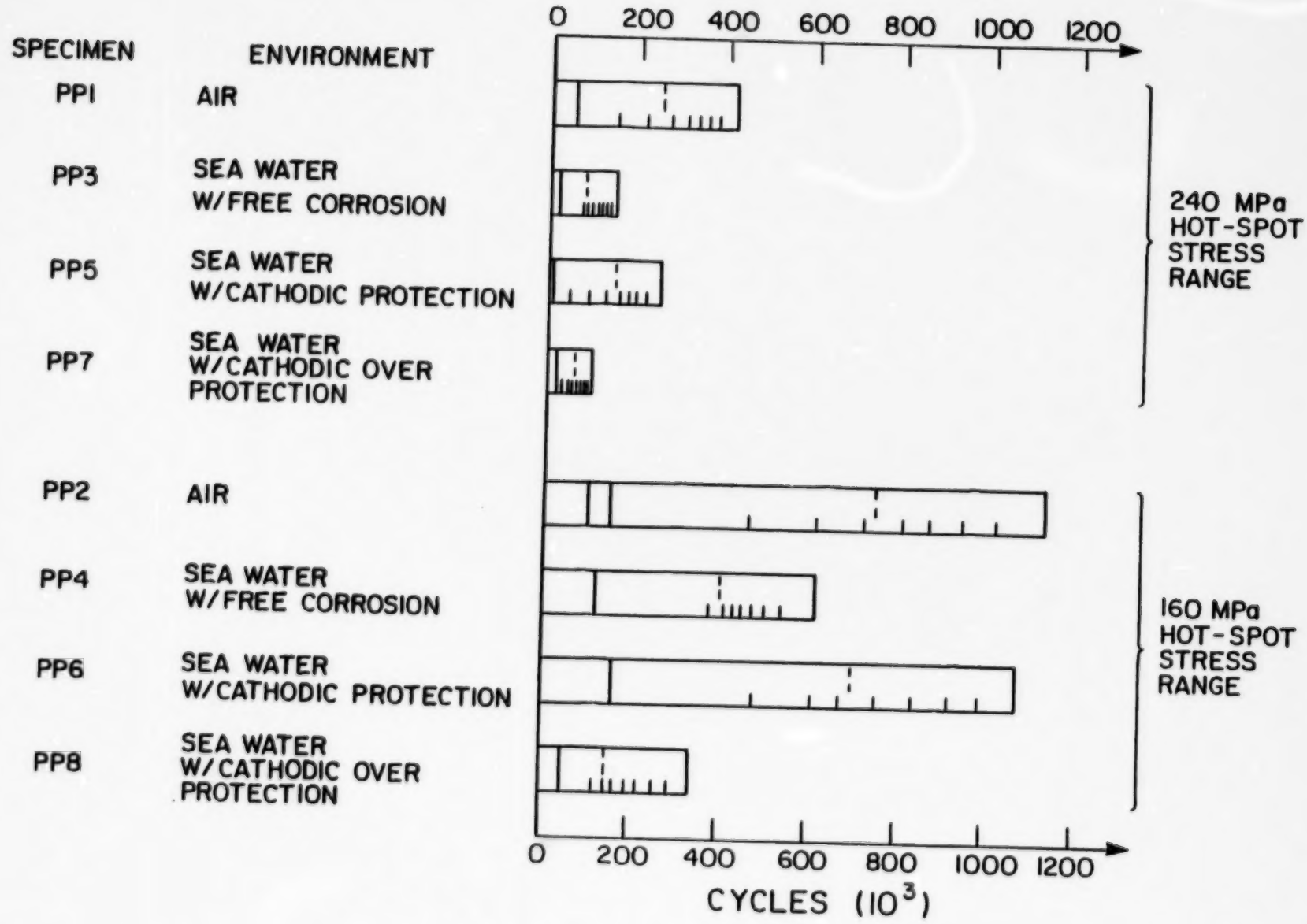

Figure 104: Summary of pipe/plate fatigue results.

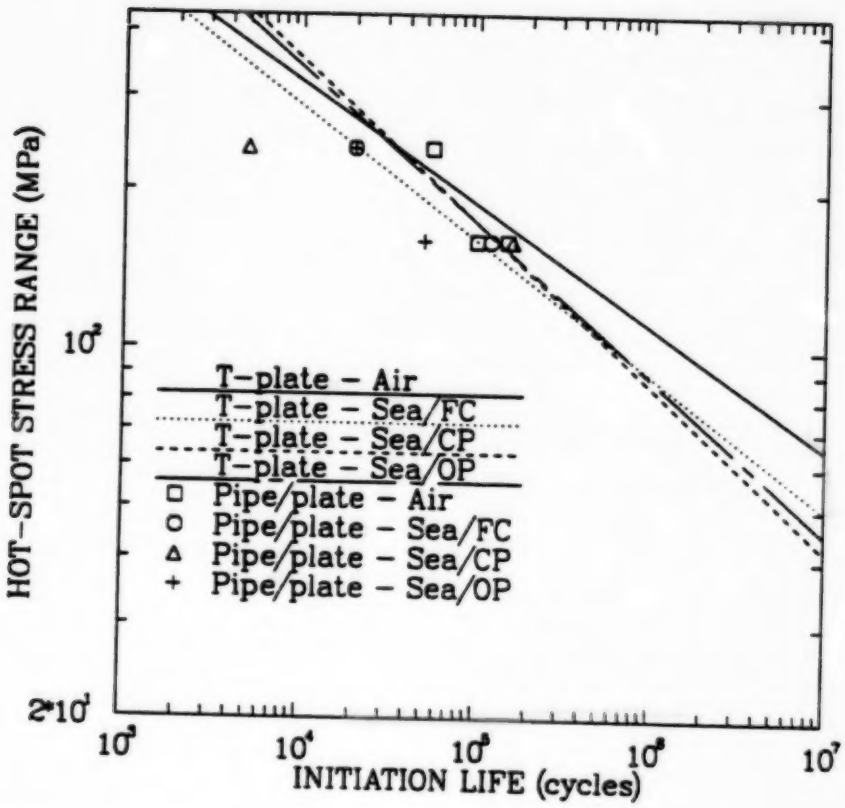

Figure 105: S-N plot of pipe/plate initiation lives, i.e. to 0.5– 1.5 mm.

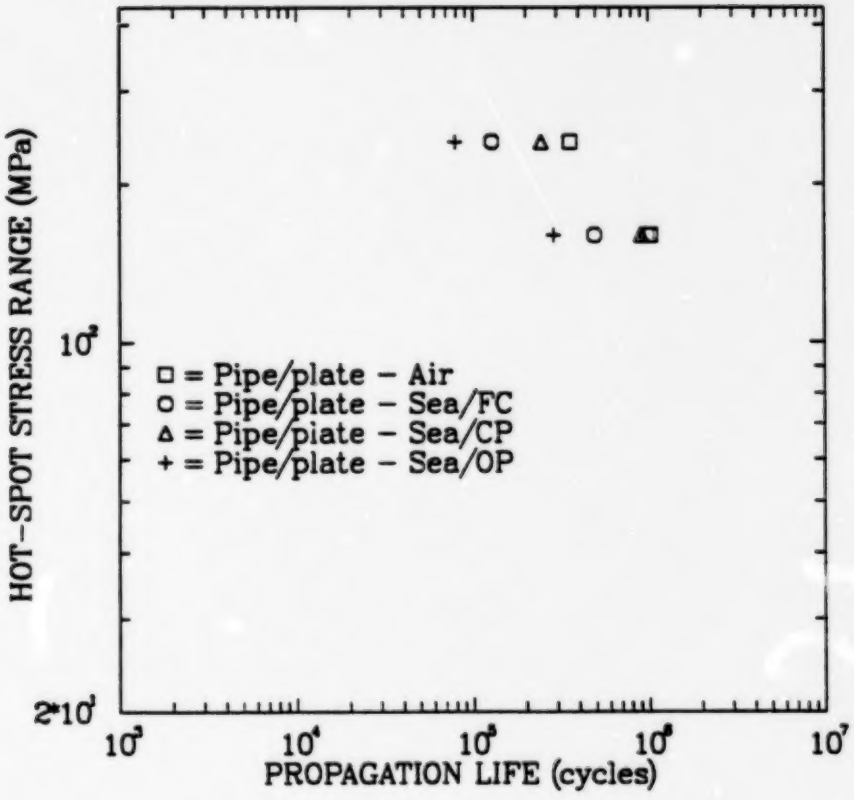

Figure 106: S-N plot of pipe/plate propagation lives.

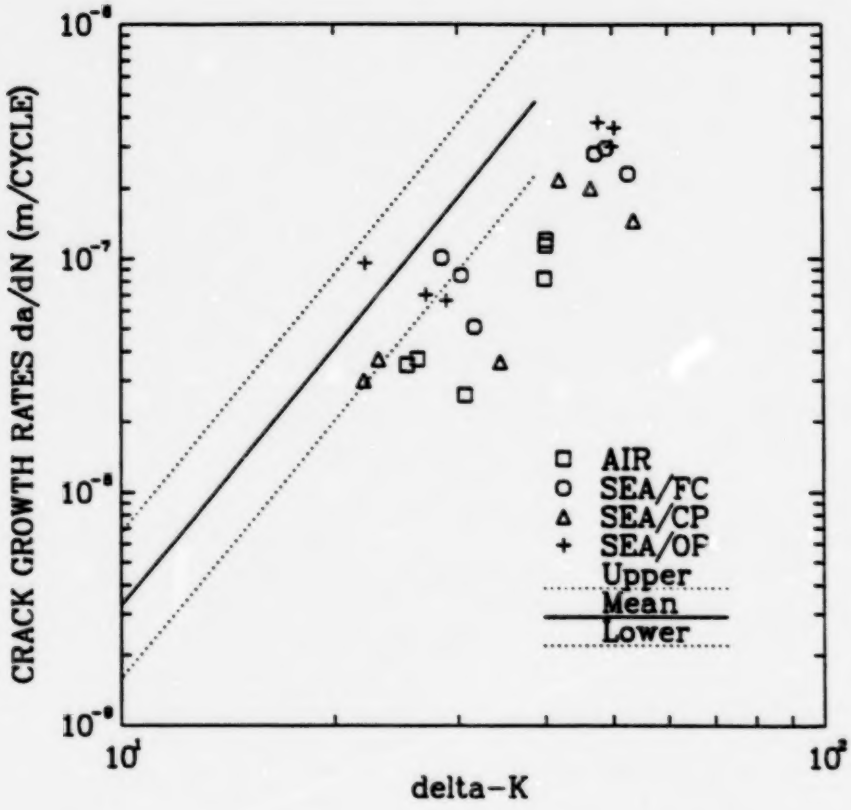

Figure 107: Pipe/plate crack growth rate behaviour.

APPENDIX I

FABRICATION DETAILS

APPENDIX 1

FABRICATION OF T-PLATES AND PIPE TO PLATES

1A. T-Plates

This phase of the program used simple T-joints with a straight 45o reinforcing fillet and utilizing the dime test at the toe of the weld to control the profile at the fatigue initiation point. Specimens were fabricated in steels conforming to either Lloyds LT60 or to CSA G40.21, Grade 350WT specifications in materials ranging from 16 to 104mm thick. Typical chemical compositions of these materials are given in Table A.

In all, a total of 29 T-plates were fabricated for test at the University of Waterloo.

All joints were fabricated in a similar fashion, i.e. in the 3G vertical up position using E48018 electrodes of 3.2 and 4.0mm diameter and adopting the stringer bead technique. A Welding Procedure Specification, BN2, is attached together with a Welding Data Sheet 2-184-037-1. No restraint was applied to the joint so that balanced welding had to be applied in order to keep the brace member of the T-plate as straight as possible with respect to the chord member which was rotating around the weld due to the contraction strains. The general welding procedure is summarized below.

Joint Type	:	45^{o} full penetration with reinforcing fillets.
Thickness	:	16mm, 25mm, 50mm, 75mm, 100mm.
Position	:	3G vertical up.
Electrode	:	E48018, 3.2mm root and cap, 4.0mm fill.
Preheat (Min.)	:	16mm and 25mm, RT, 50mm 70^{o}C, 75-100mm 120^{o}C.
Technique	:	Stringers.
Treatment	:	Root - backgouge to sound metal.
Toe Condition	:	No restraint. No postweld heat treatment. Dime test.

On completion of welding, the joints were ultrasonically tested from the back side of the chord plate to ensure that the weld metal contained no defects that could have been detrimental to the testing program. Upon release, each side of the specimen was milled down to specified size of 200mm.

1B. Pipe to Plates

The procedure for these specimens was essentially the same as that for the T-plate joints with two important differences. The welding was from one side only and was in the 2G, horizontal position.

The welding from one side only meant that the welding operator had to fuse the root correctly as back gouging to sound metal was not possible. In order to facilitate this, the operator used several mock-ups of the joint as a prequalification test which allowed proper gap setting to be studied so that the required fusion could be achieved.

After completion of welding, holes were drilled in the base plate which simulated the chord of the tubular. These holes were drilled on a pattern developed by the University of Waterloo and were to allow bolting of the chord plate to the test rig so that the stress distributed around the weld could be adjusted to simulate that occurring in a real tubular. The welding procedure for the pipe to plates is given in the Welding

Procedure Specification BN2 and the Welding Data Sheet 2-184-037-2. However, the essential details are tabulated below.

Joint Type	:	45^{o} full penetration with reinforcing fillet Thickness
Position	:	2G horizontal.
Electrode	:	E48018, 3.2mm root and cap, 4.0mm fill.
Preheat	:	Room temperature.
Technique	:	Stringers.
Treatment	:	Root fused from one side only. No restraint. No post weld heat treatment.
Toe Condition	:	Dime test.

Table A - Chemical Composition and Mechanical Properties

Chemical Composition:	*Plate Thickness (mm)*				
	16	**26**	**52**	**78**	**103**
C	0.07	0.12			0.13
Mn	1.40	1.39			1.43
Si	0.29	0.28			0.23
S	0.005	0.011			0.003
P	0.004	0.017			0.013
Al	0.045	0.027			0.015
Ni	0.25	0.15			0.24
Cr	0.25	0.17			None
Mo	None	≤0.01			None
Cu	None	0.15			None
Ti	0.012	None			0.006
V	0.075	0.053			0.06
Nb	0.022	0.41			0.02
N	0.01	-----			0.01
Mechanical Properties:					
Yield Strength (MPa)	421	405	390	370	350
UTS (MPa)	509	513	517	505	502
Elongation (%)	53	29	32	31	38

AMCA INTERNATIONAL

Welding Procedure Data Sheet
(Metric)

SPEC. No.	BN2
PROC. No.	2-184-037-1

PROCESS
Shielded Metal Arc (SMAW)

BASE MATERIAL
CSA G40.21 350WT or Lloyds LT60

WELD MATERIALS
E48018 Type

TEMP. PREHEAT / INTERPASS
See Spec'n: BN2

POLARITY
DC +ve

POSITION
3G

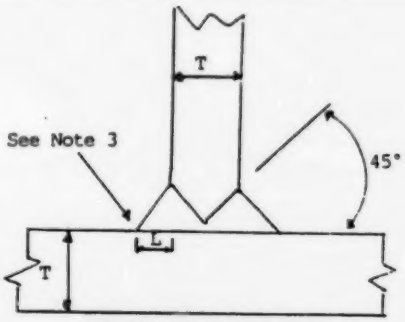

TYPICAL JOINT GEOMETRY

T	WELD SEQUENCE			ELECTRODE		WELDING VARIABLES				
	SIDE	LAYER	PASS	TYPE	SIZE mm	AMPS	VOLTS	E.S.O.	SPEED - mm/m	WFS - ipm
	1	1	1	E48018	3.2	125	20		125-150	
15	1	2-Cap	2-Cap	E48018	4.0	160	21		125-150	
to	1	Cap	Cap	E48018	3.2	125	20		125	
100mm										
		Backgouge and Grind Root								
	2	Repeat as above -- see notes								
	L.	As per tolerance described in client drawings.								

QUALIFICATION
Prequalified

BCS - CWB
N.A.

AMCA REGISTERED PROFESSIONAL ENGINEER M. J. PATES PROVINCE OF ONTARIO

NOTES
1. Root to be inspected visually.
2. Use balanced welding technique as component is not restrained.
3. Toe to conform to Dime Test as per Specification BN2.
4. UT from flange on completion.

DATE March 1984

EM-6/87

AMCA INTERNATIONAL

Welding Procedure Data Sheet
(Metric)

SPEC. No.	BN2
PROC. No.	2-184-037-2

PROCESS	Shielded Metal Arc (SMAW)
BASE MATERIAL	CSA G40.21 350WT or Lloyds LT60
WELD MATERIALS	E48018 Type
TEMP. PREHEAT / INTERPASS	See Spec'n: BN2
POLARITY	DC +ve
POSITION	2G

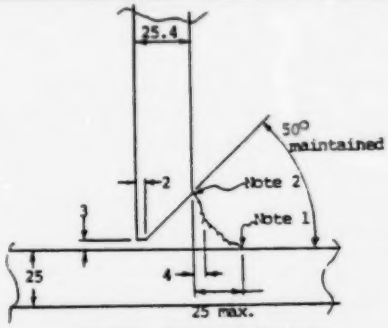

TYPICAL JOINT GEOMETRY

T	WELD SEQUENCE			ELECTRODE		WELDING VARIABLES				
	SIDE	LAYER	PASS	TYPE	SIZE mm	AMPS	VOLTS	E.S.O.	SPEED - mm/m	WFS - ipm
25	1	1	1	E48018	3.2	130	20		125	
	1	2-Cap	2-Cap	E48018	4.0	160	21		125-175	
	1	Cap	Cap	E48018	3.2	130	20		125	

QUALIFICATION

Prequalified

BCS - CWB

N.A.

AMCA

REGISTERED PROFESSIONAL ENGINEER
M. J. PATES
PROVINCE OF ONTARIO

NOTES

1. Root to be visually inspected.
2. Top pass to pipe to be blended.
3. Toe to conform to Dime Test as per Specification BN2.

DATE January 1985

EM-6/87

WELDING PROCEDURE SPECIFICATIONS - BN2

CLIENT: Department of Supply and Services for CANMET EMR

AMCA INTERNATIONAL Ref. No. BN2

Contract No. 2-184-037-099

DSS File No. 15SQ-23440-3-9104

Prepared by Gaston Proulx

Approved by .....
M.J. Pates
Project Manager

Welding Procedure Specification (WPS)

Welding Procedure Specification for the Welding of Tee Joints by the Manual Shielded Metal Arc Process in G40.21 Grade 350 WT Materials and Lloyds LT60

1. Scope

This specification covers welding and related operations for the fabrication of Tee type joints, and is generally in accordance with CSA Standard W59-1982 "Welded Steel Construction" (Metal Arc Welding).

2. Related Specifications

CSA W59-1982	Welded Steel Construction (Metal Arc Welding)
CSA W48.1-M1980	Mild Steel Covered Arc Welding Electrodes
CSA W47.1-1973	Certification of Companies for Fusion Welding of Steel Structures
UKOSRP	United Kingdom Offshore Steels Research Project - Guidelines
CSA G40.21	Structural Quality Steels

3. Welding

Welding will be performed by the Manual Shielded Metal Arc Process.

4. Base Metal

The base metal shall conform to the requirements of CSA G40.21 Grade 350 WT "Weldable Notch Tough Steel", or its equivalent.

5. Base Metal Thickness

This specification covers the welding the base metal in thicknesses up to 100mm.

6. Consumables

a) Electrodes shall be based electrodes in accordance with the requirements of CSA Standard W48.1 and shall be of the E48018 classification.

b) Storage and conditioning of electrodes shall be carried out in accordance with the requirements shown in Section 22 of this specification.

7. Weld Preparation

The welding preparation shall conform generally to the joint type M5-2 for the T-joints and M4-4 without backing for the pipe to plate joints.

8. Position of Welding

Welding shall be in the vertical up welding position (3G) for straight T joints. Welding will be in the horizontal welding position (2G) for pipe to plate joints.

9. Electrode Size and Weave

a) The electrode diameters shall be as follows:

Root Run	3.25mm diameter electrode
Fill to Cap	3.25 or 4.0mm diameter electrodes

b) Maximum permissable weave allowed during Vertical Welding

3-1/4mm	Max. Weave = 8mm
4mm	Max. Weave = 10mm

10. Preparation

Edges and surface of parts to be welded shall be prepared by flame-cutting. They shall be smooth, uniform and free from fins, tears, cracks and other defects which would adversely affect the quality or strength of the weld. Surfaces to be welded shall also be free, within two inches of any weld location, from loose or thick scale (except for tightly adhering small islands of scale), slag, rust, paint, grease, moisture and other foreign material that will prevent proper welding or produce objectionable fumes.

11. Run-Off Plates

Run-off plates used for the welding may be any of the steels or their equivalents as defined in CSA W59.

12. Preheat

a) Prior to tacking or welding, the base metal shall be preheated and the heat maintained during welding at the minimum temperature shown in the following table.

Up to 15mm inc.	None*
Over 15mm to 38mm inc.	15°C
Over 38mm to 60mm inc.	70°C
Over 60mm	120°C

*When the base metal temperature is below 0°C, preheat the base metal to 15°C and maintain this temperature during welding.

b) Preheating will be accomplished by means of flame torches.

c) Preheating shall consist of heating a band of the base metal equal to the thickness of the base metal, but not less than 3 inches on either side of the joint to the desired temperature, and maintaining this temperature during welding.

13. Distortion Control

a) In assembling and joining, the procedure and sequence shall be such as will minimize distortion and shrinkage.

b) In so far as practicable, all welds shall be deposited in a sequence that will balance the applied heat of welding while the welding progresses.

14. Electrical Characteristics

The type of current, polarity and typical current value for any electrode class or size shall be substantially as shown in the attached Welding Data Sheets and may be altered to within 15% above or below the typical value.

15. Workmanship

All welding and its related operations shall be performed in accordance with good welding practice and within the recommendations and limitations outlined in CSA W59-1982.

16. Appearance of Welding Layers

The welding current and the manner of depositing the weld metal shall be such that undercutting on the side walls of the welding groove or the adjoining base material shall be limited to .25mm for areas subject to fatigue testing.

17. Cleaning

Cleaning of previously deposited layers shall be done by wire brushing or by mechanical means, if necessary, before the next layer is deposited.

18. Defects

Surface defects appearing on any weld bead shall be removed by grinding and rewelded, if necessary, before the next layer is deposited.

19. Treatment of Second Side of Welding Groove

The root of the joint shall be arc-gouged, when required by the WDS, to produce a groove contour substantially conforming to the prequalified single U-joint, and its depth shall be adequate to ensure complete penetration into the previously deposited weld metal.

20. Finished Joint Profile

The weld profile shall conform to a 45^{0} reinforcing fillet as shown in the attached figure, and the capping runs shall be carried out by first depositing a buttering run, to give a good weld toe angle and then filling in the bulk of the capping runs. In all cases, the weld toe angle shall conform to the "dime" test as indicated in the figure. That is, a disc of radius t/2 (but the radius shall be a minimum of 8mm and a maximum of 25mm) shall be placed against the buttering weld run and the longitudinal plate, and a 1mm diameter wire shall not pass between the disc and the buttering run in the weld toe region. In all cases, the maximum amount of undercut at the weld toe shall not exceed 0.25mm. Weld leg lengths shall be as described by the Client.

21. Post Weld Heat Treatment

Post weld heat treatment is not required.

22. Storage and Conditioning of Electrodes

Basic Electrodes - All basic electrodes should be delivered in hermetically-sealed containers. All containers showing evidence of damage should not be accepted.

When a container is opened, all electrodes shall be stored in ovens held at a temperature of at least 120^{o}C.

Basic electrodes of E480 classification that are not used within 4 hours after removal from ovens shall be discarded.

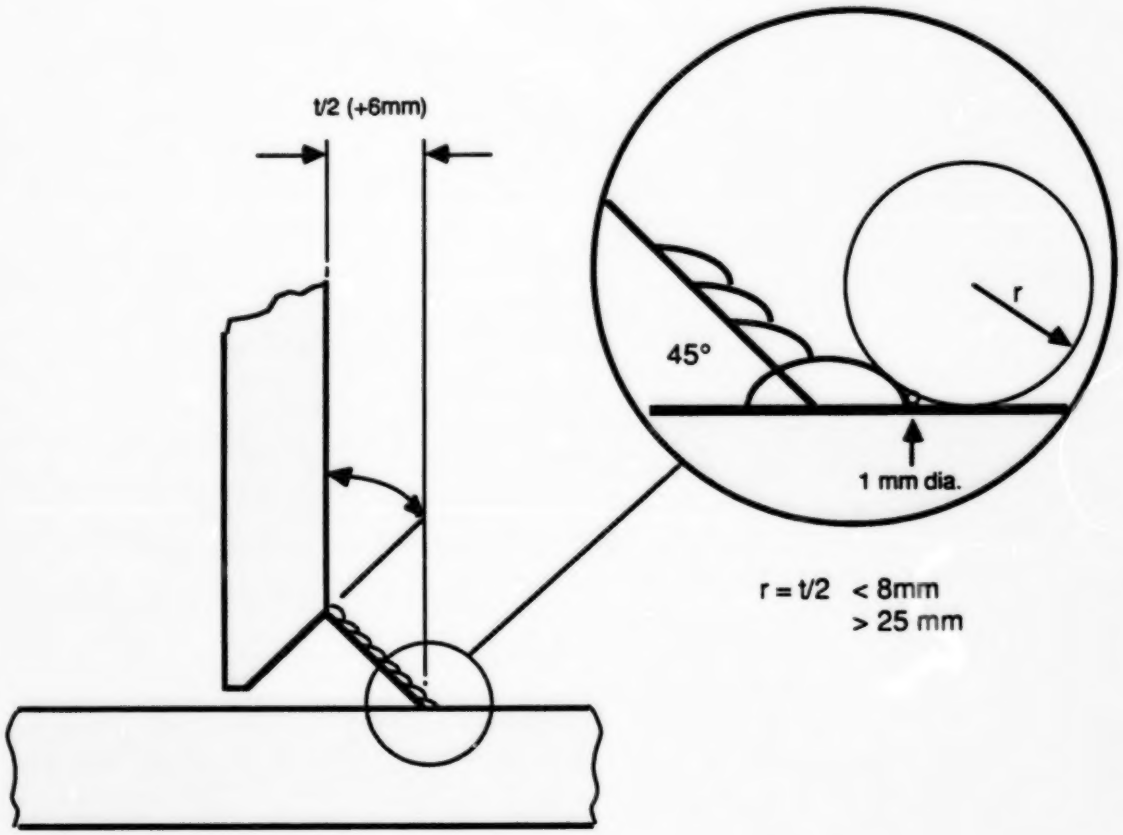

Dime Test